STUDY OF ELECTROSTATIC INSTABILITIES IN CURRENT CARRYING COLD PLASMAS

By

ROOPENDRA SINGH RAJAWAT

(PHYS06201104011)

Institute for Plasma Research, Gandhinagar

A thesis submitted to the

Board of Studies in Physical Sciences

In partial fulfillment of requirements

for the Degree of

DOCTOR OF PHILOSOPHY

of

HOMI BHABHA NATIONAL INSTITUTE

May 2018

Homi Bhabha National Institute

Recommendations of the Viva Voce Committee

As members of the Viva Voce Committee, we certify that we have read the dissertation prepared by Roopendra Singh Rajawat entitled "Study of electrostatic instabilities in current carrying cold plasmas" and recommend that it may be accepted as fulfilling the dissertation requirement for the award of Degree of Doctor of Philosophy.

____ Date:

Chairman - Prof. Amita Das

____ Date:

Guide/Convener - Prof. Sudip Sengupta

____ Date:

Examiner - Prof. Ashwini Kumar Sinha

____ Date:

Member 1 - Dr. R. Srinivasan

____ Date:

Member 2 - Dr. Devendra Sharma

____ Date:

Member 3 - Dr. Mrityunjay Kundu

Final approval and acceptance of this dissertation is contingent upon the candidate's submission of the final copies of the thesis to HBNI.

I/We hereby certify that I/we have read this thesis prepared under my/our direction and recommend that it may be accepted as fulfilling the thesis requirement.

Date:

Place: **Guide**

STATEMENT BY AUTHOR

Roopendra Singh Rajawat

DECLARATION

I, hereby declare that the investigation presented in the thesis has been carried out by me. The work is original and has not been submitted earlier as a whole or in part for a degree / diploma at this or any other Institution / University.

Roopendra Singh Rajawat

List of Publications Arising from the Thesis

1. *One dimensional PIC simulation of relativistic Buneman instability*, Roopendra Singh Rajawat and Sudip Sengupta, Physics of Plasmas 23, 102110 (2016)

2. *Particle-in-cell simulation of Buneman instability beyond quasilinear saturation*, Roopendra Singh Rajawat and Sudip Sengupta, Physics of Plasmas 24, 122103 (2017)

3. *Stationary Bernstein-Greene-Kruskal structures in a current carrying relativistic cold plasma*, Roopendra Singh Rajawat, Sudip Sengupta and Nikhil Chakrabati, arXiv:1805.00095v1 (2018)

4. *Study of decay of electron current in the presence of relativistically intense space charge wave*, Roopendra Singh Rajawat and Sudip Sengupta, **to be submitted**

Conferences and Symposium Presentations

1. **Roopendra Singh Rajawat**, Sudip Sengupta, *Study of linear and nonlinear evolution of Buneman instability* , Poster presentation in 28th National Symposium on Plasma Science & Technology (Plasma - 2013), 3rd-6th Dec., 2013, Bhubaneswar, India.

2. **Roopendra Singh Rajawat**, Sudip Sengupta, *Particle-in-cell simulation of Buneman instability*, Poster presentation in 29th National Symposium on Plasma Science and Technology & International Conference on Plasma Science and Nanotechnology (Plasma - 2014), 8th-11th Dec., 2014, Kottayam, Kerala, India.

3. **Roopendra Singh Rajawat** and Sudip Sengupta *1D PIC simulation of relativistic Buneman instability*, Poster presentation in 10th Asia Plasma and Fusion Association Conference (APFA - 2015), 14th-18th Dec., 2015, Gandhinagar, India.

4. **Roopendra Singh Rajawat**, Sudip Sengupta, *One dimensional Particle-in-cell simulation of relativistic Buneman instability*, Poster presentation in 43^{rd} IEEE International Conference on Plasma Science, 19th-23rd June, 2016, Banff, Alberta, Canada.

5. **Roopendra Singh Rajawat**, Sudip Sengupta, *PIC simulation of Buneman instability*, Poster presentation in 32nd National Symposium on Plasma Science and Technology (Plasma - 2017), 7th-10th November, 2017, Gandhinagar, India.

6. **Roopendra Singh Rajawat**, Sudip Sengupta, *Excitation of coupled hole-solitons during nonlinear evolution of Buneman instability*, Poster presentation in National Conference on Plasma Simulations, 17th-19th January, 2018, IISc Banglore, India.

Schools Attended

1. DST-SERC School on Tokamaks and Magnetized Plasma Fusion, 25th Feb. to 15th March, 2013, IPR, Gandhinagar, Gujarat, India.

DEDICATIONS

To My Family

&

Friends

ACKNOWLEDGEMENTS

At the very outset, I convey my hearty gratitude to my thesis supervisor Prof. Sudip Sengupta. His diligent, friendly and spirited support and guidance through this long journey has been the source of inspiration for me. His enthusiasm, impeccable patience and understanding and availability for discussion made the journey much easier. I am obliged to Late Prof. P. K. Kaw, Prof. Amita Das, Dr. R. Srinivasan, Dr. M. Kundu and Dr. D. Sharma for consenting to be my Doctoral Committee members. Their unstinting support and listening to their advice through the years have been a pleasant experience. It was a privilege to have them on the committee.

I would like to thank Prof. S. Mukherjee, Prof. A Chattopadhyay, Dr. S. Karkari, Dr. N. Bisai, Dr. Joydeep Ghosh, Dr. Ganesh and staff at FCIPT for their endurance while teaching us during the first year course work. Dr. Mainak Chattopadhyay and Prof. S. Mukherjee have been of continuous support and advice in Academic affairs.

The library staff, computer center staff and administrative staff of IPR have always remained cooperative. I convey my thanks to Mr. Shailendra Trivedi, Mr. Arvind Singh, Mr. Hemant Joshi, Mr. Gaurav Garg, Mr. Prashant Kumar, Mr. Govind Lokhande, Mr. Saroj Das, Mr. Shravan Kumar, Ms. Smita Parmar, Mrs. Shilpa Khandker, Mr. J. D. Patel, Mrs. Falguni Shah, Mr. H.C. Khanduri, Mr. Hitesh Mehta, Mr. Dinesh Nair, Mr. H. Chamunde, Mr. Silel Shah, Ms. Shirin Bhesania for their help during my PhD tenure. A very special thanks to Avadhesh Maurya for his help during my PhD tenure.

The long stay in IPR Hostel was made eventful and pleasant by the welcoming team of seniors Vikrant, Vikram, Kshitish, Ujjawal, Gurudatt, Prabal, Sita, Ashwin, Sharad, Pravesh, Rameshwar, Shekar, Jugal, Sanat, Sushil, Sayak, Manjit, Aditya, Soumen, Vikram Dharodi, Vedaprakhash. The hostel life was only made better by the juniors Arghya, Surbahi, Bhumika, Narayan, Ratan, Modhu, Amit, Debraj, Umesh, Sagar, Atul, Jervis, Prabhakar, Meenakshi, Pallavi, Alamgir, Sandeep, Harshita, Arun, Shivam, Rupak, Avanish and others. I am thankful to my batchmates Neeraj, Samir, Meghraj, Mangilal, Bibhu, Harish, Vara, Chandrasekhar, Vidhi, Deepa and Akansha for making my first year course work enjoyable. I am going to miss evening badminton games with Neeraj, Vara and Atul.

Thanks a lot to Arghya and Shivam, with whom I have had many useful discussion on plasma physics.

I would like to specially mention my friends Lokendra, Rakesh, Manish, Rashid, Pallavi, Paresh, Ravi, Pramod, Shayer for their constant support during good and hard times of my PhD tenure. My parents Bhairu Singh Rajawat and Bhanwar Bai have been a continuous source of impeccable support and motivation, to say the least. My heartfelt gratitude to my brother Pravendra, Devendra, Yogendra and sister Tanu Kanwar and the rest of the larger family for their goodwill and support all through my life.

Contents

Synopsis

Plasma is a quasi-neutral ionized medium consisting of charged and neutral particles that exhibits collective behavior due to long range Coulomb forces. One of the characteristics of a plasma is that it supports a variety of normal modes (plasma waves). Plasma waves can explain several naturally occurring phenomena both in laboratory and astrophysical scenarios, hence one is naturally prompted to investigate the behavior of the waves in plasma. If source of free energy (velocity, temperature, magnetic field etc.) is available, plasma waves may become unstable [1, 2]. Characteristics of free energy source decides the growth, nature (electrostatic or electromagnetic) and mechanism behind the excitation of the instability. A consequence of an instability is a greatly enhanced level of fluctuations in the plasma associated with the unstable mode that may elevate and/or inhibit the transport of particles and/or energy. For example, streaming instabilities in plasma lead to the acceleration of charged particles as observed in astrophysical shocks[3, 4, 5] , Laser Breakout afterburner [6, 7] etc.

A current carrying plasma constitutes an ideal laboratory for investigating various kinds of streaming instabilities associated with an electron beam-plasma system [8, 9, 10, 11, 12] *viz.* Buneman, Two stream, Filamentation, Weibel, and Oblique modes. The unstable mode spectrum associated with an electron beam-plasma system can be broadly classified into electrostatic (longitudinal) and electromagnetic (transverse) modes. Depending on the orientation of the wave vector with respect to electron beam velocity direction ($\vec{k}.\vec{v_b}$), the ratio of beam to plasma electron density ($\alpha = n_b/n_p$), Lorentz factor associated with the beam (γ_b) and the electron to ion mass ratio ($R = m/M$), several of the above mentioned instabilities could be excited, but the dominant one governs the dynamics in the linear phase. In the flow-aligned direction Buneman and two stream instabilities govern the evolution of the system whereas in the transverse direction, evolution is governed by filamenation and/or Weibel instabilities. Also there exist a continuum spectrum of unstable oblique modes which bridges the gap between parallel and transverse modes.

Scope of this thesis is limited to the discussion of electrostatic or flow aligned instabilities. We thus confine our study in flow aligned direction by choosing a one dimensional system, which isolates only unstable flow aligned wave modes (electrostatic modes) from the multidimensional unstable mode spectrum. In flow aligned direction two stream and Buneman modes compete [8, 9] with each other. In a charge and current neutralized system, two stream instability occurs between beam and plasma electrons while Buneman instability results due to the interaction of both beam current and plasma electron current (return current) with ions. In the dilute beam limit $\alpha << 1$, and in non-relativistic regime $\gamma_b = 1$, growth rate of the most unstable mode for two stream and Buneman instability respectively scales as $\sim \alpha^{1/3}$ and $\sim R^{1/3}$ [9]. Thus for $\alpha \leq R$, non-relativistic beam-plasma system is governed by Buneman/Buneman-like modes. In the symmetric beam limit ($\alpha = 1$), Buneman modes arising from the beam current-ion interaction merge with the return current-ion modes. Also within symmetric beam limit, both two stream and Buneman modes merge and share same unstable wavelength spectrum [9]. In the relativistic regime or in the large γ_b limit and in the dilute beam limit $\alpha << 1$, as long as the inequality $\gamma_b^3 \geq \alpha/R$ is satisfied, Buneman/Buneman-like modes govern [8, 10, 11, 12] the evolution of the system. In this thesis, we study electrostatic instabilities which arises due to relative drift between electrons and ions, the drift velocity being larger than the thermal speeds. Our studies include both immobile and mobile ions and extend from the non-relativistic to relativistic regimes. We choose our system such that all the electrons are propagating as a whole through a neutralizing background of ions so return current does not get excited and possibility of excitation of other modes is ruled out. Such a toy model is used in textbooks to isolate mode of interest from other modes.

We begin our investigation by studying pure electron plasma modes. In order to isolate electron plasma modes, ions are considered to be infinitely massive and they merely provide a positive background. Consequently, plasma waves are solely governed by electron dynamics. Cold relativistic electron beam can support variety of waves in plasma. Here we study a special class of nonlinear waves called BGK waves[13] in a cold plasma which are excited by a relativistic electron beam. In the non-relativistic regime, and in the absence of a beam, propagating BGK waves in a cold plasma have been derived by Albritton et. al. [14]. The BGK mode in this case was obtained from the exact space-time dependent solution of nonlinear plasma oscillations. Similarly propagating BGK waves in a cold relativistic plasma in the absence of a relativistic electron beam is simply obtained by transforming the governing equations in such a frame, where the wave is at rest, the so-called wave frame. Verma et. al. [15] constructed such a solution for propagating BGK waves (Akhiezer-Polovin wave [16]) from exact space-time solution of relativistic plasma oscillation [17] by choosing a special kind of transformation[14]. Wang [18] used similar kind of transformation for relativistic streaming plasmas and obtained a nonlinear dispersion relation in Vlasov-Maxwell framework. In the presence of a beam Psimpolous et. al. [19] obtained the solutions for stationary BGK waves (stationary in lab frame) in current carrying non-relativistic cold plasmas for a wide range of parameter ($\kappa = E_{max}/(4\pi n_0 m v_0^2)^{1/2}$), where E_{max} is maximum amplitude of the electric field, v_0 is averaged electron beam speed and other symbols have their usual meanings. It is found that for the range $\kappa \geq 1$, electric field becomes discontinuous which is equivalent to the wave breaking phenomenon in current carrying cold plasmas. For $\kappa < 1$, similar coherent solutions which are stationary in the lab frame have been obtained by Davidson and Schram [20] using Lagrange variables. For $\kappa \geq 1$, this method cannot be used as the transformation from Euler to Lagrange variables breaks down at $\kappa = 1$. In this thesis we have extended the study of Psimopoulos et. al. [19] by studying BGK waves in current carrying cold plasma. We have investigated stationary solution of the relativistic fluid-Maxwell system in the presence of an electron beam for a wide range of value of κ_R ($\kappa_R = E_{max}/(8\pi n_0(\gamma_0 - 1)mc^2)^{1/2}$, where γ_0 is a Lorentz factor associated with the average beam speed v_0) including those for which electric field becomes discontinuous.

Further, we discuss full space-time development of electrostatic waves on a relativistic electron beam and its consequence on net current carried by the beam. Space charge waves on relativistic electron beam plays vital role in collective acceleration of cosmic ray in pulsar magnetosphere [21], extragalactic jets [22] etc. In early attempts, Chian [23, 24, 25] sought traveling wave solution for super-luminous waves by transforming governing equations in such a frame where equations become space independent and the solution has temporal dependence only. Nonetheless, an exact solution exhibiting space-time evolution of relativistically intense wave in a homogeneous current carrying plasma with fixed neutralizing positive ion background is yet to be presented. In this thesis, we present the exact solution for space charge waves imposed on a relativistic electron beam.

We have extended our studies for finite ion to electron mass ratio. We focus on the instabilities occurring because of coupling between electrons and ions. It is already mentioned in the prequel that Buneman mode under certain condition is the most unstable mode [10] in the system. Buneman instability (BI) gets excited between electrons and ions, when Doppler shifted electron plasma frequency ($\omega_{pe} - kv_0$), resonate with ion plasma frequency (ω_{pi}) in ion rest frame; system become unstable at the expense of electron drift kinetic energy density, provided relative drift between electrons and ions is above the threshold $v_0 = 0.926(1 + R^{1/2})(2K_BT_e/m)^{1/2}$ (when $T_e = T_i$) [26, 27]. Below this threshold Buneman modes quenches through Landau damping. BI is ubiquitous in laboratory as well as in astrophysical plasmas and plays prominent role for several naturally occurring phenomena, namely, formation of strong double layer [28, 29], shock surfing acceleration [5], inertial electrostatic confinement[30, 31] etc. The Buneman wave particle interaction induces scattering of the particles which causes strong parallel heating. This novel effect widely observed in electron acceleration [32, 4, 33, 34, 35] , ion acceleration [6, 7] etc. Moreover, anomalous resistivity, which results from nonlinear evolution of BI, leads to strong turbulence between thin current layers during magnetic reconnection[36, 37, 38]. After few noteworthy analytical and simulation approaches, Hirose [39] reported that at the quasi-linear saturation (saturation of most unstable mode and its harmonics) of the BI, electrostatic energy density varies linearly with initial drift kinetic energy density (W_0) and slope of this linear relation scales with electron (m) to ion mass (M) ratio as $\approx (m/M)^{1/3}$. By extending [40] , Ishihara et. al. [41, 42] formulated a nonlinear dispersion relation using quasilinear analysis in Vlasov-Poisson framework. Ishihara's dispersion relation successfully predicted the breakdown of the linear growth, modulation of frequency and growth rate of the BI. It is found that electron trapping causes the final saturation of the BI and minimum electrostatic field energy required for quenching of the instability via electron trapping scales with initial drift kinetic energy density as $\sum_k |E_k|^2/16\pi W_0 \geq 0.11$ [41, 42]. Dynamics after quenching is strongly affected by the initial plasma parameters. If the initial drift velocity of the electron beam is not much larger than thermal velocity, then initial drift kinetic energy does not dissipate completely [43] and some part of it still remains with a nonlinear coherent structure. This net drift energy of coherent structures after quenching of Buneman instability may affect the interaction between electrons and ions. When the initial drift velocity of the electron beam is much larger than the thermal velocity of electrons, then initial kinetic energy dissipates completely [41, 42, 44] and a strong interaction between the nonlinear coherent structure and the surrounding ion may result in the formation of coupled hole-soliton (CHS). Thus, Buneman instability may decay into ion acoustic waves [45] and/or may induce [33, 44] coupled hole-solition[46].

In this thesis, by performing analytical calculations and computer experiment, we present a thorough investigation of a variety of coherent modes that a homogeneous one dimensional current carrying cold plasma can support as well as instabilities that may be excited in it.

A more systematic chapter-wise presentation of electrostatic instabilities in current carrying plasma is presented below. Thesis consists of 7 chapters.

Chapter 1: Introduction

This chapter introduces the instabilities in current carrying plasmas in the presence of stationary and mobile ions, and also the motivation behind the study is reported. Generation of mono-energetic electron beam in various laboratory and astrophysical plasmas is discussed. Natural occurrence of current carrying plasmas is also discussed in this chapter. When ions are allowed to move, plasma supports a rich spectrum of instabilities that is discussed along with their strength in different parameter regimes. Relevance of these studies is also discussed in this chapter.

Chapter 2: Method of Solution (Brief Description of Numerical Schemes)

In this chapter we give a brief introduction of numerical techniques used to simulate current carrying plasma. Computer simulation of plasmas comprises of two general techniques based on the fluid and kinetic description. MHD equations are solved numerically in fluid description. Most of the collective phenomena of plasma physics are easily simulated using fluid code, however, fluid code fails to simulate phenomenon involving wave-particle interaction, *viz.*, dynamics of plasma after wave-breaking, BGK modes, etc. which can be treated only via kinetic theory. Kinetic picture considers more detailed information by simply computing the motion of charged particles interacting through the self-consistent electromagnetic forces. Robustness and ability to simulate real plasma if adequate number of particle trajectories can be computed, makes Particle-in-cell(PIC) technique a powerful tool to understand plasma behavior ranging from laboratory to astrophysical scenarios. Basic numerical structure, limitation and differences between fluid and PIC techniques is also discussed in this chapter. Furthermore, codes are benchmarked against existing theoretical results.

Chapter 3: Study of stationary BGK structures in current carrying relativistic fluid-Maxwell system

In this chapter we study stationary BGK structures in current carrying relativistic fluid-Maxwell system using the basic set of stationary fluid-Maxwell equations. The equation of continuity imposes the condition of having constant electron flux throughout the plasma. First we derive an exact energy equation using pseudo-potential (Sagdeev potential) method. Analysis of pseudo-potential shows that BGK structures are periodic in space and, in contrast to the non-relativistic regime, wavelength of the BGK structures varies with the variation of κ_R, where $\kappa_R = E_m/(8\pi n_0(\gamma_0 - 1)mc^2)^{1/2}$. It is also found that Sagdeev potential ($V(\Phi)$) becomes undefined at the electrostatic potential $\Phi = (1-\gamma_0)/\gamma_0$ or at the energy level $\kappa_R = \kappa_R^c = 1/\sqrt{\gamma_0}$. Further, analysis of $\Phi - E$ phase space reveals that phase space curves are continuous for the range $0 \leq \kappa_R \leq \kappa_R^c$, but becomes discontinuous for the range $\kappa_R^c \leq \kappa_R$, *i.e.*, electric field becomes discontinuous periodically at some positions of space, consequently forming periodic electron sheets in the limit $\kappa_R^c \leq \kappa_R$. The charge density of periodically occurring sheets scales with κ_R and β as $\sim (\kappa_R^2 - (1-\beta^2)^{1/2})^{1/2}$. An exact expression for electrostatic potential, electric field, electron density and electron velocity as the function of position are derived which describe the nonlinear BGK structures.

Chapter 4: Evolution of relativistic electron current beam in the presence of relativistically intense space charge wave

In this chapter, we study the space-time evolution of space charge waves imposed on relativistic electron beam within the cold plasma model. In order to simplify the problem, first, governing equations are transformed in Lagrangian frame using Lagrangian transformation [47]. This transformation converts the partial differential equation into ordinary differential equation; then an exact solution is obtained. General solution is obtained for any initial conditions. In rest of the chapter, results are analyzed for different relativistic intensities ($eE_0/m\omega_{pe}c$) and flow velocities ($\beta = v_0/c$). It is observed that when an electron beam propagating with initial drift velocity v_0 is perturbed with relativistically intense wave, spatially averaged current diminishes with time due to variation of relativistic mass. Furthermore, frequency of oscillation is also obtained using Bogoliïÿăuïÿąbov and MitropolÊźski [48] method in the weakly relativistic limit, that turns out to be space dependent, which implies fine scale mixing of oscillations eventually leading to wave breaking. By analyzing exact solution it is found that amount by which spatially averaged current diminishes (ΔI) increases with increasing relativistic intensity of the wave. Rate of spatially averaged current diminishing (dI/dt) increases with increasing relativistic intensity of the wave. This novel effect may be of relevance in fast ignition scenarios [49, 50].

Chapter 5: Nonlinear evolution of Buneman instability and excitation of coupled hole-solitons

The general solution of Buneman instability offers great mathematical difficulty, therefore, the computer simulation remains strongest means of exploring the interesting physics and validating few existing analytic approaches [39, 41, 42, 51, 52] to explain nonlinear dynamics of Buneman instability. Simulation is carried out using an 1D in-house developed electrostatic particle-in-cell code. Code is initialized by putting nonzero value of initial electron drift velocity, setting a net drift between electrons and ions which consequently excites Buneman instability. We have followed space-time evolution of Buneman instability beyond final saturation. Studies are carried out for a broad range of initial drift velocities and electron to ion mass ratio and an extensive comparison is carried out between simulation and well known theoretical fluid/kinetic models [39, 41, 42]. Linear growth rate estimated from the simulation, agrees well with the growth rate obtained from the numerical solution of fourth order dispersion relation [1]. Further, ratio of electrostatic field energy to initial drift kinetic energy density at quasi-linear and final saturation stages are compared with theoretical model and simulation results are found to be respectively consistent with Hirose [39] and Ishihara's [41, 42] estimation. It is observed that, in contrast to the quasilinear saturation, the ratio of electrostatic field energy density to initial kinetic energy density at final saturation is relatively independent of the electron to ion mass ratio and is found from simulation to depend only on the initial drift velocity.

Final saturation of BI leaves behind an electron hole with inhomogeneous background of ions. A strong interaction between electron phase space holes and ions takes place; this interaction breaks the electron phase space holes into two oppositely propagating holes each attached with an ion pulse, a coupled state of an ion acoustic soliton and an electron phase space hole, *i.e.*, coupled hole-soliton (CHS)[46]. The propagation characteristics (amplitude-speed relation) of CHS (ϕ_{max}) are in conformity [44] with Saeki's [46] theoretical model of CHS. These coupled hole-solitons eventually coalesce away, finally generating a broadened electron velocity distribution function.

Chapter 5: Quasilinear evolution of relativistic Buneman instability

When electron beam is propagating with relativistic speed, dynamics of Buneman instability is strongly affected [7, 53, 54]. We start our analysis by deriving linear dispersion relation for Buneman instability in weakly relativistic regime and it is observed that relativistic effects reduces the maximum growth rate which now scales with initial drift velocity v_0 as $\gamma/\omega \approx \frac{\sqrt{3}}{2\gamma_0^{1/2}}\left(\frac{m}{2M}\right)^{1/3}$, where $\gamma_0 = 1/\sqrt{1-(v_0/c)^2}$. It is also found that, in contrast to the non-relativistic regime, range of unstable mode spectrum shrinks in relativistic regime. We further analyze relativistic Buneman instability by performing one dimensional electrostatic relativistic PIC simulation by applying relative drift between electrons and ions. Study is carried out for a broad range of initial drift velocities ($\beta = v_0/c$) and electron to ion mass ratios (m/M). Growth rate obtained from the simulation is in conformity with that obtained from the numerical solution of fourth order linear dispersion relation in weakly relativistic regime. It is found that ratio of electrostatic energy density to initial kinetic energy density at the quasilinear saturation reduces due to relativistic effects and scales with γ_0 as $\sum_k |E_k|^2/16\pi W_0 \approx \frac{1}{\gamma_0^2}(\frac{m}{M})^{1/3}$ [55], where $W_0 = n_0(\gamma_0 - 1)mc^2$ is initial kinetic energy density. This novel result on the scaling of energy densities has been found to be in quantitative agreement with our theoretical back-of-the-envelope estimation, which is obtained using fluid theory.

Chapter 7: Conclusion and Future Work

In this chapter, we conclude our results and discuss future possibilities for extending the present work in various limits.

List of Figures

List of Tables

CHAPTER 1

Introduction

The entire thesis addresses the spatio-temporal evolution of electrostatic modes/instabilities in current carrying cold plasmas in the presence of static and mobile ion background. Studies include both non-relativistic and relativistic regimes. In this chapter, we provide introduction to multidimensional unstable spectrum associated with current carrying cold plasmas and discuss the most unstable mode for different parameter regimes. We provide motivation for our study and review earlier works.

Plasma is a quasi-neutral ionized medium consisting of charged and neutral particles that exhibits collective behavior due to long range Coulomb forces. One of the characteristics of a plasma is that it supports a variety of normal modes (plasma waves). Plasma waves can explain several naturally occurring phenomena both in laboratory and astrophysical scenarios, hence one is naturally prompted to investigate the behavior of the waves in plasma. If source of free energy (velocity, temperature, magnetic field etc.) is available, plasma waves may become unstable [1, 2]. Characteristics of free energy source decides the growth, nature (electrostatic or electromagnetic) and mechanism behind the excitation of the instability. A consequence of an instability is a greatly enhanced level of fluctuations in the plasma associated with the unstable mode that may elevate and/or inhibit the transport of particles and/or energy.

A current carrying plasma constitutes an ideal laboratory for investigating various kinds of streaming instabilities [1, 2, 13] associated with an electron beam-plasma system. In 1925, Langmuir [56] first reported existence of electron plasma oscillations in the beam-plasma system. Bohm and Gross [57, 58] demonstrated that two cold counter propagating electron beams gives rise to an unstable mode spectrum and now commonly referred as two stream instability. In 1948, Pierce [59] reported that an electron beam, moving through an homogeneous ion background is itself an unstable current carrying system. A decade later, in 1958, O. Buneman [60, 26] demonstrated that a relative motion between electrons and ions give rise to an instability, known after his name as Buneman instability, provided, electron drift velocity is much larger than electron thermal velocity. Weibel [61] found that plasmas having anisotropic velocity distribution (other than Gaussian distribution function) is associated with unstable transverse waves when ion motion is neglected. A year later in 1959, Fried [62] discovered that beam-plasma system is unstable against an electromagnetic perturbation in the transverse direction of the flow (direction of electron beam) and this instability tends to break up initial homogeneous electron beam profile into small scale current filaments, so it is referred as Filamentation instability. In the vast amount of literature, Weibel and filamentation instability have been used interchangeably but recently Bret [63] reported that filamentation instability becomes purely transverse mode only if both electron beam current and return current are symmetric while Weibel instability gets excited always in a direction normal to maximum temperature [64]. Also there exists a continuum spectrum of unstable oblique modes [65, 66] which bridges the gap between parallel and transverse modes. This discussion shows that current carrying plasma is associated with multidimensional [10, 8, 11] unstable mode spectrum.

Depending on the orientation of the wave vector with respect to electron beam velocity direction ($\vec{k} \cdot \vec{v_b}$), ratio of beam to plasma electron density($\alpha = n_b/n_p$), Lorentz factor associated with electron beam (γ_b), plasma electrons (γ_p) and electron to ion mass ratio ($R = m/M$), several of the above mentioned instabilities could be excited, but dominant one governs the dynamics in the linear phase. In the flow-aligned direction electrostatic, *i.e.*, Buneman and two stream instabilities govern the evolution of the system whereas in the transverse direction evolution is governed by filamentation and/or Weibel instabilities. In a plasma with thermal anisotropy Weibel and filamentation mode can be triggered separately [67, 11] and which may sometime merge and interact [68, 69].

In this thesis, plasma is assumed to be cold by neglecting thermal motion of the particles when compared with speed of electron beam. Scope of this thesis is limited to the discussion of electrostatic or flow aligned instabilities. We thus confine our study in flow aligned direction by choosing a one dimensional system, which isolates only unstable flow aligned wave modes (electrostatic modes) from the multidimensional unstable mode spectrum. In flow aligned direction two stream and Buneman modes compete [8, 9] with each other. In a charge and current neutralized system, two stream instability occurs between beam and plasma electrons while Buneman instability results due to the interaction of both beam current and plasma electron current (return current) with ions. In the dilute beam limit $\alpha << 1$, and in non-relativistic regime $\gamma_b = 1$, growth rate of the electron two stream instability for most unstable mode $kv_b \sim \omega_{pe}$ [9] scales as $\sim \alpha^{1/3}$, while growth rate of Buneman instability (between return current and ions) for most unstable mode $kv_b/\omega_{pe} \sim 1/\alpha$ [9] scales as $\sim R^{1/3}$. Thus for $\alpha \leq R$, non-relativistic beam-plasma system is governed by Buneman/Buneman-like modes. In the symmetric beam limit ($\alpha \approx 1$), Buneman modes arising from the beam current-ion interaction merge [8] with the return current-ion modes. Also within symmetric beam limit, both two stream and Buneman modes merge and share the same unstable wavelength spectrum [9]. In the relativistic regime and in the dilute beam limit $\alpha << 1$, Buneman instability arises because of interaction between plasma electron current and plasma ions. In this regime, forward current is relativistic, return current however remains non-relativistic. Growth rate of two stream instability for the most unstable mode $kv_b \sim \omega_{pe}$ scales with γ_b as $\sim \alpha^{1/3}/\gamma_b$ and growth rate of Buneman instability for the most unstable mode $kv_b/\omega_{pe} \sim 1/\alpha$ is given by $\sim R^{1/3}$. Thus in this regime as long as the inequality $\gamma_b^3 \geq \alpha/R$ is satisfied, Buneman/Buneman-like modes govern [8, 10, 11, 12] the evolution of the system. In the symmetric beam limit, return current also becomes relativistic. As we have mentioned earlier that in this limit both two stream and Buneman unstable modes merge with each other and share a same growth rate, which scales with γ_b as $\sim R^{1/6}/\gamma_b$ [10]. It must be noted here that in large γ_b limit coupled two stream-Buneman/Buneman like modes outgrow [8, 10] all other unstable modes (including transverse) and system is governed by two-stream/Buneman modes. In this thesis, we study electrostatic instabilities which arises due to relative drift between electrons and ions, the drift velocity being larger than the thermal speeds. Our studies include both immobile and mobile ions and extend from the non-relativistic to relativistic regimes. We choose a one-dimensional system such that all the electrons are propagating as a whole through a neutralizing background of ions so return current does not get excited and possibility of excitation of other modes is ruled out. Such a toy model [1] is used in textbooks, which helps in isolating the mode of interest.

We begin our investigation by studying pure electron plasma modes. In order to isolate electron plasma modes, ions are considered to be infinitely massive and they merely provide a positive background. Consequently, plasma waves are solely governed by electron dynamics. In the section 1.1.1, we will discuss earlier works carried out for such kind of systems. Further, we extend our studies to finite ion to electron mass ratio and focus on the instabilities occurring because of coupling between electrons and ions, *i.e.*, Buneman instability. It is already mentioned in the prequel that Buneman mode under certain condition is the most unstable mode [10] in the system. Buneman instability (BI) gets excited between electrons and ions, when Doppler shifted electron plasma frequency ($\omega_{pe} - kv_0$), resonate with ion plasma frequency (ω_{pi}) in ion rest frame; system become unstable at the expense of electron drift kinetic energy density, provided relative drift between electrons and ions is above the threshold $v_0 = 0.926(1 + R^{1/2})(2K_BT_e/m)^{1/2}$ (when $T_e = T_i$, where T_e and T_i are electron and ion temperatures respectively) [26, 27]. Below this threshold Buneman modes quenches through Landau damping and a current driven ion acoustic instability may be excited in current carrying plasma provided $T_e > T_i$, otherwise ion acoustic modes are quenched through ion landau damping [45, 70]. Buneman instability is one of the most fundamental instability and a well known current dissipation mechanism in the presence of external electric field or in the field free collision-less plasma. Buneman wave-particle interaction induces strong particle heating during the final saturation of the instability, which occurs via coherent electron trapping [41, 42] in large amplitude Buneman wave potential. In section 1.1.2 we shall discuss earlier work and motivation behind the study of Buneman instability. In section 1.2, scope of this thesis will be discussed and section 1.3 presents chapter-wise organization of the thesis.

1.1 A survey of earlier work done

In this section we present a review of earlier work on electrostatic modes and instabilities in current carrying cold plasma in the presence of static and mobile ion background.

1.1.1 Electrostatic modes and instabilities in current carrying cold plasmas with static ion background.

Cold relativistic electron beam can support variety of waves in plasma. A very special class of nonlinear waves, called cold plasma form of BGK (Bernstein-Greene-Kruskal) waves[71, 13, 20] may be excited by a relativistic electron beam. In the non-relativistic regime, and in the absence of a beam, propagating BGK waves in a cold plasma have been derived by Albritton et. al. [14]. The BGK mode in this case was obtained from the exact space-time dependent solution [20] of the full nonlinear set of fluid-Maxwell equations. Similarly propagating BGK waves in a cold relativistic plasma in the absence of a relativistic electron beam is simply obtained by transforming the governing equations in such a frame, where the wave is at rest, the so-called wave frame[15]. Verma et. al. [72] constructed such a solution for propagating BGK waves (Akhiezer-Polovin wave [16, 73]) from exact space-time dependent solution [17] of the full relativistic fluid-Maxwell system. Wang [18] and Chian [23] used special transformation [14] for relativistic streaming plasmas and obtained a nonlinear dispersion relation for propagating BGK structures in Vlasov-Maxwell and fluid-Maxwell framework respectively. In the presence of a beam, Psimpolous et. al. [19] obtained the solutions for stationary BGK waves (stationary in lab frame) in current carrying non-relativistic cold plasmas for a wide range of parameter ($\kappa = E_m/(4\pi n_0 m v_0^2)^{1/2}$), where E_m is maximum amplitude of the electric field, v_0 is averaged electron beam speed and other symbols have their usual meanings. For $\kappa < 1$, similar coherent solutions which are stationary in the lab frame have been obtained by Davidson and Schram [20] using Lagrange variables. For $\kappa \geq 1$, this method can not be used as the transformation from Euler to Lagrange variables breaks down at $\kappa = 1$. It is found that for the range $\kappa \geq 1$, electric field becomes discontinuous which is equivalent to the wave breaking phenomenon in current carrying cold plasmas.

This concept of wave breaking was originally introduced by Dawson [74] for describing the limiting amplitude of nonlinear plasma wave. First, Dawson [74] conceptualized the picture of wave-breaking and defined the maximum amplitude ($eE_m/m\omega_{pe}v_{ph} = 1$, where ω_{pe} is electron plasma frequency and $v_{ph} = \omega/k$ is phase velocity of wave) of the nonlinear electron plasma wave. Above this amplitude fine scale mixing of the oscillations occur which in turn leads to wave breaking. In relativistic regime, Akhiezer-Polovin [73] described the limiting amplitude of electron plasma wave by $eE_m/m\omega_{pe}c = \sqrt{2}(\gamma_{ph} - 1)^{1/2}$, where γ_{ph} is the Lorentz factor associated with wave phase velocity. The above wave breaking limits were obtained in the absence of a beam. Chian [23, 25] obtained wave breaking limit for traveling waves in the presence of a beam and showed that wave breaking scales with initial drift velocity ($\beta = v_0/c$) as $eE_m/m\omega_{pe}c = \sqrt{2}(\gamma_{ph}(1 - \beta_{ph}\beta) - 1/\gamma_0)^{1/2}$; where $\gamma_0 = 1/\sqrt{1 - \beta^2}$, for subluminous wave, *i.e.*, $\beta < 1$, however, it was proven lately that in relativistic dynamics, a wave of an arbitrary amplitude always breaks via a phenomenon called phase mixing [75], therefore, the observation of wave breaking is not limited by Akhiezer Polovin and Chian limit. It is also noted that Chian [25] limit can be recovered by performing Lorentz transformation on Akhiezer & Polovin limit [73]. In all the aforementioned references, conventional picture of wave breaking in a cold plasma is described, *i.e.*, at the point of breaking, the electric field becomes multivalued at some spatial location. In Ref. [76], Sen analyzed a steady state system composed of two electron beams with stationary ions and showed that in a streaming plasma, electric field instead of becoming multivalued becomes discontinuous beyond a critical amplitude, however, Sen did not elaborate more on this striking feature. Later Psimpolous [19] extended Sen's argument using a relatively simplified model and reasoned that, in the presence of an electron beam or in current carrying plasma, wave breaking does not imply electric field becoming multivalued , rather, electric field becomes discontinuous at some singular points, resulting in the formation of charge sheets.

Extension of the above work to the relativistic regime and study of full space-time development of electrostatic waves in the presence of a relativistic electron beam is an open area of research. The latter study may be of crucial relevance to fast-ignition scheme [50, 77, 78] of laser fusion.

1.1.2 Electrostatic instabilities in current carrying cold plasmas with ion motion.

Pierce [59] was first to report that the low frequency oscillatory space charge waves on an electron beam are unstable against a neutralizing ion background, where author described it as electron-ion streaming unstable modes. Almost a decade later, Buneman [60] published his original paper in 1958, where Buneman successfully estimated the linear growth rate using the resonance condition ($kv_0 \approx \omega_{pe}$) and instability then was named after him as "Buneman instability". Subsequently Buneman [26] and Jackson [79] demonstrated that thermal spread of electron beam introduces Landau damping which can quench the linear growth of the instability unless the electron beam drift velocity exceeds a minimum threshold value $v_0 = 0.926(1 + R^{1/2})(2K_B T_e/m)^{1/2}$ (when $T_e = T_i$). Mantei et. al. [80] employed kinetic model to high density electron beam-plasma system and derived a criteria to separate the Buneman hydrodynamic instability from the ion acoustic kinetic instability depending on the wave energy sign which is positive for ion acoustic kinetic instability and negative for Buneman instability.

Several theoretical models on evolution and saturation of resonantly excited Buneman instability have been proposed by numerous authors. Davidson et. al. [81] carried out 1D particle-in-cell simulation of Buneman instability. Authors modeled two counter propagating cold ion beam moving through a cold homogeneous background of electrons and employed a quasilinear theory to understand the simulation results. Davidson et. al. observed that early evolution of instability is dominated by fastest growing mode that leads to the formation of coherent structure (electron phase space holes) during nonlinear evolution of the Buneman instability. Authors argued that growth terminates abruptly as electron trapping sets in and instability quenches when drift energy is drained out completely. Their quasilinear model does not include mode coupling effect so estimation of electric field energy at the saturation was rather ill defined. Ichimaru [82] used microscopic theory of transport processes to explain Buneman turbulence and Ionson [83] treated Buneman turbulence as normal mode fluctuations. Both authors have reported that the electrostatic field energy associated with the instability saturates at a value comparable to that of the initial kinetic energy of the drifting electrons, which is much larger than what Buneman suggested. Hirose [39] employed quasilinear fluid theory to explain quasi-linear saturation of the resonantly excited Buneman instability. Hirose[39] estimated that quasilinear saturation of Buneman instability occurs when ratio of electrostatic energy density($\sum\limits_k |E_k|^2/8\pi$) to initial drift kinetic energy density W_0 reaches up to $\approx 2(m/M)^{(1/3)}$. Hirose's analysis was based on the argument that, since $\gamma(kv)$ curve is very narrow around the resonant value $kv_0/\omega_{pe} \approx 1$, where k is the wave number corresponding to the most unstable mode and v_0 is initial drift velocity of electron beam, so a small change in the drift velocity can substantially reduce the growth rate of the Buneman instability. This quasilinear saturation limit derived by Hirose is found to be independent of initial drift velocity and solely depends on electron to ion mass ratio. Hirose' limit for quasilinear saturation describes saturation of the most unstable mode and its harmonics only.

Final saturation of the Buneman instability occurs via electron trapping; thus one needs to account for kinetic effects to obtain the level of electrostatic energy at the time of final saturation. Bartlett [40] formulated a nonlinear dispersion relation using quasilinear kinetic theory and mode coupling effects, which successfully predicted departure of frequency and growth rate from the linear to nonlinear regime. Nonetheless, Bartlett's nonlinear dispersion relation failed to predict final saturation of the Buneman instability because author retained the terms $\mathcal{O}(E_k^2)$ only. Ishihara et. al. [41, 42] derived a nonlinear dispersion relation using quasilinear kinetic theory (extension of Bartlett's [40] method) based on the assumption of nonlinear coherent structure and initial delta function distribution (cold beam) that accounted for the spreading of electron distribution function, *i.e.*, the deceleration of initial drift velocity and the heating of the electrons. Authors carried out 1-D kinetic simulation of Buneman instability and compared numerical solution of the nonlinear dispersion relation with simulation results which successfully predicted modulation of frequency and growth rate and departure of growth rate from linear growth period. Ishihara et. al. retained the terms $\mathcal{O}(E_k^4)$ in nonlinear dispersion relation which is why their dispersion relation successfully predicts final saturation of the instability. In nonlinear stage, electron trapping and mode coupling causes final saturation of the Buneman instability and minimum energy required for complete quenching of the Buneman instability via electron trapping is given by inequality $\sum_k |E_k|^2/16\pi W_0 \geq 0.11$. Ishihara et. al. found that electrostatic energy density at the final saturation shows weak dependence on electron to ion mass ratio.

Recently, Yoon[51] formulated a phase and spatially averaged perturbative nonlinear weak turbulence theory that involves quasi-linear velocity space diffusion and nonlinear wave particle interaction, however, it lacks the nonlinear coherent dynamics. Yoon's model includes warm beam dynamics therefore it differs from Ishihara et. al. [41, 42] model. In a companion paper[52], Yoon et. al. carried out Vlasov simulation of Buneman instability for different electron to ion temperature ratio and compared the simulation results with that derived weak turbulence theory[51], which describes the nonlinear development of the Buneman instability qualitatively, when nonlinear scattering term with wave kinetic equation is included. Results however show difference during initial stage of nonlinear evolution because of lack of nonlinear coherent dynamics in the model. Thus Yoon's model is best applicable for the problems where nonlinear coherent dynamics is absent.

Kaw et. al. [29] employed fluid model to study non-resonant Buneman instability in the low frequency ($\omega \ll kv_e$), long wavelength limit ($k\lambda_{de} \ll 1$) and neglecting electron dynamics (keeping electron current constant in the system). Authors have shown that growth rate of the Buneman instability in the linear regime comes out to be $\gamma \sim kv_0\sqrt{m/M}$ instead of $\gamma \sim kv_0(m/M)^{1/3}$ (what we found for resonant Buneman instability). Authors obtained a wave like equation with negative ratio of specific heat. Analysis of the wave like equation shows that the nonlinear evolution of Buneman instability leads to the formation of double layer type structure and its collapse. Shokri et al.[84] have investigated nonlinear dynamics of non-resonant Buneman instability in a weakly ionized un-magnetized plasma placed in an external electric field using hydrodynamic model. Shokri obtained a diffusion like equation with a negative nonlinear diffusion coefficient. Authors solved nonlinear stationary equation and showed that an initial perturbation in electron density explosively grows with time due to the nonlinear and negative diffusion coefficient. Later Hatami[85] solved Shokri's [84] nonlinear time dependent equation, which shows temporal steepening of electron density.

In the simulation works, Jain et. al.[86] modeled 1-D Vlasov simulation of Buneman instability. He used an instantaneous linear dispersion relation (derived using a double Gaussian distribution) to fit the electron distribution function at the different stages of the simulation. His simulations show that along with the low frequency Buneman mode, high frequency Langmuir mode and wave modes propagating in the opposite direction of the wave also gets excited in the nonlinear phase of the instability. Guo [43] has also reported presence of high frequency Langmuir waves during the nonlinear evolution of Buneman instability using 1D PIC simulation. Niknam[87] has carried out 1-D particle-in-cell simulation and reported steepening of electron density with time. Authors also reported that saturation time of instability increases with increasing ion to electron mass ratio. Che et. al. [88] described the rapid electron heating near final saturation of Buneman instability by carrying out 3D particle-in-cell simulation. Authors showed that near the saturation, the process of separatrix crossing (as electrons are trapped and de-trapped) is irreversible and leads to the heating of plasma. It is observed that as number of trapped particles increases (decreases), electric field energy increases (decreases), which implies that phase space holes become narrower(flatten) in phase space. The decrement in electrostatic energy after saturation of Buneman instability is attributed to flattening of electron phase space holes. They confirmed the above mentioned dynamics using test particle simulation.

Omura et al.[45, 70] have reported the role of ion temperature in the nonlinear decay processes of electron phase space holes (electrostatic waves (ESW)), which form during nonlinear evolution of Buneman instability. Authors argued that for a case with hot ions when $c_s < v_{th,i} < v_0$, ion acoustic modes are quenched through ion Landau damping and formation of large electron holes are observed through the coalescence of smaller electron holes. However, for a case of colder ions $v_{th,i} \ll v_0$ and $c_s > v_{th,i}$, electron hole decays into ion acoustic waves. Shimada et al. [33] reported that nonlinear evolution of Buneman instability results into coupled state of electron hole and ion acoustic soliton, known as coupled hole-solitons [89, 46]. Hashemzadeh et. al. [90, 91, 92] have carried out particle-in-cell simulation of Buneman instability for q non-extensive distribution and in the presence of negative ions on the Buneman instability. In the presence of negative ions, by increasing velocity of positive and negative ions the saturation time of Buneman instability increases and by increasing the masses of the positive and negative ions, growth rate decreases. For q non-extensive electron velocity distribution, growth rate increases by increasing q parameters and growth rate decreases if electron temperature increases.

Finally relativistic Buneman instability has been investigated by Haas et al.[53] using a Klein-Gordon model for the electrons and cold ions for relativistic quantum plasmas. Quantum effects have been found to have a stabilizing influence on relativistic

Buneman instability. Shorbagy [93] also reported stabilizing effects of strong high frequency electric field on the relativistic Buneman instability. Hashemzadeh et. al. [54] have carried out 1-D particle-in-cell simulation of relativistic Buneman instability in a current carrying plasma. Their simulations show that with increase in initial electron drift velocity the growth rate of Buneman instability decreases.

Above cited references deals with early nonlinear dynamics or dynamics up to the saturation of Buneman instability. Post saturation dynamics of Buneman instability is still under scanner and to the best of our knowledge very little work has been carried out to understand it. Further little work has been done to understand the evolution and saturation of relativistic Buneman instability.

1.2 Scope of the thesis and Motivation

This thesis is devoted to the study of electrostatic modes and instabilities in current carrying cold plasma for static and mobile ion background and ranging from non-relativistic to relativistic regime. Understanding of nonlinear electrostatic coherent modes and their evolution in current carrying cold plasmas, as discussed in the section 1.1, are not complete yet and still have deficiencies. In prequel, we discussed that one can obtain stationary [20, 19] and propagating [18, 23] BGK waves in the presence of an electron beam. Model of Psimpolous et al. [19] reveals that for the range $\kappa \geq 1$, electric field becomes discontinuous which is equivalent to the wave breaking phenomenon in current carrying cold plasmas. Psimpolous et al. stressed on the fact that discontinuity in the electric field implies formation of infinitesimally thin periodic negative charged plane in current carrying plasmas. Ref. [18] and [23] obtained nonlinear dispersion relation for BGK structures in relativistic regime, however, latter mentioned the possibility of wave breaking but did not elaborate more on electric field discontinuity and formation of thin negatively charged plane. In the chapter 3, we present stationary solution of the relativistic fluid-Maxwell system in the presence of an electron beam for a wide range of value of κ_R ($\kappa_R = E_{max}/(8\pi n_0(\gamma_0 - 1)mc^2)^{1/2}$, where γ_0 is a Lorentz factor associated with the average beam speed v_0) including those for which electric field becomes discontinuous. Further, to the best of our knowledge, space-time evolution of space charge waves propagating on an relativistic electron beam has not been studied so far. In chapter 4, we present an exact solution exhibiting space-time evolution of relativistically intense wave in a homogeneous current carrying plasma with fixed neutralizing positive ion background.

Next we discuss spatio-temporal evolution of Buneman instability. Linear theory of Buneman instability is well understood [1, 13] but it is nonlinear theory that is still under scanner. Electrostatic energy at quasilinear saturation is estimated successfully by Hirose [39], however, an extensive comparison between theory and simulation results has not been attempted yet. Electrostatic energy at final saturation is estimated by Ishihara et al. [41, 42]; their simulation correctly matches with theoretical estimation of final saturation, although their study were carried out only for single initial electron drift velocity. Dynamics after saturation of Buneman instability has been a debatable issue and needs to be analyzed more. For example, final stage of Ishihara et al. simulations shows large amplitude coherent ion oscillation, which are indeed supported by Hirose [94] theoretical model. Ref. [45, 70, 43] show transition of Buneman instability to ion acoustic modes. Also simulations of Shimada et al. [33] in astrophysical scenarios reported coupled hole-soliton (CHS) after saturation of Buneman instability, nonetheless, authors do not discuss nonlinear processes behind the formation of coupled hole-soliton. Following questions are addressed in the chapter 5 of the thesis (1) Development of Buneman instability from linear stage to nonlinear stage, (2) first ever comparison of electrostatic energy level at quasilinear saturation between simulation and theoretical results, (3) effect of different initial drift velocities on the final saturation of the Buneman instability and

(4) discussion of nonlinear processes behind the formation of CHSs and comparison of propagation characteristics of CHSs obtained from the simulation to well known Saeki's model [89, 46] of CHSs.

Relativistic Buneman instability is studied by several authors. Haas et al. [53] derived linear dispersion relation and shows stabilizing influence. Comparison between growth rate obtained from solution of the linear dispersion relation is not compared with that estimated from the simulation. PIC simulations of Hashemzadeh [54] shows that growth rate the relativistic Buneman instability depends on initial electron drift velocity and saturation time of instability increases with increasing drift velocity. Although this is expected from a fluid model, a detailed comparison of the characteristics of the instability with the fluid model has not been presented. The above discussion indicates that there have been some work on relativistic Buneman instability in the recent past, but to the best of our knowledge, investigation of its evolution and saturation using particle-in-cell simulation method, and a detailed comparison of the simulation results with a fluid model has not been attempted so far. We address this issue in the chapter 6 of the thesis.

1.3 Thesis organization

A more systematic chapter-wise presentation of electrostatic modes and instabilities in current carrying plasma is presented below.

Chapter 2 : Method of solution (Brief description of numerical schemes)

In this chapter we give a brief introduction of numerical techniques used to simulate electrostatic modes and instabilities in a current carrying plasma. Computer simulation of plasmas comprises of two general techniques based on the fluid and kinetic description. MHD equations are solved numerically using fluid description. Most of the collective phenomena of plasma physics are easily simulated using fluid code, however, fluid code fails to simulate phenomenon involving wave-particle interaction, *viz.*, dynamics of plasma after wave-breaking, BGK modes in a warm plasma, etc. which can be treated only via kinetic theory. Kinetic picture considers more detailed information by simply computing the motion of charged particles interacting through the self-consistent electromagnetic forces. Robustness and ability to simulate real plasma if adequate number of particle trajectories can be computed, makes Particle-in-cell(PIC) technique a powerful tool to understand plasma behavior ranging from laboratory to astrophysical scenarios. Basic numerical structure, limitation and differences between fluid and PIC techniques is also discussed in this chapter. Furthermore, codes are benchmarked against existing theoretical results.

Chapter 3: Study of stationary BGK structures in current carrying relativistic fluid-Maxwell system

In this chapter we study stationary BGK structures in current carrying relativistic fluid-Maxwell system using the full set of stationary fluid-Maxwell equations. The equation of continuity imposes the condition of having constant electron flux throughout the plasma. First we derive an exact energy equation using pseudo-potential

(Sagdeev potential) method. Analysis of pseudo-potential shows that BGK structures are periodic in space and, in contrast to the non-relativistic regime, wavelength of the BGK structures varies with the variation of κ_R, where $\kappa_R = E_m/(8\pi n_0(\gamma_0 - 1)mc^2)^{1/2}$. It is also found that Sagdeev potential ($V(\Phi)$) becomes undefined at the electrostatic potential $\Phi = (1 - \gamma_0)/\gamma_0$ or at the energy level $\kappa_R = \kappa_R^c = 1/\sqrt{\gamma_0}$. Further, analysis of $\Phi - E$ phase space reveals that phase space curves are continuous for the range $0 \leq \kappa_R \leq \kappa_R^c$, but becomes discontinuous for the range $\kappa_R^c \leq \kappa_R$, *i.e.*, electric field becomes discontinuous periodically at some positions of space, consequently forming periodic electron sheets in the limit $\kappa_R^c \leq \kappa_R$. The charge density of periodically occurring sheets scales with κ_R and β as $\sim (\kappa_R^2 - (1-\beta^2)^{1/2})^{1/2}$. An exact expression for electrostatic potential, electric field, electron density and electron velocity as the function of position are derived which describe the nonlinear BGK structures.

Chapter 4: Evolution of relativistic electron current beam propagating through static background of ions

In this chapter, using cold plasma model, we study the space-time evolution relativistic electron current beam which is perturbed by a relativistically intense space-charge waves. In order to simplify the problem, first, governing equations are transformed in Lagrangian frame using Lagrangian transformation [47]. This transformation converts the partial differential equation into ordinary differential equation; then an exact solution is obtained. General solution is obtained for arbitrary initial conditions. In rest of the chapter, results are analyzed for different relativistic intensities ($eE_0/m\omega_{pe}c$) of the imposed wave and flow velocities ($\beta = v_0/c$) of the current beam. It is observed that when an electron beam propagating with initial drift velocity v_0 is perturbed with relativistically intense wave, spatially averaged current diminishes with time due to variation of relativistic mass. Furthermore, frequency of oscillation is also obtained using Bogoliïÿăuïÿąbov and MitropolÊźski [48] method in the weakly relativistic limit, that turns out to be space dependent, which implies fine scale mixing of oscillations eventually leading to wave breaking. By analyzing the exact solution it is found that amount by which spatially averaged current diminishes (ΔI) increases with increasing relativistic intensity of the wave. Rate of diminishing of spatially averaged current (dI/dt) increases with increasing relativistic intensity of the wave. This novel effect may be of relevance to fast ignition scenarios [30, 31, 49, 50].

Chapter 5: Nonlinear evolution of Buneman instability and excitation of coupled hole-solitons

The general solution of Buneman instability offers great mathematical difficulty, therefore, the computer simulation remains strongest means of exploring the interesting physics and validating few existing analytic approaches [39, 41, 42, 51, 52] to explain nonlinear dynamics of Buneman instability. Simulation is carried out using an in-house developed electrostatic 1D particle-in-cell code. Code is initialized by putting nonzero value of initial electron drift velocity, setting a net drift between electrons and ions which consequently excites Buneman instability. We have followed space-time evolution of Buneman instability beyond final saturation. Studies are carried out for a broad range of initial drift velocities and electron to ion mass ratio and an extensive comparison is carried out between simulation and well known theoretical fluid/kinetic models [39, 41, 42]. Linear growth rate estimated from the simulation, agrees well with the growth rate obtained from the numerical solution of fourth order dispersion relation [1]. Further, ratio of electrostatic field energy density to initial drift kinetic energy density at quasi-linear and final saturation stages are compared with theoretical model and simulation results are found to be respectively consistent with Hirose [39] and Ishihara's [41, 42] model. It is observed that, in contrast to the quasilinear saturation, the ratio of electrostatic field energy density to initial kinetic energy density at final saturation is relatively independent of the electron to ion mass ratio and is found from simulation to depend only on the initial drift velocity. Final saturation of BI leaves behind an electron hole with inhomogeneous background of ions. A strong interaction between electron phase space holes and ions takes place; this interaction breaks the electron phase space holes into two oppositely propagating holes each attached with an ion pulse, a coupled state of an ion acoustic soliton and an electron phase space hole, *i.e.*, coupled hole-soliton (CHS)[46]. The propagation characteristics (amplitude-speed relation) of CHS (ϕ_{max}) are in conformity [44] with Saeki's [46] theoretical model of CHS. These coupled hole-solitons eventually coalesce away, finally generating a broadened electron velocity distribution function.

Chapter 6 : Quasilinear evolution of relativistic Buneman instability

When electron beam is propagating with relativistic speed, dynamics of Buneman instability is strongly affected [7, 53, 54]. We start our analysis by deriving linear dispersion relation for Buneman instability in weakly relativistic regime and it is observed that relativistic effects reduces the maximum growth rate which now scales with initial drift velocity v_0 as $\gamma/\omega \approx \frac{\sqrt{3}}{2\gamma_0^{1/2}}\left(\frac{m}{2M}\right)^{1/3}$, where $\gamma_0 = 1/\sqrt{1-(v_0/c)^2}$. We further analyze relativistic Buneman instability by performing one dimensional electrostatic relativistic PIC simulation by applying relative drift between electrons and ions. Study is carried out for a broad range of initial drift velocities ($\beta = v_0/c$) and electron to ion mass ratios (m/M). Growth rate obtained from the simulation is in conformity with that obtained from the numerical solution of fourth order linear dispersion relation in weakly relativistic regime. It is found that ratio of electrostatic energy density to initial kinetic energy density at the quasilinear saturation reduces due to relativistic effects and scales with γ_0 as $\sum_k |E_k|^2/16\pi W_0 \approx \frac{1}{\gamma_0^2}(\frac{m}{M})^{1/3}$ [55], where $W_0 = n_0(\gamma_0 - 1)mc^2$ is initial kinetic energy density. This novel result on the scaling of energy densities has been found to be in quantitative agreement with our theoretical back-of-the-envelope estimation, which is obtained using fluid theory.

Chapter 7: Conclusion and future work

In this chapter, we conclude our results and discuss future possibilities for extending the present work in various limits.

CHAPTER 2

Method of Solution (Brief Description of Numerical Schemes)

In this chapter, we discuss the basic numerical techniques used in different simulation methods (fluid and particle) along with their limitations. First we discuss fluid simulation techniques and use of LCPFCT [95] subroutines for solving coupled generalized continuity equations. Next, we discuss techniques used for performing Particle-in-cell simulation [96].

2.1 Introduction

It is often said that "Mathematics is the language of physics". Most of the problems encountered in various streams of the physics has been understood with the help of theoretical model using well established laws of physics. However, the complex nature of the problems encountered in plasma physics makes it difficult to do exact theoretical analysis. Computer simulation has hence paved the way to advance the knowledge of such kind of complex systems. Computer simulation has attracted much attention since it was pioneered by Dawson and Birdsall in late 1950's, due to its robustness and ability to mimic exact physical system if appropriate spatial and temporal resolution are taken into account.

Computer simulation of plasmas comprises of two general techniques based on the fluid and kinetic description. In section 2.2 fluid description and fluid simulation method is discussed. Section 2.3 describes detailed particle-in-cell method [96].

2.2 Fluid Model

In fluid description, each plasma species is described by average physical quantities, viz., number density, average velocity and average energy. These average fluid quantities are obtained by solving continuity, momentum and energy equations. These equations are easily deduced by taking velocity moments of the Boltzmann equation. Coupling of fluid equations with the Maxwell equations make a complete set of equations for describing self consistent dynamics of a plasma.

Below we describe the basic techniques required to setup an one dimensional electrostatic relativistic two fluid code using "LCPFCT - A Flux-Corrected Transport Algorithm for Solving Generalized Continuity Equations" [95] subroutines.

2.2.1 Basic Equations

The governing set of fluid equations required to simulate current carrying cold plasma in one dimension can be written as

$$\frac{\partial n_s}{\partial t} + \frac{\partial n_s v_s}{\partial x} = 0, \tag{2.1}$$
$$\frac{\partial p_s}{\partial t} + v_s \frac{\partial p_s}{\partial x} = q_s E, \tag{2.2}$$
$$\frac{\partial E}{\partial x} = 4\pi e(n_i - n_e), \tag{2.3}$$

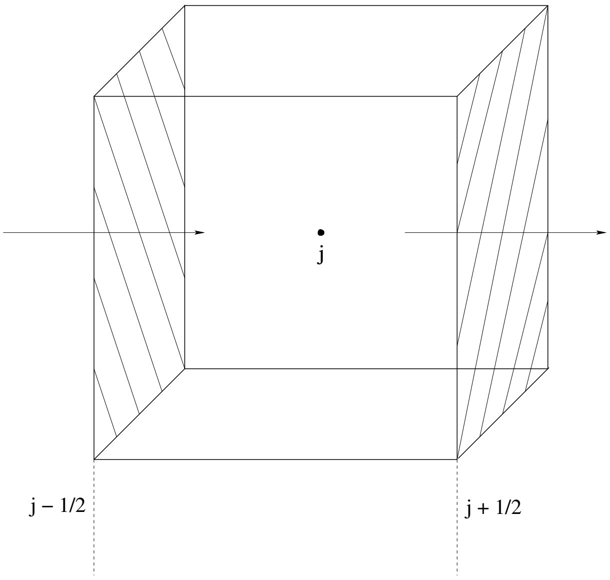

Figure 2.1: A schematic of computation cell used in LCPFCT package.

where s stands for species electron/ion. Here n_s,v_s and $p_s = \gamma_s m_s v_s$ respectively represent charge density, velocity and momentum of fluid particles and E stands for electric field. The normalization used are $x \rightarrow k_L x$, $t \rightarrow \omega_{pe} t$, $v_s \rightarrow k_L v_s / m_s \omega_{pe}$, $p_s \rightarrow k_L p_s / \omega_{pe}$, $n \rightarrow n_s / n_0$, $E \rightarrow e k_L E / m \omega_{pe}^2$ and , $\phi \rightarrow e k_L^2 \phi / m \omega_{pe}^2$.

To carry out numerical solution of the set of fluid equations ((2.1) - (2.3)), we use LCPFCT package [95]. LCPFCT is used for solving generalized continuity equations in Cartesian, cylindrical and spherical co-ordinates. LCPFCT is written in Fortran 77 and comprises of multiple subroutines. LCPFCT works on the principle of flux corrected transport scheme which is discussed briefly in following paragraph.

A schematic of the computational cell is shown in Fig. 2.1, where at each time step in and out flow fluxes across the cell boundaries changes the total amount (mass, momentum etc.) contained in the cell volume. It is an obvious property of a fluid that density can never become negative anywhere regardless of the velocity field specified. To retain positivity, some amount of flux is added whenever density is feared to be negative, this process is called diffusion. Strong diffusion introduces the issues of lack of monotonic solution so some fluxes are subtracted (anti-diffusion) such that solution remains monotonic. LCPFCT is advance version of this method in a way that diffusion and anti-diffusion are adjusted using nonlinear flux correction method. In LCPFCT scheme fluxes are successively added (diffusion) and subtracted (anti-diffusion) along the array of densities $\{n_j^0\}$ so that the overall conservation of mass is satisfied by construction.

The basic set of fluid equations ((2.1) - (2.3)) can be rewritten in flux conserved form as

for electrons,

$$\frac{\partial n_e}{\partial t} + \frac{\partial n_e v_e}{\partial x} = 0, \tag{2.4}$$

$$\frac{\partial n_e p_e}{\partial t} + \frac{\partial n_e v_e p_e}{\partial x} = -n_e E, \tag{2.5}$$

for ions,

$$\frac{\partial n_i}{\partial t} + \frac{\partial n_i v_i}{\partial x} = 0, \tag{2.6}$$

$$\frac{\partial n_i p_i}{\partial t} + \frac{\partial n_i v_i p_i}{\partial x} = +\frac{m}{M} n_i E. \tag{2.7}$$

Equation (2.4),(2.6) and (2.5),(2.7) respectively represent no. density and momentum density in flux conserved form.

Minimal number of subroutines required to advance one or more generalized continuity equations using LCPFCT subroutines in a single time step is shown in flow chart 2.2. Here we summarize these four subroutines and calling sequences. A detailed description of these subroutines is given in ref. [95].

1. **MAKEGRID**:- This subroutine sets up the finite volume grid and must be called at the initial stage of the simulation or when cell definition is changed at the initial or during the simulation stage.

2. **VELOCITY**:- All the velocity dependent terms, *i.e.*, diffusion and antidiffu-

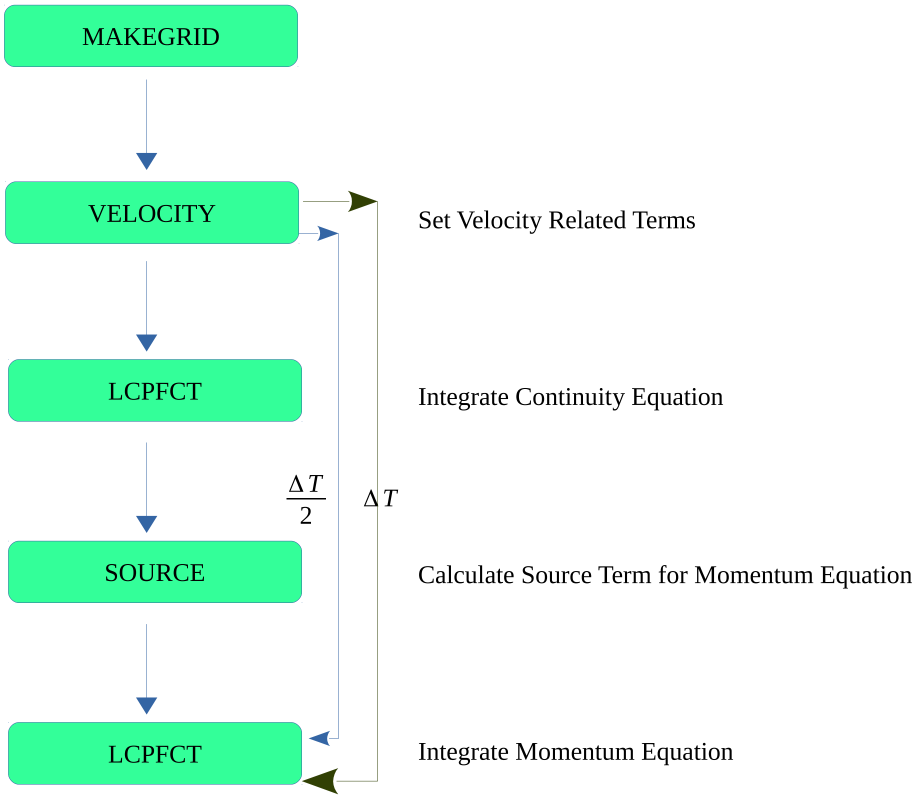

Figure 2.2: Flow chart for using LCPFCT subroutine.

sion are calculated in this subroutine.

3. **SOURCE**:- In this subroutine, all the source terms are set for integration of continuity equation.

4. **LCPFCT**:- This subroutine integrates continuity equation and updates new values of number and momentum density using old values at the cell centers. All the boundary related terms goes in this subroutine.

In LCPFCT subroutine, equations (2.4)-(2.7) are integrated using predictor corrector method which is second order accurate. First generalized continuity equations are integrated for half time step and time-centered spatial derivatives and fluxes are calculated. Then generalized continuity equations are integrated for full time step using fluxes calculated at half time step. Electric field is determined using Gauss law. Gauss Law is solved using central difference method (matrix form of Gauss elimination) (detailed discussion is presented later in this chapter).

2.2.2 Numerical Scheme for Fluid Simulation

We start the simulation by choosing appropriate system length "L". We discretize system length in NG equidistant cells and specify initial conditions (density (n_s^0) and flux ($n_s^0 v_s^0$)) on the cell centers. Neighboring boundary between two cells is called interface and center of each cell is usually called grid point. In our simulation grid number varies from 0 to NG. We choose periodic boundary condition such that 0^{th} and NG^{th} grid points are identical. After discretizing the system length 'L', we call the subroutine MAKEGRID, that sets up the finite volume grid at the initial stage of the simulation.

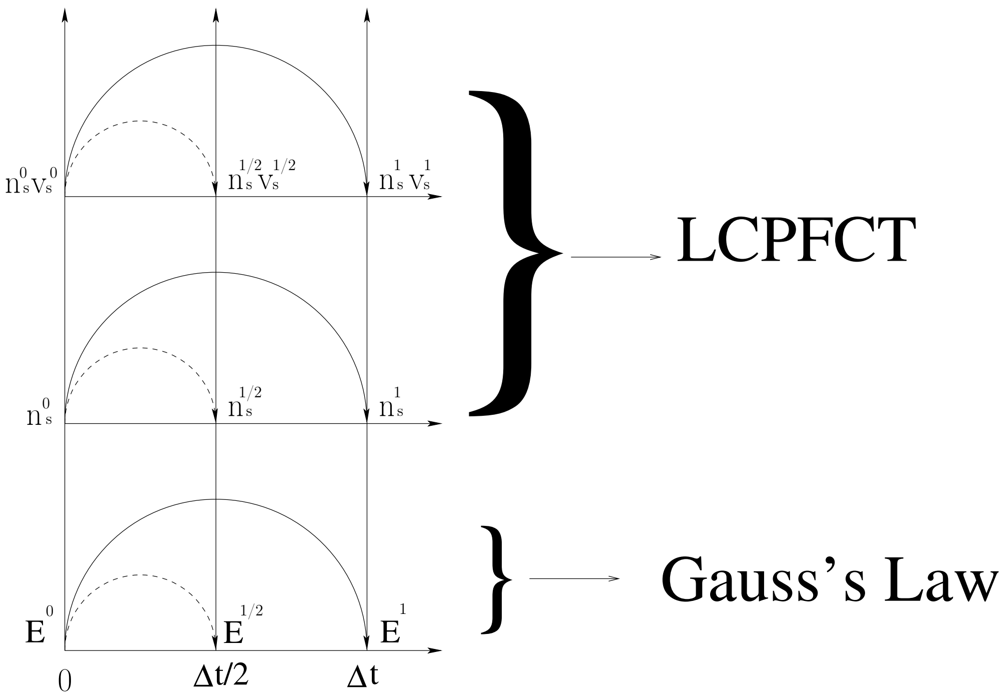

Figure 2.3: Time step scheme for solving generalized continuity equation.

In our model, grid definition does not change during the simulation thus time looping as shown in flow chart 2.2 is started after defining grid. First we calculate electric field on grid points which will be used for obtaining source term to integrate momentum equation. Subsequently fluid velocity for a constituent species is calculated at cell interfaces following by calling the subroutine VELOCITY which determines velocity related terms (diffusion and anti-diffusion). Now equation of continuity is integrated by calling subroutine LCPFCT which gives density at finite time step. We set up source term for integrating momentum equation by calling subroutine SOURCES and at last subroutine LCPFCT is called again which integrates momentum equation using the source terms described in subroutine SOURCES. The sequence from calculating fluid velocity at interfaces to integrating momentum equation is repeated for other species also (ions).

Integration of generalized continuity equations in time stepping scheme is elucidated more clearly in Fig. 2.3 and more elaborate description is given in following bullet form as

1. Evaluate the electric field $\{E_j^0\}$ using Gauss law.
2. Calculate $\{v_j^0\}$ using the old values of $\{n_j^0\}$ known at the beginning of the time step. Then we calculate $\{v_{j\pm1/2}^0\}$ to determine velocity related terms by calling subroutine VELOCITY.
3. Convect $\{n_j^0\}$ at half timestep to $\{n_j^{1/2}\}$ by calling subroutine LCPFCT.
4. Evaluate source term $\{-n_j^0 E_j^0\}$ for the momentum equation and call subroutine SOURCES.
5. Convect $\{n_j^0 p_j^0\}$ to $\{n_j^{1/2} p_j^{1/2}\}$ using $\{-n_j^0 E_j^0\}$ by calling LCPFCT.
6. Repeat the steps from 2 - 4 for ion species where source term is $\{(m/M)n_j^0 E_j^0\}$. Now we integrate the generalized continuity equations for a whole timestep Δt using the half time step results.
7. Evaluate the electric field $\{E_j^{1/2}\}$ using $\{n_j^{1/2}\}$.

8. Calculate $\{v_j^{1/2}\}$ using the values evaluated at half time step $\{n_j^{1/2}\}$. Then we calculate $\{v_{j\pm1/2}^{1/2}\}$ to determine velocity related terms by calling VELOCITY.

9. Convect $\{n_j^0\}$ for full timestep to $\{n_j^1\}$ by calling subroutine LCPFCT.

10. Evaluate source term $\{-n_j^{1/2}E_j^{1/2}\}$ for the momentum equation and call subroutine SOURCES.

11. Convect $\{n_j^0p_j^0\}$ to $\{n_j^1p_j^1\}$ using $\{-n_j^{1/2}E_j^{1/2}\}$ by calling subroutine LCPFCT.

12. Repeat the steps from 8 - 11 for ion species to evaluate ion density and momentum using the source term $\{(m/M)n_j^{1/2}E_j^{1/2}\}$ for the full time step Δt.

    This process is repeated for thousands of time steps.

2.2.3 Limitation of Fluid Model

The fluid modeling of plasma is a very powerful technique to describe the plasma behavior. However, fluid model fails to simulate phenomenon involving wave-particle interaction, viz., dynamics of plasma after wave-breaking, BGK modes, etc. which can be treated only via kinetic theory.

2.3 Particle-in-cell Model

Particle-in-cell [96] simulation is a scheme where millions of super particles are evolved through self consistent average electromagnetic forces. Superparticles are tracked by solving fundamental equations, viz., Newton-Lorentz equation for the motion of charged particles coupled with Maxwell equations for the self-consistent calculation of electric and magnetic fields. The governing equations, viz., the equation of particle position and velocity, and the Poisson equation in normalized forms are for non-relativistic case,

$$\frac{dx_s}{dt} = v_s, \tag{2.8}$$
$$\frac{dv_s}{dt} = \pm E, \tag{2.9}$$
$$\frac{\partial E}{\partial x} = (n_i - n_e), \tag{2.10}$$

for relativistic case,

$$\frac{dx_s}{dt} = \frac{u_s}{\gamma_s}, \tag{2.11}$$
$$\frac{du_s}{dt} = \pm E, \tag{2.12}$$
$$\frac{\partial E}{\partial x} = (n_i - n_e). \tag{2.13}$$

Then normalization used are $x \to k_L x$, $t \to \omega_{pe} t$, $v_s \to k_L v_s/\omega_{pe}$, $u_s \to k_L u_s/\omega_{pe}$, $E \to ek_L E/m\omega_{pe}^2$ and , $\phi \to ek_L^2 \phi/m\omega_{pe}^2$

Now we describe the basic module for simulating plasma using particle-in-cell method; a typical flow chart is shown in Fig. 2.4. We consider one dimensional system of length $'L'$ of N particles interacting through self consistent electrostatic forces. We have taken plasma to be of infinite extent which is modeled by keeping boundary conditions periodic. The length of the system is chosen to be equal to the wavelength of the shortest k mode supported by the system. The system is divided into NG equidistant cells of width $\Delta x = L/NG$, numbered from 0 to NG. The center of the cells are known as grid points. Periodic boundary condition implies 0^{th} and NG^{th} being identical. All the field quantities, viz., electric field, potential, charge and number density are determined at the grid points.

After discretizing the system into cells, particles are then loaded into continuum phase space according to given initial density and momentum (velocity) distribution.

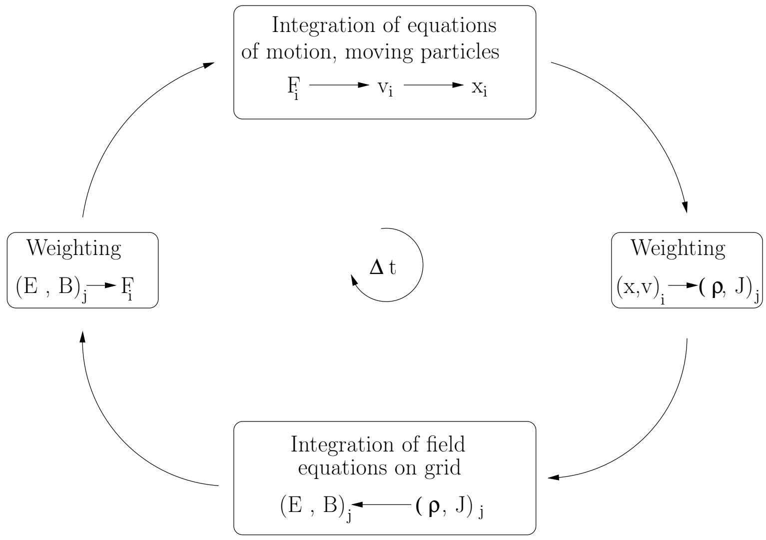

Figure 2.4: Flow chart for particle-in-cell simulation code.

The particle positions and momenta (velocity) are obtained by inverting the required distribution function. Once the initial conditions are specified the charge density is calculated on the grid points using weighting scheme. Weighting is carried out from particle positions to the grid points using some kind of interpolation scheme. In our code we use quadratic spline weighting scheme.

In next step of the simulation, we evaluate electric field on the grid by solving Gauss's law using central difference scheme. After calculation of the electric field, the forces acting on the particles are evaluated using an interpolation scheme. We use the same interpolation scheme that was used for charge interpolation on the grid points. One must use same interpolation scheme as has been used for charge assignment. This is important because it can be shown [97] that for identical charge assignment and force interpolation schemes and correctly space - centered difference approximations for derivatives, the self force on a particle arising due to various particles to grid and grid to particles interpolations is zero and the total momentum of the system is identically conserved.

Now the forces have been calculated on the particle positions, in next step, we use forces to determine new position of the particles by solving equation of motion. We solve equation of motion using standard leap-frog scheme, which is fast and second order accurate.

2.3.1 Numerical Scheme for PIC Simulation

This section gives more elaborate details of the various numerical schemes used in the particle-in-cell code. We start with the particle loading method and then go over to charge density calculation on the grid points, solution of field equation, force calculation on the particles and leap frog scheme for solving the equations of motion.

2.3.1.1 Particle Loading Scheme

A physical system is specified by its initially specified average density $n_0(x)$ and momentum (velocity) $f_0(u)(f_0(v))$ profile. It is necessary to find position and momentum (velocity) of all the particles in order to generate these profile in the simulation model. To do this, density and momentum (velocity) profiles have to be inverted to get required position and momentum (x_i, p_i) or position and velocity (x_i, v_i) in phase space. In this section, we describe the method of density loading [98] . Loading of particles in momentum (velocity) space will be discussed later. Let $n(x)$ be the initial density profile confined in the region $a \leq x \leq b$. The probability of finding the particle between x and $x + dx$ is $\frac{n(x)}{N}dx$, where $N = \int\limits_a^b n(x)dx$. is the total number of particles and $p(x) = \frac{n(x)}{N}$ is the probability density. If we consider that distribution of particles is uniform between (a, b) then the probability density $p(x)$ is constant and is given by $p(y) = 1/(b - a)$.

Let y be the position of a given particles in this case. To generate $p(x)$ from this, y has to be moved to a different position, consider x, which is unknown. Now unknown x is evaluated by equating the total number of particles up to y to the total number of particles upto x. Therefore

$$N\int_a^y p(y)dy = N\int_a^x p(x')dx', \tag{2.14}$$

$$\frac{y-a}{b-a} = \int_a^x \frac{n(x')}{N}dx', \tag{2.15}$$

$$\frac{y-a}{b-a} = \frac{\int_a^x n(x')dx'}{\int_a^b n(x')dx'}. \tag{2.16}$$

By equating $\frac{y-a}{b-a}$ to an uniform distribution of numbers R_i, where $0 < R_i < 1$, and solving the equation (2.16), x_i corresponding to position y_i for the i_{th} particle can be determined.

Using similar scheme, we do particle loading in velocity space. Maxwellian distribution in velocity v is represented as $\exp(-v^2/2v_t^2)$, where v_t is thermal velocity of the electrons. Consider a range of velocity $v_l \geq v \geq v_u$ such that all particles are confined within this range, where v_u and v_l respectively are upper and lower bound on velocity. Then the probability of finding the particle within the range (v_u, v_l) is $\int_{v_l}^{v_u} \exp(-v^2/2v_t^2)dv$. Therefore cumulative distribution function for the speed is given by

$$R_s = F(v) = \frac{\int_0^v \exp\left(\frac{-v^2}{2v_t^2}\right)dv}{\int_{v_l}^{v_u} \exp\left(\frac{-v^2}{2v_t^2}\right)dv}, \tag{2.17}$$

where R_s is a set of quasirandom numbers ranging from 0 to 1. In our simulation code we choose Sobol set [99] of quasirandom numbers. By solving integrals in equation (2.17) yields following equation

$$R_s = \frac{\operatorname{erf}\left(\frac{v}{\sqrt{2}v_t}\right)}{\operatorname{erf}\left(\frac{v_u}{\sqrt{2}v_t}\right) - \operatorname{erf}\left(\frac{v_l}{\sqrt{2}v_t}\right)}, \tag{2.18}$$

where erf is an error function. By inverting equation (2.18) for quasirandom numbers

R_s loads the required Gaussian distribution in velocity space. This method does not only give global Gaussian, but also Gaussian locally.

2.3.1.2 Charge Density Calculation

The charge density at the grid points is evaluated by interpolating the charges from the particle positions to the grid points. In our simulation code, we use quadratic spline weighting scheme, which distributes the charge of a particle among three neighboring grid points. Weighting function for quadratic spline scheme [97] is given by

$$W_j(X_j - x) = \left[\frac{3}{4} - \left(\frac{x - X_j}{\Delta x}\right)^2\right] \tag{2.19}$$

$$W_{j\pm1}(X_{j\pm1} - x) = \frac{1}{2}\left[\frac{2}{2} \pm \frac{x - X_j}{\Delta x}\right]^2. \tag{2.20}$$

2.3.1.3 Solution of Field Equation

In our simulation, Gauss's law is solved using central difference scheme as

$$\frac{E_{j+1} - E_{j-1}}{2\Delta x} = \rho_j, \tag{2.21}$$

where ρ is charge density accumulated at the j_{th} grid point. As we are using periodic boundary conditions, the R.H.S. of equation (2.21) is periodic $\rho_0 = \rho_{NG}$; implies $E_0 = E_{NG}$. In terms of potential, equation (2.21) can be written as

$$\frac{\phi_{j+1} - 2\phi_j + \phi_{j-1}}{\Delta x^2} = -\rho_j, \tag{2.22}$$

which can be reduced in the form of tridiagonal matrix as

$$A\Phi = \rho, \tag{2.23}$$

where

$$A = \begin{bmatrix} -2 & 1 & 0 & \ldots\ldots & & \\ 1 & -2 & 1 & \ldots\ldots & & \\ 0 & 1 & -2 & \ldots\ldots & & \\ & & & \ldots\ldots & & \\ & & & \ldots\ldots & -2 & 1 \\ & & & \ldots\ldots & 1 & -2 \end{bmatrix}, \Phi = \begin{bmatrix} \phi_0 \\ \phi_1 \\ \phi_2 \\ \ldots \\ \phi_{NG-2} \\ \phi_{NG-1} \end{bmatrix} \text{ and } \rho = \begin{bmatrix} \rho_0 \\ \rho_1 \\ \rho_2 \\ \ldots \\ \rho_{NG-2} \\ \rho_{NG-1} \end{bmatrix},$$

The system of linear equations (2.23) are solved using Gauss elimination method. After determining electrostatic potential on the grid points, electric field is calculated very easily using following central difference scheme

$$E_j = -\frac{\phi_{j+1} - \phi_{j-1}}{2\Delta x}. \tag{2.24}$$

This field is further used for pushing the particles by solving equation of motion.

2.3.1.4 Calculation of Force

In previous section, we evaluated field on grid points. In this section we describe the method required to calculate force on the particles. This is carried out by interpolating the fields from the grid points to the particle positions. For this we use similar weighting function, that we used for charge assignment as

$$F(x_j) = \left[\frac{3}{4} - \left(\frac{x_i - X_j}{\Delta x}\right)^2\right] E_j + \frac{1}{2}\left[\frac{1}{2} + \frac{x_i - X_j}{\Delta x}\right]^2 E_{j+1} + \frac{1}{2}\left[\frac{1}{2} - \frac{x_i - X_j}{\Delta x}\right]^2 E_{j-1}. \tag{2.25}$$

2.3.1.5 Leap-Frog Scheme

In this section we describe the Leap-Frog scheme, which is used for solving the equation of motion which pushes the particles forward in space and time in single time step. The time centered difference forms of equations (2.9), (2.8) and (2.12), (2.11) in respective non-relativistic and relativistic regimes are

for non-relativistic case,

$$\frac{v^{n+\frac{1}{2}} - v^{n-\frac{1}{2}}}{\Delta t} = E^n, \tag{2.26}$$

$$\frac{x^{n+1} - x^n}{\Delta t} = v^{n+\frac{1}{2}}, \tag{2.27}$$

for relativistic case,

$$\frac{u^{n+\frac{1}{2}} - u^{n-\frac{1}{2}}}{\Delta t} = E^n, \tag{2.28}$$

$$\frac{x^{n+1} - x^n}{\Delta t} = \frac{u^{n+\frac{1}{2}}}{\gamma^{n+\frac{1}{2}}}, \tag{2.29}$$

where $u = \gamma v$ and $\gamma^2 = 1 + u^2/c^2$. Superscript 'n' represent values at integral time steps and superscript $n + 1/2$ represent values at half integral time steps. Time centering in Leap frog scheme is achieved by staggering velocities and positions of the particles by $\Delta t/2$. As we define the initial positions and velocities at $t = 0$, which is why to fit the leap-frog scheme, velocities are move backward once by $-\Delta t/2$.

In the section 2.3, we have described all the basic numerical schemes required for setting up an one dimensional particle-in-cell code. The process from calculation of charge density to solving the equation of motion using leap-frog scheme is repeated for thousands of time steps, which is also described in flow chart 2.4 .

2.4 Summary

In this chapter, we have presented a brief description of numerical schemes (fluid and particle-in-cell model) used for simulation of current carrying cold plasmas. We have employed LCPFCT [95] package for solving continuity and momentum equation while Poisson equation is solved using central difference scheme. Due to limitation of fluid model, one requires more generalized numerical scheme and Particle-in-cell [96] simulation indeed provides more detailed information about the dynamics of plasmas. However, fluid models are much more cost effective than PIC models. It must be noted here that results of fluid model could be recovered from particle model if sufficient temporal and spatial resolution is taken into account. Results of simulation carried out using fluid and particle-in-cell simulation code in different parameter regime are discussed from chapter 4 onwards. Benchmarking of codes against existing theoretical results is presented from chapter 4 onwards where an extensive comparison is carried out between simulation and theoretical results.

Chapter 3

Study of stationary BGK structures in current carrying relativistic fluid-Maxwell system

In this chapter, nonlinear stationary structures, formed in cold plasma with immobile ions, in the presence of a spatially modulated relativistic electron current beam have been investigated analytically in the collisionless limit. These are cold plasma version of the relativistic BGK waves. The structure profile is governed by the ratio of maximum electrostatic field energy density to the relativistic kinetic energy density of the electron beam, i.e., $\kappa_R = E_m/(8\pi n_0(\gamma_0 - 1)m_0c^2)^{1/2}$, where E_m is the maximum electric field associated with the nonlinear structure and γ_0 is the Lorentz factor associated with average beam speed. In the linear limit, i.e., $\kappa_R \ll 1/\sqrt{\gamma_0}$, the fluid variables, viz, density, electric field, and velocity vary harmonically in space. In the range $0 < \kappa_R \leq 1/\sqrt{\gamma_0}$, the fluid variables exhibit an-harmonic behaviour. For values of $\kappa_R > 1/\sqrt{\gamma_0}$, the electric field shows finite discontinuities at specific spatial locations indicating formation of negatively charged planes at these locations. Dis-

continuity in the electric field momentarily stops the electrons, resulting in the formation of periodic electrostatic (BGK) structures consists of negatively charged planes.

In this chapter we derive exact stationary solutions of BGK structures in current carrying cold relativistic fluid-Maxwell system. An exact expression for electrostatic potential, electric field, electron density and electron velocity as a function of position are derived which describe the nonlinear BGK structures. It is also shown that, in an appropriate limit, results of relativistic theory coincide with the non-relativistic results. In section 3.1 we give an introduction of the problem. In section 3.1.1, we derive linear results and in section 3.1.2 nonlinear theory is derived and results are described. We end the chapter with a brief discussion in section 3.2.

3.1 Introduction

Cold relativistic electron beam can support variety of waves in plasma. Here we study a special class of nonlinear waves called stationary BGK waves [13] in a cold plasma which are excited by a relativistic electron beam. In the non-relativistic regime, and in the absence of a beam, propagating BGK waves in a cold plasma have been derived by Albritton et. al. [14]. The BGK mode in this case was obtained from the exact space-time dependent solution [20] of the full nonlinear fluid-Maxwell set of equations. Similarly propagating BGK waves in a cold relativistic plasma in the absence of a relativistic electron beam is simply obtained by transforming the governing equations in such a frame, where the wave is at rest, the so-called wave frame [15]. Verma et. al. [72] also constructed such a solution for propagating BGK waves (Akhiezer-Polovin wave [16]) from exact space-time dependent solution [17] of the full relativistic fluid-Maxwell set of equations by choosing a special kind of transformation[14]. Wang [18] used similar kind of transformation for relativistic streaming plasmas and obtained a nonlinear dispersion relation in Vlasov-Maxwell framework. In the presence of a beam Psimpolous et. al. [19] obtained the solutions for stationary BGK waves (stationary in lab frame) in current carrying non-relativistic cold plasmas for a wide range of parameter ($\kappa = E_m/(4\pi n_0 m v_0^2)^{1/2}$), where E_m is maximum amplitude of the electric field, v_0 is average electron beam speed and other symbols have their usual meanings.

In this chapter, we study BGK structures in a relativistic electron beam propagating through an immobile homogeneous positive background of ions. Under the influence of applied harmonic perturbation, periodic compression and rarefaction occurs in density, so according to equation of continuity electrons accelerate and retard periodically in space, to maintain the constant flux throughout the system. These periodic departures from charge neutrality induce in turn a longitudinal electric field which produces the necessary force on the electrons so that the whole system is kept in stationary state. It is found that the basic parameter that embodies the nonlinear effects in the system, is a ratio of maximum electrostatic energy density to total relativistic kinetic energy density, *i.e.*, $\kappa_R = E_m/(8\pi n_0(\gamma_0 - 1)m_0c^2)^{1/2}$, where E_m is the maximum amplitude of the electric field, γ_0 is the Lorentz factor associated with average beam speed (v_0), n_0 and m_0 are respectively the density and rest mass of the electron and c being the speed of light.

In the non-relativistic limit [19], it is found that if $\kappa_{NR} \to \kappa_{NR}^c = E_m/(4\pi n_0 m v_0^2)^{1/2} = 1$, electric field gradient becomes infinitely steep, periodically in space; so according to Poisson's law, electron density also becomes infinitely large. In the case of a relativistic beam and in the presence of relativistically intense wave, the critical parameter κ_R^c is modified and is found to depend on the average beam speed v_0 as $\kappa_R^c = \frac{1}{\sqrt{\gamma_0}}$. If $\kappa_R \ll \kappa_R^c$, the fluid variables $v_e(x)$, $n_e(x)$, $\phi(x)$, and $E(x)$ vary harmonically in space in accordance with linear theory. As κ_R increases, and approaches $\approx \kappa_R^c$ within the interval $0 \ll \kappa_R < \kappa_R^c$, the above variables gradually become anharmonic in space. In the case of $\kappa_R \geq \kappa_R^c$ it is shown that gradient of electric field becomes infinitely steep periodically at certain singular points which in turn implies discontinuity in electric field and explosive behavior of electron density. This discontinuous electric field implies formation of negatively charged perfectly conducting planes, infinitely extended in the transverse direction. In the limit $\kappa_R \to \infty$ the BGK structure collapses to a 1-D crystal. It is also shown that in this limit, results of nonlinear relativistic theory coincide with the nonlinear non-relativistic theory.

3.1.1 Linear Theory

Let us consider an infinitely long 1D system, where a relativistic electron beam of density n_0 and velocity v_0 is propagating through an immobile homogeneous positive background of ions of density n_0. The basic set of governing equations required to study nonlinear stationary BGK structures are

$$\frac{\partial n_e v_e}{\partial x} = 0, \tag{3.1}$$

$$v_e \frac{\partial p_e}{\partial x} = -eE, \tag{3.2}$$

$$\frac{\partial E}{\partial x} = 4\pi e(n_0 - n_e) \tag{3.3}$$

where $p_e = \gamma m_0 v_e$ is momentum of electrons, v_e is electron velocity, n_e is electron density, E is electric field and other symbols have their usual meaning.

In the linear limit $\kappa_R \ll 1$ and in the spirit of weakly relativistic flow $v_0 < c$, fluid variables describing the spatial profile can be obtained using linearized set of steady state fluid equations. The continuity equation is

$$n_0 \frac{\partial v_e}{\partial x} + v_0 \frac{\partial n_e}{\partial x} = 0, \tag{3.4}$$

the momentum equation is

$$v_0 \frac{\partial p_e}{\partial x} = e \frac{\partial \phi}{\partial x}, \tag{3.5}$$

and the Poisson equation is,

$$\frac{\partial E}{\partial x} = 4\pi e (n_0 - n_e). \tag{3.6}$$

Using equations (3.4), (3.5) and (3.6), solution of stationary equations in the linear limit can be obtained straightforwardly as

$$E(x) = E_m \sin\left(\frac{x}{s_R}\right),$$

$$\phi(x) = \phi_0 + \frac{\gamma_0 m_0 c^2}{e} \kappa_R \beta \sqrt{2\gamma_0(\gamma_0 - 1)} \cos\left(\frac{x}{s_R}\right), \tag{3.7}$$

$$v_e(x) = v_0 \left(1 + \frac{\kappa_R \sqrt{2(\gamma_0 - 1)}}{\beta \gamma_0^{3/2}} \cos\left(\frac{x}{s_R}\right)\right), \tag{3.8}$$

and

$$n_e(x) = n_0 \left(1 - \frac{\kappa_R \sqrt{2(\gamma_0 - 1)}}{\beta \gamma_0^{3/2}} \cos\left(\frac{x}{s_R}\right)\right), \tag{3.9}$$

where ϕ_0 is an arbitrary additive potential, $\beta = v_0/c$, and $s_R = v_0 \gamma_0^{3/2}/\omega_{pe}$ is the wavelength of stationary waves in the linear limit $\kappa_R \ll \kappa_R^c$. It is readily seen that in the linear limit fluid variables of stationary waves are harmonic in space. At $\phi = \phi_0$, amplitude of electric field is $E = E_m$ and fluid variables becomes equal to their average value. Equations (3.7) - (3.9) can be rewritten in terms of normalized parameters as

$$E(X) = \kappa_R \sin X,$$

$$\Phi(X) = \kappa_R \beta \sqrt{2\gamma_0(\gamma_0 - 1)} \cos X, \tag{3.10}$$

$$v_e(X) = \beta \left(1 + \frac{k_R \sqrt{2(\gamma_0 - 1)}}{\beta \gamma_0^{3/2}} \cos X\right), \tag{3.11}$$

and

$$n_e(X) = \left(1 - \frac{k_R \sqrt{2(\gamma_0 - 1)}}{\beta \gamma_0^{3/2}} \cos X\right), \tag{3.12}$$

where $X = x/s_R$, $E \to E/E_0$, $E_0 = (8\pi n_0(\gamma_0 - 1)m_0c^2)^{1/2}$, $\Phi = e(\phi - \phi_0)/\gamma_0 m_0 c^2$, $v_e \to v_e/c$ and $n_e \to n_e/n_0$. Fig. 3.1 and 3.2 show the potential, electric field, velocity and density for two different average beam speeds $\beta = 0.1$ and $\beta = 0.9$ respectively and nonlinear parameter $\kappa_R = 0.01$. In Fig. 3.1 and 3.2 continuous curves are obtained from the linear theory.

3.1.2 Nonlinear Theory

The set of nonlinear stationary relativistic fluid equations are

$$v_e \frac{\partial p_e}{\partial x} = e \frac{\partial \phi}{\partial x}, \tag{3.13}$$

$$\frac{\partial n_e v_e}{\partial x} = 0, \tag{3.14}$$

$$\frac{\partial E}{\partial x} = 4\pi e(n_0 - n_e). \tag{3.15}$$

Now integrating equation (3.13) and assuming that at $\phi = \phi_0$ at $v = v_0$, relation between electron velocity and electrostatic potential is obtained as

$$\frac{m_0 c^2}{\sqrt{1 - v_e^2/c^2}} - \frac{m_0 c^2}{\sqrt{1 - v_0^2/c^2}} = e(\phi(x) - \phi_0). \tag{3.16}$$

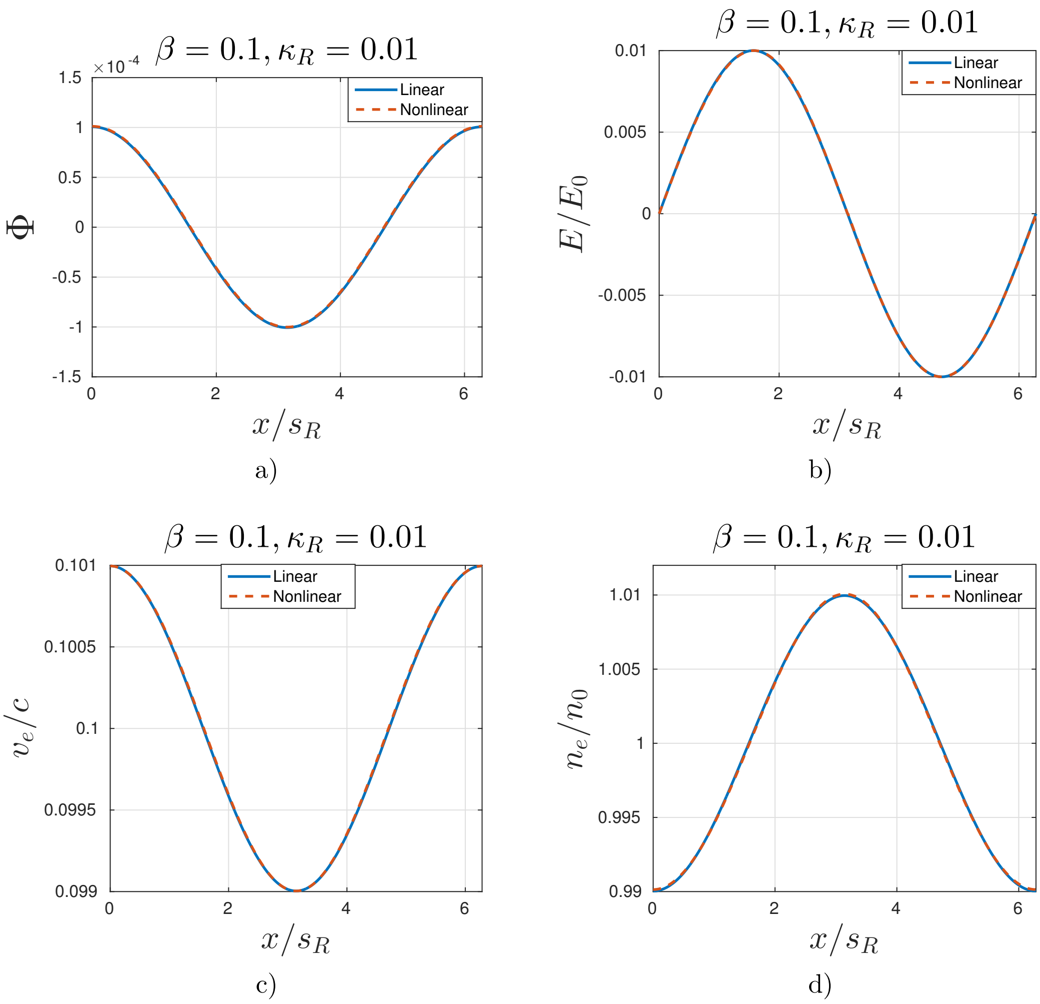

Figure 3.1: Fig shows (a) potential (b) electric field (c) velocity and (d) density for the parameters $\beta = 0.1;\kappa_R = 0.01$. Here continuous curves are obtained from linear theory and dashed curves are result of nonlinear theory.

Using equation (3.14), (3.15) and (3.16), gradient of electric field as a function of potential can be written as

$$\frac{d^2\Phi}{dX^2} = -\beta^2\gamma_0^2\left(1 - \beta\frac{1+\Phi}{\sqrt{(1+\Phi)^2 - 1 + \beta^2}}\right), \tag{3.17}$$

or

$$\frac{d^2\Phi}{dX^2} = -\frac{dV_1(\Phi)}{d\Phi}, \tag{3.18}$$

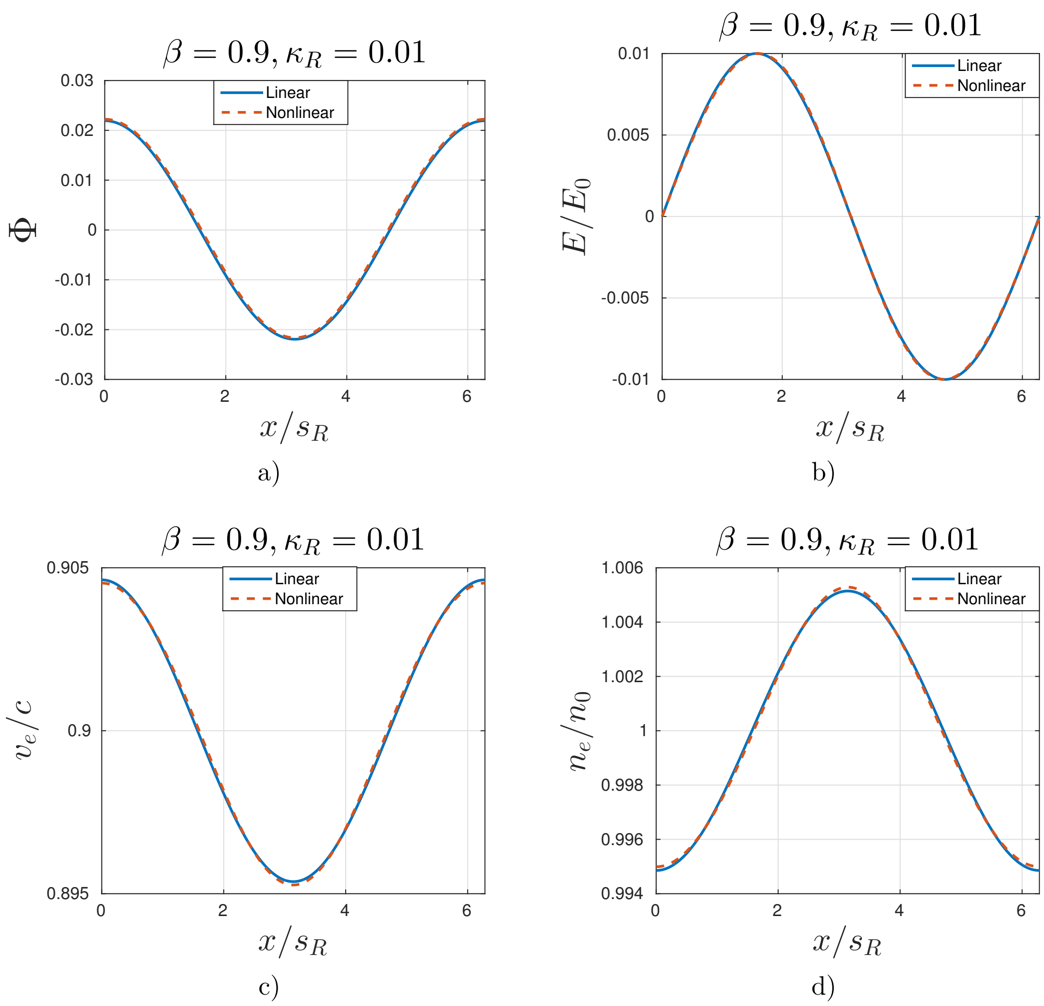

Figure 3.2: Fig shows (a) potential (b) electric field (c) velocity and (d) density for the parameters $\beta = 0.9$;$\kappa_R = 0.01$. Here continuous curves are obtained from linear theory and dashed curves are result of nonlinear theory.

$$\frac{d}{d\Phi}\left\{\frac{1}{2}\left(\frac{d\Phi}{dX}\right)^2 + V_1(\Phi)\right\} = 0, \tag{3.19}$$

or

$$\frac{1}{2}\left(\frac{d\Phi}{dX}\right)^2 + V_1(\Phi) = constant, \tag{3.20}$$

which is an energy equation. Here $V_1(\Phi)$ is a Sagdeev potential and given by

$$V_1(\Phi) = \beta^4\gamma_0^2\left(1 + \frac{\Phi}{\beta^2} - \sqrt{1 + \frac{2\Phi}{\beta^2} + \frac{\Phi^2}{\beta^2}}\right). \tag{3.21}$$

Now putting $d\Phi/dX = -\beta(2\gamma_0(\gamma_0-1))^{1/2}\, E$ in the equation (3.20), yields

$$E^2 + \frac{V_1(\Phi)}{\beta^2\gamma_0(\gamma_0-1)} = constant, \tag{3.22}$$

or

$$E^2 + V(\Phi) = constant, \tag{3.23}$$

constant in equation (3.23) can be obtained using the condition that at $\Phi = 0$; $V(\Phi) = 0$ and $E = \kappa_R$, then equation (3.23) becomes

$$E^2 + V(\Phi) = \kappa_R^2 \tag{3.24}$$

Equation (3.24) gives a family of curves in the phase space $\Phi - E$ modulated by the parameter κ_R and β, where $V(\Phi)$ is defined as

$$V(\Phi) = \frac{1+\gamma_0}{\gamma_0}\left(1 + \frac{\Phi}{\beta^2} - \sqrt{1 + \frac{2\Phi}{\beta^2} + \frac{\Phi^2}{\beta^2}}\right) \tag{3.25}$$

In Fig. 3.3 solid blue curve shows variation of Sagdeev potential with the electrostatic potential Φ for different average beam speeds $\beta \approx 0.1$, $\beta \approx 0.5$, $\beta \approx 0.9$ and $\beta \approx 0.99$. It is noticed here that Sagdeev potential becomes undefined at $\Phi^c = -(\gamma_0 - 1)/\gamma_0$ (below this value of potential, the square root term becomes imaginary). Substituting this value of Φ^c in $V(\Phi)$, the critical value of pseudo-energy (κ_R) turns out to be $\kappa_R^c = 1/\sqrt{\gamma_0}$. The κ_R^c is the critical value of κ_R, above which periodic solutions do not exist. The straight lines in Fig. 3.3 show different values of $\kappa_R \lesssim \kappa_R^c$ for which periodic solutions exist; corresponding to these values of κ_R closed orbits are seen in $\Phi - E$ space (Fig. 3.4).

In Fig. 3.4 the relation $\Phi - E$ is plotted for different values of the parameters (κ_R) and relativity (β) parameters. It is readily noticed by looking at the Fig. 3.4 that the variation of β modulates the shape of phase space curves as well as changes

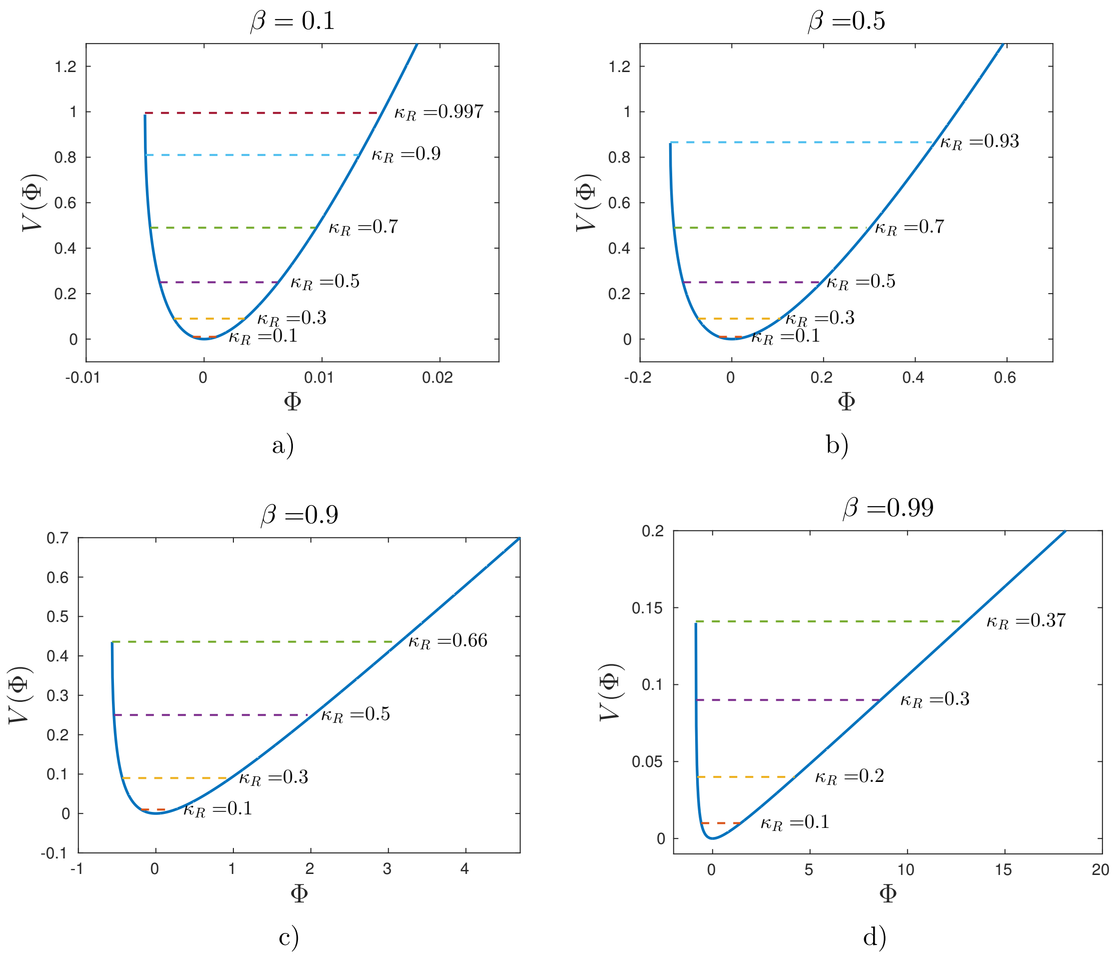

Figure 3.3: In this Fig. continuous line shows Sagdeev potential for different speed ratios (a) $\beta = 0.1$ (b) $\beta = 0.5$ (c) $\beta = 0.9$ and (d) $\beta = 0.99$ and dotted line shows level of pseudo-energy for different value of κ_R.

the range of electrostatic potential Φ. It is also noticed that phase space becomes discontinuous after a critical value of κ_R and this critical value as mentioned above is $\kappa_R = \kappa_R^c = 1/\sqrt{\gamma_0}$. It is found that at the $\kappa_R = \kappa_R^c$, gradient of electric field becomes infinite, *i.e.*, $dE/dX \to \infty$, which is a sign of wave breaking of stationary BGK structures in current carrying plasmas.

The range of electrostatic potential Φ for $0 \leq \kappa_R \leq \kappa_R^c$ and for $\kappa_R^c \leq \kappa_R < \infty$, can be obtained from equation (3.24) and are respectively given by equations (3.26) and (3.27) below

$$\gamma_0(\gamma_0 - 1)\left(\kappa_R^2 - \kappa_R\beta\sqrt{\kappa_R^2 + \frac{2}{\gamma_0(\gamma_0-1)}}\right) \leq \Phi \leq$$

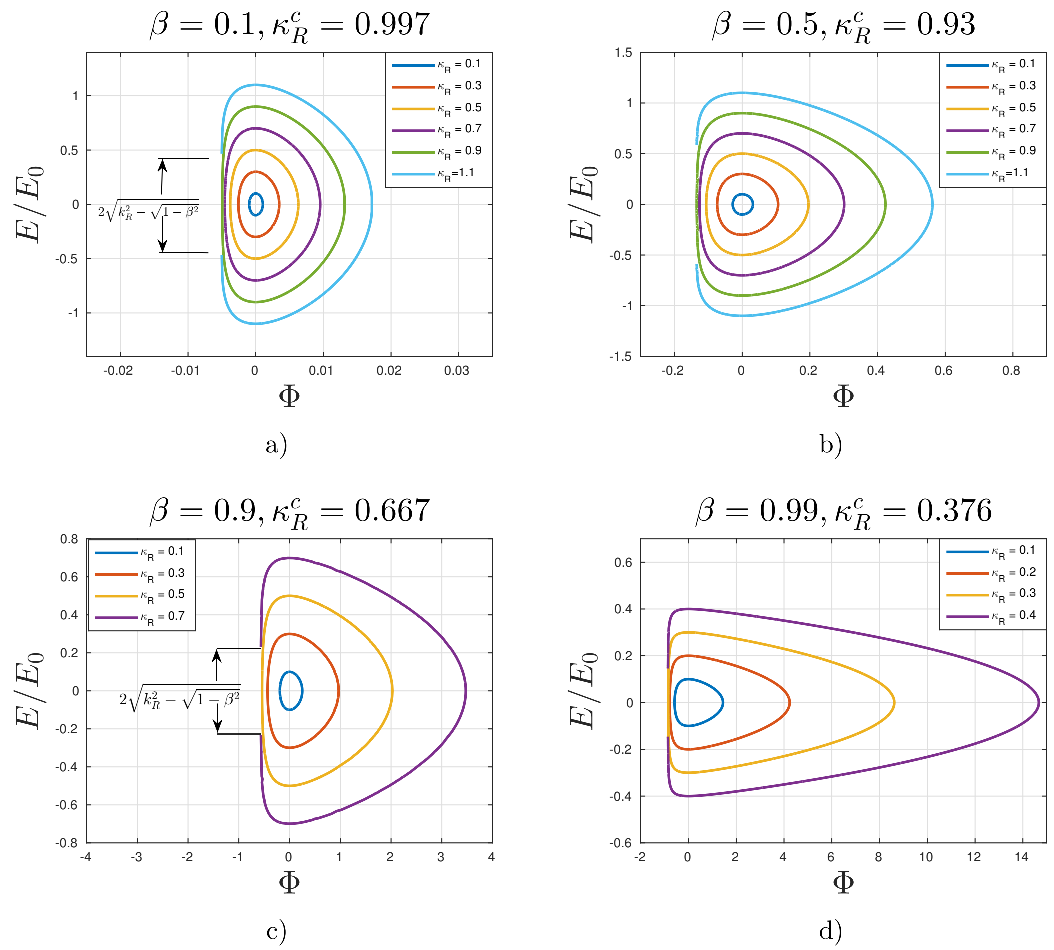

Figure 3.4: $\Phi - E$ phase space for different nonlinear parameter and ratio of average speed of the beam to speed of light (a) $\beta \approx 0.1$, (b) $\beta \approx 0.5$, (c) $\beta \approx 0.9$, (d) $\beta \approx 0.99$.

$$\gamma_0(\gamma_0 - 1)\left(\kappa_R^2 + \kappa_R\beta\sqrt{\kappa_R^2 + \frac{2}{\gamma_0(\gamma_0-1)}}\right) \qquad 0 \leq \kappa_R \leq \frac{1}{\sqrt{\gamma_0}} \tag{3.26}$$

$$-\left(1 - \frac{1}{\gamma_0}\right) \leq \Phi \leq \gamma_0(\gamma_0 - 1)\left(\kappa_R^2 + \kappa_R\beta\sqrt{\kappa_R^2 + \frac{2}{\gamma_0(\gamma_0-1)}}\right) \qquad \frac{1}{\sqrt{\gamma_0}} \leq \kappa_R < \infty \tag{3.27}$$

In the range $0 \leq \kappa_R \leq \kappa_R^c$, curves of equation (3.24) are continuous and E is found to be oscillating in the range $-\kappa_R \leq E \leq \kappa_R$. In the range $\kappa_R \geq \kappa_R^c$, E becomes discontinuous at $\Phi^c = (1-\gamma_0)/\gamma_0$ and jumps from $E = -\sqrt{\kappa_R^2 - \sqrt{1-\beta^2}}$ to $E = \sqrt{\kappa_R^2 - \sqrt{1-\beta^2}}$. This implies that $E(X)$ is discontinuous at the positions X satisfying the condition $\Phi = e(\phi(X) - \phi_0)/\gamma_0 m_0 c^2 = (1-\gamma_0)/\gamma_0$. The critical electrostatic potential at which its gradient $(E(X))$ becomes discontinuous, is not constant as in non-relativistic regime ($\Phi^c_{non-relativistic} = -1$) [19], rather, relativity brings the dependency of critical electrostatic potential on the average beam speed by the relation $e(\phi(X) - \phi_0)/\gamma_0 m_0 c^2 = (1-\gamma_0)/\gamma_0$. Figure 3.5 shows variation of critical nonlinear parameter κ_R^c and critical electrostatic potential Φ^c with respect to ratio of average beam speed to speed of light. Potential varies from $\Phi^c = 0 - (-1)$ for the range $\beta = 0 - 1$; $\gamma_0 = 1 - \infty$. This implies $E(X)$ is discontinuous at the positions X satisfying $e(\phi(X) - \phi_0)/\gamma_0 m_0 c^2 = 0 - (-1)$.

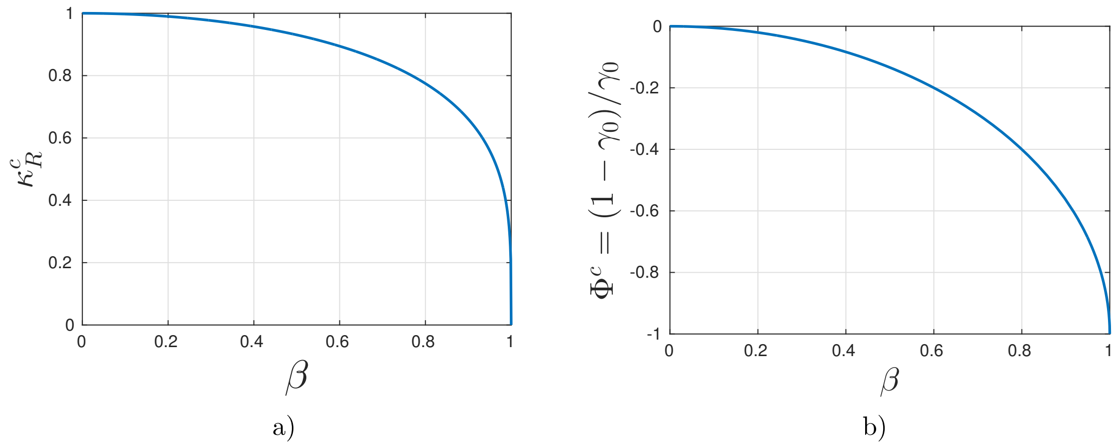

Figure 3.5: Variation of (a) critical nonlinear parameter $\kappa_R^c = 1/\sqrt{\gamma_0}$ (b) critical potential $\Phi^c = (1-\gamma_0)/\gamma_0$ with respect to ratio of average beam speed to the speed of light (β).

Using $E = \frac{-1}{\beta(2\gamma_0(\gamma_0-1))^{1/2}}\frac{d\Phi}{dX}$, and assuming $\Phi = \Phi_u = \gamma_0(\gamma_0-1)\left(\kappa_R^2 + \kappa_R\beta\sqrt{\kappa_R^2 + \frac{2}{\gamma_0, (\gamma_0-1)}}\right)$ at $X = 0$, the energy equation (3.24) can be integrated to obtain potential as a function of position as

$$\beta(2\gamma_0(\gamma_0-1))^{1/2}\int_0^X dX = -\int_\Phi^{\Phi_u} \frac{d\Phi}{\left(\kappa_R^2 - \frac{1+\gamma_0}{\gamma_0}\left(1 + \frac{\Phi}{\beta^2} - \sqrt{1 + \frac{2\Phi}{\beta^2} + \frac{\Phi^2}{\beta^2}}\right)\right)^{1/2}}. \quad (3.28)$$

For simplification, we assume $\Phi + 1 = \xi\sqrt{1-\beta^2}$, then integrand of R.H.S. of equation (3.28) takes the form

$$\frac{d\Phi}{\left(\kappa_R^2 - \frac{1+\gamma_0}{\gamma_0}\left(1+\frac{\Phi}{\beta^2} - \sqrt{1+\frac{2\Phi}{\beta^2}+\frac{\Phi^2}{\beta^2}}\right)\right)^{1/2}} =$$

$$\frac{\sqrt{1-\beta^2}d\xi}{\left(\kappa_R^2 - \frac{1+\gamma_0}{\gamma_0}\left(1+\frac{\xi\sqrt{1-\beta^2}-1}{\beta^2} - \frac{\sqrt{1-\beta^2}}{\beta}\sqrt{\xi^2-1}\right)\right)^{1/2}}. \tag{3.29}$$

For the sake of convenience, we define a new mathematical quantity α as

$$\alpha = (\gamma_0 - 1)\kappa_R^2 + \frac{1}{\gamma_0}, \tag{3.30}$$

which transforms the equation (3.29) into

$$\frac{d\Phi}{\left(\kappa_R^2 - \frac{1+\gamma_0}{\gamma_0}\left(1+\frac{\Phi}{\beta^2} - \sqrt{1+\frac{2\Phi}{\beta^2}+\frac{\Phi^2}{\beta^2}}\right)\right)^{1/2}} = \frac{\beta}{(1+\gamma_0)^{1/2}}\frac{d\xi}{\left(\alpha - \xi + \beta\sqrt{\xi^2-1}\right)^{1/2}}. \tag{3.31}$$

In order to further simplify the calculation of the above integral, a new variable transformation is introduced which is defined as

$$\sqrt{\xi^2-1} = \chi^2 - \xi, \tag{3.32}$$

and

$$d\xi = \left(\chi - \frac{1}{\chi^3}\right)d\chi, \tag{3.33}$$

then the integral (3.31) changes into

$$-\int_{\xi}^{\xi_u} \frac{\beta d\xi}{\sqrt{1+\gamma_0}\left(\alpha - \xi + \beta\sqrt{\xi^2-1}\right)^{1/2}} =$$

$$-\left(\frac{1+\beta}{1-\beta}\right)^{1/2}\left(\frac{2}{1+\gamma_0}\right)^{1/2}\int_{\chi}^{\chi_u}\frac{(\chi^2-1/\chi^2)d\chi}{((r^2-\chi^2)(\chi^2-s^2))^{1/2}}, \tag{3.34}$$

where r^2 and s^2 are function of X and are defined as

$$r^2 = \frac{\alpha + \sqrt{\alpha^2 + \beta^2 - 1}}{1-\beta}, \tag{3.35}$$

$$s^2 = \frac{\alpha - \sqrt{\alpha^2 + \beta^2 - 1}}{1-\beta}. \tag{3.36}$$

It must be noted here that substitution of new variable $\chi(X)$, is merely a mathematical manipulation, and does not imply any restriction on the range of the potential. Now equation (3.34) is in standard form and can be reduced easily in the form of elliptic integral upon using new substitution

$$\sin^2\theta = \frac{r^2 - \chi^2}{r^2 - s^2} \tag{3.37}$$

this implies

$$d\chi = -\frac{(r^2 - s^2)\sin\theta\cos\theta}{\sqrt{r^2\cos^2\theta + s^2\sin^2\theta}} \tag{3.38}$$

Thus, the exact solution of equation (3.28) can be written as

$$Xr^3 = -\frac{(1+\beta)^{1/4}}{\gamma_0\beta(1-\beta)^{1/4}}\left(\left(\frac{r^4(k^2-1)+1}{k^2-1}\right)E(\theta,k) - \frac{k^2\sin 2\theta}{2(k^2-1)(1-k^2\sin^2\theta)^{1/2}}\right) + c1(\Phi) \tag{3.39}$$

where $E(\theta, k)$ is an incomplete elliptic integral of second kind and $c1(\Phi)$ is the constant of integration that can be obtained using the boundary condition that at position $X = 0$, potential is maximum, which is $\Phi_u = \gamma_0(\gamma_0 - 1)\left(\kappa_R^2 + \kappa_R\beta\sqrt{\kappa_R^2 + (2/\gamma_0(\gamma_0-1))}\right)$; then the complete solution becomes

$$\begin{aligned} Xr^3 = -\frac{(1+\beta)^{1/4}}{\gamma_0\beta(1-\beta)^{1/4}}\Bigg[&\left(\frac{r^4(k^2-1)+1}{k^2-1}\right)(E(\theta_u,k) - E(\theta,k)) \\ &- \frac{k^2\sin 2\theta_u}{2(k^2-1)(1-k^2\sin^2\theta_u)^{1/2}} + \frac{k^2\sin 2\theta}{2(k^2-1)(1-k^2\sin^2\theta)^{1/2}}\Bigg] \end{aligned} \tag{3.40}$$

Here the variables k, θ_u and θ are defined as

$$k^2 = \frac{r^2 - s^2}{r^2} = \frac{2\sqrt{\alpha^2 + \beta^2 - 1}}{\alpha + \sqrt{\alpha^2 + \beta^2 - 1}},$$

$$\sin^2\theta_u = \frac{r^2 - \gamma_0(1 + \Phi_u + \sqrt{\beta^2 + 2\Phi_u + \Phi_u^2})}{r^2 - s^2},$$

$$\sin^2\theta = \frac{r^2 - \gamma_0(1 + \Phi + \sqrt{\beta^2 + 2\Phi + \Phi^2})}{r^2 - s^2}. \tag{3.41}$$

Equation (3.40) gives implicit relation between potential and position. The potential $\Phi(X)$ as a function of position X for different values of k_R and β can be obtained by numerical solution of equation (3.40) and (3.41).

The half wavelength (spatial variation between maxima to minima of the electrostatic potential) of the BGK structures can be obtained for the range $\kappa_R \leq \kappa_R^c$ and $\kappa_R \geq \kappa_R^c$ by putting the minimum values of Φ ($\Phi_l = \gamma_0(\gamma_0 - 1)\left(\kappa_R^2 - \kappa_R\beta\sqrt{\kappa_R^2 + (2/\gamma_0(\gamma_0 - 1))}\right)$ and $\Phi_l = \Phi^c = (1-\gamma_0)/\gamma_0$ respectively) in the equation (3.40). In the range $0 \leq \kappa_R \leq \kappa_R^c$ wavelength turns out to be

$$\lambda = 2\mu s_R, \tag{3.42a}$$

where

$$\mu = -\frac{(1+\beta)^{1/4}}{\gamma_0\beta(1-\beta)^{1/4}}\left[\left(\frac{r^4(k^2-1)+1}{r^3(k^2-1)}\right)(E(\theta_l,k) - E(\theta_u,k)) - \frac{k^2\sin 2\theta_u}{2r^3(k^2-1)(1-k^2\sin^2\theta_u)^{1/2}} + \frac{k^2\sin 2\theta_l}{2r^3(k^2-1)(1-k^2\sin^2\theta_l)^{1/2}}\right] \tag{3.42b}$$

and for the range $\kappa_R^c \leq \kappa_R < \infty$ it becomes

$$\lambda = 2\mu_c s_R, \tag{3.43a}$$

where

$$\mu_c = -\frac{(1+\beta)^{1/4}}{\gamma_0\beta(1-\beta)^{1/4}}\Bigg[\left(\frac{r^4(k^2-1)+1}{r^3(k^2-1)}\right)(E(\theta_c,k)-E(\theta_u,k)) \\ -\frac{k^2\sin 2\theta_u}{2r^3(k^2-1)(1-k^2\sin^2\theta_u)^{1/2}}+\frac{k^2\sin 2\theta_c}{2r^3(k^2-1)(1-k^2\sin^2\theta_c)^{1/2}}\Bigg]. \quad (3.43b)$$

Here wavelengths $\mu(\kappa_R,\beta)$ and $\mu_c(\kappa_R,\beta)$ are explicit functions of nonlinear parameter κ_R and speed β. Corresponding non-relativistic expression for wavelength can be found in reference [19]. For the non-relativistic case, in the linear limit $0 \leq \kappa_{NR} \leq 1$, Psimpoulous' observed that wavelength of the BGK structure is constant and independent of κ_{NR}, however, in the limit $1 \leq \kappa_{NR} < +\infty$, wavelength becomes a function of κ_{NR} and wavelength increases with increasing nonlinear parameter κ_{NR}. In the relativistic regime, it is readily seen that wavelengths (equation (3.42b) and (3.43b)) are not only a function of nonlinear parameter (κ_R) but also has dependence on ratio of average beam speed to the speed of light (β) through the variable k; where k is defined by equation (3.41). In the relativistic regime, within the range $0 \leq \kappa_R \leq \kappa_R^c$, it is found that wavelength depends on β as well as on κ_R (wavelength turns out to be independent of κ_{NR} in non-relativistic regime as long as κ_{NR} lies within the range $0 \leq \kappa_R \leq 1$). Figure 3.6 shows variation of wavelength of the BGK structure with the nonlinear parameter (κ_R) for two different average beam speeds, *i.e.*, $\beta = 0.1$ (3.6a) and $\beta = 0.9$ (3.6b). In fig 3.6 for the speed $\beta = 0.1$ (Fig. 3.6a), in the range $0 \leq \kappa_R \leq \kappa_R^c$ (blue color curve), wavelength is almost constant or in other words, in the range $\beta \ll 1$ wavelength of relativistic BGK structure turns out to be independent of κ_R, a feature which is seen in the non-relativistic case also [19]. However, for the speed $\beta = 0.9$ (Fig. 3.6b), wavelength increases with increasing κ_R as shown in Fig. 3.6b, *i.e.*, wavelength shows strong dependence for large values of β. Therefore, dependence of wavelength on average beam speed is purely a relativistic effect. In the highly nonlinear limit $\kappa_R^c \leq \kappa_R < \infty$, wavelength for all value of β increases with increasing κ_R (orange curve in Fig. 3.6). The dashed vertical line in Figs. 3.6a and 3.6b separates the regime $0 \leq \kappa_R \leq \kappa_R^c$ and $\kappa_R^c \leq \kappa_R < \infty$. The

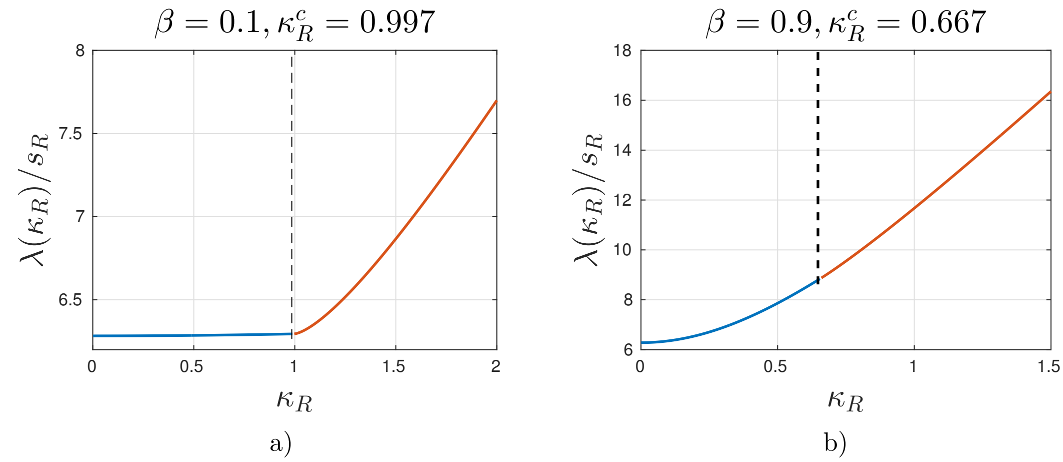

Figure 3.6: Variation of wavelength of relativistic BGK structure for the speed ratio (a) $\beta = 0.1$ and (b) $\beta = 0.9$.

rate of increase of wavelength with κ_R increases with increasing β. Fig. 3.7 shows wavelength as a function of nonlinear parameter κ_R for different value of $\beta \approx 0.1$, 0.9, 0.99 and 0.999. It is clearly seen that slope ($d\lambda/d\kappa_R$ and $d\lambda_c/d\kappa_R$) of wavelength increases with increasing β.

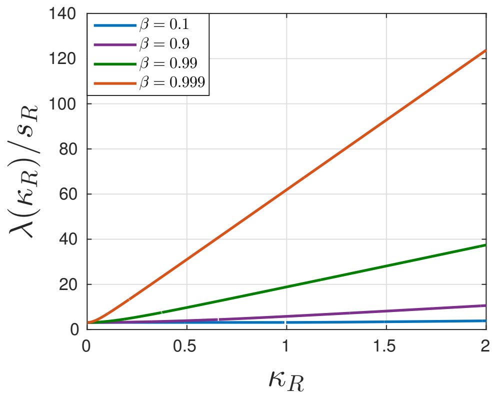

Figure 3.7: Comparison of wavelengths with a range of nonlinear parameter κ_R for different values of β.

The potential $\Phi(X)$ for two different speeds $\beta \approx 0.1$; $\beta \approx 0.9$ and for a wide range of nonlinear parameter (κ_R) is plotted in figure 3.8 and 3.9. Maxima and minima of electrostatic potential for both the range of κ_R, *i.e.*, $0 \leq \kappa_R \leq \kappa_R^c$ and $\kappa_R^c \leq \kappa_R < \infty$, coincide with the range of electrostatic potential (equation (3.26) and (3.27)) obtained using $\Phi - E$ relation. In first case, when $\beta \approx 0.1$ is considered, plot (Fig. 3.8a) of potential $\Phi(X)$ is shown for nonlinear parameter $k_R \approx 0.1, 0.3, 0.5, 0.7, 0.9$. As it has already been discussed that for $\beta \approx 0.1$, wavelength of the BGK structure remains independent of κ_R ($\beta \ll 1$) as shown in Fig. 3.6a(blue color curve), therefore, minima of the potential occurs at $X \approx \pi$ for the nonlinear parameter range $0 \leq \kappa_R \leq \kappa_R^c$, that is clearly illustrated in Fig. 3.8a. In second case when $\beta = 0.9$ is considered (Fig. 3.8b), wavelength increases with increasing nonlinear parameter (see orange curve in Fig. 3.6) so the position of minima of the electrostatic potential occurs at $X = \mu$ as can be seen in Fig. 3.8b. In the limit $\kappa_R^c \geq \kappa_R$, the minima of the electrostatic potential $\Phi(X)$ is manifested at $X = \mu_c \approx 3.18$ for speed ratio $\beta \approx 0.1$, as it is shown in figure 3.9a, and for the speed ratio $\beta \approx 0.9$, Fig. 3.9b illustrates that minima of $\Phi(X)$ is manifested at $X = \mu_c \approx 4.59$.

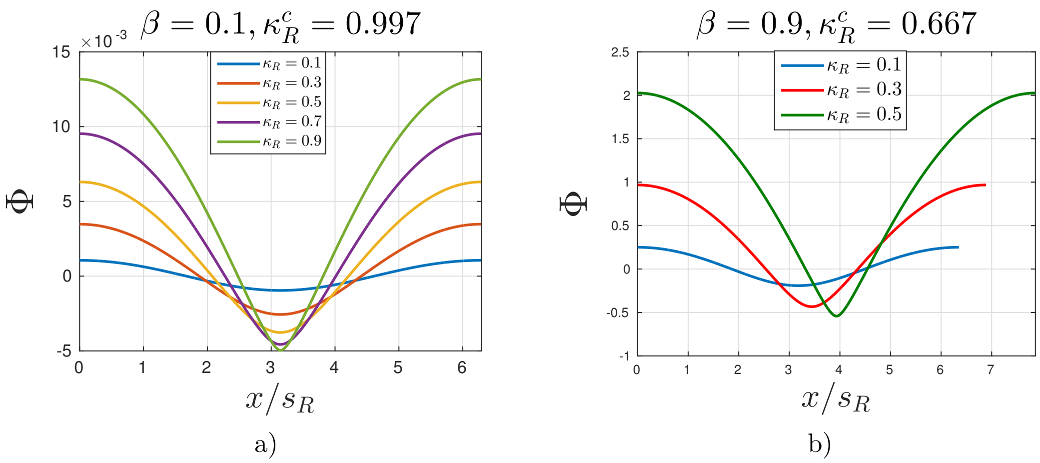

Figure 3.8: Plot of electrostatic potential $\Phi(X)$ for (a) $\kappa_R \approx= 0.1, 0.3, 0.5, 0.7, 0.9$ and $\beta \approx 0.1$, (b) $\kappa_R \approx 0.1$, 0.3, 0.5 and $\beta \approx 0.9$

We can derive electric field in terms of position X by solving equation (3.24) and considering two branches depending on the sign of potential Φ

$$\Phi > 0;\ \Phi = \gamma_0(\gamma_0 - 1)(E^2 - \kappa_R^2)\left(1 + \beta\left(1 + \frac{2}{\gamma_0(\gamma_0 - 1)(E^2 - \kappa_R^2)}\right)^{1/2}\right)$$

$$\Phi < 0;\ \Phi = \gamma_0(\gamma_0 - 1)(E^2 - \kappa_R^2)\left(1 - \beta\left(1 + \frac{2}{\gamma_0(\gamma_0 - 1)(E^2 - \kappa_R^2)}\right)^{1/2}\right) \quad (3.44)$$

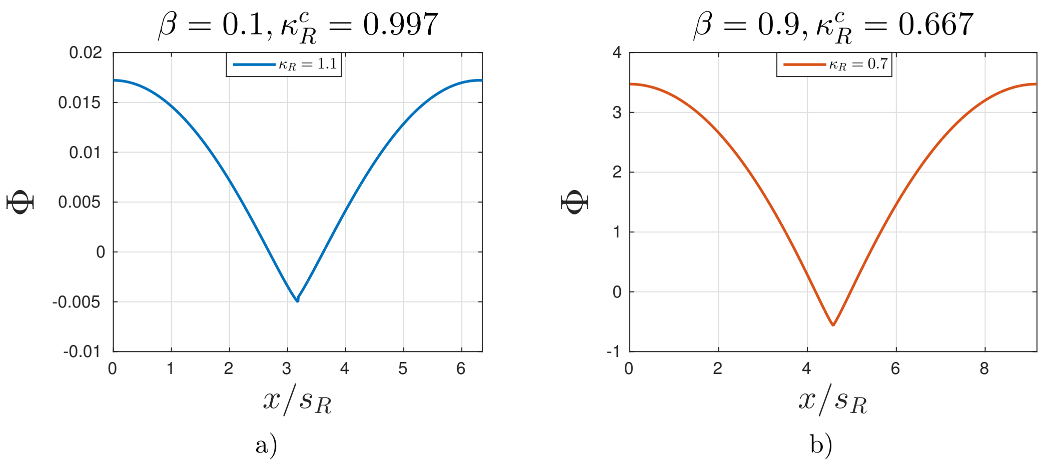

Figure 3.9: Plot of electrostatic potential $\Phi(X)$ for (a) $\kappa_R \approx 0.7$ and $\beta \approx 0.1;\mu \approx 3.18$, (b) $\kappa_R \approx 0.7$ and $\beta \approx 0.9;\mu \approx 4.59$

Range of E can be estimated using equation (3.24):(i) if $0 \leq \kappa_R \leq \kappa_R^c$, we have $0 \leq E \leq \kappa_R$ for both branches; (ii) if $\kappa_R^c \leq \kappa_R < +\infty$ we have $0 \leq E \leq \kappa_R$ for $\Phi > 0$ and $\sqrt{\kappa_R^2 - \sqrt{1-\beta^2}} \leq E \leq \kappa_R$ for $\Phi < 0$. We observe that in the linear limit $\kappa_R \ll \kappa_R^c$, results obtained from nonlinear theory coincide with the harmonic solution obtained from the linear theory. Fig. 3.1 and 3.2 show the fluid variables in the linear limit for the speed $\beta \approx 0.1$ and $\beta \approx 0.9$ respectively, where continuous curves show results obtained from the linear theory and dashed curves show results obtained from the nonlinear theory in the linear limit. Both continuous and dashed curves clearly coincide on each other for both value of β. In the range $0 \leq \kappa_R < \kappa_R^c$, we obtain that at $X \approx \mu$ implies $E = 0$ and

$$\frac{dE}{dX} = \left(\frac{\gamma_0(\gamma_0+1)}{2}\right)^{1/2}\left(1 - \frac{\beta(\Phi+1)}{(\Phi^2+2\Phi+\beta^2)^{1/2}}\right), \tag{3.45}$$

is always negative if $\Phi^c < \Phi < 0$. A gradual steepening of wave form occurs as $\Phi \to \Phi^c$. If $\Phi = \Phi^c$, κ_R becomes κ_R^c that implies $E = 0; dE/dX = -\infty$ at $X = \mu_c$. If $\kappa_R > \kappa_R^c$, E becomes discontinuous at $X = \mu_c$ and E jumps from $-\sqrt{\kappa_R^2 - \sqrt{1-\beta^2}}$ to $\sqrt{\kappa_R^2 - \sqrt{1-\beta^2}}$. This jump in electric field implies the formation of negatively charged plane at $X = \mu_c$. The surface charge density ρ of these planes is defined as

$$\rho = \Delta E/4\pi = \Delta E = \frac{E_0}{2}(\kappa_R^2 - \sqrt{1-\beta^2})^{1/2}. \tag{3.46}$$

Fig. 3.10a and 3.10b show spatial variation of electric field for two particular case $\beta \approx 0.1$ and 0.9. In first case when $\beta \approx 0.1$ in Fig. 3.10a, gradual steepening of electric field is seen at $X \approx \pi$ as $\kappa_R \to \kappa_R^c; \Phi \to \Phi^c$. Similar dynamics follows for the second case when $\beta \approx 0.9$, where gradual steepening of E occurs at $X = \mu$ as shown in Fig. 3.10b. When $\kappa_R > \kappa_R^c$, a discontinuity of E is seen to be manifested at the position $X \approx 3.17$ for $\beta \approx 0.1$ and at $X \approx 4.59$ for $\beta \approx 0.9$ as shown in Fig. 3.11a and 3.11b respectively. It is also found that in the range $\beta \to 0$ and/or $\kappa_R \to \infty$ range, electron beam is transformed into a crystal of "negatively charged plane" with inter-distance $\lambda_0 = E_m/2\pi n_0 e$ having surface charge density $\sim E_m/2\pi$, which matches with the results found in non-relativistic regime [19].

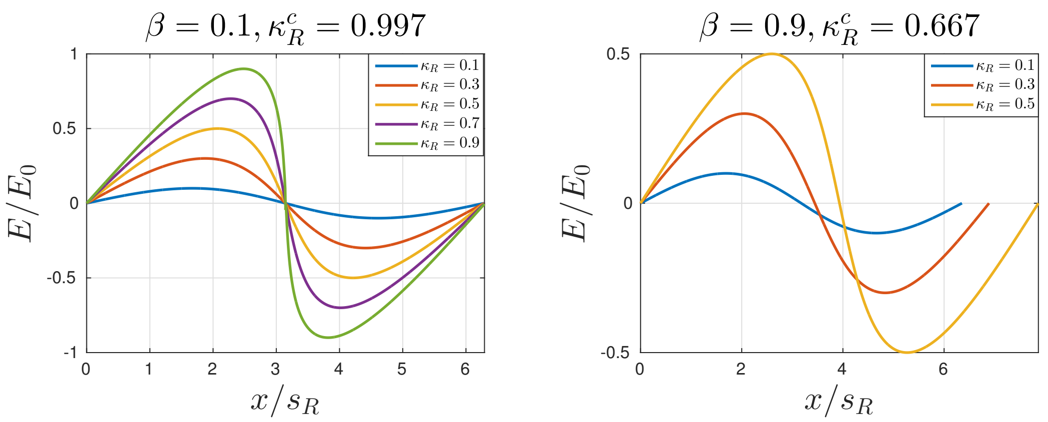

a) b)

Figure 3.10: Plot of electric field for (a) $\beta = 0.1; \kappa_R = 0.1, 0.3, 0.5, 0.7, 0.9$ at $X = \pi$ (b) $\beta = 0.9; \kappa_R = 0.1, 0.3, 0.5$ at $X = \mu$.

The gradual steepening and discontinuity of the electric field modulates the electron speed profile. The $E - v_e$ phase relation can be constructed using equation (3.16) and (3.24) as

$$E^2 - \kappa_R^2 = \frac{1}{\gamma_0(\gamma_0 - 1)}\left(1 - \frac{\gamma_0(1-\beta v_e)}{\sqrt{1-v_e^2}}\right) \tag{3.47}$$

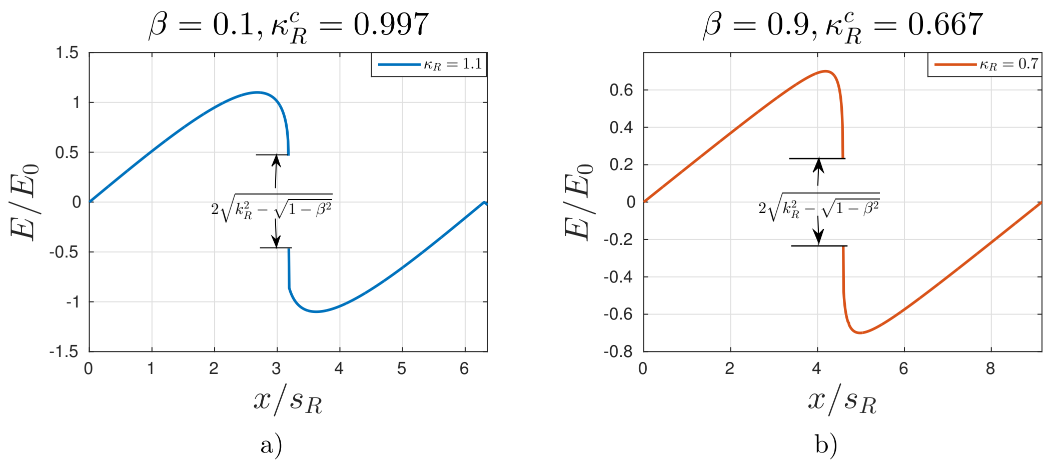

Figure 3.11: Plot of electric field for (a) $\beta \approx 0.1$;$\kappa_R \approx 1.1$ at $X \approx 3.17$ and (b) $\beta \approx 0.9$;$\kappa_R \approx 0.7$ at $X \approx 4.59$.

Fig. 3.12 shows $E - v_e$ phase space modulated by the nonlinear parameter κ_R

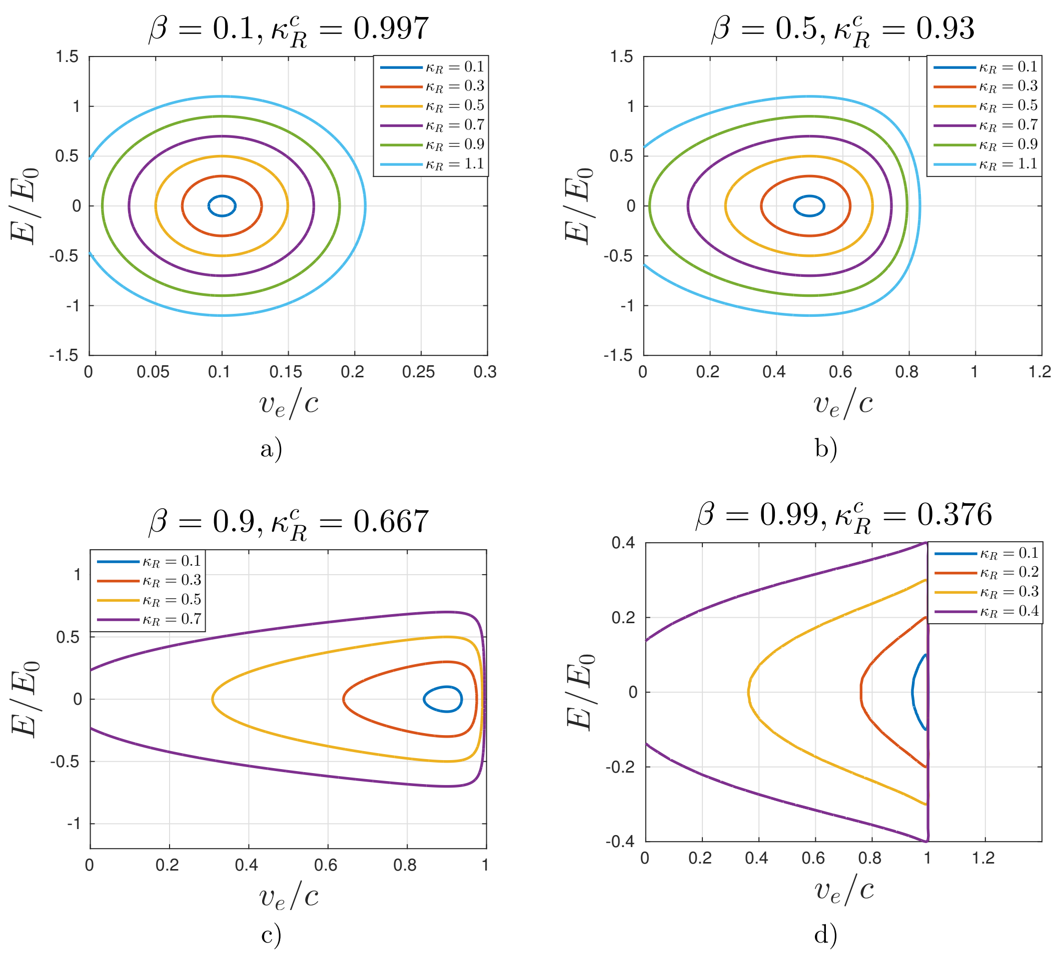

Figure 3.12: Plot $E - v_e$ phase space for different nonlinear parameter and ratio of average beam speed to the speed of light (a) $\beta \approx 0.1$, (b) $\beta \approx 0.5$, (c) $\beta \approx 0.9$, (d) $\beta \approx 0.99$.

and ratio of average beam speed to the speed of light β. It is readily seen that in the range $\kappa_R > \kappa_R^c$, $E - v_e$ phase space becomes discontinuous and E jumps from $-\sqrt{\kappa_R^2 - \sqrt{1-\beta^2}}$ to $\sqrt{\kappa_R^2 - \sqrt{1-\beta^2}}$ at the potential satisfying $\Phi = \Phi^c$.

The fluid velocity as function of position can be obtained using equation (3.16)

$$v_e = \pm \left(\frac{\Phi^2 + 2\Phi + \beta^2}{\Phi^2 + 2\Phi + 1} \right)^{1/2} \tag{3.48}$$

Equation (3.48) gives the relation between velocity and self consistent electrostatic potential. Since we strictly exclude the existence of trapped electrons in the system therefore $+ve$ sign of the velocity is taken in the account. As $\kappa_R \to \kappa_R^c; \Phi \to \Phi^c$ at the position satisfying $X = \mu$, numerator of equation (3.48) tends to zero in the limit $\Phi \to \Phi^c$, thus, a gradual decrement in electron velocity occurs at the position $X = \mu$. If $\kappa_R \geq \kappa_R^c$ then $\Phi = \Phi^c$ at the position $X = \mu_c$, this implies that numerator of the equation (3.48) becomes zero at that position, in other words velocity becomes zero. This means electrons stop momentarily at the position $X = \mu_c$ and then continue their motion in $+x$ direction. This short time rest of the electrons, consequently, leads to the accumulation of the charge particles at the position $X = \mu_c$ that is further manifested in density burst or, in other words, in order to maintain the electron current, electron density has to increases at the positions where electrons speed decreases. Fig. 3.13a and 3.13b show electron velocity for the speed ratios $\beta \approx 0.1$ and 0.9 respectively, and a gradual decrement of electron velocity can be seen clearly at the position $X = \pi$ for $\beta \approx 0.1$ and at $X = \mu$ for $\beta = 0.9$. Fig. 3.14a and 3.14b illustrates that in the limit $\kappa_R \geq \kappa_R^c; \Phi = \Phi^c$, velocity becomes zero at the position satisfying $X = 3.17$ for $\beta = 0.1$ and $X = 4.59$ for $\beta = 0.9$.

The electron density can be written as

$$n_e(X) = 1 - \left(\frac{2}{\gamma_0(\gamma_0 - 1)} \right)^{1/2} \frac{\partial E}{\partial X}. \tag{3.49}$$

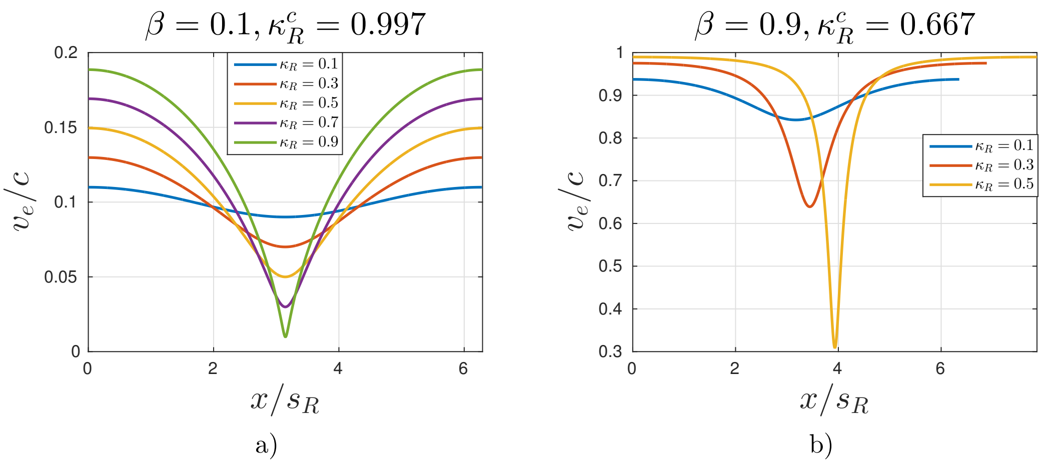

Figure 3.13: Plot of electron velocity for the parameters (a) $\beta \approx 0.1$;$\kappa_R \approx 0.1, 0.3, 0.5, 0.7, 0.9$ at $X \approx \pi$ (b) $\beta \approx 0.9$;$\kappa_R \approx 0.1, 0.3, 0.5$ at $X = \mu$.

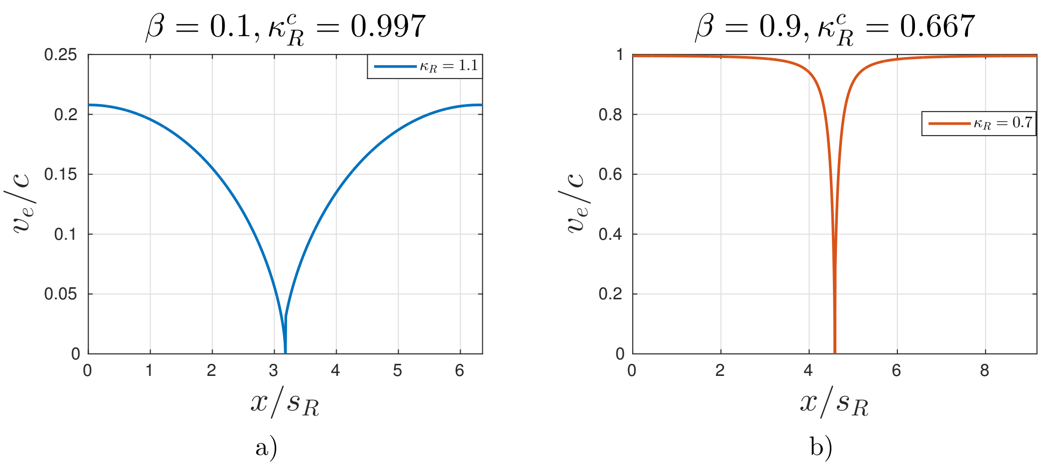

Figure 3.14: Plot of electron velocity for the parameters (a) $\beta \approx 0.1$;$\kappa_R \approx 1.1$ at $X \approx 3.17$ and (b) $\beta \approx 0.9$;$\kappa_R \approx 0.7$ at $X \approx 4.59$.

Using equation (3.45), the electron density is therefore may be reduced to a function of electrostatic potential

$$n_e(X) = \frac{\beta(\Phi + 1)}{(\Phi^2 + 2\Phi + \beta^2)^{1/2}}, \tag{3.50}$$

equation (3.50) gives implicit relation between electron density and spatial position by eliminating electrostatic potential using equation (3.40) and (3.41). As it has already been discussed that in the range $0 \leq \kappa_R < \kappa_R^c$, Φ approaches to Φ^c and modulation of the electrostatic potential leads to the steepening of the density which can be clearly seen in the Fig. 3.15a for $\beta \approx 0.1$ at $X = \pi$ and in Fig. 3.15b for

$\beta \approx 0.9$ at $X = \mu$. When $\kappa_R \geq \kappa_R^c$ then $\Phi = \Phi^c$ and denominator of the equation (3.50) vanishes. This explosive behavior beyond κ_R^c can be clearly seen in Figs. 3.16a and 3.16b, where density burst is manifested at $X \approx 3.17$ for $\beta \approx 0.1$ (in Fig. 3.16a) and at $X \approx 4.59$ for $\beta \approx 0.9$ (in Fig. 3.16b) respectively.

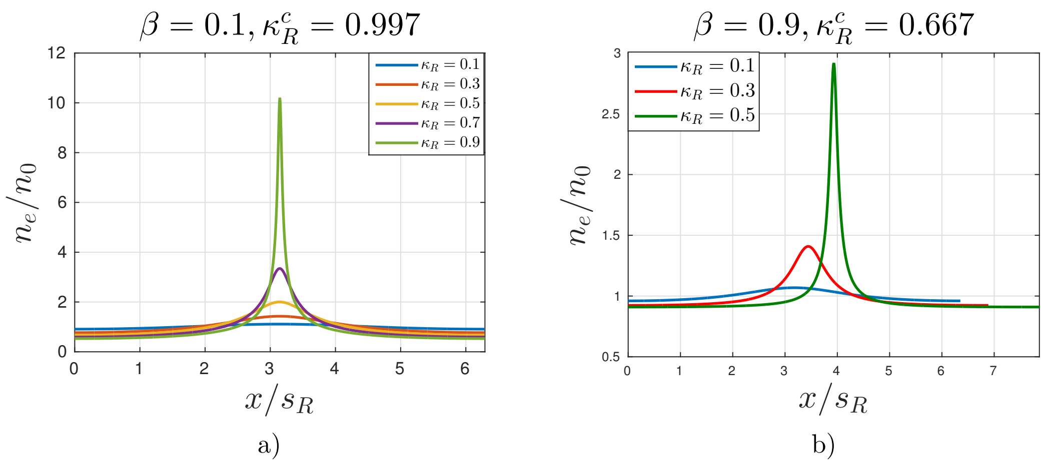

Figure 3.15: Electron density modulation (a) $\beta \approx 0.1$;$\kappa_R \approx 0.1, 0.3, 0.5, 0.7, 0.9$ at $X \approx \pi$ (b) $\beta \approx 0.9$;$\kappa_R \approx 0.1, 0.3, 0.5$ at $X = \mu$.

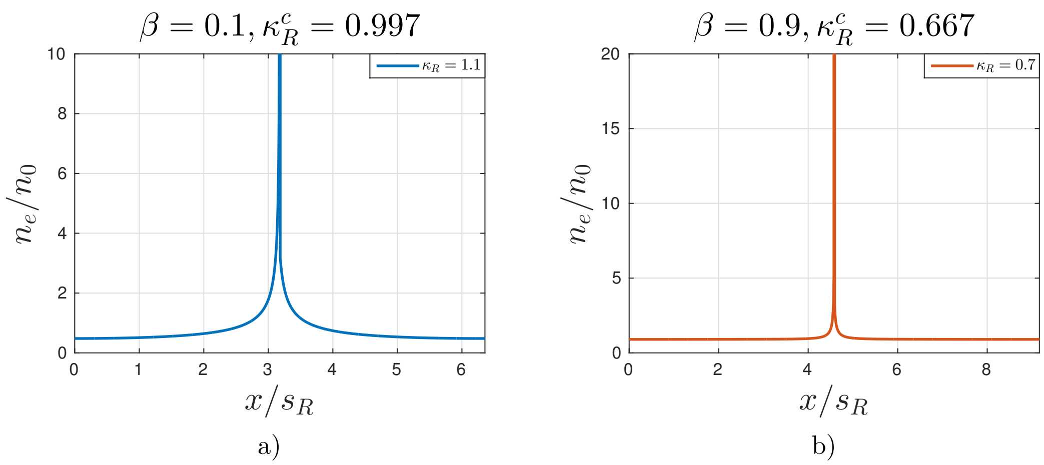

Figure 3.16: Electron density for (a) $\beta \approx 0.1$;$\kappa_R \approx 1.1$ at $X \approx 3.17$ and (b) $\beta \approx 0.9$;$\kappa_R \approx 0.7$ at $X \approx 4.59$.

It must also be noticed from equations (3.48) and (3.49) that product of electron density and velocity (electron flux) remains constant for each value of κ_R, *i.e.*, $n_e v_e = \beta$.

3.2 Conclusion

An analytical study is carried out for stationary BGK structures in relativistic current carrying fluid-Maxwell system. It is observed that nonlinear BGK structures is governed by the nonlinear parameter $\kappa_R = E_m/(8\pi n_0 m_0(\gamma_0 - 1)c^2)^{1/2}$. Critical nonlinear parameter scales with average beam speed v_0 as $\kappa_R = 1/\sqrt{\gamma_0}$. Amplitude of nonlinear parameter (κ_R) embodies the nonlinear effects in the problem. In the linear limit $\kappa_R \ll 1/\sqrt{\gamma_0}$, fluid variables vary harmonically in space and results of nonlinear theory coincides with the results of linear theory in this range. As $\kappa_R \to 1/\sqrt{\gamma_0}$ fluid variables gradually begin to shown anharmonic features. In the nonlinear limit $\kappa_R \geq 1/\sqrt{\gamma_0}$, electric field becomes discontinuous at certain singular points in space. Average beam speed decreases at the position of electric field discontinuity, so to keep the current constant, density has to shoots up. This process manifests as a density burst periodically in space. These density burst may approach finite values on inclusive of thermal effects. It is found that in the $\beta \to 0$ and/or $\kappa_R \to \infty$ range, electron beam is transformed into a crystal of "negatively charged plane" of inter-distance $\lambda_0 = E_m/2\pi n_0 e$ having surface charge density $\sim E_m/2\pi$, which matches with the results found in non-relativistic regime [19]. Study of excitation and stability of these BGK structures using a PIC/fluid code is left for future studies.

CHAPTER 4

Evolution of relativistic electron current beam moving through a fixed homogeneous background of ions

In this chapter, an analytical study of evolution of relativistic electron beam propagating through a cold homogeneous plasma with immobile ions has been carried out by employing the method of Lagrange transformation. It is found that beam current when longitudinally perturbed by an electrostatic wave, diminishes with time due to phase mixing effects arising because of spatial variation of relativistic mass. Study has been conducted for various flow velocities (v_0/c) and relativistic intensities ($\frac{eE_0}{m\omega_{pe}c}$) of the perturbed wave. It is found that the rate of decrease of current decreases with increasing flow velocity and increases with increasing wave intensity. Analytical results are compared with that obtained from simulations.

In previous chapter, we studied stationary BGK structures in a current carrying relativistic Fluid-Maxwell system. In this chapter, we carry out full spatio-temporal study of the effects of a relativistically intense wave on the relativistic electron beam. An exact solution for density and momentum has been derived by transforming the governing equations into Lagrangian co-ordinates. In section 4.1, we give an introduction of the problem. In section, 4.2.1 we first present exact solution for the corresponding problem, *i.e.*, non-relativistic electron plasma waves propagating on non-relativistic electron beam and section 4.2.2 presents the exact solution for relativistically intense wave propagating on relativistic electron beam. Next, in the section 4.3, we discuss results obtained from the analytical solution and compare with that obtained from simulations. We end this chapter by summarizing the results in the section 4.4.

4.1 Introduction

The problem of nonlinear electron plasma oscillation in a nonrelativistic cold plasma was solved exactly by Davidson [20, 47] by employing the method of Lagrange transformation, which converts partial differential equations into ordinary differential equations. Author showed that any initial periodic profile with wavelength $2\pi/k$ leads to a well defined oscillation, provided that electric field does not exceed a critical value which is $ek_L E/m\omega_{pe}^2 = 0.5$. Above this threshold wave breaks and coherent motion of the particle changes into random motion. The space time development of nonlinear electron plasma oscillation in a relativistic cold plasma has been addressed exactly by Infeld [17] using method of Lagrange transformation. In relativistic regime, wave breaking is not limited by finite amplitude of electric field as found in nonrelativistic regime. Drake et. al. [100] and Sengupta et. al. [75] have shown that in a cold plasma due to relativistic dynamics, a wave always phase mix away for any arbitrary initial condition, thus leading to wave breaking. Highly energetic particles produced via wave breaking process have been observed in several plasma based particle acceleration schemes [101, 102].

In this chapter, we extend our consideration to current carrying plasmas. To the best of our knowledge, very little work has been carried out to understand spatio-temporal evolution of space charge waves on relativistic electron beam propagating through a plasma. In some early attempts, Chian et. al. [23, 24] obtained a nonlinear dispersion relation for subluminous waves in such a frame where governing equations become space independent. Chian [25] obtained wave breaking limit for subluminous waves as $E_m = \sqrt{2}(m\omega_{pe}c/e)[\gamma_{ph}(1-\beta_{ph}\beta_0) - 1/\gamma_0]^{1/2}$, where γ_{ph} and β_0 are respectively the Lorentz factor associated with wave phase velocity v_{ph} and velocity of electron beam v_0. Study by Chian et. al. was limited to seeking travelling wave solution and authors sole purpose was to obtain wave breaking limit in current carrying plasma. We obtain exact analytical solution for space charge wave in relativistic current carrying cold plasma.

4.2 Theory

We consider one dimensional infinitely long physical system, where a relativistic electron beam of density n_0 and velocity v_0 is propagating through an immobile, homogeneous, neutralizing background of ions. The basic set of governing equation required to study the spatio-temporal evolution of relativistically intense wave in the presence of a beam propagating through an immobile background of ions are

$$\frac{\partial n_e}{\partial t} + \frac{\partial n_e v_e}{\partial x} = 0, \tag{4.1a}$$

$$\frac{\partial p_e}{\partial t} + v_e \frac{\partial p_e}{\partial x} = -eE, \tag{4.1b}$$

$$\frac{\partial E}{\partial x} = 4\pi e(n_0 - n_e) \tag{4.1c}$$

$$\frac{\partial E}{\partial t} = 4\pi e n_e v_e - 4\pi e n_0 v_0 \tag{4.1d}$$

where n_e, $p_e = \gamma m v_e$, v_e are density, momentum and velocity of the electrons respectively, E is electric field. Other symbols have their usual meaning.

Before carrying out exact solution of space charge wave in the presence of a relativistic electron beam, we first solve the corresponding set of non-relativistic nonlinear equation and in a later section relativistic effects on the space charge wave will be discussed.

4.2.1 Evolution of non-relativistic electron beam in the presence of non-relativistic electron plasma wave

We consider an infinite system where an electron beam of density n_0 with non-relativistic speed $v_0 \ll c$ is propagating through an immobile homogeneous neutralizing background of ions of density n_0. Thus, in the non-relativistic limit, the set of governing fluid equations (4.1a) - (4.1d) is reduced to

$$\frac{\partial n_e}{\partial t} + \frac{\partial n_e v_e}{\partial x} = 0, \tag{4.2a}$$

$$\frac{\partial v_e}{\partial t} + v_e \frac{\partial v_e}{\partial x} = -\frac{eE}{m}, \tag{4.2b}$$

$$\frac{\partial E}{\partial x} = 4\pi e(n_0 - n_e), \tag{4.2c}$$

$$\frac{\partial E}{\partial t} = 4\pi e n_e v_e - 4\pi e n_0 v_0, \tag{4.2d}$$

An exact solution for above set of equations (4.2a) - (4.2d), can be obtained using Lagrangian co-ordinates (x_0, τ), where Lagrangian transformation is defined as

$$x = x_0 + \int_0^\tau v(x_0, \tau) d\tau, \ \tau = t, \tag{4.3a}$$

$$\frac{\partial}{\partial x} \equiv \left[1 + \int_0^\tau d\tau' \frac{\partial}{\partial x_0} v(x_0, \tau')\right]^{-1} \frac{\partial}{\partial x_0}, \tag{4.3b}$$

$$\frac{\partial}{\partial t} \equiv \frac{\partial}{\partial \tau} - v(x_0, \tau) \left[1 + \int_0^\tau d\tau' \frac{\partial}{\partial x_0} v(x_0, \tau')\right]^{-1} \frac{\partial}{\partial x_0}. \tag{4.3c}$$

The basic set of equations (4.2a) - (4.2d) using Lagrangian transformation can be written as,

$$\frac{\partial v_e}{\partial \tau} = -eE/m, \tag{4.4}$$

$$\frac{\partial E}{\partial \tau} = 4\pi e n_0 v_e - 4\pi e n_0 v_0, \tag{4.5}$$

which can be combined to give,

$$\frac{\partial^2 v_e}{\partial \tau^2} + \omega_{pe}^2 v_e = \omega_{pe}^2 v_0. \tag{4.6}$$

Solution of equation (4.6) using following initial conditions,

$$n_e(x_0, 0) = n_0(1 + \Delta \cos kx_0), \tag{4.7a}$$

$$v_e(x_0, 0) = v_0, \tag{4.7b}$$

can be written as

$$\frac{n_e(x_0, \tau)}{n_0} = \frac{1 + \Delta \cos kx_0}{1 + \Delta \cos kx_0(1 - \cos \omega_{pe}\tau)}, \tag{4.8}$$

$$\frac{k v_e(x_0, \tau)}{\omega_{pe}} = \frac{k v_0}{\omega_{pe}} + \Delta \sin kx_0 \sin \omega_{pe}\tau, \tag{4.9}$$

$$\frac{ekE(x_0, \tau)}{m\omega_{pe}^2} = -\Delta \sin kx_0 \cos \omega_{pe}\tau, \tag{4.10}$$

where relation between Euler and Lagrange co-ordinates is defined as

$$kx = kx_0 + kv_0\tau + \Delta\sin(kx_0)(1 - \cos(\omega_{pe}\tau)), \tag{4.11}$$

where Δ is an amplitude of initial density perturbation and k is the wave number. Equation (4.8), (4.9) and (4.10) respectively exhibit space-time evolution of density, velocity and electric field of fluid variables associated with the electron beam, when a nonlinear perturbation is applied longitudinally. Equation (4.11) gives relation between Eulerian (x) and Lagrangian (x_0) position co-ordinates. Electron density is

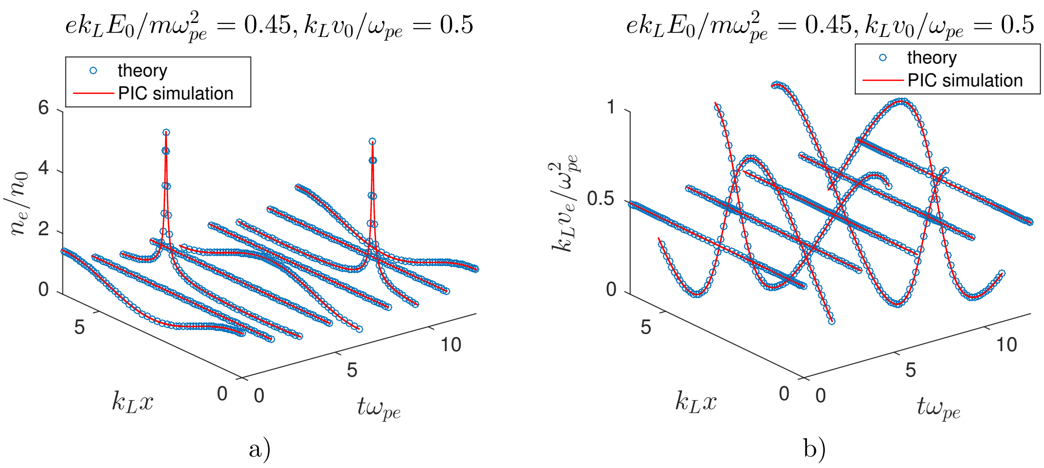

Figure 4.1: Spatio-temporal evolution of (a) electron density and (b) electron velocity for the parameters $ek_LE_0/m\omega_{pe}^2 = 0.45$ and initial drift velocity $k_Lv_0/\omega_{pe} = 0.5$. Here continuous line represents result of PIC simulation and dots are obtained from analytical solution.

plotted in Fig. 4.1a at different time steps for the parameters $ek_LE_0/m\omega_{pe}^2 = 0.45$ and $k_Lv_0/\omega_{pe} = 0.5$, where continuous lines are the result of PIC simulation and dots are taken from analytical solution. The observed nonlinear oscillations are maintained indefinitely and wave breaking does not take place as long as amplitude of initial density perturbation is less than wave breaking limit for cold un-magnetized plasma, i.e., $ek_LE_0/m\omega_{pe}^2 \leq 0.5$. In Fig. 4.2a average current is plotted with time, where continuous line shows result of simulation and dots are a result of analytical solution. It is clear from Fig. 4.2a that current remains constant with time. In non-relativistic regime the beam merely provides a drift to background electron fluid. This can also be seen by transforming the governing equations to another Galilean frame propagating with velocity v_0.

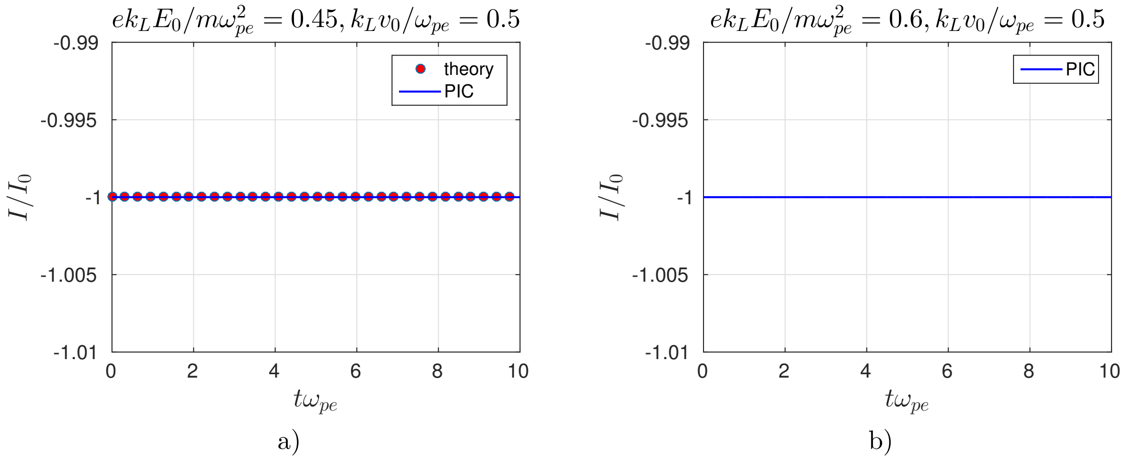

Figure 4.2: Temporal evolution of spatially averaged current for (a) $ek_L E_0/m\omega_{pe}^2 = 0.45$; $k_L v_0/\omega_{pe} = 0.5$ and (b) $ek_L E_0/m\omega_{pe}^2 = 0.6$; $k_L v_0/\omega_{pe} = 0.5$. Here continuous line represents result of PIC simulation and dots are obtained from analytical solution.

We now perturb the electron beam with an electrostatic wave having an amplitude more than wave breaking limit, *i.e.*, $ek_L E_0/m\omega_{pe}^2 > 0.5$, which leads to wave breaking within a plasma period. We found in our simulation that drift energy of electron beam does not play any pivotal role in breaking of wave. Spatially averaged current for the parameters $ek_L E_0/m\omega_{pe}^2 = 0.6$ and $k_L v_0/\omega_{pe} = 0.5$ is plotted in Fig. 4.2b, which clearly illustrates that current remains constant with time even after wave breaking has taken place.

4.2.2 Evolution of electron beam in the presence of relativistically intense electron plasma wave

In this section, analysis is generalized to describe the nonlinear behaviour of relativistically intense space charge wave on relativistic electron beam. We consider a similar physical system, where a relativistic electron beam of density n_0 and initial drift velocity v_0 is propagating through a neutralizing immobile background of ions of density n_0. System is governed by the equations (4.1a), (4.1b), (4.1c) and (4.1d).

The electron beam is perturbed with a relatively high amplitude, which excites large amplitude relativistically intense ($eE_0/m\omega_p c$) electron plasma wave. Using aforementioned Lagrangian hydrodynamics, set of nonlinear equation (4.1a) - (4.1d) can be transformed in the Lagrangian frame as,

$$\frac{\partial p_e}{\partial \tau} = -eE, \tag{4.12a}$$

$$\frac{\partial E}{\partial \tau} = 4\pi e n_0 v_e - 4\pi e n_0 v_0, \tag{4.12b}$$

which can be combined to give,

$$\frac{\partial^2 p_e}{\partial \tau^2} + \omega_{pe}^2 \frac{p_e}{\sqrt{1 + \left(\frac{p_e}{mc}\right)^2}} = m\omega_{pe}^2 v_0. \tag{4.13}$$

Here p_e is a function of Lagrangian co-ordinates x_0 and τ. Equation (4.13) is a second order differential equation in time, which closely resembles the governing equation of a forced driven relativistic harmonic oscillator, which is often encountered in nonlinear mechanics, however, here applied external force (R.H.S. of equation) is constant with time. Equation (4.13) can be reduced to a first order differential equation by multiplying with $\frac{\partial p_e}{\partial t}$ on both side and integrating once with respect to time,

$$\frac{\partial p_e}{\partial \tau} = \pm\sqrt{2}\omega_{pe} mc \left(a + \left(\frac{v_0}{c}\right)\frac{p_e}{mc} - \sqrt{1 + \frac{p_e^2}{m^2c^2}} \right)^{1/2} \tag{4.14}$$

where a is a first integration constant and is a function of x_0. For simplicity, we write equation in terms of dimensionless parameter ($p_e \to p_e/mc$, $\beta \to v_0/c$ and $\tau \to \omega_{pe}\tau$)

as

$$\frac{\partial p_e}{\partial \tau} = \pm\sqrt{2}\left(a + \beta p_e - \sqrt{1+p_e^2}\right)^{1/2}. \tag{4.15}$$

Equation (4.15) corresponds to the conservation of energy in nonlinear mechanics and contains two turning points, namely $p_e/mc = (a\beta \pm \sqrt{a^2+\beta^2-1})/1-\beta^2$.

Equation (4.15) can be solved by defining the new variables r, κ and θ through

$$r^2 = \frac{a + \sqrt{a^2+\beta^2-1}}{1-\beta}, \tag{4.16a}$$

$$\kappa^2 = \frac{2\sqrt{a^2+\beta^2-1}}{a+\sqrt{a^2+\beta^2-1}}, \tag{4.16b}$$

$$\sin^2\theta = \frac{a + (a^2+\beta^2-1)^{1/2} - (1-\beta)\left(p_e/mc + \sqrt{1+(p_e/mc)^2}\right)}{2(a^2+\beta^2-1)^{1/2}}, \tag{4.16c}$$

then the solution of equation (4.15) upon integrating with time again can be written as

$$\pm(1-\beta)^{1/2}\omega_{pe}\tau = \mp\left(\frac{r^4(\kappa^2-1)-1}{(\kappa^2-1)}E(\theta,\kappa) + \frac{\kappa^2\sin 2\theta}{2(\kappa^2-1)(1-\kappa^2\sin^2\theta)^{1/2}}\right) + \phi(x_0) \tag{4.17}$$

where $E(\theta,\kappa)$ is incomplete integral of second kind and $\phi(x_0)$ is a secondary arbitrary function of x_0. A detailed solution of equation (4.15) is presented in appendix B.1.

A complete solution of the set of equations (4.1a) - (4.1c) is obtained for arbitrary initial conditions. We choose the similar initial conditions as we used in non-relativistic case, *i.e.*

$$n_e(x_0,0) = n_0(1 \pm \Delta\cos kx_0), \tag{4.18a}$$

$$p_e(x_0,0) = p_0, \tag{4.18b}$$

where p_0 is the initial momentum of relativistic electron beam. Now arbitrary integration constant $\phi(x_0)$ is obtained using initial conditions specified by (4.18); then complete solution can be written as

$$(1-\beta)^{1/2}\omega_{pe}\tau = \frac{r^4(\kappa^2-1)-1}{r^3(\kappa^2-1)}\left(E(\theta_0,\kappa)-E(\theta,\kappa)\right) \tag{4.19}$$

$$+\frac{\kappa^2\sin 2\theta_0}{2r^3(\kappa^2-1)(1-\kappa^2\sin^2\theta_0)^{1/2}}-\frac{\kappa^2\sin 2\theta}{2r^3(\kappa^2-1)(1-\kappa^2\sin^2\theta)^{1/2}}$$

where

$$\sin^2\theta_0 = \frac{a+(a^2+\beta^2-1)^{1/2}-(1-\beta)\left(p_0/mc+\sqrt{1+(p_0/mc)^2}\right)}{2(a^2+\beta^2-1)^{1/2}} \tag{4.20}$$

Further, electron density n can be obtained in terms of elliptic functions, and θ, κ and r as the basic parameters by eliminating Lagrangian variables, then electron density in parametric form $n_e(x,t)$ is given by (for detailed calculation see appendix B.2.)

$$n_e(x,t) = \frac{n_0(1\pm\Delta\cos kx)}{D}, \tag{4.21}$$

where D is defined as

$$D = 1\mp\frac{\Delta'^2\,kc\,\sqrt{1-\beta}\,\sin 2kx_0}{\omega_{pe}}\left[A1+A2-A3\right], \tag{4.22}$$

and

$$A1 = \frac{1}{4r\kappa^2(1-\beta)}\left[\frac{\left((1-\kappa^2\sin^2\theta)(2-\kappa^2)+2(1-\kappa^2)\right)\sin 2\theta}{(1-\kappa^2\sin^2\theta)^{3/2}}\right. \tag{4.23a}$$

$$\left.-\frac{\left((1-\kappa^2\sin^2\theta_0)(2-\kappa^2)+2(1-\kappa^2)\right)\sin 2\theta_0}{(1-\kappa^2\sin^2\theta_0)^{3/2}}\right]$$

$$A2 = \left(\frac{4(\kappa^2-1)(\cos 2\theta + \kappa^2 \sin^4\theta)}{4(r^4(\kappa^2-1)-1)(1-\kappa^2\sin^2\theta)^2 + \kappa^4\sin^2 2\theta + 4\kappa^2\cos 2\theta(1-\kappa^2\sin^2\theta)}\right) \tag{4.23b}$$

$$\left[-\frac{3r^2\tau}{2\kappa^2(1-\beta)} + \frac{(r^4(\kappa^2-1)-1)}{(1-\beta)r^3(\kappa^2-1)}\left\{\left(\frac{\kappa^2+1}{\kappa^2(\kappa^2-1)}\right)\Big(E(\theta_0,\kappa)-E(\theta,\kappa)\Big) + F(\theta_0,\kappa)\right.\right.$$
$$\left. - F(\theta,\kappa)\right\} + \frac{\Big(\kappa^2(\kappa^2+1)\sin^2\theta_0 - 2\Big)\sin 2\theta_0}{2r(1-\beta)(1-\kappa^2\sin^2\theta_0)^{3/2}} - \frac{\Big(\kappa^2(\kappa^2+1)\sin^2\theta - 2\Big)\sin 2\theta}{2r(1-\beta)(1-\kappa^2\sin^2\theta)^{3/2}}$$
$$+\left\{\left(\frac{p_0}{mc}+\gamma_0\right)\Big(1+\beta+(1-\beta)r^4\Big) + 2r^6\kappa^2(\kappa^2-1)(1-\beta)^2\right\}$$
$$\left.\left\{\frac{4\Big(r^4(\kappa^2-1)-1\Big)(1-\kappa^2\sin^2\theta_0)^2 + \kappa^4\sin^2 2\theta_0 + 4\kappa^2\cos 2\theta_0(1-\kappa^2\sin^2\theta_0)}{4\,r^7\,\kappa^6\,(1-\beta)^3\,(\kappa^2-1)\sin 2\theta_0(1-\kappa^2\sin^2\theta_0)^{3/2}}\right\}\right],$$

$$A3 = \frac{(\cos 2\theta_0 + \kappa^2\sin^4\theta_0)}{(1-\beta)^3 r^7\kappa^6\sin 2\theta_0(1-\kappa^2\sin^2\theta_0)^{3/2}}\left[2r^6\kappa^2(\kappa^2-1)(1-\beta)^2 + \Big\{(1+\beta)\right. \tag{4.23c}$$
$$\left. + (1-\beta)r^4\Big\}\left(\frac{p_0}{mc}+\gamma_0\right)\right].$$

The relation between Eulerian and Lagrangian co-ordinates is given by,

$$kx = kx_0 + kv_0 t \mp \frac{kc\,r\,\kappa^2\,\sqrt{1-\beta}}{2\omega_{pe}}\left(\frac{\sin 2\theta}{(1-\kappa^2\sin^2\theta)^{1/2}} - \frac{\sin 2\theta_0}{(1-\kappa^2\sin^2\theta_0)^{1/2}}\right). \tag{4.24}$$

The set of equations (4.22) - (4.24) gives the exact solution of electron density in Eulerian co-ordinates and governed by the dimensionless parameters Δ, $\beta = v_0/c$ and $\tilde{E}_0 = eE_0/m\omega_{pe}c$. When the elliptic integrals in $A2$ are extended beyond $\pi/2$, secular behavior is observed and denominator of equation (4.22) vanishes. This secular behavior can be explicitly seen if solution is obtained for set of equations in the weakly relativistic limit. We use Krylov-Bogoliubov-Mitropolskii [48] perturbation technique to solve the second order equation (4.14), which yields

$$n_e = \frac{n_0(1+\Delta\cos kx_0)}{D1} \tag{4.25a}$$

$$D1 = 1 - \Delta\cos kx_0\left[\frac{p_0^2}{m^2c^2a_0^2}(1-\cos\tilde{\omega}_{pe}\tau) + \frac{\Delta'^2}{a_0^2}\sin^2 kx_0\left(1-\cos\tilde{\omega}_{pe}\tau - \frac{3}{8}a_0^2\,\omega_{pe}\tau\sin\tilde{\omega}_{pe}\tau\right)\right.$$
$$\left. + \frac{3}{8}\frac{p_0}{mc}\omega_{pe}\tau\Delta'\sin kx_0\cos\tilde{\omega}_{pe}\tau\right], \tag{4.25b}$$

$$\tilde{\omega}_{pe} = \omega_{pe}\left[1 - \frac{3}{16}\left(\frac{p_0^2}{m^2c^2} + \Delta'^2\sin^2 kx_0\right)\right], \tag{4.25c}$$

$$kx = kx_0 + kv_0\tau + \frac{kp_0}{\omega_{pe}}\sin\tilde{\omega}_{pe}\tau - \Delta\sin kx_0(1-\cos\tilde{\omega}_{pe}\tau), \tag{4.25d}$$

$$a_0 = \pm\left(\frac{p_0^2}{m^2c^2} + \Delta'^2\sin^2 kx_0\right)^{1/2}. \tag{4.25e}$$

(See appendix B.3 for detailed calculation.) In equation (4.25c), first term represents the plasma frequency and second term represents the nonlinear frequency shift due to variation of relativistic electron mass and depends on the initial amplitude of density perturbation Δ, initial position x_0 of the electron fluid and initial momentum p_0 of the electron beam. So under very general initial conditions, a relativistic wave will always break at arbitrarily low amplitudes via a phenomenon called phase mixing. Secular terms can be explicitly seen in the denominator of equation (4.25b), which implies that electron oscillations become aperiodic with time and denominator of equation (4.25b) vanishes, exhibiting a density burst.

4.3 Discussion of results

In the previous section, we obtained analytical solution for spatio-temporal evolution of relativistically intense wave propagating on relativistic electron beam. In this section, we compare results obtained from analytical solution with results obtained from one dimensional particle-in-cell and fluid simulation using initial density perturbation (Δ), relativistic intensity ($eE_0/m\omega_{pe}c$) and flow velocity ($\beta = v_0/c$) as input parameters. Table 4.1 shows the simulation parameters used for carrying out PIC/fluid simulations.

Table 4.1: List of physical parameters used in our PIC/fluid simulations.

Parameter	Symbol	Value
No of grid points	NG	1024
System Length	L	2π
Time step	Δt	$0.0196349\,\omega_{pe}^{-1}$
Grid Spacing	$k_L\Delta x$	L/NG = 0.006
Total no of electron	N_e	102400
Electron Plasma Frequency	ω_{pe}	1
Amplitude of Density Perturbation	Δ	0.3
Initial electron drift velocity	v_0/c	0, 0.1, 0.99
Relativistic Intensity	$eE_0/m\omega_{pe}c$	5, 10, 100

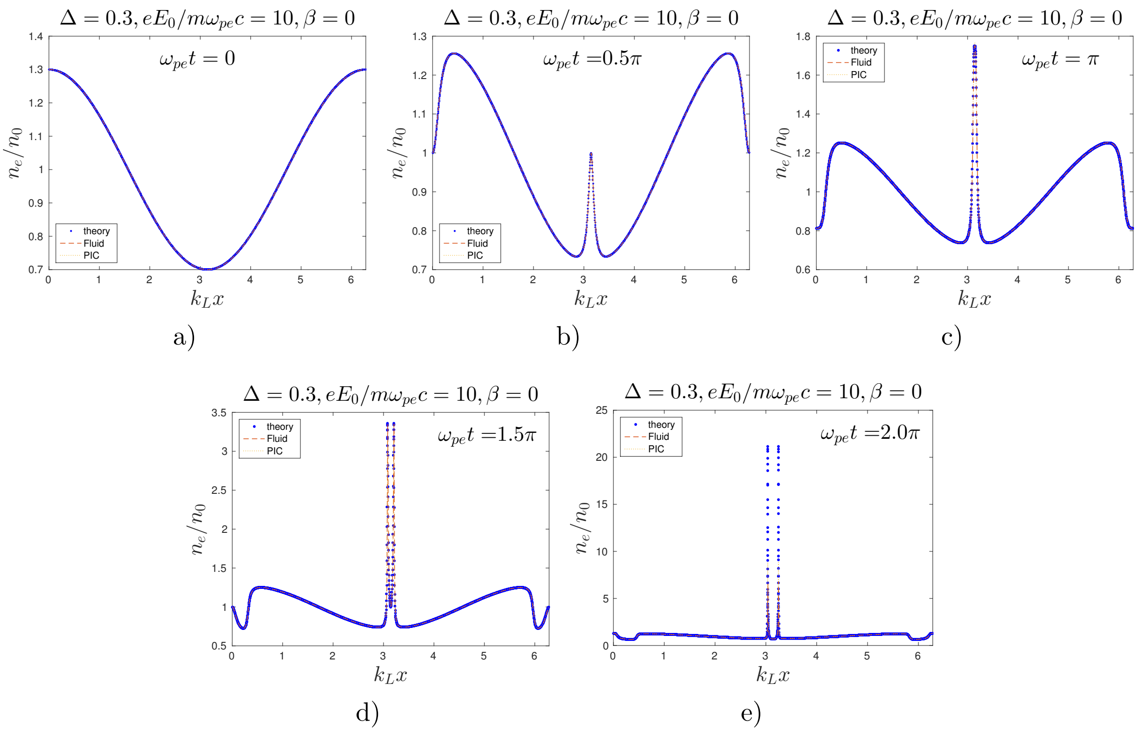

Figure 4.3: Snaps of space-time evolution of electron number density for the parameters $\Delta \approx 0.3$, $\tilde{E}_0 = 10$ and $\beta = 0$. In this Fig., dots represent result of our theory, dashed line is a result of Infeld theory and dot-dashed line represents result of PIC simulation.

Infeld [17] obtained an exact analytical solution describing nonlinear plasma oscil-

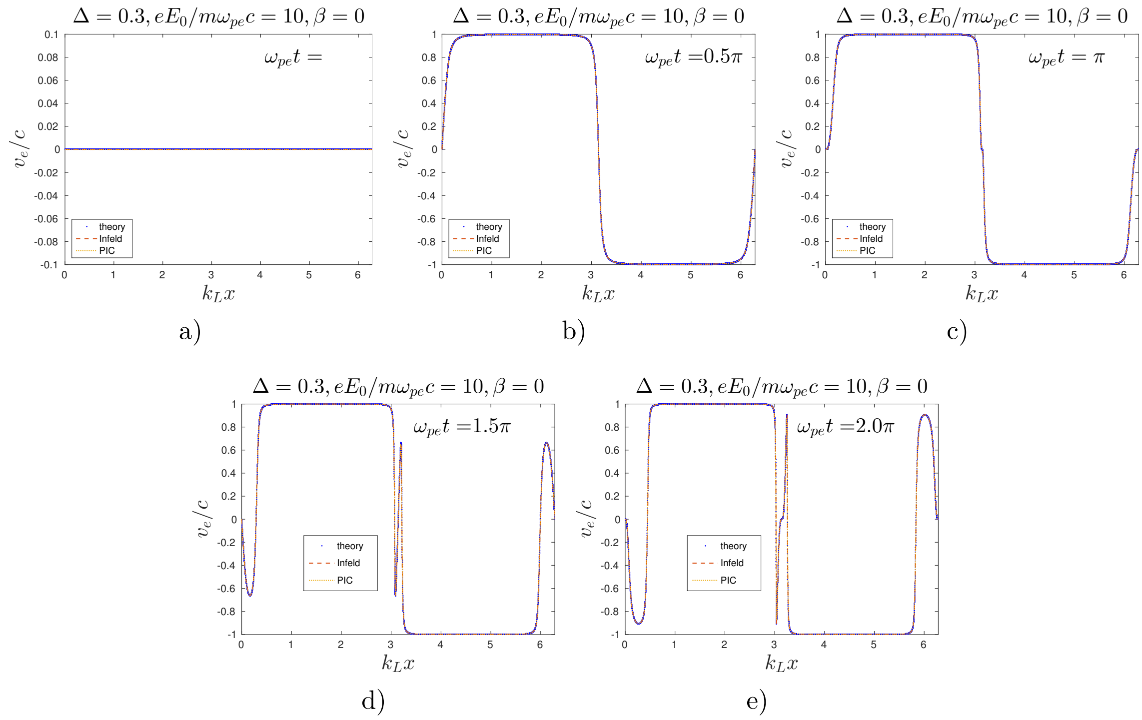

Figure 4.4: Snaps of space-time evolution of electron velocity for the parameters $\Delta \approx 0.3$, $\tilde{E}_0 = 10$ and $\beta = 0$. In this Fig., dots represent result of our theory, dashed line is a result of Infeld theory and dot-dashed line represents result of PIC simulation.

lations in a relativistic cold plasma. As a check, we reproduce nonlinear oscillations for stationary electron plasma (Infeld theory) by putting initial drift velocity equal to zero in our solution. Fig. 4.3 and 4.4 show evolution of electron number density and velocity at different time for $\Delta \approx 0.3$, $\tilde{E}_0 = 10$ and $\beta = 0$. Here continuous line is a result from our theory, dash line is a result of Infeld [17] theory and dot-dash line represents result of PIC simulation. A very good match between both theories and simulation shows the validity of our analytical solution.

In Fig. 4.5, we have plotted space-time evolution of electron number density for the parameters $\Delta \approx 0.3$, $\tilde{E} = 100$ and $\beta \approx 0.99$, where dash line is a result from PIC simulation, dash-dots line represents result of fluid simulation and dots represent result obtained from analytical solution. Fig. 4.5 clearly shows the appearance of spike which signifies wave breaking via phase mixing of relativistic intense wave. For similar parameters, electron velocity is plotted in Fig. 4.6.

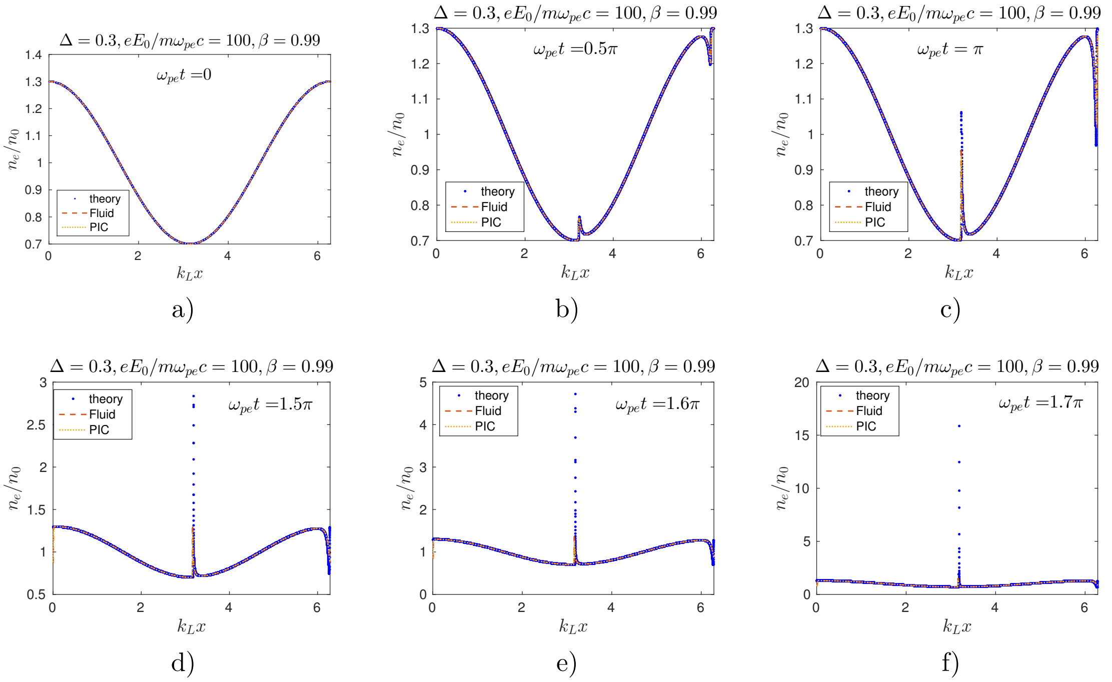

Figure 4.5: Snaps of space-time evolution of electron number density for the parameters $\Delta \approx 0.3$, $\tilde{E}_0 = 100$ and $\beta \approx 0.99$, where dots are a result of theory and dash/dot-dash line represents result of fluid/PIC simulation respectively.

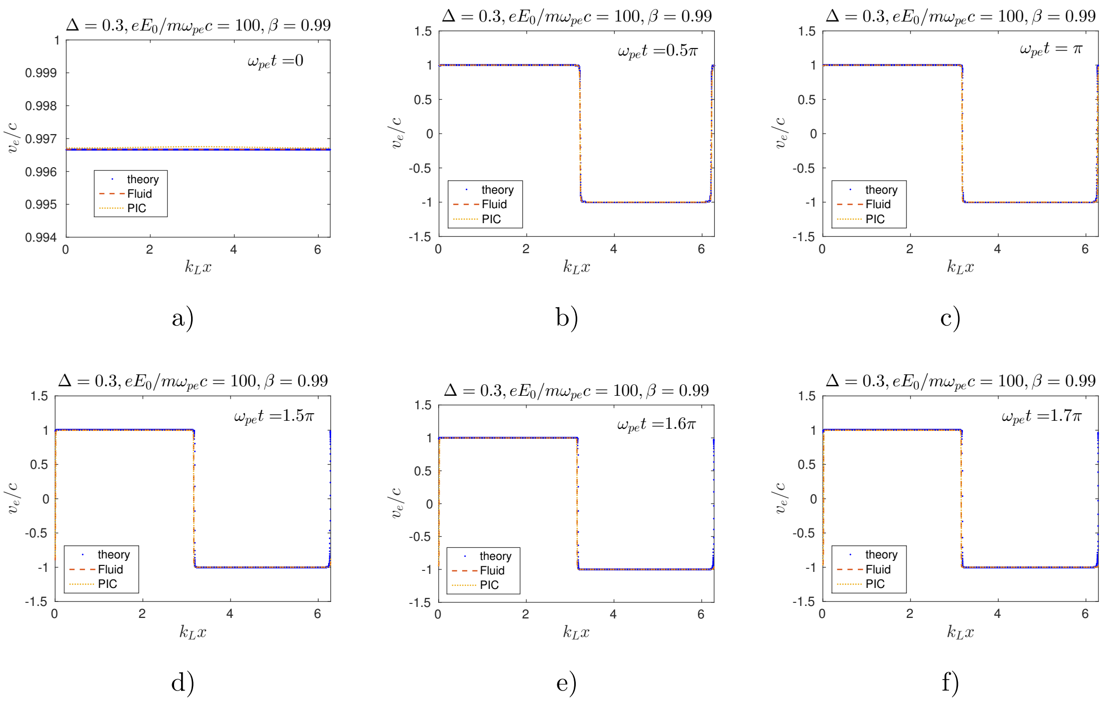

Figure 4.6: Snaps of space-time evolution of electron velocity for the parameters $\Delta \approx 0.3$, $\tilde{E}_0 = 100$ and $\beta \approx 0.99$, where dots are a result of theory and dash/dot-dash line represents result of fluid/PIC simulation respectively.

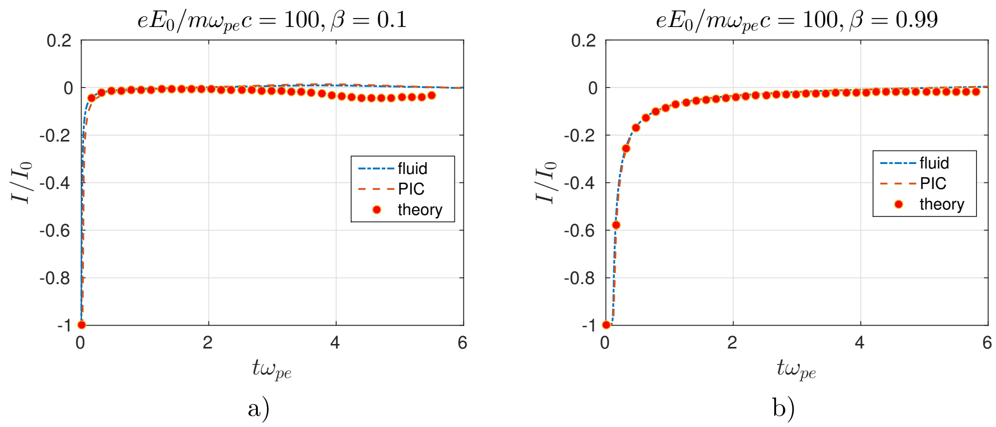

Figure 4.7: Temporal evolution of spatially averaged current for $\Delta \approx 0.3$, relativistic intensity $\tilde{E}_0 = 100$ and flow velocities (a) $\beta \approx 0.1$ and (b) $\beta \approx 0.99$. Here dash/dot-dash line represents result of PIC/fluid simulation and dots are taken from analytical solution.

In Fig. 4.7 we have plotted spatially averaged current for the parameters $\tilde{E}_0 = 100$ and $\beta \approx 0.1$ and $\beta \approx 0.99$, where dash/dot-dash lines are a result of PIC/fluid simulation respectively and dots represent analytical solution. Fig. 4.7 shows that spatially averaged current diminishes with time, which is in contrast with the results in non-relativistic regime, where spatially averaged current always remains constant. Thus, current decay is purely a relativistic effect, attributed to phase mixing phenomena, occurring because of variation of relativistic mass.

In Figs. 4.8 and 4.9, space-time evolution of current has been plotted for $\tilde{E}_0 = 10$ and $\beta \approx 0.1, 0.99$, where dot represents result of theory, dash/dot-dash represents result of fluid/PIC simulation respectively. In Figs. 4.10 and 4.11 space-time evolution of current has been plotted for $\tilde{E}_0 = 5$ and $\beta \approx 0.1, 0.99$.

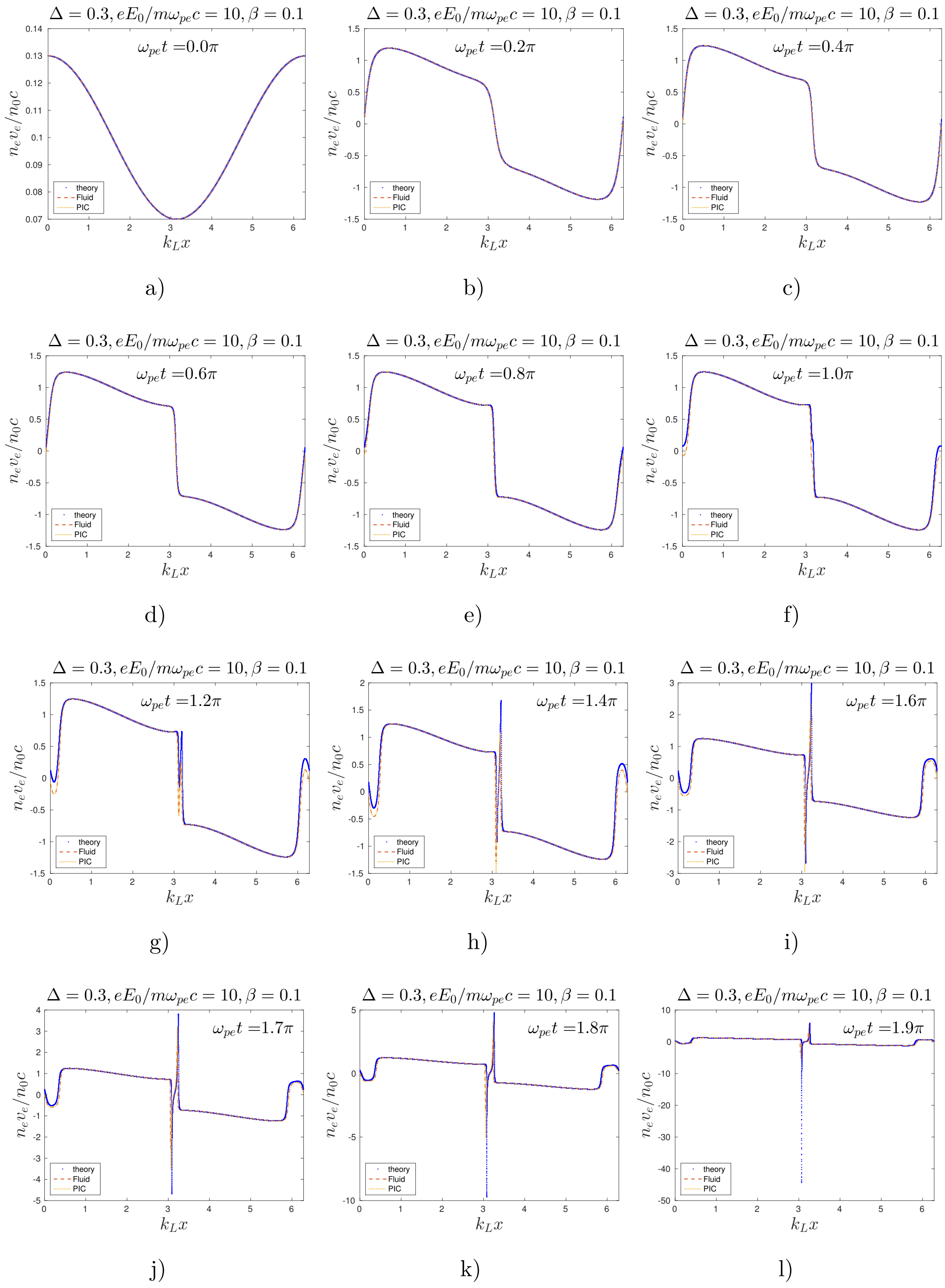

Figure 4.8: Spatio-temporal evolution of current for the parameters $\tilde{E}_0 = 10$ and $\beta \approx 0.1$, where dots show result of theory, dash lines show result of fluid simulation and dot-dashed lines represent result obtained from PIC simulation.

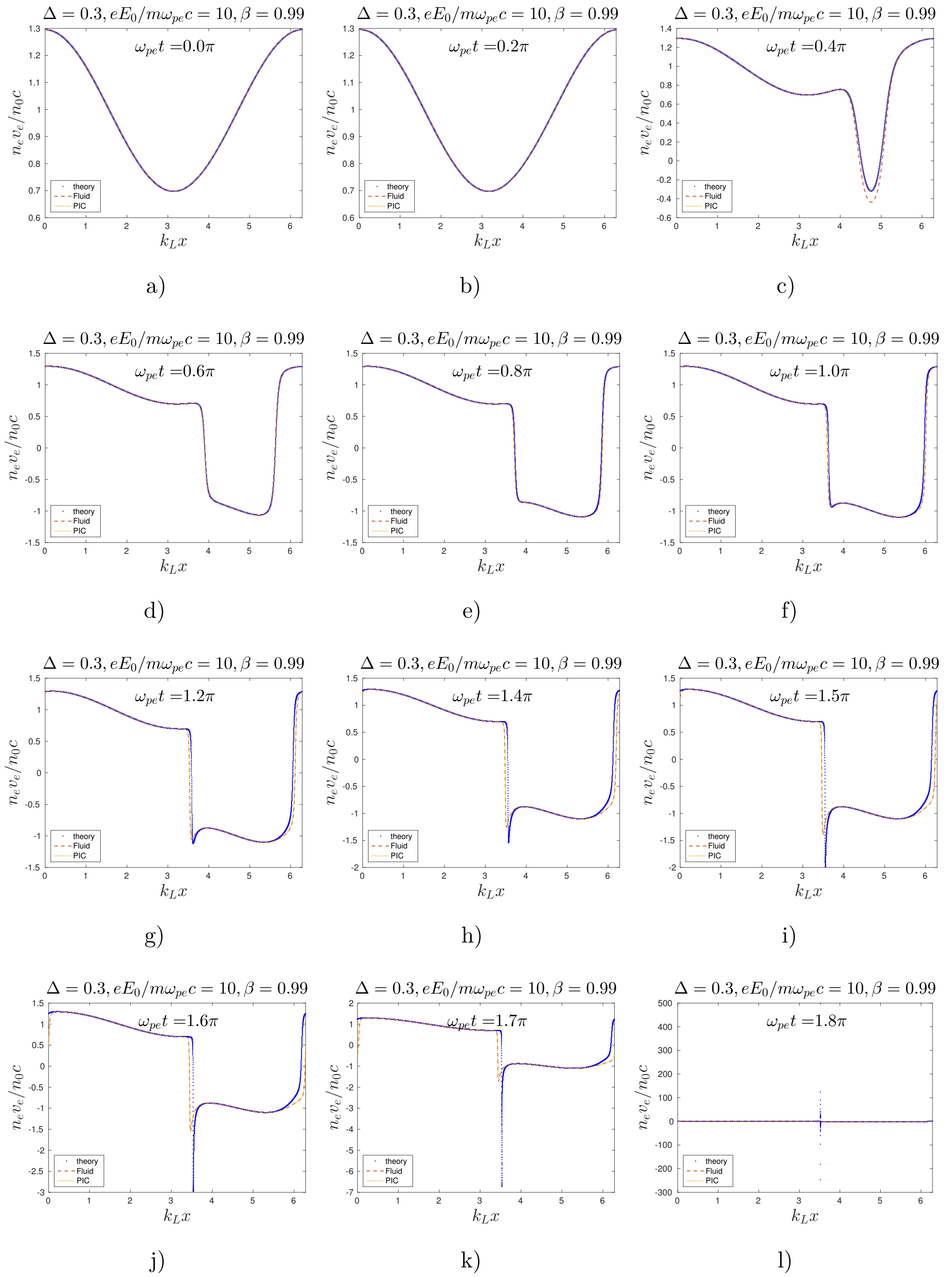

Figure 4.9: Spatio-temporal evolution of current for the parameters $\tilde{E}_0 = 10$ and $\beta \approx 0.99$, where dots show result of theory, dash lines show result of fluid simulation and dot-dash lines represent result obtained from PIC simulation.

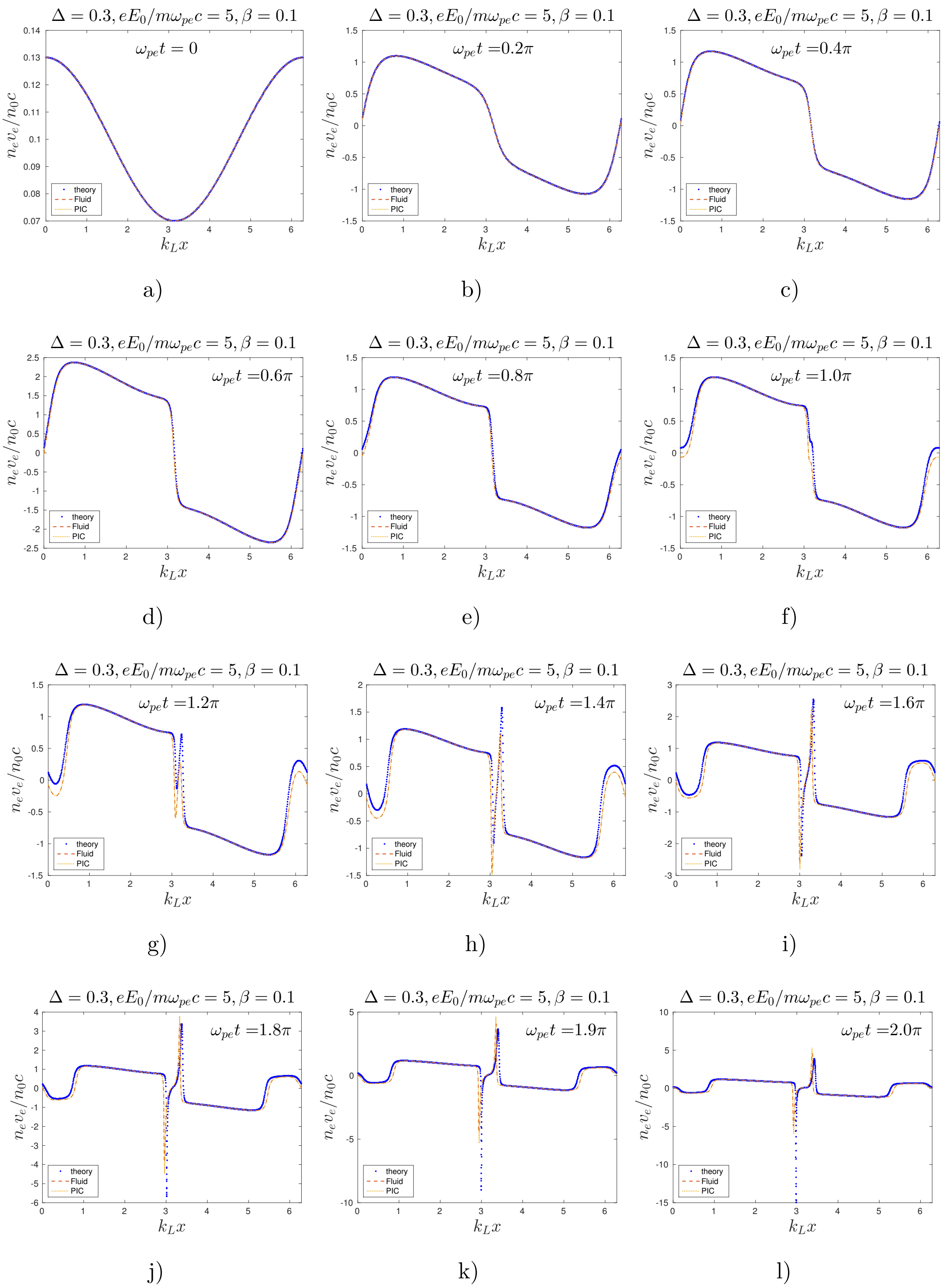

Figure 4.10: Spatio-temporal evolution of current for the parameters $\tilde{E}_0 = 5$ and $\beta \approx 0.1$, where dots show result of theory, dash lines show result of fluid simulation and dot-dash lines represent result of PIC simulation.

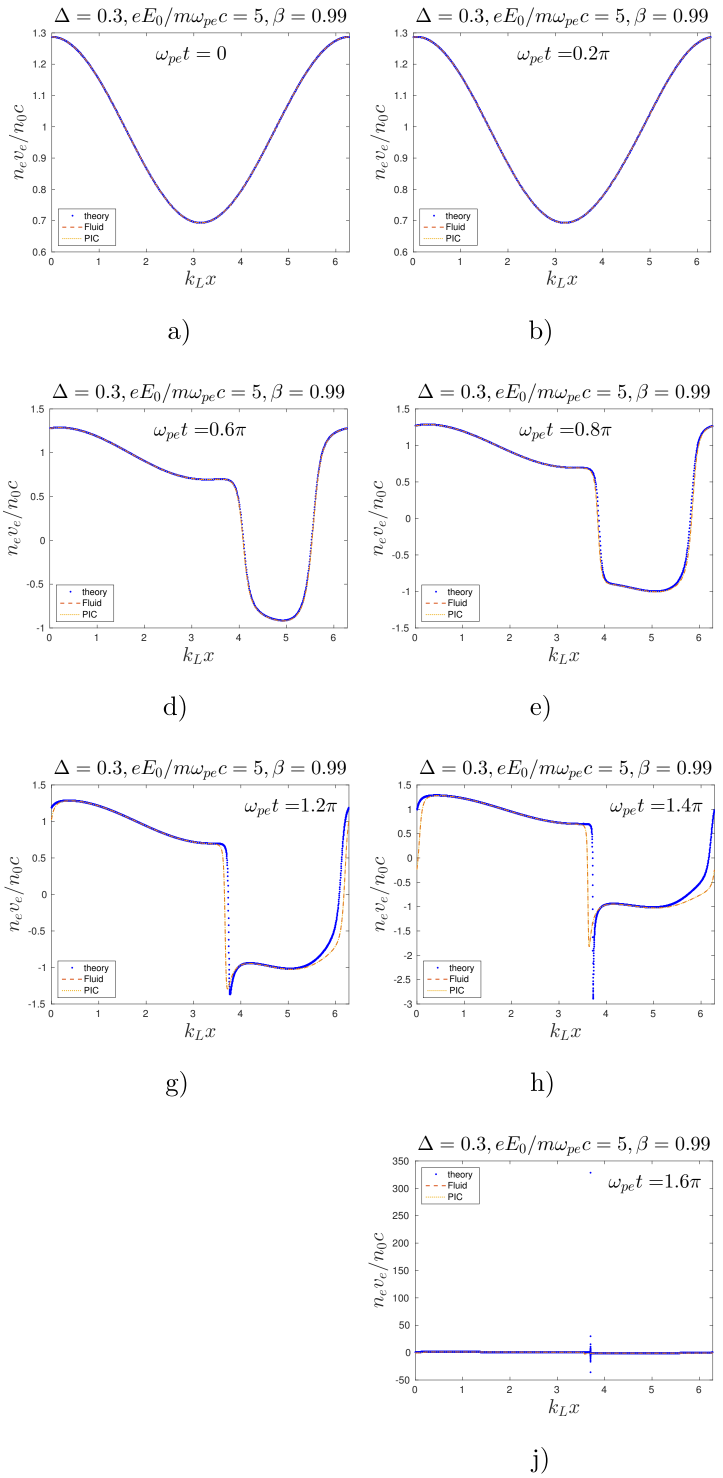

Figure 4.11: Spatio-temporal evolution of current for the parameters $\tilde{E}_0 = 5$ and $\beta \approx 0.99$, where dots show result of theory, dash lines show result of fluid simulation and dot-dashed lines represent result obtained from PIC simulation.

In Fig. 4.12 spatially averaged currents are compared for different value of $\tilde{E}_0$ and β, where continuous blue, green and pink lines are plotted for the parameters $\beta \approx 0.99$ and $\tilde{E}_0 = 5$, 10 and 100 respectively and dash blue, green and pink lines are plotted respectively for $\beta \approx 0.1$ and $\tilde{E}_0 = 5$, 10 and 100. Fig. 4.12 clearly demonstrates that as the relativistic intensity of wave is increased, slope of continuous lines and/or dash lines increases and as the flow velocity increases, slope of two similar color continuous and dash line decreases. Thus it is found that the rate of decrease of current decreases with increasing flow velocity and increases with increasing wave intensity. It is also seen that amount by which spatially averaged current diminishes, increases with increasing relativistic intensity.

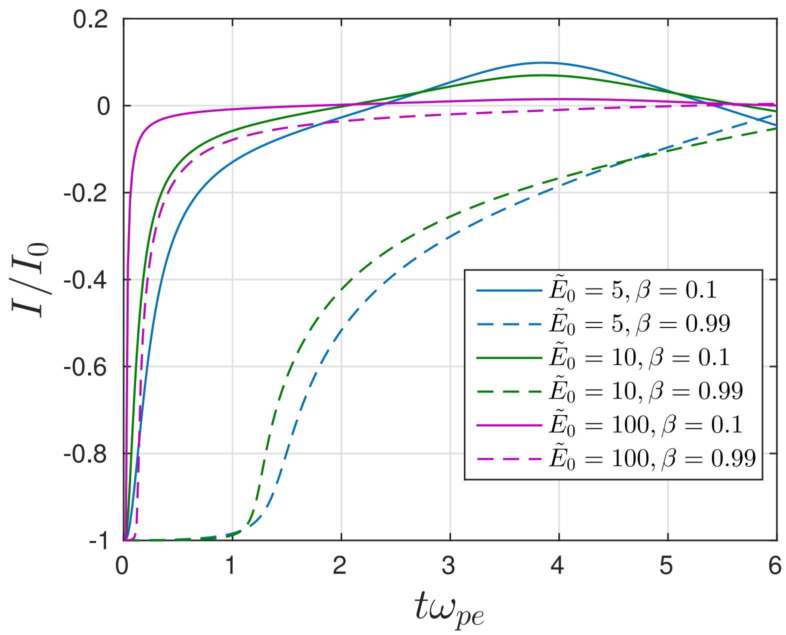

Figure 4.12: Comparison between temporal evolution of spatially averaged current for relativistic intensities $\tilde{E}_0 = 5$, 10, 100 and for $\beta \approx 0.1$ and 0.99.

4.4 Summary

In this chapter, we present exact space-time solution for relativistically intense wave propagating on an electron beam. It is found that when an electron beam is perturbed with relativistically intense wave, spatially averaged current diminishes with time. This novel effect is attributed to phase mixing effects arising because of variation of relativistic mass. It is also found that amount by which spatially averaged current diminishes (ΔI) increases with increasing relativistic intensity of the wave and rate of decrease of current decreases with increasing flow velocity and increases with increasing wave intensity.

Our findings may be of relevance in fast ignition scenarios [77, 78]. Fast ignition is a novel variant of inertial confinement fusion, which has shown promising results [77, 78]. In fast ignition scenarios [30, 31] , the relativistic electron beam is generated by direct interaction of the laser pulse with the coronal plasma and reaches the precompressed fuel core after propagating in the dense plasma region. In dense plasma region, forward moving relativistic electron beam current is compensated by backward moving coronal plasma electron current (return current) [50]. This current neutralization is satisfied on global scale rather than on local, subsequently introducing several beam-plasma instabilities (filamentation and/or Weibel) in the system. Owing to that energy transport is inhibited and coupling of energy from laser to precompressed target is hence compromised. Efficiency of energy transport is also a key factor in alternative fast ignition schemes. Increment in the efficiency of energy transport through relativistic electron beam is currently a hot issue and needs to be addressed in order to achieve inertial fusion confinement using fast ignition schemes. When there is no return current present, self consistent electric field of beam can reach up to $10^{12} V/m$ [50] in 1 fs. According to our findings on effects of space charge waves on relativistic electron beam, this self consistent electric field may modulate electron beam and total spatially averaged current may be diminished which would inhibit the excitation of other beam-plasma instabilities.

CHAPTER 5

Nonlinear evolution of Buneman instability and excitation of coupled hole-soliton

In this chapter we have numerically followed spatio-temporal evolution of Buneman instability till its quasilinear quenching and beyond, using an in-house developed electrostatic 1D particle-in-cell (PIC) simulation code. For different initial drift velocities and for a wide range of electron to ion mass ratios, growth rate obtained from simulation agrees well with the numerical solution of the fourth order dispersion relation. Quasi-linear saturation of Buneman instability occurs when ratio of electrostatic field energy density to initial electron drift kinetic energy density reaches up to a constant value, which as predicted by Hirose [39], is independent of initial electron drift velocity but varies with electron to ion mass ratio (m/M) as $\approx (m/M)^{1/3}$. *This result stands verified in our simulations. Growth of the instability beyond the first saturation (quasilinear saturation) till its final saturation [41] follows an algebraic scaling with time. In contrast to the quasilinear saturation, the ratio of final saturated electrostatic field* *energy density to initial kinetic energy density, is relatively independent of electron to ion mass ratio and is found from simulation to depend only on the initial drift velocity. Beyond the final saturation, electron phase space holes coupled to large amplitude ion solitary waves, a state known as coupled hole-soliton, have been identified in our simulations. The propagation characteristics (amplitude - speed relation) of these coherent modes, as measured from present simulation is found to be consistent with the theory of Saeki et. al. [46] . Our studies thus represent the first extensive quantitative comparison between PIC simulation and fluid/kinetic model of Buneman instability..*

In chapter 3 and 4 pure electron plasma modes have been discussed by considering infinitely massive ions. In this chapter, we have extended our studies for finite ion to electron mass ratio. We focus on the instabilities occurring because of coupling between electrons and ions. It is already mentioned in chapter 1 that Buneman mode under certain condition is the most unstable mode in the system. Buneman instability (BI) gets excited between electrons and ions, when Doppler shifted electron plasma frequency ($\omega_{pe} - kv_0$), resonate with ion plasma frequency (ω_{pi}) in ion rest frame; system become unstable at the expense of electron drift kinetic energy density, provided relative drift between electrons and ions is above the threshold $v_0 = 0.926(1+(m/M)^{1/2})(2K_BT_e/m)1/2$ (when $T_e = T_i$, where T_e and T_i respectively are electron and ion temperatures). Below this threshold Buneman modes quenches through Landau damping. We report quantitative effects of initial drift velocity on the space-time evolution and saturation of linear and nonlinear phase of Buneman instability. We study spatio-temporal evolution of Buneman instability using an in-house developed 1-D electrostatic particle-in-cell code. We have performed four simulation runs for various initial drift velocities $k_Lv_0/\omega_{pe} \approx 1$, 0.5, 0.33, 0.1 and observed the effect of initial drift velocity on the growth, quasilinear saturation, final saturation and post saturation dynamics of the Buneman instability. In section 5.1, we give an extensive introduction to the problem. For the sake of completeness in section 5.2 we revisit the linear theory of Buneman instability. Section 5.3 presents a brief description of method of solution. Section 5.4.1 describes evolution of instability upto the quasi-linear saturation. Section 5.4.2 reports evolution of instability upto final saturation and formation of couple hole-soliton after quenching of the instability. We end this chapter with a summary of our results in section 5.5.

5.1 Introduction

Streaming plasmas plays a key role in the generation of shock waves [103], enhances turbulence in tokamaks [104], induces anomalous resistivity [37, 38] and used in astrophysical scenarios, *viz.*, shock surfing acceleration [33], formation of strong double layer [28, 29] , generation of broadband electrostatic noise [45] etc. Instabilities[1, 2] associated with streaming plasmas are well known current dissipation mechanism in the presence of external electric field or in the field free collision-less plasma. Being a fundamental current carrying instability, Buneman [60, 26] instability has been the center of attraction for decades. Buneman instability gets excited when relative drift velocity between electrons and ions is sufficiently larger than thermal velocity of electrons. Buneman wave particle interaction induces scattering of the particles that causes strong parallel heating [88]. This novel effect is widely observed/used in electron acceleration [5, 34, 35, 105], ion acceleration [6, 7] and in inertial electrostatic confinement [30, 31, 106] etc.

Since the pioneering work of Oscar Buneman [60, 26]; a lot of work has been done to understand linear and nonlinear evolution of Buneman instability in the non-relativistic[82, 83, 39, 41, 42, 51, 52, 86, 85, 107, 87, 108, 88, 109, 91, 90] and relativistic [6, 7, 110, 54, 55] regime. Various approaches are attempted by several authors[82, 83, 39] to estimate the saturation value of the Buneman instability; among them Hirose's[39] model successfully predicted that at the quasilinear saturation (or first saturation) the ratio of electrostatic energy density ($\sum_k |E_k|^2/8\pi$) to initial kinetic energy density ($W_0 = (1/2)n_0 m v_0^2$) varies with electron to ion mass ratio as $\sim (m/M)^{1/3}$. Ishihara et. al.[41, 42] derived a nonlinear dispersion relation using quasi-linear analysis for initial delta function distribution (cold beam) for electrons. Ishihara et. al. carried out 1-D kinetic simulation of Buneman instability and compared numerical solution of the nonlinear dispersion relation with simulation results that successfully predicted the breakdown of the linear growth, frequency and growth rate modulation. These authors observed that electron trapping causes the final saturation of the Buneman instability and estimated minimum electrostatic field energy required for quenching of the instability via electron trapping and found that it scales with initial kinetic energy density as $\sum_k |E_k|^2/16\pi \geq 0.11 W_0$.

Yoon[51] has formulated a phase and spatially averaged perturbative nonlinear weak turbulence theory that involves quasi-linear velocity space diffusion and nonlinear wave particle interaction. In the companion paper[52], Yoon carried out Vlasov simulation of Buneman instability for different electron to ion temperature ratio and compared the simulation results with that derived using weak turbulence theory[51]. Their theory successfully predicted nonlinear development of the Buneman instability qualitatively, when nonlinear scattering term with wave kinetic equation is included . In recently carried out simulation works, Jain et. al.[86] and Guo [43] have carried out 1-D Vlasov and particle-in-cell simulation respectively. Their simulations show that along with the low frequency Buneman mode and high frequency Langmuir mode; wave modes propagating in the opposite direction of the Buneman wave also gets excited in the nonlinear phase of the instability. Niknam[87] has carried out 1-D particle-in-cell simulation and reported density steepening at late times as well as dependence of time development of electrostatic energy densities with a range of mass ratios. Hashemzadeh [90, 91, 92] has carried out particle-in-cell simulation of Buneman instability for q non-extensive distribution and effect of negative ions on the Buneman instability. There is ample amount of other simulation works dealing with Buneman instability in various applications in space and laboratory plasmas that are too numerous to cite.

Above cited references deal with early nonlinear dynamics or dynamics up to the saturation of Buneman instability. Post saturation dynamics of Buneman instability is still under scanner and to the best in our knowledge very little work has been carried out to understand it. Dynamics after quenching is strongly affected by initial plasma parameter. If initial drift velocity of the electron beam is not much larger than thermal velocity, then initial drift kinetic energy does not dissipate completely [43] and some part of it still remains with nonlinear coherent structure. This net drift energy of coherent structures after quenching of Buneman instability may affect interaction between electrons and ions. When initial drift velocity of the electron beam is much larger than thermal velocity of electrons, then initial kinetic energy dissipates completely [41, 42] and a strong interaction between nonlinear coherent structure and surrounding ion may result into formation of coupled hole-soliton [89, 46]. Thus, Buneman instability may decay into ion acoustic wave [70] and/or may induce coupled hole-solition [89, 46, 33].

5.2 Theory

Consider a cold electron beam of density n_0 and velocity v_0 moving through a homogeneous background of ions of density n_0. Buneman instability gets excited when initial electron drift velocity is sufficiently larger than electron thermal velocity, *i.e.*, $v_0/v_{th} \gg 1$. The basic set of fluid equations governing the space-time evolution of Buneman instability in one dimension system can be written as

The continuity equation is

$$\frac{\partial n_s}{\partial t} + \frac{\partial (n_s v_s)}{\partial x} = 0, \tag{5.1}$$

The momentum equation is

$$\frac{\partial v_s}{\partial t} + v_s \frac{\partial (v_s)}{\partial x} = q_s \frac{E}{m_s}, \tag{5.2}$$

Poisson equation can be written as

$$\frac{\partial E}{\partial x} = 4\pi e(n_i - n_e), \tag{5.3}$$

where s stands for species electron/ion, e is charge of electrons and ions and, v_s, n_s,q_s and m_s are velocity, density, electrostatic charge and mass of respective species and E is self consistent electric field. Hereinafter we use $m_e = m$; $q_e = -e$ and $m_i = M$; $q_i = e$.

5.2.1 Derivation of linear dispersion relation

For electrons, linearized continuity and momentum equations become

$$-\iota\omega\delta n_e + \iota k n_0 \delta v_e + \iota k v_0 \delta n_e = 0, \tag{5.4}$$

$$-\iota\omega\delta v_e + \iota k v_0 \delta v_e = -\frac{eE}{m}, \tag{5.5}$$

where δn_e and δv_e are respectively the perturbed density and velocity. Eliminating δv_e from equation ((5.4)) and ((5.5)), perturbed electron density is

$$\delta n_e = \frac{-\iota e k n_0}{m(\omega - k v_0)^2} E. \tag{5.6}$$

Following a similar procedure as above, the linearized perturbed ion density is given by

$$\delta n_i = \frac{\iota e k n_0}{M\omega^2} E. \tag{5.7}$$

Now linearized Poisson equation can be written as

$$\iota kE = 4\pi(\delta n_i - \delta n_e). \tag{5.8}$$

Using equation (5.6),(5.7) and (5.8), we get linear dispersion relation as

$$1 = \frac{\omega_{pi}^2}{\omega^2} + \frac{\omega_{pe}^2}{(\omega - kv_0)^2}, \tag{5.9}$$

where k is a wave number, $\omega_{pi} = \sqrt{\frac{4\pi n_0 e^2}{M}}$ and $\omega_{pe} = \sqrt{\frac{4\pi n_0 e^2}{m}}$ are ion and electron plasma frequencies, respectively. The linear dispersion relation is a fourth degree polynomial in the wave frequency ω.

5.2.2 Estimation of the linear growth rate

Growth rate for the most unstable mode (resonant mode) can be estimated by putting the resonance condition $kv_0 \approx \omega_{pe}$ in equation (6.11), gives

$$1 \approx \frac{\omega_{pi}^2}{\omega^2} + \frac{\omega_{pe}^2}{(\omega - \omega_{pe})^2}. \tag{5.10}$$

Roots of above written fourth order polynomial presents normal modes of the Buneman instability. A general solution of linear dispersion relation is presented in appendix. Now by expanding the denominator using $\omega/\omega_{pe} \ll 1$, gives the following relation

$$\omega^3 = -\frac{m}{2M}\omega_{pe}^3, \tag{5.11}$$

which is a cubic equation.

Complex roots of cubic equation can be written as

$$\Omega = \omega + \iota\gamma = (1 \pm \iota\sqrt{3})\left(\frac{m}{16M}\right)^{(1/3)}\omega_{pe}, \tag{5.12}$$

where taking only positive sign gives the growth rate of the most unstable mode as

$$\gamma_{max} = \sqrt{3}\left(\frac{m}{16M}\right)^{(1/3)}\omega_{pe}. \tag{5.13}$$

Even though the relative drift velocity between electrons and ions is the key factor which excites the instability, nevertheless, maximum growth rate still turns out to be independent of the initial drift velocity and merely depends on the electron to ion mass ratio. Above described method only yield three roots of equation (5.9); see appendix C, where we have estimated all four roots of equation (5.9).

5.3 Method Of Solution

In order to understand the spatio-temporal evolution of Buneman instability beyond the linear stage, we use an in-house developed one dimensional electrostatic particle-in-cell simulation code. The governing equations, *viz.*, the particle position and velocity equations and Poisson equation in normalized forms are

$$\frac{dx}{dt} = v_s \tag{5.14}$$

$$\frac{dv_s}{dt} = \pm E(x,t) \tag{5.15}$$

$$\frac{\partial E}{\partial x} = (n_i - n_e) \tag{5.16}$$

Then normalization used are $x \to k_L x$, $t \to \omega_{pe} t$, $v_s \to k_L v_s/\omega_{pe}$, $E \to \frac{ek_L E}{m\omega_{pe}^2}$ and $\phi \to \frac{ek_L^2\phi}{m\omega_{pe}^2}$, where k_L is the wavenumber corresponding to the longest wavelength supported by the simulation box.

Parameters used in the numerical experiment of Buneman instability are written in table 5.1. System length is chosen to be equal to longest mode(L = $2\pi/k_L$, k_L=1) supported by the system. System length is divided in NG equidistant cells, so field quantities electric field, electron/ion density are calculated at the cell center(grid

Table 5.1: List of physical parameters used in our simulations.

Parameter	Symbol	Value
No of grid points	NG	1024
System Length	L	2π
Time step	Δt	$0.0196349\,\omega_{pe}^{-1}$
Grid Spacing	$k_L \Delta x$	L/NG = 0.006
Total no of electron	N_e	102400
Total no of ion	N_i	102400
Mass ratio	M/m	500, 1836, 18360
Electron Plasma Frequency	ω_{pe}	1
Ion Plasma Frequency	ω_{pi}	$(m/M)^{1/2}\,\omega_{pe}^{-1}$
Initial electron drift velocity	$k_L v_0/\omega_{pe}$	0.1, 0.33, 0.5, 1.0
Initial ion drift velocity	$k_L v_{i0}/\omega_{pe}$	0.0
Electron thermal velocity	$v_{th,e}/v_0$	0.003
Ion thermal velocity	$v_{th,i}/v_0$	0.0

points) and particle quantities like velocities are calculated at the particle positions. Periodic boundary conditions are used that allows only integer mode as k = 1,2,3...512 in the system. A small thermal spread $< [v(0) - \overline{V}(0)] >= 3 \times 10^{-3}$ added to the electron beam to avoid nonphysical cold beam instability [96]. Plasma is cold ($v_0/v_{th} \approx 1000$) with a very small thermal spread that fulfills necessary condition $v_{drift} \gg v_{thermal}$, so system has favorable condition for excitation of Buneman instability.

In this simulation, we have followed the ion and electron trajectory in the self consistently generated electric field. Initially electrons and ions are placed in phase space with their respective position and velocity. Then for a given ion and electron density, electric field is calculated on the grid points by solving Poisson's equation. Using this electric field, force is calculated on the grid points and then interpolated on particle positions. Further ion and electron momentum equations are solved using this force that yields a new position and velocity. This new particle position is weighted on the grid points to estimate density over the grid points using second order polynomial interpolation. This process is repeated for thousands of time steps.

5.4 Results and Discussion

We begin our simulation from an initial state where all the electrons are flowing as a whole with a single velocity (delta-function velocity distribution) against a homogeneous background of stationary, cold ions. This initial state is unstable to longitudinal perturbations, and as time progresses, small amplitude density (electron and ion density) and velocity oscillations arise from background noise. Since the system is unstable, as the electron beam provides free energy, these small oscillations begin to grow at the expense of the initial beam kinetic energy. In 5.4.1, we discuss the evolution of the instability till the quasilinear saturation and in 5.4.2 we present the evolution after quasilinear saturation till the final saturation and beyond.

5.4.1 Linear growth and quasilinear saturation

Initially, the growth of the instability is dominated by the most unstable mode and its harmonics; the most unstable mode being given by the resonance condition $kv_0/\omega_{pe} \approx 1$. Therefore for electron beam velocities $k_L v_0/\omega_{pe} \approx$ 1, 0.5, 0.33, 0.1, the corresponding most unstable modes are respectively given by $k/k_L \approx$ 1, 2, 3, 10 where the normalizing wave number k_L is associated with the longest wavelength that can be supported by the simulation box size.

Fig. 5.1 shows the evolution of electric field amplitude in Fourier space for the mass ratio M/m = 1836 and for the initial electron drift velocity $k_L v_0/\omega_{pe} \approx 0.33$. For these parameters, the most unstable mode turns out to be $k/k_L \approx 3$ whose growth rate is given by $\gamma_{max}/\omega_{pe} \approx 0.054$. Fig. 5.2 shows the temporal evolution of different Fourier modes for the same set of parameters. The violet, yellow and red line respectively show the growth of the most unstable mode and its first and second harmonic. Growth rates are obtained by measuring the slope of the curves in Fig.

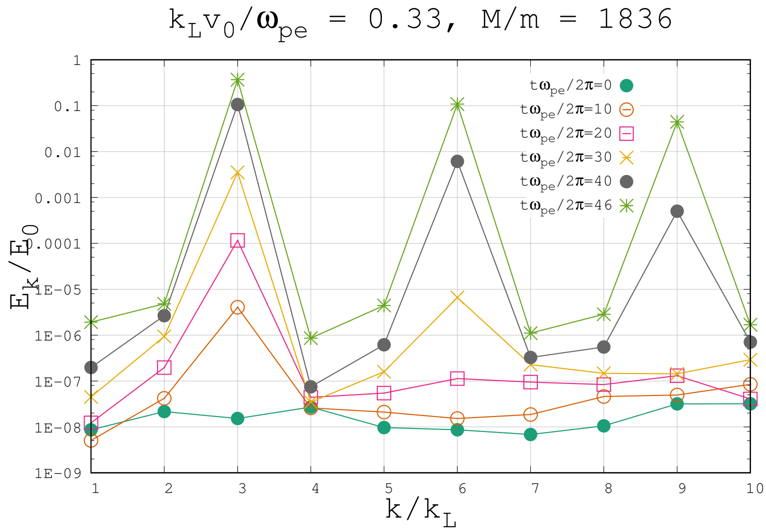

Figure 5.1: Evolution of electric field amplitude in Fourier space for $k_L v_0/\omega_{pe} \approx 0.33$ and M/m = 1836.

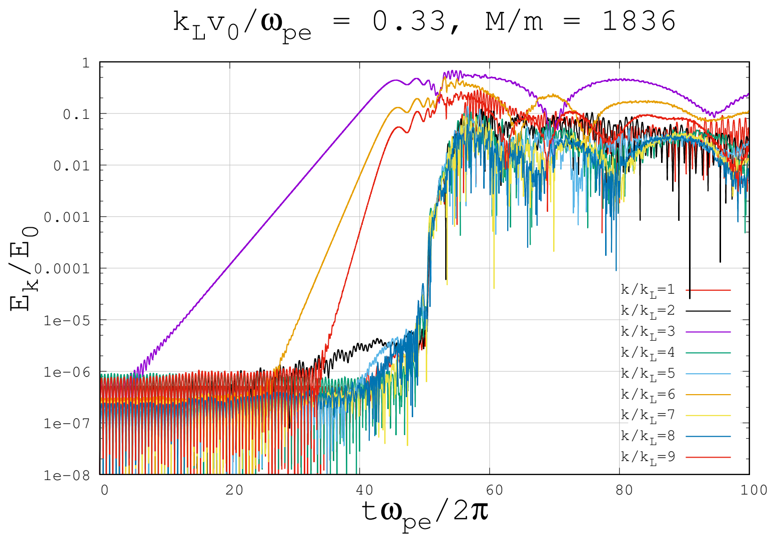

Figure 5.2: Temporal evolution of Fourier modes for $k_L v_0/\omega_{pe} \approx 0.33$ and M/m = 1836.

5.2 from initial stage of the instability to quasilinear saturation. Most unstable mode grows with the growth rate $\gamma_{max}/\omega_{pe} \approx 0.054$ and its first and second harmonics, which appear later in time, respectively grow with twice and thrice the growth rate of the most unstable mode. Fig. 5.3 shows the growth rate (γ/ω_{pe}) as a function of mode number for different initial drift velocities ($k_L v_0/\omega_{pe} \approx 0.1, 0.2, 0.33$) and for a fixed mass ratio (M/m = 1836). The continuous line curves show the theoretical growth rate as a function of mode number obtained from numerical solution of the linear dispersion relation, i.e. the solution of the fourth degree polynomial (equation

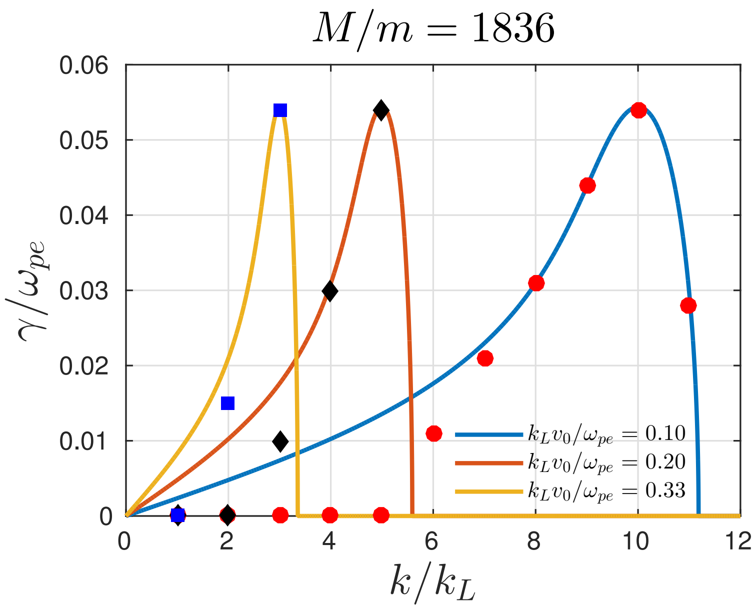

Figure 5.3: Comparison between theoretical growth rate (points) and growth rate obtained from the simulation (continuous line) as a function of mode number (k/k_L) for the initial drift velocities $k_L v_0/\omega_{pe} \approx 0.1$, 0.2, 0.33 and mass ratio M/m = 1836.

(5.9)) while the dots show the growth rate obtained from simulations; which show a reasonably good match between fluid theory and simulation. Fig. 5.3, also shows that the growth rate of most unstable mode (maxima of the curves) is independent of the initial electron drift velocity, and with increasing $k_L v_0/\omega_{pe}$ the most unstable mode shifts towards shorter wavenumbers; these are in conformity with equation (5.13). In Fig. 5.4, we show the dependence of growth rate of the most unstable mode (γ_{max}/ω_{pe}) on the electron to ion mass ratio (m/M) for a fixed initial drift velocity $k_L v_0/\omega_{pe} \approx 0.33$. The dots represent the simulation points and continuous line is a fit through the points. The linear variation of γ_{max}/ω_{pe} with $(m/M)^{1/3}$ again confirms equation (5.13). Quasi-linear growth of the instability ceases when exponential growth of the most unstable mode and its harmonics terminate. Fig. 5.5 and 5.6, respectively show the temporal evolution of the electrostatic field energy density for different initial electron drift velocities $k_L v_0/\omega_{pe} \approx 0.1, 0.33, 0.5, 1$, for two different mass ratios $M/m = 500$, 1836. At quasilinear saturation, time evolution of electrostatic energy density shows a hiccup as shown in inset of Fig. 5.5 and 5.6. This hiccup represents the first saturation (termination of exponential growth) of

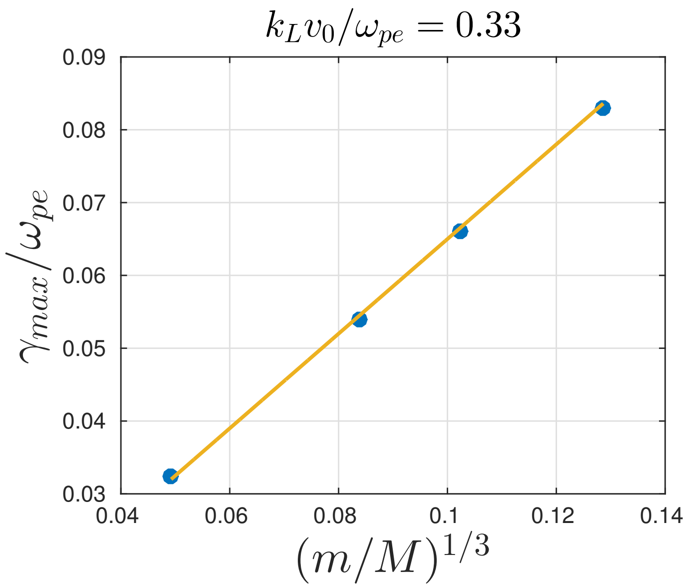

Figure 5.4: Comparison of growth rate of the most unstable mode for the initial drift velocity $k_L v_0/\omega_{pe} \approx 0.33$ and different mass ratios.

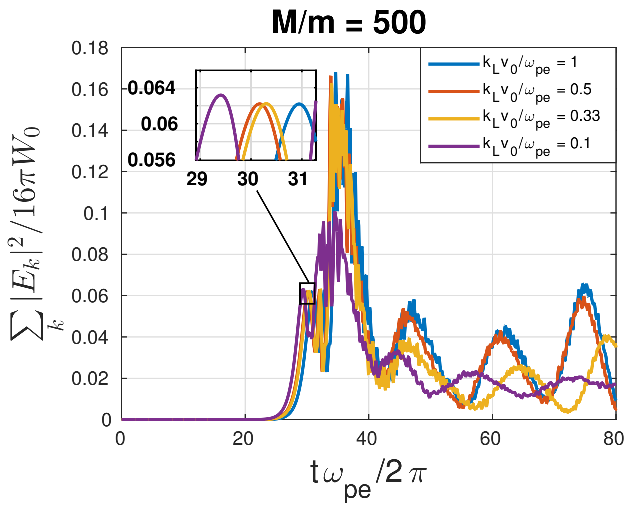

Figure 5.5: Temporal evolution of ratio of electrostatic energy density to different initial drift kinetic energy density for the mass ratio M/m = 500.

the Buneman instability. Since the growth rate of the most unstable mode in the linear regime is independent of the initial electron drift velocity, the "hiccups" in electrostatic field energy, for different initial drift velocities appear nearly at the same time. This first saturation occurs when the ratio of electrostatic energy density $(\sum_k |E_k|^2/16\pi)$ to initial drift kinetic energy density $(\frac{1}{2}n_0 m v_0^2)$ reaches a constant value $\approx (m/M)^{(1/3)}$ *i.e*

$$\sum_k \frac{|E_k|^2}{16\pi W_0} \approx \left(\frac{m}{M}\right)^{(1/3)} \tag{5.17}$$

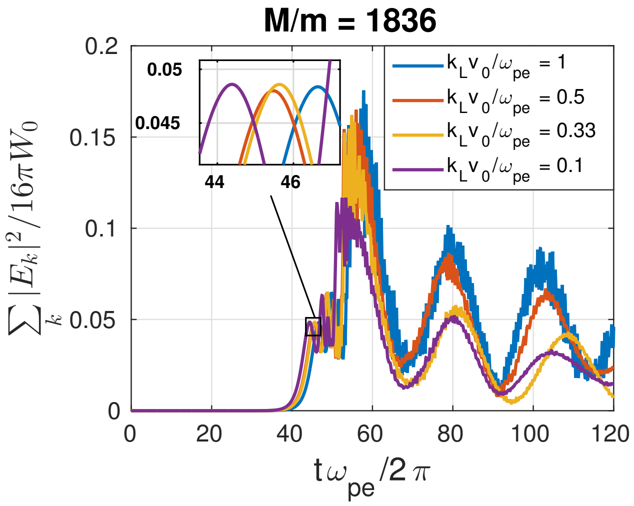

Figure 5.6: Temporal evolution of ratio of electrostatic energy density to different initial drift kinetic energy density for the mass ratio M/m = 1836.

where W_0 is the initial drift kinetic energy density of electrons. The reason for quasilinear saturation of the instability at this low value of the ratio, is because of the narrow width(FWHM) of the growth rate (γ/ω_{pe}) vs mode number (kv_0/ω_{pe}) curve around the resonance point $kv_0 \approx \omega_{pe}$ (see Fig. 5.3). This figure shows a drastic drop in the growth rate of the instability for any small change in the electron drift velocity. When change in drift velocity ($\sim k\Delta v_0/\omega_{pe}$) becomes comparable to FWHM ($\sim \Delta(kv_0/\omega_{pe}$) of the γ/ω_{pe} vs kv_0/ω_{pe} curve $i.e.(k\Delta v_0/\omega_{pe} \approx \Delta(kv_0/\omega_{pe}))$ then exponential growth of the instability terminates [39]. Based on this argument and a quasilinear calculation, Hirose et. al. [39] showed that at the first saturation, electrostatic field energy density scales linearly with the initial electron drift kinetic energy density with a slope which depends on the electron to ion mass ratio as $(m/M)^{1/3}$ (equation (5.17) above). This result is verified in our simulation as shown in Fig. 5.7, where we have plotted the electrostatic field energy density at the first saturation point vs. initial drift kinetic energy density for different mass ratios 500, 1836 and 18360. The linear variation is in conformity with Hirose's scaling [39]. To the best of our knowledge, this is the first verification of Hirose's scaling using a PIC code.

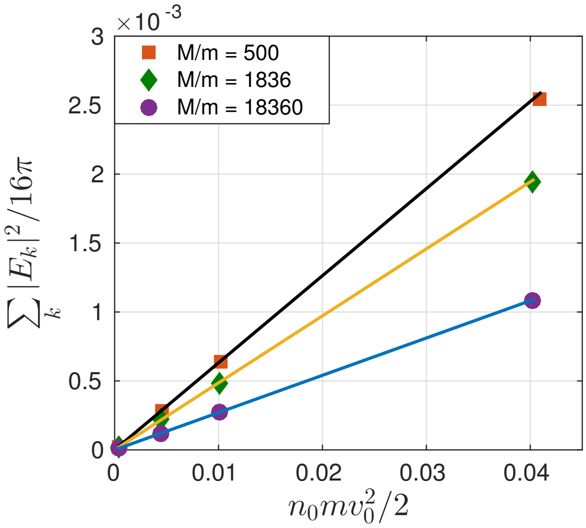

Figure 5.7: Figure shows variation of electrostatic energy density with different initial kinetic energy density for the mass ratios M/m = 500, 1836, 18360.

5.4.2 Beyond quasilinear saturation: Formation of Coupled hole solitons

Termination of quasi linear growth does not imply complete saturation of the instability. Beyond this point the instability evolves with algebraic growth up to the final saturation [41]. This algebraic growth stage (time between quasilinear saturation and final saturation) decreases with the decreasing ion to electron mass ratio as shown in fig 5.8b and 5.8a where we have plotted the temporal evolution of electrostatic field energy density for $k_L v_0/\omega_{pe} \approx 0.33$ and $k_L v_0/\omega_{pe} \approx 1$ respectively, for different mass ratios.

As mentioned earlier, the resonant mode (*i.e.* the most unstable mode) and its harmonics govern the evolution of the instability up to the quasi-linear saturation. Beyond the quasilinear saturation, the evolution of the instability is governed by the rapid growth of the non-resonant modes (see Fig. 5.2). Evolution of the instability in this regime has been studied by several authors [85] who have predicted steepening of electron density profile at late times (*i.e.* beyond quasilinear saturation). Figure 5.9 and 5.10 respectively show the time development of electron and ion density

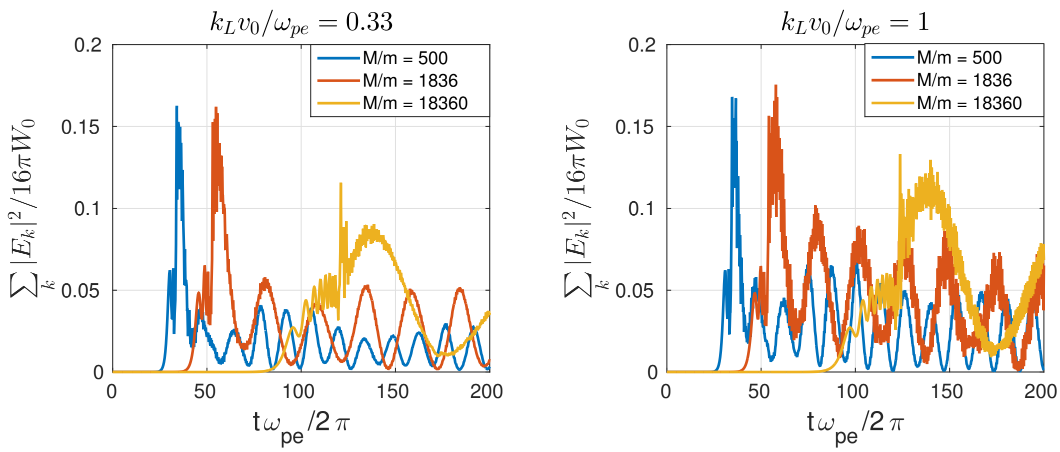

a) b)

Figure 5.8: Time development of ratio of electrostatic energy density to initial kinetic drift energy density with various mass ratio for the initial drift velocities (a) $k_L v_0/\omega_{pe} \approx 0.33$ and (b) $k_L v_0/\omega_{pe} \approx 1$.

profiles at different time steps. Both electron and ion density show small oscillations growing out of background noise; these oscillation eventually steepen and gain large amplitude at late times.

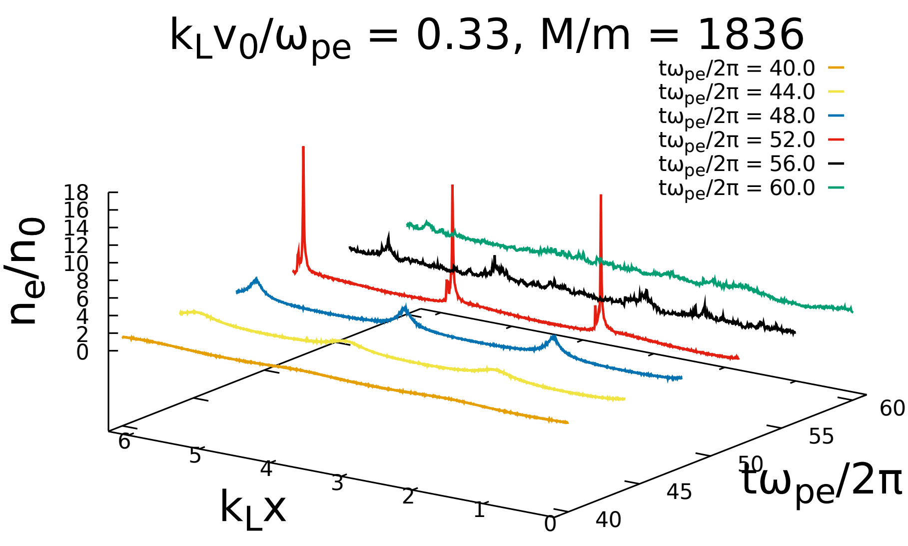

Figure 5.9: Evolution of electron density at different time instances for $k_L v_0/\omega_{pe} \approx$ 0.33 and M/m = 1836.

When the wave potential becomes large enough, some electrons are trapped in this self consistently generated nonlinear wave potential well; these trapped particle population generate a counter streaming population of electrons in the plasma (see

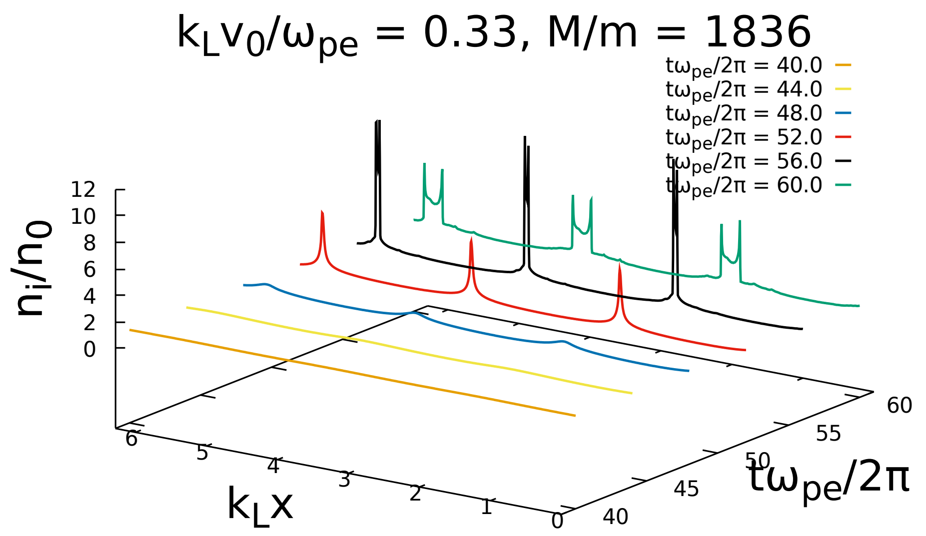

Figure 5.10: Evolution of ion density at different time instances for $k_L v_0/\omega_{pe} \approx 0.33$ and M/m = 1836.

figure 5.12). This counter streaming population excites electron-electron two stream instability that leads to the formation of holes in electron phase space.

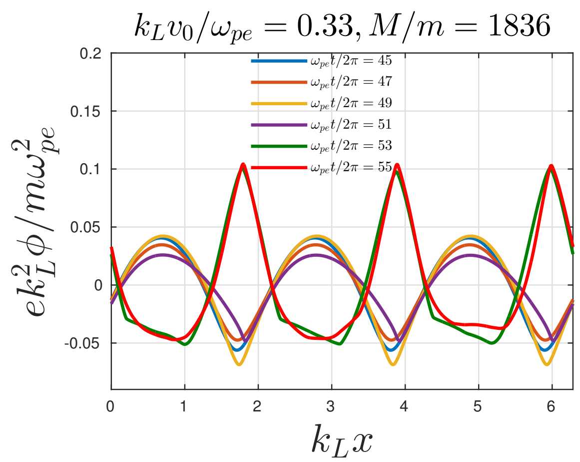

Figure 5.11: Phase reversal of electrostatic potential during particle trapping for $k_L v_0/\omega_{pe} \approx 0.33$ and M/m = 1836.

When large number of electrons are trapped in the wave potential well, the instability saturates abruptly. After completion of trapping, instability is quenched and potential shows sudden phase reversal[41] at the time of trapping. Fig. 5.11 shows the evolution of the potential profile beyond the quasilinear saturation upto the final saturation ($\omega_{pe}t/2\pi \sim 45 - 55$) for $k_L v_0/\omega_{pe} \sim 0.33$ and $M/m = 1836$.

Phase reversal of potential is clearly seen at $\omega_{pe}t/2\pi \sim 53$. Around the same time the electron phase space plots (see figure 5.12)) also show enhanced trapping (phase space holes). Based on the argument that the final saturation of the instability is caused by electron trapping, Ishihara[41] et. al. calculated the ratio of electrostatic field energy density to initial electron drift kinetic energy density at the final saturation point and showed that $\sum_k \frac{|E_k|^2}{16\pi W_0} \geq 0.11$. Thus in contrast to quasilinear saturation, this ratio is independent of mass ratio (equation (5.17)). Our simulations show, that this ratio is not very sensitive to the mass ratio but depends on the initial electron drift velocity. For the mass ratio M/m = 1836, the ratio of electrostatic field energy density to initial electron drift kinetic energy density at the final saturation varies with initial drift velocities as

$$\sum_k \frac{|E_k|^2}{16\pi W_0} \approx 0.11(k_L v_0/\omega_{pe} = 0.1) \sim 0.18(k_L v_0/\omega_{pe} = 1) \tag{5.18}$$

This is in conformity with Ishihara's[42] inequality. Equation (5.18) shows that the field energy required for complete trapping depends on initial drift velocity and increases with increasing initial drift velocity. We have performed simulations with wide range of initial drift velocities and mass ratios (see figures (5.5 and 5.6) which respectively show final saturation level for two different mass ratios (M/m = 500 & 1836) and different initial drift velocities; and in each case it is found that the ratio of electrostatic field energy density at the final saturation to the initial electron drift kinetic energy density follows Ishihara [41] inequality, *i.e.*, ($\sum_k \frac{|E_k|^2}{16\pi W_0} \geq 0.11$).

Figure (5.12) shows snapshots of electron phase space at different times. As mentioned above, around $\omega_{pe}t/2\pi \sim 55$ phase space holes are seen in the electron fluid, the number of holes being equal to the most unstable wavenumber ($k/k_L = 3$ for $k_L v_0/\omega_{pe} \approx 0.33$). At this time *i.e.* $\omega_{pe}t/2\pi \sim 55$ the time of final saturation, the mean electron drift velocity nearly goes to zero. The electron phase space holes are thus almost stationary, resulting in strong interaction with the surrounding ions.

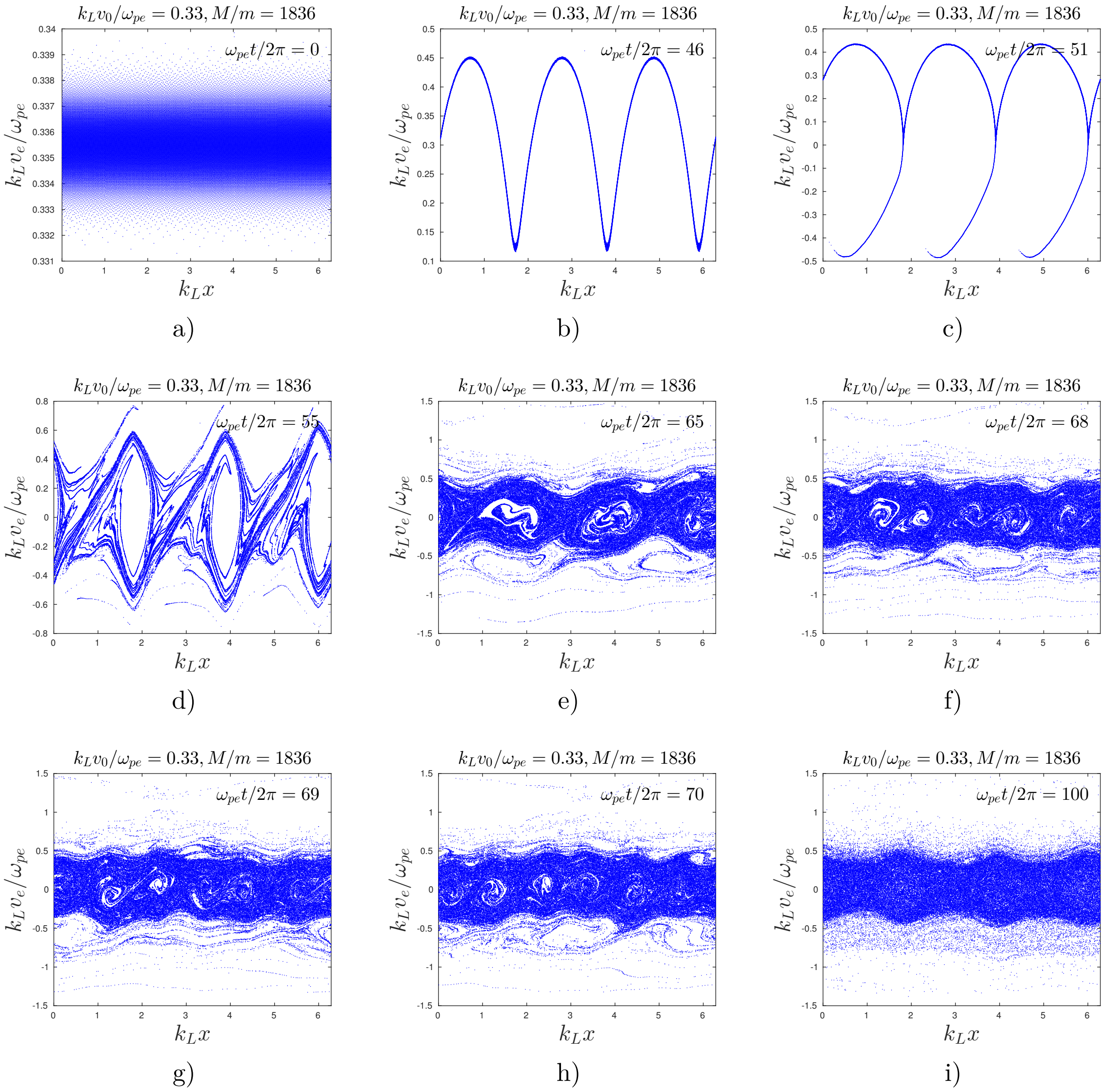

Figure 5.12: Evolution of electron phase space at the different stages of simulation for $k_L v_0/\omega_{pe} \approx 0.33$ and M/m = 1836.

This strong interaction of the electron phase space holes with the surrounding ions exhibits very interesting dynamics involving both electrons and ions. To begin with, the positive potential associated with an electron phase space hole starts reflecting the surrounding ions causing compression in the ion fluid on both sides of the electron hole. This compression induces ion pulses close to the edges of the electron hole which in turn pulls electrons from the edges resulting in disruption of the hole itself. As a consequence, each electron hole (mother hole) is elongated and gets divided into two holes (daughter holes; see time frames between $\omega_{pe}t/2\pi \sim 65 - 70$ in Figure (5.12)).

The resulting daughter holes which are accompanied by ion pulses start propagating in directions opposite to each other. Each of these new coherent structure thus formed, is a combination of an electron hole and an ion pulse. Below we identify them as coupled hole-soliton (CHS) as described by Saeki at. al. [89, 46]. For a better visualization of the entire process of breaking of electron phase holes into daughter holes ultimately leading to the formation of coupled hole-solitons, we present the electron phase space, the ion phase space and the associated potential profile, at various time steps for a different initial electron drift velocity ($k_Lv_0/\omega_{pe} \sim 0.5$; see figure 5.13).

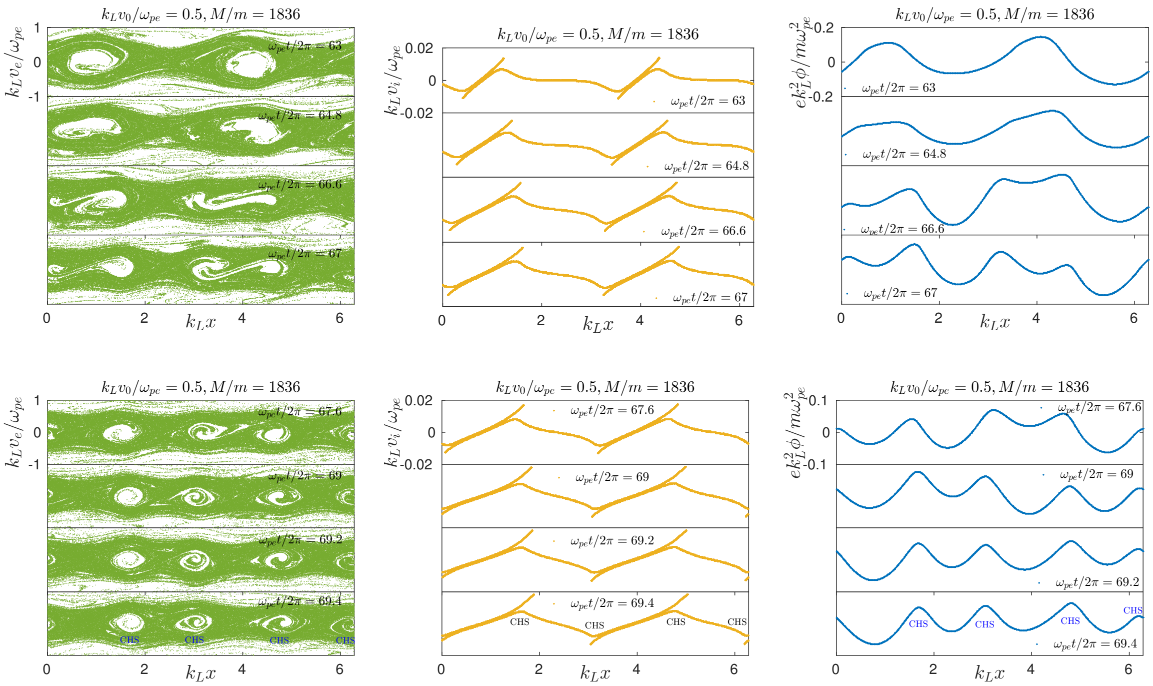

Figure 5.13: Breaking of electron hole and generation of CHS for $k_Lv_0/\omega_{pe} \approx 0.5$ and M/m = 1836.

Figure (5.13) shows evolution of electron phase space and ion phase space along with the potential profile at different instances, for $k_Lv_0/\omega_{pe} \sim 0.5$ and $M/m = 1836$. At $\omega_{pe}t/2\pi \approx 63.0$ the electron phase space shows two holes corresponding to the most unstable wave number, which in this case is $k/k_L = 2$. These phase space holes are nearly stationary. As time progresses, the dynamics described in the previous paragraph is seen, *i.e.* each hole interacts with the surrounding ions, becomes elongated and eventually breaks into two holes which start propagating in opposite directions (see time frames between $\omega_{pe}t/2\pi = 63 - 67.6$ in figure (5.13)). The associated potential profile also evolves starting from two peaks at $\omega_{pe}t/2\pi \sim 63.0$ (corresponding to mother holes) to four peaks at $\omega_{pe}t/2\pi \sim 67.6$ (corresponding to daughter holes). As mentioned above, each daughter hole is accompanied by an ion pulse and the resultant coherent structures propagate in opposite directions (see time frames between $\omega_{pe}t/2\pi = 67.6 - 69.4$ in figure (5.13)). We now compare the relation between the measured speed (Mach number M) and the associated potential maximum (ϕ_{max}) for a daughter hole having phase space area (S) with the theoretical relation amongst the same quantities for coupled hole solitons as proposed by Saeki et. al. [46]. According to the model proposed by Saeki et. al. [46] the phase space area (S) of a coupled hole-soliton is related to the associated potential maximum ϕ_{max} and its speed (Mach no. $\mathcal{M}$), through the integral

$$S = 4\int_{W_0^2/2}^{\phi_{max}} \left(\frac{-W_0^2 + 2\phi}{-2V(\phi, \mathcal{M}, W_0, \alpha)}\right)^{1/2} d\phi \tag{5.19}$$

where S is normalized to $(k_L\lambda_D)^2$ and ϕ_{max} is the normalized maximum potential $e\phi_{max}/T_e$. α^2 is the electron to ion mass ratio (m/M) and W_0 is a parameter which is related to ϕ_{max}, $\mathcal{M}$ and α through the equation $V(\phi_{max}, \mathcal{M}, W_0, \alpha) = 0$, where $V(\phi, \mathcal{M}, W_0, \alpha)$ is the Sagdeev potential which is given by the expression

$$\begin{aligned} V(\phi, \mathcal{M}, W_0, \alpha) = -\frac{1}{6}\{[(1-\alpha\mathcal{M})^2 + 2\phi]^{3/2} + [(1+\alpha\mathcal{M})^2 + 2\phi]^{3/2} - (1-\alpha\mathcal{M})^3 \\ -(1+\alpha\mathcal{M})^3\} + \frac{1}{3}\theta(-W_0^2 + 2\phi)[-W_0^2 + 2\phi]^{3/2} + \mathcal{M}[\mathcal{M} - (\mathcal{M}^2 - 2\phi)^{1/2}] \end{aligned} \tag{5.20}$$

Saeki's [46] model for coupled hole-solitons is based on water bag distribution for electrons where the velocity distribution at the position of the hole vanishes. The electron velocity distribution function measured around the holes (shown in red and blue in figure (5.14a)), is shown in figure (5.14b); it shows a reasonable approximation to the theoretical distribution.

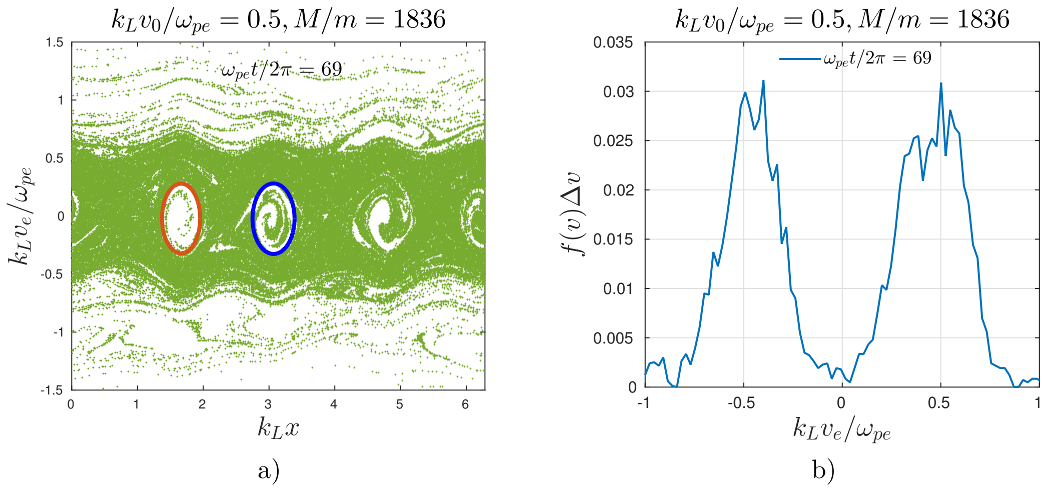

Figure 5.14: Electron distribution function for a CHS which closely resembles to the water bag distribution.

The measured phase space area S is similar for the red and blue holes and is around $\sim$ 1.9. The respective Mach numbers and the potential maximum are $\mathcal{M} \approx 2.01$, $\phi_{max} \approx 0.47$ and $\mathcal{M} \approx 3.1$, $\phi_{max} \approx 0.342$. These points (shown in red and blue dots) lie very well on the continuous $\phi_{max} - \mathcal{M}$ curve generated for $S \approx 1.9$ using Saeki's [46] theory (equation (5.19) and (5.20), figure 5.15). The black dot shown in the same figure (Fig. 5.15) is for another coupled hole soliton ($S \approx 3.4$) which is excited using a different set of initial conditions ($k_L v_0/\omega_{pe} \sim 1$ and $M/m = 1836$); thus our simulation results show good agreement with the theory of coupled hole solitons.

After final saturation electrostatic field energy density decreases sharply (see figure (5.6) which is plotted for $M/m = 1836$ with different initial electron drift velocities) and exhibits oscillatory behaviour with a frequency which is approximately twice the ion plasma frequency. Decrease in electrostatic field energy is accompanied by stretching of phase space holes, formation of coupled hole solitons (as described above) and finally detrapping of electrons. This trapping and detrapping of electrons

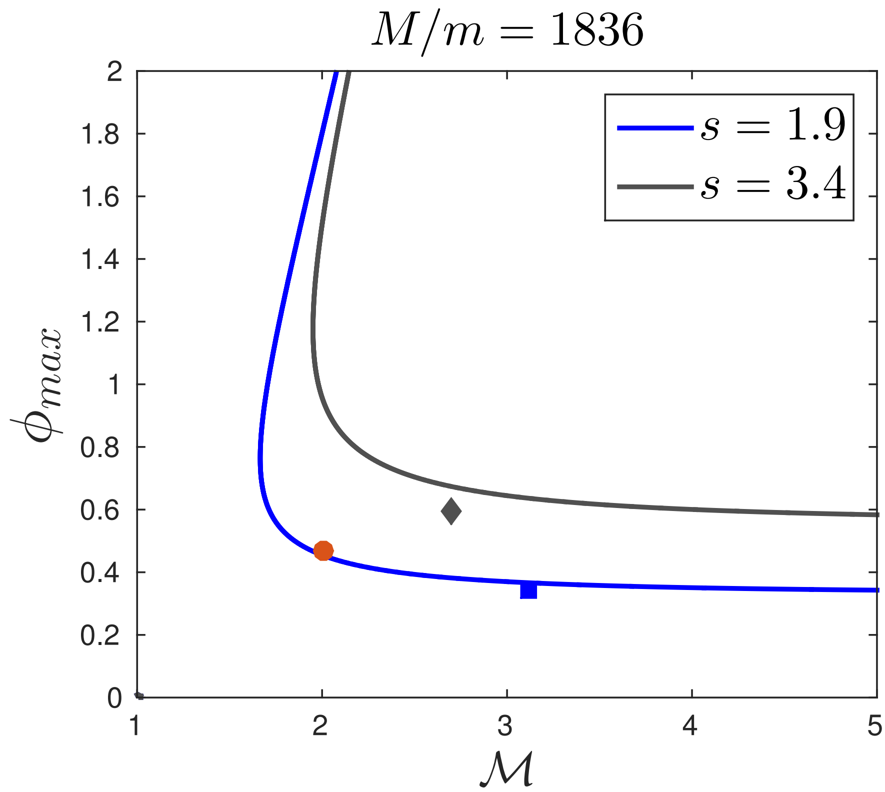

Figure 5.15: Theoretical $\mathcal{M} - \phi_{max}$ curve for the mass ratio M/m = 1836. Lines show theoretical relation for a fixed area of the CHS while dots are taken from simulation.

results in heating of electrons at late times $\omega_{pe}t/2\pi \sim 100$ through the process of separatrix crossing, as discussed in Che et. al., [109]. At around $\omega_{pe}t/2\pi \approx 100$ electron phase space holes coalesce away. Figure (5.16) shows the spatially averaged electron distribution function at different times which clearly show broadening of distribution function at late times.

5.5 Summary

In this chapter, we have studied spatio-temporal evolution of Buneman instability using an in-house developed 1-D particle-in-cell simulation code. Quasilinear saturation (or first saturation) occurs when the electrostatic energy density becomes $\sim (m/M)^{1/3}$ times the initial drift kinetic energy density, *i.e.* $\sum_k |E_k|^2/16\pi \approx (m/M)^{(1/3)} W_0$; the ratio of electrostatic field energy density to the initial drift kinetic energy density at

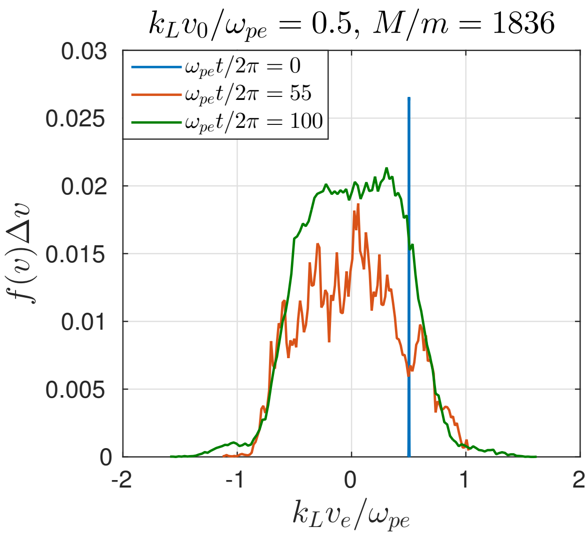

Figure 5.16: Evolution of electron distribution function at the time $\omega_{pe}t/2\pi \approx 0$, 55 and 100 for $k_L v_0/\omega_{pe} \approx 0.5$ and M/m = 1836.

the quasilinear saturation point is independent of the initial drift velocity. Further, electron trapping and nonlinear mode coupling leads to the final saturation of the instability. In contrast to quasilinear saturation, at the final saturation the ratio of electrostatic field energy density to initial kinetic energy density depends on the initial drift velocity but is independent of the mass ratio. The above mentioned ratio follows the inequality suggested by Ishihara et. al. [41], *i.e.*, $\sum_k \frac{|E_k|^2}{8\pi W_0} \geq 0.11$. To the best of our knowledge, this is the first verification of Hirose's [39] and Ishihara's [41, 42] results using a PIC code.

After final quenching of Buneman instability, strong interaction between electron phase space holes and surrounding ions is observed; this interaction breaks the electron phase space holes into two oppositely propagating holes each attached with an ion pulse. These oppositely propagating coherent structures have been identified as coupled hole-solitons using the theory of Saeki et. al. [46]. These coupled hole solitons eventually coalesce away finally generating a broadened electron velocity distribution function.

CHAPTER 6

Quasilinear evolution of relativistic Buneman instability

In this chapter, spatio-temporal evolution of the relativistic Buneman instability has been investigated in one dimension using an in-house developed particle-in-cell simulation code. Starting from the excitation of the instability, its evolution has been followed numerically till its quenching and beyond. The simulation results have been quantitatively compared with fluid theory and are found to be in conformity with the well known fact that the maximum growth rate (γ_{max}) reduces due to relativistic effects and varies with γ_{e0} and m/M as $\gamma_{max} \sim \frac{\sqrt{3}}{2\sqrt{\gamma_{e0}}}(\frac{m}{2M})^{1/3}$, where γ_{e0} is the Lorentz factor associated with the initial electron drift velocity (v_0) and (m/M) is the electron to ion mass ratio. Further it is observed that in contrast to the non-relativistic results [39] at the saturation point, ratio of electrostatic field energy density ($\sum_k |E_k|^2/8\pi$) to initial drift kinetic energy density (W_0) scales with γ_{e0} as $\sim 1/\gamma_{e0}^2$. This novel result on scaling of energy densities have been found to be in quantitative agreement *with the scaling derived using fluid theory.*

In the previous chapter, we studied spatio-temporal evolution of Buneman instability, when electron beam is propagating with the non-relativistic velocities. However, when electron beam propagates with relativistic velocities, dynamics of Buneman instability (relativistic Buneman instability) is affected strongly. In this chapter, we study spatio-temporal evolution of Buneman instability in weakly relativistic regime. In section 6.1, we give a thorough introduction to the problem along with the parameter domain, where Buneman/Buneman like modes dominate the evolution of the system [10] . In section 6.2, we present the dispersion relation for relativistic Buneman instability in the weakly relativistic limit; section 6.2.1 presents an estimate of the maximum growth rate and its comparison with the numerical solution of the dispersion relation. In section 6.3, we give a brief description of the particle-in-cell simulation scheme. Section 6.4, contains a presentation and discussion of our results on evolution and quasilinear saturation of relativistic Buneman instability. Finally we end our chapter with a summary of our results in section 6.5.

6.1 Introduction

A current carrying plasma constitutes an ideal laboratory for investigating various kind of streaming instabilities associated with a relativistic electron beam-plasma system *viz.* Buneman, Two stream, Filamentation, Weibel and Oblique modes [9, 111, 8, 10, 12, 11, 112, 113, 114]. The unstable mode spectrum associated with an electron beam-plasma system can be broadly classified into electrostatic (longitudinal) and electromagnetic (transverse) modes. Depending on the orientation of the wave vector with respect to electron beam velocity direction ($\vec{k} \cdot \vec{v_b}$), ratio of beam to plasma electron density($\alpha = n_b/n_p$), Lorentz factor associated with beam (γ_b) and electron to ion mass ratio (m/M), several of the above mentioned instabilities could be excited, but dominant one governs the dynamics in the linear phase. In the flow-aligned direction Buneman and two stream instabilities govern the evolution of the system whereas in the transverse direction evolution is governed by filamentation and/or Weibel instabilities. In a plasma with thermal anisotropy Weibel and filamentation mode can be triggered separately [67] and which may sometime merge and interact [8, 69]. Also there exists a continuum spectrum of unstable oblique modes which bridges the gap between parallel and transverse modes. A detailed discussion of the growth rate of various instabilities and their dependence on the parameters $(\vec{k} \cdot \vec{v_b})$, $\alpha = n_b/n_p$, γ_b and m/M is given in references [9, 111, 8, 10, 12, 11]. It turns out that in the dilute beam ($\alpha \ll 1$) and large γ_b limit ($\gamma_b \geq \alpha \frac{M}{m}$), Buneman/Buneman like modes dominate the evolution of relativistic electron beam-plasma system [8, 10, 12]. The simplest way in which electrostatic Buneman [60] instability gets excited is when all the plasma electrons drift as a whole and the relative drift velocity between the electrons and ions exceeds the electron thermal velocity. It is associated with novel physical effects like anomalous resitivity [39, 115, 116], double layer formation [28, 29] etc. Buneman instability is of importance in many laboratory plasma experiments with intense parallel electric fields (such as in turbulent tokamaks) [30, 31, 106] and in astrophysical situations with relativistic jets [117]. Recent interest in studying space time evolution and eventual saturation of Buneman instability is due to its application to a number of physical scenario's of practical interest *viz.* laser driven ion acceleration[6, 7], strong double layer formation [28, 29], acceleration of charged particles [5, 34, 35, 105] etc.

Since the pioneering work of Oscar Buneman [60, 26] a lot of work has been done to understand the linear and nonlinear evolution of Buneman instability[82, 83, 39, 41, 42, 51, 52, 86, 85, 107, 87, 108, 88, 109, 91, 90] in the non-relativistic regime [118]. Saturation of Buneman instability in the non-relativistic regime has also been studied by numerous authors [82, 83, 39]. Hirose[39] reported that quasilinear saturation of Buneman instability occurs when the ratio of electrostatic energy density$(\sum_k |E_k|^2/8\pi)$

to initial drift kinetic energy density W_0 reaches up to $\approx 2(m/M)^{(1/3)}$. Using quasilinear theory, Ishihara et. al. [41] derived a nonlinear dispersion relation which they verified by performing a 1-D Vlasov simulation. They further reported that quasilinear saturation of the Buneman instability in non-relativistic regime is consistent with the Hirose's [39] scaling.

Recently some authors have attempted to understand the mechanism of Buneman instability in the relativistic regime. Using particle-in-cell simulation, Yin et. al. [6] have found a new laser driven ion-acceleration mechanism *viz.* laser break-out afterburner (BOA) for production of mono-energetic ion beams in the Gev energy regime. The underlying mechanism of production of such energetic ion beams has been attributed to relativistic Buneman instability. This has been further confirmed by Albright et. al. [7] by matching the results of numerical solution of dispersion relation for relativistic Buneman instability with the modes found from BOA simulation. References [34, 35, 105] have investigated the acceleration of electrons via their interaction with electrostatic waves, driven by the relativistic Buneman instability, in a system dominated by counter-propagating proton beams. Haas[53] et. al. has investigated quantum relativistic Buneman instability using a Klein-Gordon model for the electrons and cold ions. Recently Hashemzadeh et. al. [54] have carried out 1-D particle-in-cell simulation of relativistic Buneman instability in a current carrying plasma. Their simulations show that with increase in initial electron drift velocity the growth rate of Buneman instability decreases. Although this is expected from a fluid model, a detailed comparison of the characteristics of the instability with the fluid model has not been reported. The above discussion indicates that there has been some work on relativistic Buneman instability in the recent past, but to the best of our knowledge, investigation of its evolution and saturation using particle-in-cell simulation method, and a detailed comparison of the simulation results with a fluid model has not been attempted so far.

6.2 Derivation of Linear Dispersion Relation

In this section we present a derivation of linear dispersion relation for relativistic Buneman instability. Consider a cold relativistic electron beam of density n_0 and velocity v_0 propagating through a homogeneous background of ions of density n_0. Buneman instability occurs when relative drift velocity between electron and ion is sufficiently larger than electron thermal velocity *i.e.* $v_0 \gg v_{th,e}$. The basic equation governing the space-time evolution of Buneman instability in 1D are as follows.
The continuity equation for electrons and ions

$$\frac{\partial n_s}{\partial t} + \frac{\partial (n_s v_s)}{\partial x} = 0 \tag{6.1}$$

The relativistic momentum equation for electrons and ions

$$\frac{\partial p_s}{\partial t} + v_s \frac{\partial (p_s)}{\partial x} = q_s E \tag{6.2}$$

and the Poisson equation

$$\frac{\partial E}{\partial x} = 4\pi e(n_i - n_e) \tag{6.3}$$

where s stands for the species(electron and ion) and $p_s = \frac{m_s v_s}{\sqrt{1 - (\frac{v_s}{c})^2}}$ is the relativistic momentum for species s. Here we use $m_e = m$; $q_e = -e$ and $m_i = M$; $q_i = e$ as the rest mass and electrostatic charge of electron and ion respectively; other symbols have their usual meaning.

For electrons linearized continuity and momentum equation becomes

$$-\iota\omega\delta n_{ex} + \iota k n_0 \delta v_{ex} + \iota k v_0 \delta n_{ex} = 0 \tag{6.4}$$

$$\gamma_{e0}^3(-\iota\omega\delta v_{ex} + \iota k v_0 \delta v_{ex}) = -\frac{eE}{m} \tag{6.5}$$

where γ_{e0} is a Lorentz factor associated with the initial electron drift velocity. Eliminating δv_{ex} from equation (6.4) and (6.5), perturbed electron density is

$$\delta n_{ex} = \frac{-\iota e}{m\gamma_{e0}^3(\omega - kv_0)^2}E \tag{6.6}$$

Again linearized continuity and momentum equation for ions can be written as

$$-\iota\omega\delta n_{ix} + \iota k n_0 \delta v_{ix} = 0 \tag{6.7}$$

$$-\iota\omega\delta v_{ix} = \frac{eE}{M} \tag{6.8}$$

eliminating δv_{ix} from equation (6.7) and (6.8), gives linearized perturbed ion density as

$$\delta n_{ix} = \frac{\iota e k n_0}{M\omega^2}E \tag{6.9}$$

Substituting from equation (6.6) and (6.9), Poisson equation gives

$$\iota k E = 4\pi(\delta n_{ix} - \delta n_{ex}) \tag{6.10}$$

Using equation (6.6),(6.9) and (6.10), we get the dispersion relation for Buneman instability in the weakly relativistic limit as

$$1 = \frac{\omega_{pi}^2}{\omega^2} + \frac{\omega_{pe}^2}{\gamma_{e0}^3(\omega - kv_0)^2} \tag{6.11}$$

where k is the wave number, $\omega_{pi} = \sqrt{\dfrac{4\pi n_0 e^2}{M}}$ and $\omega_{pe} = \sqrt{\dfrac{4\pi n_0 e^2}{m}}$ are ion and electron plasma frequency respectively.

6.2.1 Estimation of the growth rate of the instability

Equation (6.11) is a fourth order polynomial equation in ω. The growth rate of the relativistic Buneman instability is given by the complex root of the equation (6.11) with positive imaginary part. We first give an approximate estimate of the growth rate and then compare it with that obtained using direct numerical solution of the dispersion relation. Following Haas et. al.[53] we use the resonant condition $kv_0 \approx \frac{\omega_{pe}}{\gamma_{e0}^{3/2}}$; substituting this condition in the dispersion relation and using $\omega \ll kv_0$, leads to the following cubic equation in ω.

$$\omega^3 = -\frac{m}{2M}{\gamma_{e0}}^{-3/2}\omega_{pe}^3 \tag{6.12}$$

Two complex roots of cubic equation can be written as

$$\omega = \frac{(1 \pm \iota\sqrt{3})}{\sqrt{\gamma_{e0}}}\left(\frac{m}{16M}\right)^{1/3}\omega_{pe} \tag{6.13}$$

The positive sign gives the growth rate of the most unstable mode as

$$\gamma_{max} = \frac{\sqrt{3}}{\sqrt{\gamma_{e0}}}\left(\frac{m}{16M}\right)^{1/3}\omega_{pe} \tag{6.14}$$

Here $\gamma_{e0}^{-1/2}$ is a relativistic correction to the growth rate which explicitly shows that as γ_{e0} increases, growth rate decreases. Most unstable k mode depends on the initial drift velocity, for example, for $k_Lc/\omega_{pe} \approx 1$ to be the most unstable mode, initial electron drift velocity turns out to be $v_0/c \approx 0.65586$. Table 6.1 shows the comparison between estimated (using equation (6.14)) and numerically calculated growth rate, for the most unstable mode *i.e.* $k_Lc/\omega_{pe} \approx 1$. Good matching is seen between growth rate, estimated using resonance condition (equation (6.14)) and the growth rate obtained from numerical solution of dispersion relation.

The physics underlying the resonance condition may be illustrated as follows; When

Table 6.1: Table shows comparison between estimated and numerically calculated growth rate

M/m	$\frac{\sqrt{3}}{\sqrt{\gamma_{e0}}}\left(\frac{m}{16M}\right)^{1/3}\omega_{pe}$	Numerical solution
1836	0.04855	0.04664
5×1836	0.0247	0.0278
10×1836	0.02258	0.02214
20×1836	0.0156	0.1553
40×1836	0.01422	0.01405

electrons and ions are perturbed longitudinally by very small(linear) perturbation($\propto \exp^{\iota(kx-\omega t)}$), both species start to oscillates around their mean position with the frequency $\tilde{\omega}_{pe}$ and ω_{pi} in their respective frame of reference, where $\tilde{\omega}_{pe} = \frac{\omega_{pe}}{\gamma_{e0}^{3/2}}$ is the relativistically correct electron plasma frequency and ω_{pi} is ion plasma frequency. The Doppler shifted electron plasma oscillation can resonate with ion plasma oscillation ($\tilde{\omega}_{pe} - kv_0 \approx \omega_{pi}$); in the limit of heavier ions ($\frac{\omega_{pi}}{\omega_{pe}} \to 0$), this leads to the resonance condition as $kv_0 \approx \frac{\omega_{pe}}{\gamma_{e0}^{3/2}}$; This resonance can make ions unstable at the expense of electron drift kinetic energy and this instability is called Buneman instability. Since we get the resonance condition in the limit of heavier ions so the growth rate estimated using equation (6.14) and the one calculated numerically come closer as the mass ratio increases.

6.3 Method of solution

The basic set of equations, required to study the evolution of relativistic Buneman instability in 1-D, using a particle-in-cell code[96], are the momentum and Poisson's equation. Ions are assumed to be at rest to begin with, and provide a neutralizing background while all the electrons are flowing with a single velocity v_0. The governing equations in normalized form are

$$\frac{dx}{dt} = v_s(x,t) \tag{6.15}$$

$$\frac{d\gamma_s v_s}{dt} = \pm E(x,t) \tag{6.16}$$

$$\frac{\partial E}{\partial x} = (n_i - n_e) \tag{6.17}$$

All physical quantities are used in normalized units. The normalization used are $k \rightarrow k_L x$, $t \rightarrow t\omega_{pe}$, $v \rightarrow k_L v/\omega_{pe}$, $n_s \rightarrow n_s/n_0$, $E \rightarrow \frac{ek_L E}{m\omega_{pe}^2}$, where k_L is the wave number corresponding to the longest wavelength, which is the system length. Here γ_s is a Lorentz factor and s denotes the species electrons/ions.

Parameters used in the numerical experiment of relativistic Buneman instability are written in table 6.2. System length is divided into 1024 equidistant cells; field quantities *viz.* electric field and particle density are calculated at the cell center(grid points) and particle quantities like velocities are calculated at particle positions. Each species has 102400 particles spread within 1024 grid cells, so each cell contain 100 particles. Periodic boundary conditions are used that allows only integer mode numbers as k = 1,2,3...512 in the system. Time step is taken to be $\Delta t = 0.0196349\omega_{pe}^{-1}$ (Δt is chosen such that $\omega_{pe}\Delta t \ll 1$; we have chosen 320 time steps in a plasma period). A small thermal spread $v_{th,e}/v_0 = 3 \times 10^{-4}$ is given to the electron beam in order to avoid nonphysical cold beam instability [96]. Plasma is cold($v_{th,e}/v_0 \approx 0.0003$) with a very small thermal spread that fulfills the necessary condition $v_{drift} \gg v_{thermal}$, so system has favorable condition to excite Buneman instability.

In this simulation we have followed ion and electron trajectories in the self consistently generated electric field. Initially electrons and ions are placed in phase space. For a given ion and electron density, electric field is calculated on the grid points by solving Poisson's equation. Using this electric field, force is calculated on the grid points; this force is then interpolated on the particle positions. Then ion and electron momentum equations are solved using this force that yields new position and velocity. This new particle position is weighted on the grid points to evaluate density over the grid points using second order polynomial interpolation scheme

Table 6.2: List of physical parameters used in our simulations.

Parameter	Symbol	Value
No of grid points	NG	1024
System Length	L	2π
Time step	Δt	$0.0196349\,\omega_{pe}^{-1}$
Grid Spacing	$k_L \Delta x$	L/NG = 0.006
Total no of electron	N_e	102400
Total no of ion	N_i	102400
Mass ratio	M/m	500, 1000, 1836, 18360
Electron Plasma Frequency	ω_{pe}	1
Ion Plasma Frequency	ω_{pi}	$(m/M)^{1/2}\,\omega_{pe}^{-1}$
Initial electron drift velocity	$k_L v_0/\omega_{pe}$	0.1, 0.31, 0.66
Initial ion drift velocity	$k_L v_{i0}/\omega_{pe}$	0.0
Electron thermal velocity	$v_{th,e}/v_0$	0.003
Ion thermal velocity	$v_{th,i}/v_0$	0.0

which is further used to calculate the new force. This process is then repeated for thousands of time steps.

6.4 Results and Discussion

In this section we present results carried out using 1D particle-in-cell simulation code. Section 6.4.1 presents the discussion on quasilinear evolution of relativistic Buneman instability and section 6.4.2 contains discussion about quasilinear saturation of relativistic Buneman instability.

6.4.1 Evolution of relativistic Buneman instability

We start our simulation when the plasma is in equilibrium *i.e.* electrons are flowing with a single velocity, like a cold electron beam (delta function distribution) with respect to a uniform homogeneous background of ions, resulting in an uniform electron current to begin with. Specifically the initial conditions of our PIC simulation may be described as

$$n_e(x,0) = n_0 \qquad n_i(x,0) = n_0 \qquad k_L v_e(x,0)/\omega_{pe} = v_0/c \qquad k_L v_i(x,0)/\omega_{pe} = 0$$

As time progresses, small amplitude electron, ion density and velocity oscillations evolve from background noise. Since the system is unstable and beam energy provides free energy, these small perturbations start to grow at the expense of initial beam kinetic energy density. Different modes grow at different rates.

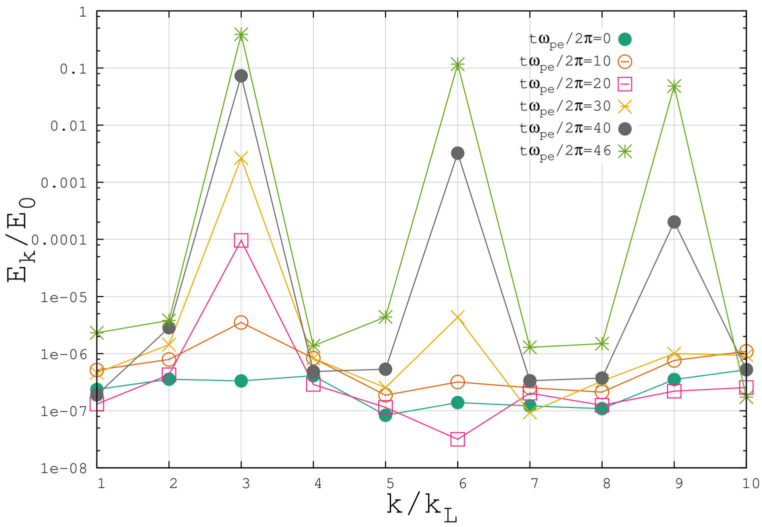

Figure 6.1: Evolution of k spectrum of electric field for the velocity $v_0/c = 0.3105$ ($\gamma_0 = 1.052$) at different time steps.

Figure (6.1,6.2) show evolution of amplitude of electric field in Fourier space for the mass ratio M/m = 1836 and for initial electron drift velocity $v_0/c \approx 0.3105$. For these parameters, the most unstable mode number turns out to be $k/k_L \approx 3$. This can be seen from the resonance condition $kv_0 \approx \frac{\omega_{pe}}{\gamma_{e0}^{3/2}} \implies k/k_L \approx 3$. As expected it is observed that the most unstable growing mode supported by the system grows faster than the other modes. Temporal evolution of different Fourier modes is shown in figure (6.2). The black line shows the evolution of the most unstable mode and, green and brown lines respectively show the evolution of the first and second harmonic of the most unstable mode. Growth rates are obtained by measuring the slope of the curves in Fig. 6.2 from initial stage of the instability to quasilinear saturation. Around $\omega_{pe}t/2\pi \approx 4$, the most unstable mode ($k/k_L = 3$) starts to evolve with growth rate $\gamma_{max} \approx 0.0529\omega_{pe}$. It is observed that higher harmonics ($2k/k_L$ & $3k/k_L$) of the most unstable mode ($k/k_L = 3$) appear at later times ($\omega_{pe}t/2\pi \approx 25$ and 35

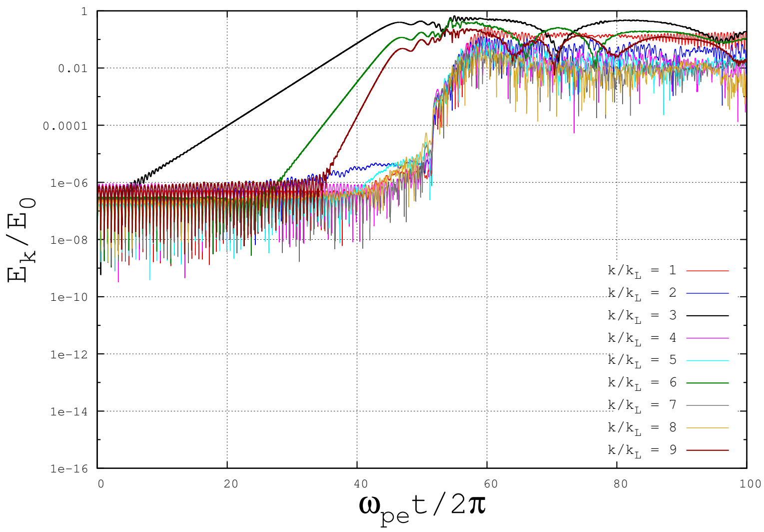

Figure 6.2: Temporal evolution of k^{th} mode of electric field for the velocity $v_0/c = 0.3105$ ($\gamma_0 = 1.052$).

respectively) and are found to grow at twice and thrice the growth rate of the most unstable mode. For the above parameters linear growth of relativistic Buneman instability saturates at $\omega_{pe}t/2\pi \approx 46.6$.

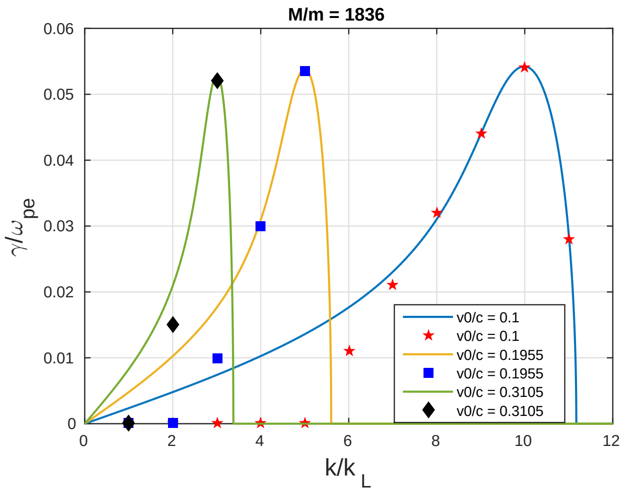

Figure 6.3: Comparison between theory and simulation dispersion relation. Here line curves shows numerical solution of dispersion relation and dots shows growth rate taken from simulation

Figure (6.3) shows the growth rate (γ/ω_{pe}) as a function of mode number for different initial electron drift velocities and for a fixed electron to ion mass ratio. The continuous lines are obtained by numerically solving the dispersion relation (equation (6.11)) and the dots represent the simulation points; which shows a reasonably good match between theory and simulation. We see that range of unstable mode numbers increases as the initial electron drift velocity decreases. It is also clear from figure (6.3) that with the increase in velocity (relativistic effects), the peak growth rate (growth rate corresponding to the most unstable mode) reduces for a fixed electron to ion mass ratio (m/M). This is in contrast to the non-relativistic result where the maximum growth rate corresponding to the most unstable mode number is independent of the initial electron beam drift velocity. Figure (6.4) shows the variation of maximum growth rate with electron to ion mass ratio for different initial electron drift velocities. It is observed that the maximum growth rate (γ_{max}/ω_{pe}) varies linearly with $(m/M)^{(1/3)}$ and decreases with increasing $v_0(\gamma_{e0})$ is conformity with equation (6.14). Thus the above results show that relativistic effects have a stabilizing influence on the Buneman instability.

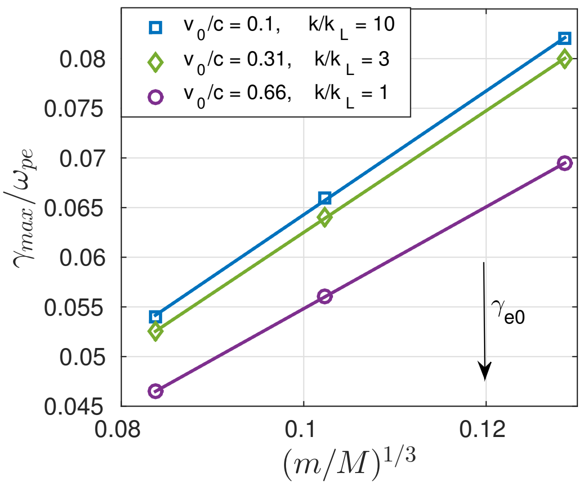

Figure 6.4: Comparison of growth rate for different velocity with mass ratios from left to right M/m = 1836, 1000 and 500.

As mentioned in the last paragraph with the increase in initial electron drift velocity, growth rate decreases due to relativistic effects, so saturation time of instability increases. Figure (6.5) and (6.6) respectively show the temporal evolution of the electrostatic field energy for different initial electron drift velocity $v_0/c \approx 0.1$, 0.3105, 0.66 for two different mass ratios M/m = 500 and 1836. These figures clearly show that as the initial electron drift velocity increases, the saturation time also increases. This is in contrast to the non-relativistic case, where the saturation time is independent of the initial electron drift velocity, and depends only on the electron to ion mass ratio (m/M). Using the saturation time for the non-relativistic [44] case and taking $t_{sat} \sim 1/\gamma_{max}$, we may estimate the saturation time in the relativistic case, for a fixed mass ratio (m/M) and for different initial electron drift velocities as $t_{sat}^{rel} \approx (1 + \Delta\gamma/\gamma_{max}^{rel}) t_{sat}^{non-rel}$, where t_{sat}^{rel} and $t_{sat}^{non-rel}$ are the saturation times of Buneman instability for the relativistic and non-relativistic case respectively and $\Delta\gamma = \gamma_{max}^{non-rel} - \gamma_{max}^{rel}$ is the difference in growth rate of the most unstable mode in the non-relativistic and relativistic case. For example, for mass ratio M/m = 1836 and for initial electron drift velocity ($v_0/c = 0.3105$), the growth of the most unstable mode (in the case $k/k_L \approx 3$) in the non-relativistic case is $\gamma_{max}^{non-rel}/\omega_{pe} = 0.054$ (This may be estimated either by putting $\gamma_{e0} = 1$ in the relativistic dispersion relation; or by performing 1-D non-relativistic particle-in-cell simulation (see section 5.4.1)) and $t_{sat}^{non-rel}\omega_{pe}/2\pi \approx 44.46$. For the above parameters, the growth rate in the relativistic case turns out as $\gamma_{max}^{rel}/\omega_{pe} \approx 0.0525$ (estimated using equation (6.14)). Thus the estimated saturation time in the relativistic case is $t_{sat}^{rel}\omega_{pe}/2\pi \approx 45.73$ which is close to that observed in simulations (figure 6.5b). Similar estimates of t_{sat}^{rel} can be made for other initial electron drift velocities and mass ratios which also show a good match with that observed in simulation.

6.4.2 Quasilinear Saturation of the Instability

Quasilinear saturation of the Buneman instability occurs when the most unstable growing mode saturates along with its harmonics. At the saturation point, electrostatic energy density shows a hiccup as shown in the figure (6.5) and (6.6) (see inset), this hiccup represents the breaking of exponential growth or linear saturation of the instability.

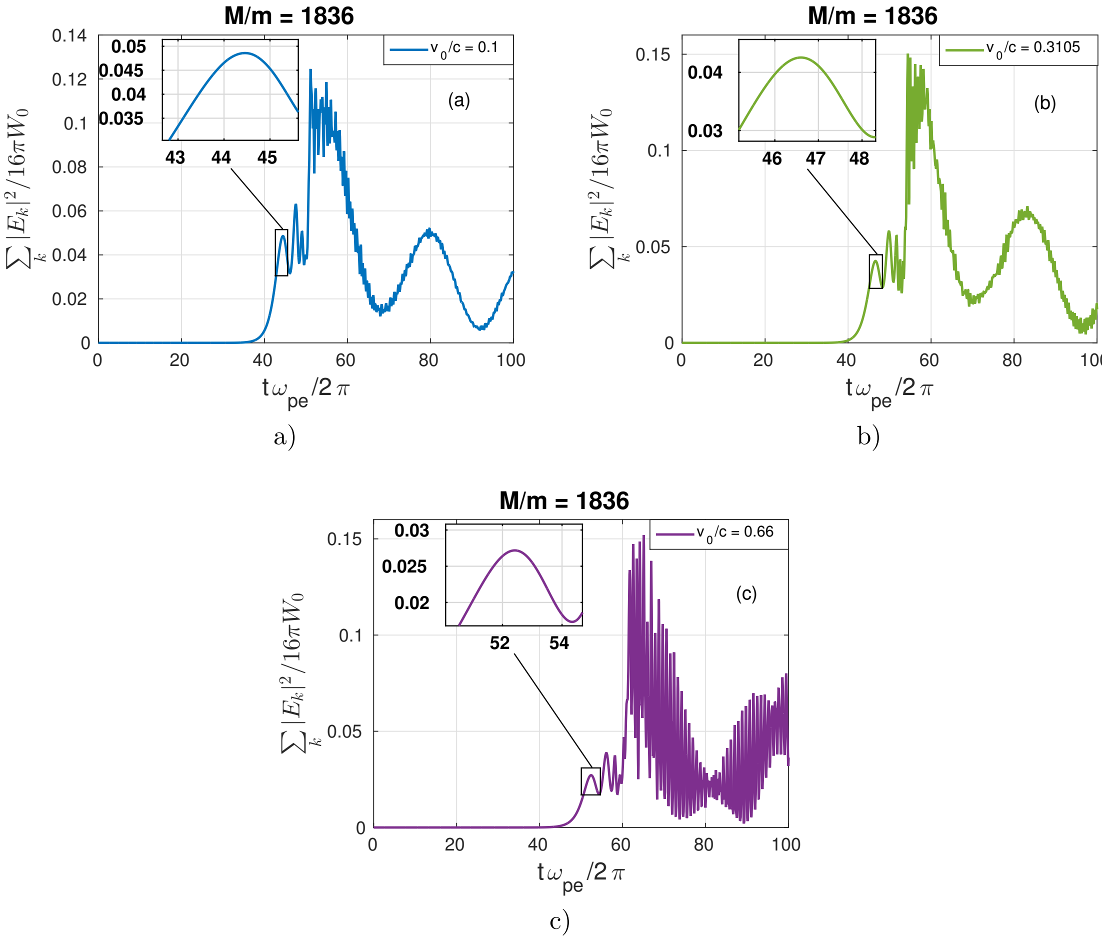

Figure 6.5: Figure shows temporal evolution of $\sum_k |E_k|^2/16\pi W_0$ for different initial drift velocities (6.5a) 0.1 ($\gamma_0 = 1.005$), (6.5b) 0.31 ($\gamma_0 = 1.052$), (6.5c) 0.66 ($\gamma_0 = 1.33$) for mass ratio M/m = 1836.

The scaling of electrostatic field energy density at the saturation point with initial beam kinetic energy density may be derived by an analysis similar to Hirose's [39] for the non-relativistic case. We first reproduce Hirose's [39] argument here for the sake of continuity. Analysis of non-relativistic Buneman instability shows that for a given initial electron drift velocity v_0, the growth rate (γ/ω_{pe}) maximizes at the resonant wave number given by $kv_0 \sim \omega_{pe}$ and sharply drops for small changes in the drift velocity; the width of the γ/ω_{pe} vs kv_0/ω_{pe} curve scales with electron to ion mass ratio as $\Delta(kv_0/\omega_{pe}) \sim (m/M)^{1/3}$. Thus any small change in the electron drift velocity drastically reduces the growth rate resulting in quenching of the instability. This idea has been used by Hirose[39] to estimate the saturated electrostatic field

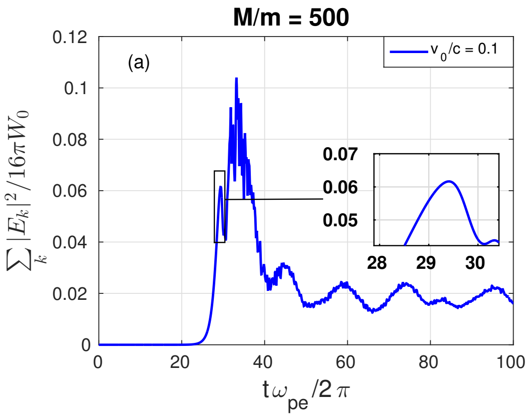

a)

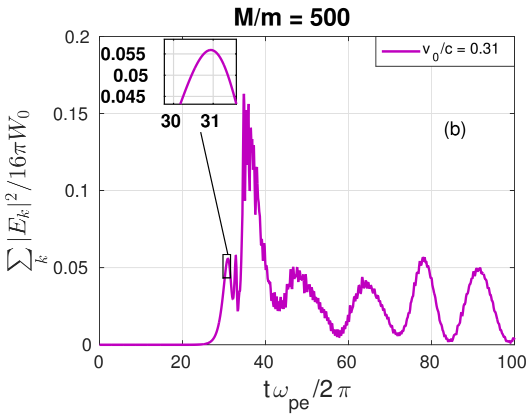

b)

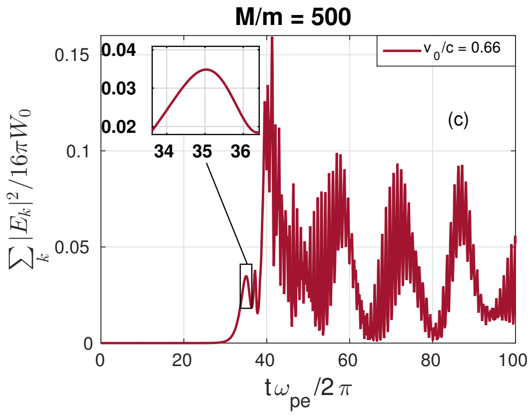

c)

Figure 6.6: Figure shows temporal evolution of $\sum_k |E_k|^2/16\pi W_0$ for different initial drift velocities (6.6a) 0.1 ($\gamma_0 = 1.005$), (6.6b) 0.31 ($\gamma_0 = 1.052$), (6.6c) 0.66 ($\gamma_0 = 1.33$) for mass ratio M/m = 500

energy density for a given initial beam kinetic energy density. Based on a quasi-linear calculation, Hirose [39] has shown that the ratio of $k\Delta v_0/\omega_{pe}$ (where "k" is the resonant wave number and Δv_0 is the difference between the drift velocity at the saturation time and the initial time) and $\Delta(kv_0/\omega_{pe})$ (the width of γ/ω_{pe} vs kv_0/ω_{pe} curve) is given by

$$\frac{k\Delta v_0}{\Delta(kv_0)} \approx \sum_k \frac{|E_k|^2}{16\pi W_0}\left(\frac{M}{m}\right)^{1/3} \approx \frac{\textit{Field energy density}}{\textit{Initial beam kinetic energy density}}\left(\frac{M}{m}\right)^{1/3} \tag{6.18}$$

where W_0 is the initial beam kinetic energy density. In the non-relativistic case Hirose [39] argued that this ratio at the saturation time should be of order unity and therefore the electrostatic field energy density at the saturation point scales linearly with initial beam kinetic energy density, with a slope which depends on electron to ion mass ratio as $(m/M)^{1/3}$ (we have verified this scaling in previous chapter).

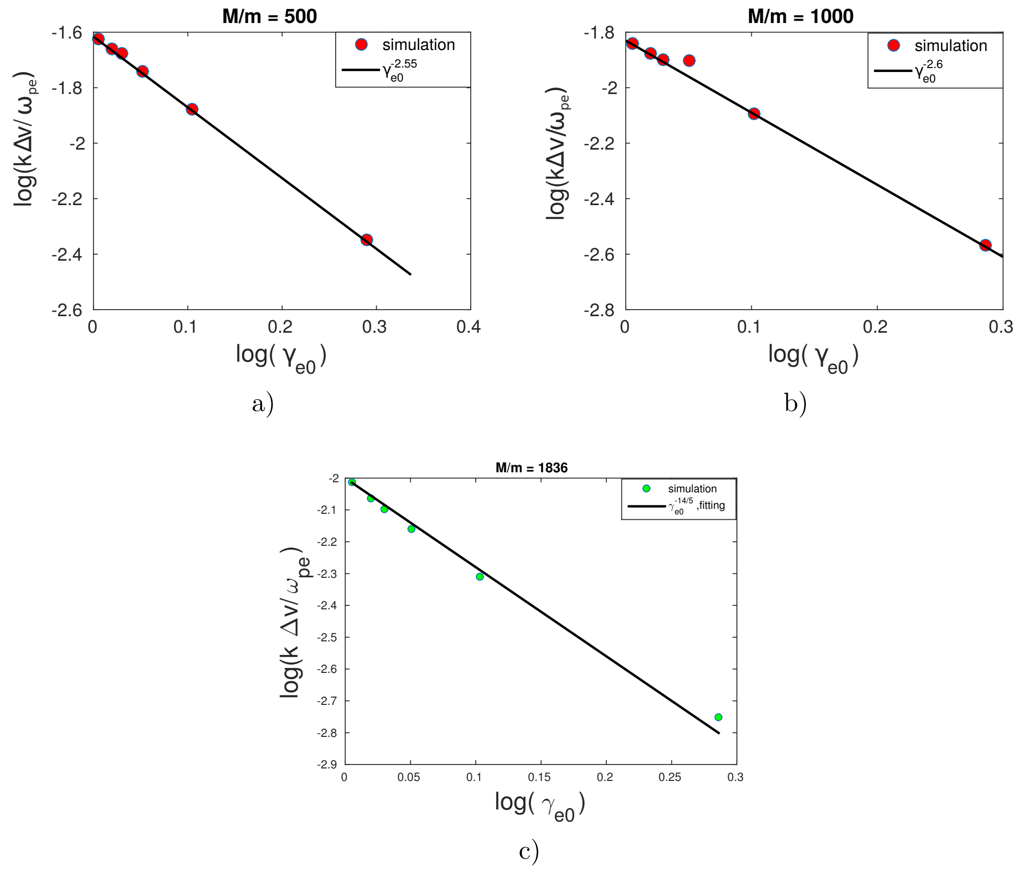

Figure 6.7: Figure shows scaling of $\frac{k\Delta v}{\omega_{pe}}$ with γ_{e0} in log-log plot, it follows (6.7a) $\gamma_{e0}^{-2.55}$ (6.7b) $\gamma_{e0}^{-2.6}$ and (6.7c) $\sim \gamma_{e0}^{-14/5}$ scalings.

Following an argument similar as above, in the relativistic case the growth rate (γ/ω_{pe}) maximizes at the resonant wave number given as $kv_0 \sim \omega_{pe}/\gamma_{e0}^{3/2}$, which also sharply drops for small changes in the drift velocity; the width of the γ/ω_{pe} vs kv_0/ω_{pe} curve may be estimated by replacing electron mass m by $m_{eff} = m\gamma_{e0}^3$ and ω_{pe} by $\omega_{pe}^{'} = \omega_{pe}/\gamma_{e0}^{3/2}$ in the weakly relativistic dispersion relation (equation (6.11)) which leads to $\Delta(kv_0/\omega_{pe}) \sim \frac{1}{\gamma_{e0}^{1/2}}\left(\frac{m}{M}\right)^{1/3}$. Further the change in electron drift velocity at the saturation point may be estimated from the resonance condition as $\frac{k\Delta v_0}{\omega_{pe}} \sim -\frac{3}{2}\frac{1}{\gamma_{e0}^{5/2}}\Delta\gamma_{e0}$ implying that $\frac{k\Delta v_0}{\omega_{pe}}$ scales with relativistic factor γ_{e0} as $\frac{k\Delta v_0}{\omega_{pe}} \sim \frac{1}{\gamma_{e0}^{5/2}} \sim \frac{1}{\gamma_{e0}^{2.5}}$. We have verified this scaling in our simulations. Figure (6.7) shows the variation of $k\Delta v_0/\omega_{pe}$ with γ_{e0} for different mass ratios. The dots represent the points obtained from simulation and the straight line fit shows a scaling as $k\Delta v_0 \sim \frac{1}{\gamma_{e0}^{2.8}}$ (for M/m = 1836, see Fig. 6.7c) which closely agrees with our back-of-the envelope estimate. Therefore the ratio $\frac{k\Delta v_0}{\Delta(kv_0)}$ scales with γ_{e0} as $\frac{k\Delta v_0}{\Delta(kv_0)} \sim \gamma_{e0}^{-2}$. Now assuming Hirose's [39] [equation (6.18)] holds in the weakly relativistic limit, we note that the ratio of electrostatic field energy density at the saturation point to initial electron drift kinetic energy density scales with γ_{e0} as

$$\frac{|E|^2}{16\pi W_0} \sim \frac{k\Delta v_0}{\Delta(kv_0)}\left(\frac{m}{M}\right)^{1/3} \sim \frac{1}{\gamma_{e0}^2}\left(\frac{m}{M}\right)^{1/3} \tag{6.19}$$

We have verified the above scaling in our simulations. Figure (6.8) shows the variation of electrostatic field energy density at the saturation point with initial beam kinetic energy density for different mass ratios. The Yellow curve shows $\sim \frac{1}{\gamma_{e0}^2}$ scaling and the blue straight line shows the scaling for the non-relativistic case (presented here for comparison [44]). Figure (6.9) shows the variation of the ratio of electrostatic field energy density at the saturation point to initial electron beam kinetic energy density with electron to ion mass ratio for different initial electron drift velocities. The linear variation with $(m/M)^{1/3}$ again confirms equation (6.19).

6.5 Summary

In this chapter, we have studied the evolution and saturation of the relativistic Buneman instability in 1-D using an in-house developed particle-in-cell simulation code. Our results clearly show that relativistic effects have a stabilizing influence on the instability. The growth rates of unstable modes as measured from simulation show a good match with that obtained from fluid model. Further at the saturation point the electrostatic field energy density scales with the initial electron drift kinetic energy density as $\sim \frac{1}{\gamma_{e0}^2}$, where γ_{e0} is the Lorentz factor associated with the initial

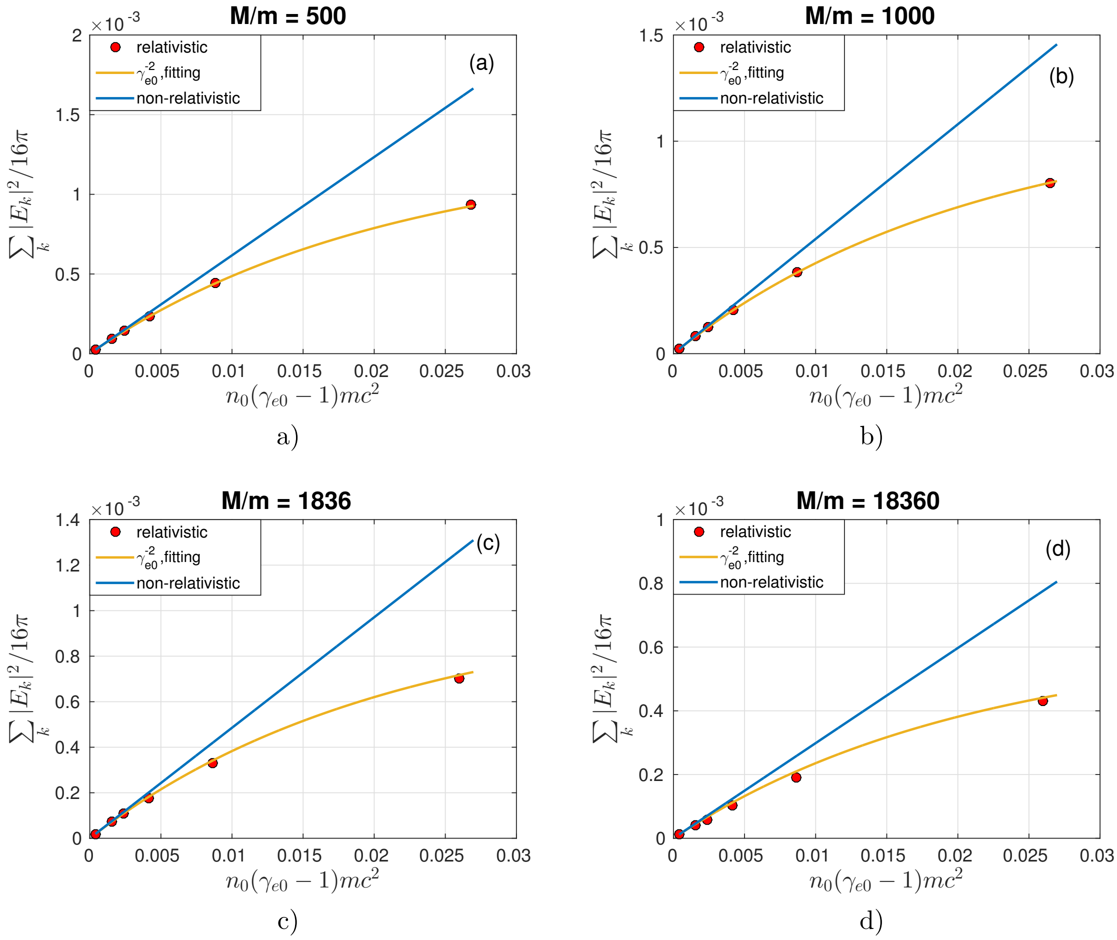

Figure 6.8: Evolution of electrostatic energy density with initial drift kinetic energy density for the mass ratio (6.8a) 500, (6.8b) 1000, (6.8c) 1836, (6.8d) 18360

.

electron drift velocity. This scaling closely matches our back-of-the envelope estimate based on Hirose's [39] analysis. Similar calculations for two-stream instability and filamentation/Weibel instability have been carried out by several other authors [12, 119, 120, 121], whose results we quote here. For relativistic two-stream instability the growth rate and the ratio of electrostatic field energy density to initial beam kinetic energy density at the saturation point scales with γ_{e0} as γ_{e0}^{-1} and $\gamma_{e0}^{-3/2}$ respectively (this is derived in the weak beam limit *i.e* ratio of beam to plasma density $n_b/n_0 \ll 1$)[12, 119] whereas for filamentation / Weibel instability, the growth rate scale as $\gamma_{e0}^{-1/2}$ and the ratio of energy densities at the saturation point is independent of γ_{e0} [120, 121]. We note that our simulation being 1-D in nature has limitations as compared to a full 3-D EM PIC simulation. In a pure 1-D system

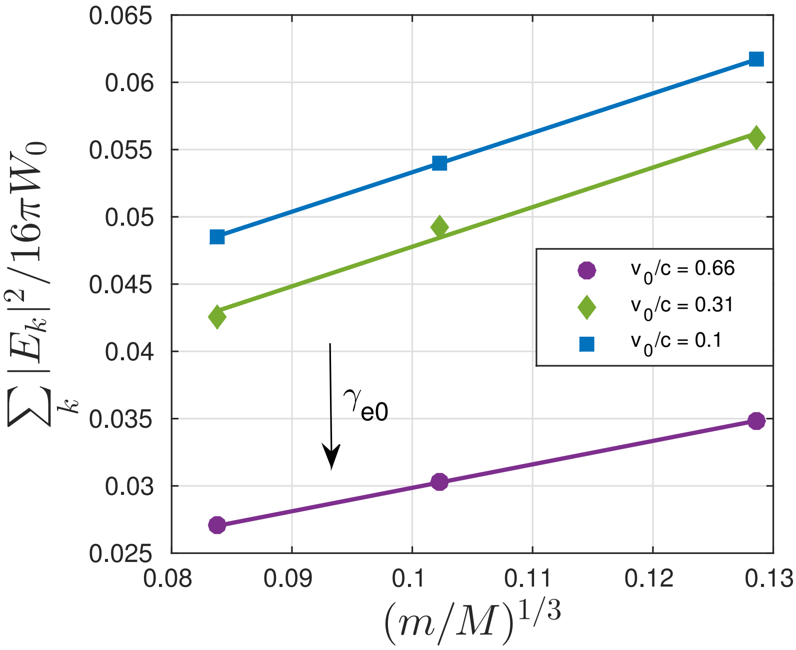

Figure 6.9: Figure shows variation of $\sum_k |E_k|^2/16\pi W_0$ with mass ratio for different initial drift velocities for mass ratios from left to right M/m = 1836, 1000 and 500.

such as the one considered in this work, where there is no variation in the transverse directions (the transverse size of the beam is infinite) and all the plasma electrons are drifting as a whole with respect to ion background, no return current gets excited. In such a case because of interaction between the electron beam and background ions, Buneman is the only instability which gets excited. Such a toy mode is used in textbooks [1] which helps in isolating Buneman from other beam-plasma instabilities. In order to simulate higher dimensional effects such as finite beam width (that leads to excitation of return current) one needs to carry out 3-D EM PIC simulations. Depending on the values of the parameters such as orientation of the wave vector with respect to beam direction ($\vec{k} \cdot \vec{v_b}$), beam to plasma electron density ratio ($\alpha = n_b/n_p$), Lorentz factor associated with beam electrons (γ_b) and electron to ion mass ratio (m/M), several longitudinal and transverse instabilities may be excited. As shown in references [8, 10, 12] in a cold plasma, in the dilute beam limit ($\alpha \ll 1$) as long as the inequality $\gamma_b R \geq \alpha$ ($R = m/M$) is satisfied Buneman/Buneman like modes govern the evolution of relativistic electron beam-plasma system. For our choice of parameters $\gamma_b R$ ranges from $5.5 \times 10^{-4} - 2.7 \times 10^{-3}$. Therefore for values of α lower than the above thresholds, Buneman/Buneman like modes dominate the evolution of the relativistic electron beam-plasma system. In this chapter, we have emphasized only on the linear evolution and saturation of the relativistic Buneman instability. In the linear stage, Buneman is the dominant mode, although in the nonlinear stage of the evolution, it may couple to oblique modes [122] and excite Weibel instability after nonlinear saturation [123].

CHAPTER 7

Conclusion & Future Work

In this chapter, we summarize the important results obtained in various chapters of this thesis. We also discuss possible extension of present work in various limits later in this chapter.

The main focus of this thesis has been on the study of electrostatic modes and instabilities in current carrying cold plasmas with static and mobile ion background ranging from non-relativistic to relativistic regime. We present here a brief overview of the work carried out and summarize the results which have been presented in detail in various chapters of this thesis.

The thesis work begins with the brief overview of numerical techniques used for simulating current carrying cold plasmas. Chapter 2 presents two generalized techniques based on the description of fluid and particle picture of plasma. Fluid code uses LCPFCT [95] subroutines to solve generalized flux conserved fluid equations. Particle-in-cell [96] solves the basic Newton-Maxwell set using time centered finite difference schemes. The codes are benchmarked in the following chapters where an extensive comparison between the theoretical and computational results has been carried out.

In chapter 3, we present an analytical study, carried out for stationary BGK structures in relativistic current carrying fluid-Maxwell system. This study is motivated by the investigation carried out in the ref. [19], where author found that in the presence of a non-relativistic electron beam with average speed v_0, electric field becomes discontinuous for $\kappa \geq 1$ (where $\kappa = E_m/(4\pi n_0 m v_0)^{1/2}$, E_m is maximum amplitude of electric field), which is equivalent to wave breaking in current carrying cold plasmas. This chapter presents an extension in relativistic regime of the work carried out in the aforementioned ref. [19]. In this chapter, we show that relativistic BGK structures are governed by the nonlinear parameter $\kappa_R = E_m/(8\pi n_0 m(\gamma_0 - 1)c^2)^{1/2}$, where γ_0 is the Lorentz factor associated with the average beam speed and other symbols have their usual meanings. We have derived an energy equation using pseudo-potential (Sagdeev potential) method. Analysis of pseudo-potential (Sagdeev potential) shows that BGK structures are periodic in space and, in contrast to the non-relativistic regime, wavelength of the BGK structures varies with the variation of κ_R. It is also observed that pseudo potential ($V(\phi)$) becomes undefined at the electrostatic potential $\Phi^c = (1 - \gamma_0)/\gamma_0$ or at the pseudo-energy level $\kappa_R = \kappa_R^c = 1/\sqrt{\gamma_0}$, thus method of pseudo potential becomes invalid for the values of pseudo-energy $\kappa_R \geq \kappa_R^c$. Therefore, analysis of BGK structures is carried out by studying $\Phi - E$ phase space, which reveals that phase space curves are continuous in the range $0 \leq \kappa_R \leq \kappa_R^c$, but becomes discontinuous in the range $\kappa_R^c \leq \kappa_R$, *i.e.*, electric field becomes discontinuous periodically at some positions of space, thus forming periodic electron sheets (negatively charge plane). The charge density of periodically occurring electron sheets scales with κ_R and β as $\sim (\kappa_R^2 - (1 - \beta^2)^{1/2})^{1/2}$. It must be noted here that in the limit $\beta \to 0$ and/or $\kappa_R \to \infty$, electron beam is transformed into a crystal of "negatively charged plane" with inter-distance $\lambda_0 = E_m/2\pi n_0 e$ having surface charge density $\sim E_m/2\pi$. Further, a relation between electron velocity and position shows that as $\kappa_R \to \kappa_R^c$, electron velocity decreases and for the range $\kappa_R \geq \kappa_R^c$, electron velocity vanishes at the positions where electron sheets are formed. In order to keep current constant, density burst occurs at the similar positions where electron velocity is vanished or electron sheets are formed. These density burst may approach finite values on inclusion of thermal effects.

Full space-time evolution of relativistic current carrying fluid-Maxwell system with static ion background is studied in chapter 4. We obtained an exact solution using method of Lagrangian transformation, describing spatio-temporal evolution of relativistically intense space charge waves propagating on relativistic electron beam. We found that when a relativistic electron beam is perturbed longitudinally with relativistically intense wave, the spatially averaged current diminishes with time due to variation of relativistic mass. By analyzing solution it is found that amount by which spatially averaged current diminishes (ΔI) increases with increasing relativistic intensity of the wave. It is found that the rate of decrease of current (dI/dt) decreases with increasing flow velocity and increases with increasing wave intensity.

Our findings may be of relevance in fast ignition [77, 78] of laser fusion. In fast ignition scenarios [30, 31] , the relativistic electron beam is generated by direct interaction of the laser pulse with the coronal plasma and reaches the precompressed fuel core after propagating in the dense plasma region. In dense plasma region, forward moving relativistic electron beam current is compensated by backward moving coronal plasma electron current (return current) [50]. This current neutralization is satisfied on global scale rather than on local, subsequently introducing several beam-plasma instabilities (filamentation and/or Weibel) in the system. Owing to which energy transport is inhibited and coupling of energy from laser to precompressed target is hence compromised. Efficiency of energy transport is also a key factor in alternative fast ignition schemes. Increment in the efficiency of energy transport through relativistic electron beam is currently a hot issue and needs to be addressed in order to achieve inertial fusion confinement using fast ignition schemes. When there is no return current present, self consistent electric field of beam can reach up to $10^{12} V/m$ [50] in 1 fs. According to our findings on effects of space charge waves on relativistic electron beam, this self consistent electric field may modulate electron beam and total spatially averaged current may be diminished which would inhibit the excitation of other beam-plasma instabilities.

Further, we have extended the scope of our thesis for electrostatic instabilities occurring because of coupling between electrons and ions. Buneman mode under certain condition turns out to be the strongest unstable mode. General solution of Buneman instability offers great mathematical difficulty so computer simulation is needed to understand nonlinear dynamics of Buneman instability. In chapter 5, we present nonlinear evolution of Buneman instability, which is carried out using 1-D particle-in-cell simulation code. For different initial drift velocities and for a wide range of electron to ion mass ratios, the growth rate obtained from simulation agrees well with the numerical solution of the fourth order dispersion relation. The time when linear growth rate saturates along with its harmonics is known as quasilinear or first saturation time and can be identified as first hiccup in time evolution of electrostatic energy density. We have found that quasilinear saturation (or first saturation) occurs when the electrostatic energy density becomes $\sim (m/M)^{1/3}$ times the initial drift kinetic energy density, *i.e.* $\sum_k |E_k|^2/16\pi \approx (m/M)^{(1/3)} W_0$, which is estimated analytically by Hirose[39]. The energy level at the time of quasilinear saturation is observed to be independent of the initial drift velocity. Further, electron trapping and nonlinear mode coupling leads to the final saturation of the instability. In contrast to quasilinear saturation, at the final saturation the ratio of electrostatic field energy density to initial kinetic energy density depends on the initial drift velocity but is independent of the mass ratio. The energy level at the time of final saturation follows the inequality suggested by Ishihara et. al. [41], *i.e.*, $\sum_k \frac{|E_k|^2}{16\pi W_0} \geq 0.11$. To the best of our knowledge, this is the first verification of Hirose's [39] and Ishihara's [41, 42] theoretical scaling using a PIC simulation.

The most interesting feature that has emerged from this chapter is, after final quenching of Buneman instability, strong interaction between electron phase space holes and surrounding ions leads to the breaking of the electron phase space holes into two oppositely propagating holes each attached with an ion pulse. We have identified these oppositely propagating coherent structures as coupled hole-solitons (CHSs). A very good match is found between computational and theoretical amplitude-speed relation, where theoretical amplitude-speed relation is taken from theoretical model of Saeki et. al. [46]. Specifically, this is first ever confirmation which shows explicit formation and identification of CHSs after saturation of Buneman instability. These coupled hole-solitons eventually coalesce away finally generating a broadened electron velocity distribution function.

In chapter 6, we have extended our study on Buneman instability for the cases, when electron beam is moving with weakly relativistic speed. Simulation is carried out using 1D relativistic particle-in-cell code. In the relativistic regime, dynamics of Buneman instability (also known as relativistic Buneman instability) is strongly affected[7, 53, 54]. It is observed that growth rate is reduced in relativistic regime and maximum growth rate now scales with initial drift velocity v_0 as $\gamma/\omega \approx \frac{\sqrt{3}}{2\gamma_{e0}^{1/2}}\left(\frac{m}{2M}\right)^{1/3}$ (where γ_{e0} is the Lorentz factor associated with the initial electron drift velocity), consequently, relativistic effects have a stabilizing influence on the instability. The growth rates of unstable modes as measured from simulation show a good match with that obtained from the numerical solution of fourth order dispersion relation. Further at the time of quasi-linear saturation, the ratio of electrostatic field energy density to initial kinetic energy density is found to be depending of initial drift velocity and scales as $\sum_k |E_k|^2/16\pi W_0 \approx \frac{1}{\gamma_{e0}^2}\left(\frac{m}{2M}\right)^{1/3}$, where $W_0 = (\gamma_{e0}-1)n_0 mc^2$. This novel result on the scaling of energy densities has been found to be in quantitative agreement with our theoretical back-of-the-envelope estimation, which is based on Hirose's [39] analysis.

We end this section by making a comment that in our thesis we have studied several electrostatic modes and instabilities with static and mobile background occurring in current carrying cold plasmas. In next section we discuss possible extension of present work in various limits.

7.1 Future Scope

The results presented in this thesis illustrate several interesting physical phenomena and provide a basis for further investigations as direct extensions to this work. In this section, we discuss some open problems, which can be attempted in future.

1. In chapter 3, stationary solutions for relativistic BGK structures are obtained for the range $\kappa_R \geq \kappa_R^c$. Study of excitation and stability of these BGK structures using a PIC/fluid code needs to be carried out.

2. In chapter 4, we studied effect of relativistically intense wave on homogeneous relativistic electron beam. This study must be extended for in-homogeneous relativistic electron beam propagating through homogeneous background of ions and for homogeneous relativistic electron beam propagating through in-homogeneous background of ions. These studies may shed new light in fast ignition scheme, relativistic jets etc.

3. In chapter 5, we found coupled-hole solitons after quenching of Buneman instability, which eventually phase mix away. However, this is not the complete relaxation of the system thus long time simulation must be carried out to know final relaxation stage after saturation of the Buneman instability. It would also be interesting to carry out PIC simulation of non-resonant Buneman instability, which is expected to follow growth rate obtained by Kaw et al. [29] in linear regime.

4. An analytical model for nonlinear evolution of relativistic Buneman instability must be developed using quasilinear kinetic theory. This analytical model will help to estimate energy scaling for quasilinear and nonlinear saturation of the relativistic Buneman instability.

Appendix A

Estimation of interdistance (wavelength) between the crystals in the limit $\kappa_R \to \infty$

In this appendix, we estimate the wavelength for the crystal formation in the range $\kappa_R \to \infty$ and/or $\beta \to 0$. First we will reduce all the variables in above described range as,

$$\alpha = (\gamma_0 - 1)\kappa_R^2 + \frac{1}{\gamma_0},$$
$$\alpha = (\gamma_0 - 1)\frac{\kappa_E^2}{(\gamma_0 - 1)} + \frac{1}{\gamma_0},$$
$$\alpha = \kappa_E^2 + 1, \tag{A.1}$$

where $\kappa_E = E_m/(8\pi n_0 mc^2)^{1/2}$.

$$r^2 = \frac{\alpha + \sqrt{\alpha^2 + \beta^2 - 1}}{1 - \beta} = \alpha + \sqrt{\alpha^2 - 1}, \tag{A.2}$$
$$s^2 = \frac{\alpha - \sqrt{\alpha^2 + \beta^2 - 1}}{1 - \beta} = \alpha - \sqrt{\alpha^2 - 1}, \tag{A.3}$$
$$k^2 = \frac{2\sqrt{\alpha^2 - 1}}{\alpha + \sqrt{\alpha^2 - 1}}. \tag{A.4}$$

Maximum value of the potential reduces into

$$
\begin{aligned}
\Phi_u &= \gamma_0(\gamma_0 - 1)\left(\kappa_R^2 + \kappa_R\beta\sqrt{\kappa_R^2 + \frac{2}{\gamma_0(\gamma_0-1)}}\right),\\
\Phi_u &= \gamma_0(\gamma_0 - 1)\left(\frac{\kappa_E^2}{(\gamma_0-1)} + \frac{\kappa_E}{(\gamma_0-1)^{1/2}}\beta\sqrt{\frac{\kappa_E^2}{(\gamma_0-1)} + \frac{2}{\gamma_0(\gamma_0-1)}}\right),\\
\Phi_u &= \gamma_0\left(\kappa_E^2 + \kappa_E\beta\sqrt{\kappa_R^2 + \frac{2}{\gamma_0}}\right),\\
\Phi_u &= \kappa_E^2 = \alpha - 1.
\end{aligned}
\tag{A.5}
$$

$$
\begin{aligned}
\sin^2\theta_u &= \frac{r^2 - \gamma_0(1 + \Phi_u + \sqrt{\beta^2 + 2\Phi_u + \Phi_u^2})}{r^2 - s^2},\\
\sin^2\theta_u &= \frac{\alpha + \sqrt{\alpha^2-1} - (1 + \alpha - 1 + \sqrt{2\alpha - 2 + (\alpha-1)^2})}{2\sqrt{\alpha^2-1}},\\
\sin^2\theta_u &= \frac{\alpha + \sqrt{\alpha^2-1} - (\alpha + \sqrt{\alpha^2-1})}{2\sqrt{\alpha^2-1}},\\
\sin^2\theta_u &= 0,\\
\sin\theta_u &= 0.
\end{aligned}
\tag{A.6}
$$

Critical value of the potential becomes

$$
\begin{aligned}
\Phi_c &= \frac{(\gamma_0 - 1)}{\gamma_0},\\
\Phi_c &= 0.
\end{aligned}
\tag{A.7}
$$

$$
\begin{aligned}
\sin^2\theta_c &= \frac{r^2 - \gamma_0(1 + \Phi_c + \sqrt{\beta^2 + 2\Phi_c + \Phi_c^2})}{r^2 - s^2},\\
\sin^2\theta_c &= \frac{\alpha + \sqrt{\alpha^2-1} - 1}{2\sqrt{\alpha^2-1}},\\
\sin^2\theta_c &= \frac{1}{2}\left(1 + \sqrt{\frac{\alpha-1}{\alpha+1}}\right),\\
\sin\theta_c &= \frac{1}{\sqrt{2}}\left(1 + \sqrt{\frac{\alpha-1}{\alpha+1}}\right)^{1/2},
\end{aligned}
$$

$$\cos\theta_c = \frac{1}{\sqrt{2}}\left(1 - \sqrt{\frac{\alpha-1}{\alpha+1}}\right)^{1/2}. \tag{A.8}$$

$$\begin{aligned}
1-\kappa^2\sin^2\theta_c &= 1 - \left(\frac{2\sqrt{\alpha^2-1}}{\alpha+\sqrt{\alpha^2-1}}\right)\left(\frac{\alpha+\sqrt{\alpha^2-1}-1}{2\sqrt{\alpha^2-1}}\right),\\
1-\kappa^2\sin^2\theta_c &= 1-1+\frac{1}{r^2},\\
1-\kappa^2\sin^2\theta_c &= \frac{1}{r^2}.
\end{aligned} \tag{A.9}$$

$$\begin{aligned}
E(\theta_c,\kappa^2) &= \int_0^{\theta_c} \sqrt{1-\kappa^2\sin^2\theta_c}\, d\theta_c,\\
E(\theta_c,\kappa^2) &= \frac{1}{r}\int_0^{\theta_c} d\theta_c,\\
E(\theta_c,\kappa^2) &= \frac{\theta_c}{r}.
\end{aligned} \tag{A.10}$$

$$\begin{aligned}
\frac{r^4(k^2-1)+1}{r^4(k^2-1)} &= 1+\frac{1}{r^4(k^2-1)},\\
\frac{r^4(k^2-1)+1}{r^4(k^2-1)} &= 1+\frac{1}{r^4\left(\frac{r^2-s^2}{r^2}-1\right)},\\
\frac{r^4(k^2-1)+1}{r^4(k^2-1)} &= 1-\frac{1}{r^2s^2},\\
\frac{r^4(k^2-1)+1}{r^4(k^2-1)} &= 1-\frac{1}{(\alpha+\sqrt{\alpha^2-1})(\alpha-\sqrt{\alpha^2-1})},\\
\frac{r^4(k^2-1)+1}{r^4(k^2-1)} &= 0.
\end{aligned} \tag{A.11}$$

From the equation , wavelength in the limit $\kappa_R \geq \kappa_R^c$ written as

$$\begin{aligned}
\frac{\omega_{pe}\lambda_0}{v_0\gamma_0^{3/2}} = -\frac{2(1+\beta)^{1/4}}{\gamma_0\beta(1-\beta)^{1/4}}\Bigg[&\left(\frac{r^4(k^2-1)+1}{r^3(k^2-1)}\right)\left(E(\theta_c,k^2)-E(\theta_u,k^2)\right)\\
&-\frac{k^2\sin 2\theta_u}{2r^3(k^2-1)(1-k^2\sin^2\theta_u)^{1/2}}+\frac{k^2\sin 2\theta_c}{2r^3(k^2-1)(1-k^2\sin^2\theta_c)^{1/2}}\Bigg],
\end{aligned}$$

eliminating variables using the equations (A.1) - (A.11), yields

$$\frac{\omega_{pe}\lambda_0}{c} = -2\left[0\left(\frac{\theta_c}{r} - 0\right) - 0 + \frac{\frac{2\sqrt{\alpha^2-1}}{\alpha+\sqrt{\alpha^2-1}} 2\,\frac{1}{\sqrt{2}}\left(1+\sqrt{\frac{\alpha-1}{\alpha+1}}\right)^{1/2} \frac{1}{\sqrt{2}}\left(1-\sqrt{\frac{\alpha-1}{\alpha+1}}\right)^{1/2}}{2(\alpha+\sqrt{\alpha^2-1})\left(\frac{2\sqrt{\alpha^2-1}}{\alpha+\sqrt{\alpha^2-1}} - 1\right)}\right],$$

$$\frac{\omega_{pe}\lambda_0}{c} = -2\left[\frac{\frac{2}{1+\alpha}\sqrt{\alpha^2-1}}{(\alpha+\sqrt{\alpha^2-1})\left(-\alpha+\sqrt{\alpha^2-1}\right)}\right],$$

$$\begin{aligned}
\frac{\omega_{pe}\lambda_0}{c} &= 4\sqrt{\alpha-1}, \\
\frac{\omega_{pe}\lambda_0}{c} &= 4\kappa_E, \\
\lambda_0 &= \frac{E_m}{2\pi n_0 e}.
\end{aligned} \tag{A.12}$$

Thus in the limit $\beta \to 0$, the beam is transformed into a "crystal" of negatively charged planes with interdistance λ_0.

APPENDIX B

Solution for spatio-temporal evolution of relativistic electron beam

B.1 Detailed calculation for obtaining exact solution in Lagrangian frame

To find the exact solution of equation (4.14), first, we introduce a new variable ξ through,

$$\sqrt{1+p_e^2} = p_e - \xi^2, \tag{B.1}$$

where ξ is a function of x_0 and τ. It must be noteworthy here that substitution of new variable ξ is merely a mathematical manipulation and does not put any limit on the range of momentum (p_e), instead, just eases up the calculation to find the exact solution.

$$p_e = \frac{\xi^4 - 1}{2\xi^2},$$

$$dp_e = \left(\xi + \frac{1}{\xi^3}\right) d\xi. \tag{B.2}$$

Using relation (B.2), equation transforms into

$$\begin{aligned}
\frac{1}{(1-\beta)^{1/2}}\frac{\partial \xi}{\partial \tau} &= \pm \frac{\xi^2}{1+\xi^4}\left[\frac{2a}{1-\beta}\xi^2 - \frac{1-\beta^2}{(1-\beta)^2} - \xi^4\right]^{1/2}, \\
\frac{1}{(1-\beta)^{1/2}}\frac{\partial \xi}{\partial \tau} &= \pm \frac{\xi^2}{1+\xi^4}\left[\frac{2a}{1-\beta}\xi^2 - \xi^4 - \frac{1+a^2-a^2-\beta^2}{(1-\beta)^2}\right]^{1/2}, \\
\frac{1}{(1-\beta)^{1/2}}\frac{\partial \xi}{\partial \tau} &= \pm \frac{\xi^2}{1+\xi^4}\left[\frac{2a}{1-\beta}\xi^2 + \frac{\sqrt{a^2+\beta^2-1}}{1-\beta}\xi^2 - \frac{\sqrt{a^2+\beta^2-1}}{1-\beta}\xi^2 - \xi^4\right. \\
&\quad \left. - \frac{a-\sqrt{a^2+\beta^2-1}}{(1-\beta)}\frac{a-\sqrt{a^2+\beta^2-1}}{(1-\beta)}\right]^{1/2}, \\
\frac{1}{(1-\beta)^{1/2}}\frac{\partial \xi}{\partial \tau} &= \pm \frac{\xi^2}{1+\xi^4}\left[\frac{a+\sqrt{a^2+\beta^2-1}}{1-\beta}\xi^2 - \xi^4 + \frac{\sqrt{a-a^2+\beta^2-1}}{1-\beta}\xi^2\right. \\
&\quad \left. - \frac{a-\sqrt{a^2+\beta^2-1}}{(1-\beta)}\frac{a-\sqrt{a^2+\beta^2-1}}{(1-\beta)}\right]^{1/2}.
\end{aligned} \tag{B.3}$$

We define new variables r and s as,

$$r^2 = \frac{a+\sqrt{a^2+\beta^2-1}}{1-\beta}, \tag{B.4}$$

$$s^2 = \frac{a-\sqrt{a^2+\beta^2-1}}{1-\beta}, \tag{B.5}$$

which reduces equation (B.3) written in the standard form,

$$\begin{aligned}
\frac{1}{(1-\beta)^{1/2}}\frac{\partial \xi}{\partial \tau} &= \pm \frac{\xi^2}{1+\xi^4}\left\{r^2\xi^2 - \xi^4 + s^2\xi^2 - r^2 s^2\right\}^{1/2}, \\
\frac{1}{(1-\beta)^{1/2}}\frac{\partial \xi}{\partial \tau} &= \pm \frac{\xi^2}{1+\xi^4}\left\{(r^2-\xi^2)(\xi^2-s^2)\right\}^{1/2}, \\
(1-\beta)^{1/2} d\tau &= \pm \frac{\xi^2 d\xi}{\left\{(r^2-\xi^2)(\xi^2-s^2)\right\}^{1/2}} \pm \frac{d\xi}{\xi^2\left\{(r^2-\xi^2)(\xi^2-s^2)\right\}^{1/2}}.
\end{aligned} \tag{B.6}$$

Now, we introduce a new transformation through variables θ and κ

$$\begin{aligned}\sin^2\theta =& \frac{r^2-\xi^2}{r^2-s^2},\\ \cos^2\theta =& \frac{\xi^2-s^2}{r^2-s^2},\end{aligned} \tag{B.7}$$

$$\kappa^2 = \frac{r^2-s^2}{r^2} = \frac{2\sqrt{a^2+\beta^2-1}}{a+\sqrt{a^2+\beta^2-1}}, \tag{B.8}$$

where θ is a function of x_0 and τ and κ is a function of x_0 only.

$$d\xi = \mp\,\frac{r}{2}\frac{\kappa^2}{(1-\kappa^2\sin^2\theta)^{3/2}}d\theta, \tag{B.9}$$

This substitution of equations (B.7), (B.8) and (B.9) into equation (B.6), yields,

$$\pm\,(1-\beta)^{1/2}d\tau = \mp\left(r\left(1-\kappa^2\sin^2\theta\right)^{1/2}\,d\theta + \frac{d\theta}{r^3\left(1-\kappa^2\sin^2\theta\right)^{3/2}}\right). \tag{B.10}$$

By integrating equation (B.10), the solution of equation (4.14) can be written as

$$\pm\,(1-\beta)^{1/2}\tau = \mp\left(\frac{r^4(\kappa^2-1)-1}{r^3(\kappa^2-1)}E(\theta,\kappa) + \frac{\kappa^2\sin 2\theta}{2r^3(\kappa^2-1)(1-\kappa^2\sin^2\theta)^{1/2}}\right) + \phi(x_0), \tag{B.11}$$

where $E(\theta,\kappa)$ is incomplete integral of second kind and $\phi(x_0)$ is secondary arbitrary coefficient, which is a function of x_0.

B.2 Calculation of Electron Density

In this appendix, we present thorough calculation to obtain electron density in terms of Eulerian co-ordinates. First, we obtain derivatives of some variables, which will be used for easing up the calculations.

$$a = \frac{\Delta'^2}{2}\sin^2 kx_0 - \beta\frac{p_0}{mc} + \sqrt{1+\frac{p_0^2}{m^2c^2}}, \tag{B.12}$$

differentiate the equation (B.12), gives the relation

$$\frac{da}{dx_0} = \frac{k\Delta'^2}{2}\sin 2kx_0. \tag{B.13}$$

Taking the derivative of (B.4) with respect to x_0 gives,

$$\begin{aligned}
\frac{dr}{dx_0} &= \frac{1}{r\kappa^2(1-\beta)}\frac{da}{dx_0},\\
\frac{dr}{dx_0} &= \frac{k\Delta'^2\sin 2kx_0}{2r\kappa^2(1-\beta)}
\end{aligned} \tag{B.14}$$

Again taking the derivative of κ, yields

$$\begin{aligned}
\kappa^2 &= \frac{2\sqrt{a^2+\beta^2-1}}{a+\sqrt{a^2+\beta^2-1}},\\
\frac{d\kappa}{dx_0} &= \frac{1}{\kappa}\frac{a-\sqrt{a^2+\beta^2-1}}{\sqrt{a^2+\beta^2-1}\left(a+\sqrt{a^2+\beta^2-1}\right)}\frac{da}{dx_0},\\
\frac{d\kappa}{dx_0} &= -\frac{k\Delta'^2(\kappa^2-1)\sin 2kx_0}{r^2\kappa^3(1-\beta)}.
\end{aligned} \tag{B.15}$$

Now we calculate $d\theta/dx_0$ using the equation

$$\begin{aligned}
\sin^2\theta_0 &= \frac{a+\sqrt{a^2+\beta^2-1}-(1-\beta)\left(\frac{p_0}{mc}+\gamma_0\right)}{2\sqrt{a^2+\beta^2-1}},\\
\sin^2\theta_0 &= \frac{1}{\kappa^2}-\frac{(1-\beta)\left(\frac{p_0}{mc}+\gamma_0\right)}{2\sqrt{a^2+\beta^2-1}},
\end{aligned} \tag{B.16}$$

as

$$\begin{aligned}
\sin 2\theta_0\frac{d\theta_0}{dx_0} &= -\frac{2}{\kappa^3}\frac{d\kappa}{dx_0}+\frac{a(1-\beta)\left(\frac{p_0}{mc}+\gamma_0\right)}{2(a^2+\beta^2-1)^{3/2}}\frac{da}{dx_0},\\
\sin 2\theta_0\frac{d\theta_0}{dx_0} &= -\frac{2k\Delta'^2(1-\kappa^2)\sin 2kx_0}{r^2\kappa^6(1-\beta)}+\frac{a(1-\beta)\left(\frac{p_0}{mc}+\gamma_0\right)}{2(a^2+\beta^2-1)^{3/2}}\frac{k\Delta'^2\sin 2kx_0}{2},\\
\sin 2\theta_0\frac{d\theta_0}{dx_0} &= -\frac{2k\Delta'^2(1-\kappa^2)\sin 2kx_0}{r^2\kappa^6(1-\beta)}+k\Delta'^2(1-\beta)\sin 2kx_0\left(\frac{p_0}{mc}+\gamma_0\right)\frac{(1+\beta+(1-\beta)r^4)}{(1-\beta)^3r^8\kappa^6},
\end{aligned}$$

$$\frac{d\theta_0}{dx_0} = \frac{k\Delta'^2 \sin 2kx_0}{r^8\kappa^6(1-\beta)^2\sin 2\theta_0}\left\{\left(\frac{p_0}{mc}+\gamma_0\right)\left(1+\beta-r^4(1-\beta)\right)-2r^6(1-\beta)(1-\kappa^2)\right\}, \tag{B.17}$$

where we have used the relations

$$\begin{aligned} a &= \frac{1+\beta+r^4(1-\beta)}{2r^2}, \\ (a^2+\beta^2-1)^{3/2} &= \frac{r^6\kappa^6(1-\beta)^3}{8}. \end{aligned} \tag{B.18}$$

Now differentiating complete solution (equation (4.19)) with respect to x_0, yields,

$$\begin{aligned} (1-\beta)^{1/2}\tau 3r^2\frac{dr}{dx_0} &= \left\{4r^3\frac{dr}{dx_0}+\frac{2\kappa}{(\kappa^2-1)^2}\frac{d\kappa}{dx_0}\right\}\{E(\theta_0,\kappa)-E(\theta,\kappa)\}+\left(r^4-\frac{1}{\kappa^2-1}\right) \\ &\left\{\frac{E(\theta_0,\kappa)-F(\theta_0,\kappa^2)}{\kappa}-\frac{E(\theta,\kappa)-F(\theta,\kappa^2)}{\kappa}\right\}\frac{d\kappa}{dx_0}+\left(r^4-\frac{1}{\kappa^2-1}\right)\left\{\sqrt{1-\kappa^2\sin^2\theta_0}\frac{d\theta_0}{dx_0}\right. \\ &\left.-\sqrt{1-\kappa^2\sin^2\theta}\frac{d\theta}{dx_0}\right\}-\left\{\frac{\kappa\sin\theta_0}{(\kappa^2-1)^2\sqrt{1-\kappa^2\sin^2\theta_0}}-\frac{\kappa\sin\theta}{(\kappa^2-1)^2\sqrt{1-\kappa^2\sin^2\theta}}\right\}\frac{d\kappa}{dx_0} \\ &+\frac{\kappa^2\sin 2\theta_0}{2(\kappa^2-1)(1-\kappa^2\sin^2\theta_0)^{3/2}}\left(\kappa\sin^2\theta_0\frac{d\kappa}{dx_0}+\frac{\kappa^2}{2}\sin 2\theta_0\frac{d\theta_0}{dx_0}\right)-\frac{\kappa^2\sin 2\theta}{2(\kappa^2-1)(1-\kappa^2\sin^2\theta)^{3/2}} \\ &\left(\kappa\sin^2\theta\frac{d\kappa}{dx_0}+\frac{\kappa^2}{2}\sin 2\theta\frac{d\theta}{dx_0}\right)+\frac{\kappa^2\cos 2\theta_0}{(\kappa^2-1)(1-\kappa^2\sin^2\theta_0)^{1/2}}\frac{d\theta_0}{dx_0}-\frac{\kappa^2\cos 2\theta}{(\kappa^2-1)(1-\kappa^2\sin^2\theta)^{1/2}}\frac{d\theta}{dx_0}, \end{aligned} \tag{B.19}$$

after rearranging some terms and doing some simple algebraic manipulation, gives

$$\begin{aligned} 3r^2\tau(1-\beta)^{1/2}\frac{dr}{dx_0} &= 4r^3\left\{E(\theta_0,\kappa)-E(\theta,\kappa)\right\}\frac{dr}{dx_0}+\frac{2\kappa}{(\kappa^2-1)^2}\Big(E(\theta_0,\kappa)-E(\theta,\kappa)\Big) \\ &+\left(r^4-\frac{1}{\kappa^2-1}\right)\left\{\frac{E(\theta_0,\kappa)-F(\theta_0,\kappa^2)}{\kappa}-\frac{E(\theta,\kappa)-F(\theta,\kappa^2)}{\kappa}\right\}\frac{d\kappa}{dx_0} \\ &+\frac{\kappa^3(\kappa^2+1)\sin^2\theta_0-2\kappa}{2(\kappa^2-1)^2(1-\kappa^2\sin^2\theta_0)^{3/2}}\sin 2\theta_0\frac{d\kappa}{dx_0}-\frac{\kappa^3(\kappa^2+1)\sin^2\theta-2\kappa}{2(\kappa^2-1)^2(1-\kappa^2\sin^2\theta)^{3/2}}\sin 2\theta\frac{d\kappa}{dx_0} \\ &+\frac{4\{r^4(\kappa^2-1)-1\}(1-\kappa^2\sin^2\theta_0)^2+\kappa^4\sin 2\theta_0+4\kappa^2\cos 2\theta_0(1-\kappa^2\sin^2\theta_0)}{4(\kappa^2-1)(1-\kappa^2\sin^2\theta_0)^{3/2}}\frac{d\theta_0}{dx_0} \\ &-\frac{4\{r^4(\kappa^2-1)-1\}(1-\kappa^2\sin^2\theta)^2+\kappa^4\sin 2\theta+4\kappa^2\cos 2\theta(1-\kappa^2\sin^2\theta)}{4(\kappa^2-1)(1-\kappa^2\sin^2\theta)^{3/2}}\frac{d\theta}{dx_0}, \end{aligned} \tag{B.20}$$

then $\partial\theta/\partial x_0$ is obtained as

$$\begin{aligned}\frac{\partial\theta}{\partial x_0} =& \frac{4(\kappa^2-1)(1-\kappa^2\sin^2\theta)^{3/2}}{4\{r^4(\kappa^2-1)-1\}(1-\kappa^2\sin^2\theta)^2+\kappa^4\sin 2\theta+4\kappa^2\cos 2\theta(1-\kappa^2\sin^2\theta)} \\ & \Bigg[-3r^2\tau(1-\beta)^{1/2}\frac{dr}{dx_0}+4r^3\Bigg\{E(\theta_0,\kappa)-E(\theta,\kappa)\Bigg\}\frac{dr}{dx_0}+\frac{2\kappa}{(\kappa^2-1)^2}\Bigg\{E(\theta_0,\kappa) \\ & -E(\theta,\kappa)\Bigg\}\frac{d\kappa}{dx_0}+\left(r^4-\frac{1}{\kappa^2-1}\right)\Bigg\{\frac{E(\theta_0,\kappa)-F(\theta_0,\kappa^2)}{\kappa}-\frac{E(\theta,\kappa)-F(\theta,\kappa^2)}{\kappa}\Bigg\}\frac{d\kappa}{dx_0} \\ & +\frac{\kappa^3(\kappa^2+1)\sin^2\theta_0-2\kappa}{2(\kappa^2-1)^2(1-\kappa^2\sin^2\theta_0)^{3/2}}\sin 2\theta_0\frac{d\kappa}{dx_0}-\frac{\kappa^3(\kappa^2+1)\sin^2\theta-2\kappa}{2(\kappa^2-1)^2(1-\kappa^2\sin^2\theta)^{3/2}}\sin 2\theta\frac{d\kappa}{dx_0} \\ & +\frac{4\{r^4(\kappa^2-1)-1\}(1-\kappa^2\sin^2\theta_0)^2+\kappa^4\sin 2\theta_0+4\kappa^2\cos 2\theta_0(1-\kappa^2\sin^2\theta_0)}{4(\kappa^2-1)(1-\kappa^2\sin^2\theta_0)^{3/2}}\frac{d\theta_0}{dx_0}\Bigg],\end{aligned} \tag{B.21}$$

now eliminating all the derivatives dr/dx_0, $d\kappa/dx_0$ and $d\theta_0/dx_0$ using equations (B.14), (B.15) and (B.17) respectively, $\partial\theta/\partial x_0$ becomes

$$\begin{aligned}\frac{\partial\theta}{\partial x_0} =& \frac{4k\Delta'^2\sin 2kx_0(\kappa^2-1)(1-\kappa^2\sin^2\theta)^{3/2}}{4\{r^4(\kappa^2-1)-1\}(1-\kappa^2\sin^2\theta)^2+\kappa^4\sin 2\theta+4\kappa^2\cos 2\theta(1-\kappa^2\sin^2\theta)}\Bigg[-\frac{3r\tau}{\kappa^2(1-\beta)^{1/2}} \\ & +\frac{2r^2}{\kappa^2(1-\beta)}\Bigg\{E(\theta_0,\kappa)-E(\theta,\kappa)\Bigg\}-\frac{2}{r^2\kappa^2(1-\beta)(\kappa^2-1)}\Bigg\{E(\theta_0,\kappa) \\ & -E(\theta,\kappa)\Bigg\}-\left(\frac{r^4(\kappa^2-1)-1}{r^2\kappa^3(1-\beta)}\right)\Bigg\{\frac{E(\theta_0,\kappa)-F(\theta_0,\kappa^2)}{\kappa}-\frac{E(\theta,\kappa)-F(\theta,\kappa^2)}{\kappa}\Bigg\} \\ & -\frac{\kappa^2(\kappa^2+1)\sin^2\theta_0-2}{2(\kappa^2-1)(1-\kappa^2\sin^2\theta_0)^{3/2}}\frac{\sin 2\theta_0}{r^2\kappa^2(1-\beta)}+\frac{\kappa^2(\kappa^2+1)\sin^2\theta-2}{2(\kappa^2-1)(1-\kappa^2\sin^2\theta)^{3/2}}\frac{\sin 2\theta}{r^2\kappa^2(1-\beta)} \\ & +\frac{4\{r^4(\kappa^2-1)-1\}(1-\kappa^2\sin^2\theta_0)^2+\kappa^4\sin 2\theta_0+4\kappa^2\cos 2\theta_0(1-\kappa^2\sin^2\theta_0)}{4(\kappa^2-1)(1-\kappa^2\sin^2\theta_0)^{3/2}} \\ & \Bigg\{\frac{1}{r^8\kappa^6(1-\beta)^2\sin 2\theta_0}\Bigg\{\left(\frac{p_0}{mc}+\gamma_0\right)\Big(1+\beta-r^4(1-\beta)\Big)-2r^6(1-\beta)(1-\kappa^2)\Bigg\}\Bigg\}\Bigg],\end{aligned} \tag{B.22}$$

$$\begin{aligned}\frac{\partial\theta}{\partial x_0} =& \frac{4k\Delta'^2\sin 2kx_0(\kappa^2-1)(1-\kappa^2\sin^2\theta)^{3/2}}{4\{r^4(\kappa^2-1)-1\}(1-\kappa^2\sin^2\theta)^2+\kappa^4\sin 2\theta+4\kappa^2\cos 2\theta(1-\kappa^2\sin^2\theta)}\Bigg[-\frac{3r\tau}{\kappa^2(1-\beta)^{1/2}} \\ & +\left(\frac{r^4(\kappa^2-1)-1}{r^2\kappa^4(1-\beta)}\right)\Bigg\{\frac{\kappa^2+1}{\kappa^2(\kappa^2-1)}\Big(E(\theta_0,\kappa)-E(\theta,\kappa)\Big)+F(\theta_0,\kappa^2)-F(\theta,\kappa^2)\Bigg\} \\ & -\frac{\kappa^2(\kappa^2+1)\sin^2\theta_0-2}{2(\kappa^2-1)(1-\kappa^2\sin^2\theta_0)^{3/2}}\frac{\sin 2\theta_0}{r^2\kappa^2(1-\beta)}+\frac{\kappa^2(\kappa^2+1)\sin^2\theta-2}{2(\kappa^2-1)(1-\kappa^2\sin^2\theta)^{3/2}}\frac{\sin 2\theta}{r^2\kappa^2(1-\beta)}\end{aligned}$$

$$+\frac{4\{r^4(\kappa^2-1)-1\}(1-\kappa^2\sin^2\theta_0)^2+\kappa^4\sin 2\theta_0+4\kappa^2\cos 2\theta_0(1-\kappa^2\sin^2\theta_0)}{4(\kappa^2-1)(1-\kappa^2\sin^2\theta_0)^{3/2}}$$
$$\left\{\frac{1}{r^8\kappa^6(1-\beta)^2\sin 2\theta_0}\left\{\left(\frac{p_0}{mc}+\gamma_0\right)\Big(1+\beta-r^4(1-\beta)\Big)-2r^6(1-\beta)(1-\kappa^2)\right\}\right\}\Bigg], \tag{B.23}$$

Now the electron density can be written as

$$n_e(x_0,\tau)=\frac{n(x_0,0)}{D}, \tag{B.24}$$

where D is defined by

$$\begin{aligned}
D =&1+k\frac{\partial}{\partial x_0}\int_0^\tau v_e(x_0,\tau')d\tau',\\
D =&1+k\frac{\partial}{\partial x_0}\int_0^\tau \frac{p_e}{\sqrt{1+\left(\frac{p_e}{mc}\right)^2}}d\tau',\\
D =&1+k\frac{\partial}{\partial x_0}\int_0^\tau \left(-\frac{1}{\omega_{pe}^2}\frac{\partial^2 p_e}{\partial\tau^2}+v_0\right)d\tau',\\
D =&1-\frac{k}{\omega_{pe}^2}\frac{\partial}{\partial x_0}\left[\frac{\partial p}{\partial\tau}-\left.\frac{\partial p_e}{\partial\tau}\right|_{\tau=0}\right],\\
D =&1\mp\frac{\sqrt{2}kc}{\omega_{pe}}\frac{\partial}{\partial x_0}\left[\left(a+\beta\frac{p_e}{mc}+\sqrt{1+\left(\frac{p_e}{mc}\right)^2}\right)^{1/2}-\left(a+\beta\frac{p_0}{mc}+\sqrt{1+\left(\frac{p_0}{mc}\right)^2}\right)^{1/2}\right],
\end{aligned} \tag{B.25}$$

$$\begin{aligned}
D =&1\mp\frac{kc\sqrt{1-\beta}}{\omega_{pe}}\frac{\partial}{\partial x_0}\left[\frac{r\kappa^2\sin 2\theta}{2(1-\kappa^2\sin^2\theta)^{1/2}}-\frac{r\kappa^2\sin 2\theta_0}{2(1-\kappa^2\sin^2\theta_0)^{1/2}}\right],\\
D =&1\mp\frac{kc\sqrt{1-\beta}}{\omega_{pe}}\Bigg[\left(\frac{\kappa^2\sin 2\theta}{2(1-\kappa^2\sin^2\theta)^{1/2}}-\frac{\kappa^2\sin 2\theta_0}{2(1-\kappa^2\sin^2\theta_0)^{1/2}}\right)\frac{dr}{dx_0}+\Bigg\{\frac{r\kappa\sin 2\theta}{(1-\kappa^2\sin^2\theta)^{1/2}}\\
&+\frac{r\kappa^3\sin^2\theta\sin 2\theta}{2(1-\kappa^2\sin^2\theta)^{3/2}}-\frac{r\kappa\sin 2\theta_0}{(1-\kappa^2\sin^2\theta_0)^{1/2}}-\frac{r\kappa^3\sin^2\theta_0\sin 2\theta_0}{2(1-\kappa^2\sin^2\theta_0)^{3/2}}\Bigg\}\frac{d\kappa}{dx_0}\\
&+\left\{\frac{2r\kappa^2\cos 2\theta}{2(1-\kappa^2\sin^2\theta)^{1/2}}+\frac{r\kappa^4\sin^2 2\theta}{4(1-\kappa^2\sin^2\theta)^{3/2}}\right\}\frac{\partial\theta}{\partial x_0}-\Bigg\{\frac{2r\kappa^2\cos 2\theta_0}{2(1-\kappa^2\sin^2\theta_0)^{1/2}}
\end{aligned}$$

$$+ \frac{r\kappa^4 \sin^2 2\theta_0}{4(1-\kappa^2\sin^2\theta_0)^{3/2}}\Bigg\}\frac{d\theta_0}{dx_0}\Bigg], \tag{B.26}$$

by carrying simple algebraic calculation gives

$$\begin{aligned} D =& 1 \mp \frac{kc\sqrt{1-\beta}}{\omega_{pe}}\Bigg[\left(\frac{\kappa^2\sin 2\theta}{2(1-\kappa^2\sin^2\theta)^{1/2}} - \frac{\kappa^2 \sin 2\theta_0}{2(1-\kappa^2\sin^2\theta_0)^{1/2}}\right)\frac{dr}{dx_0} \\ &+ r\kappa\frac{d\kappa}{dx_0}\left\{\frac{(2-\kappa^2\sin^2\theta)\sin 2\theta}{2(1-\kappa^2\sin^2\theta)^{3/2}} - \frac{(2-\kappa^2\sin^2\theta_0)\sin 2\theta_0}{2(1-\kappa^2\sin^2\theta_0)^{3/2}}\right\} \\ &+ r\kappa^2\frac{\partial\theta}{\partial x_0}\left\{\frac{\cos 2\theta+\kappa^2\sin^4\theta}{(1-\kappa^2\sin^2\theta)^{3/2}}\right\} - r\kappa^2\frac{d\theta_0}{dx_0}\left\{\frac{\cos 2\theta_0+\kappa^2\sin^4\theta_0}{(1-\kappa^2\sin^2\theta_0)^{3/2}}\right\}\Bigg], \end{aligned} \tag{B.27}$$

now eliminating dr/dx_0, dk/dx_0, $d\theta/dx_0$ and $\partial\theta_0/\partial x_0$ using the equations (B.14), (B.15), (B.17) and (B.27), yields

$$\begin{aligned} D =& 1 \mp \frac{\Delta'^2\, kc\sqrt{1-\beta}\,\sin 2kx_0}{\omega_{pe}}\Bigg[\Bigg\{\frac{\{4-3\kappa^2+\kappa^2(\kappa^2-2)\sin^2\theta\}\sin 2\theta}{4r\kappa^2(1-\beta)(1-\kappa^2\sin^2\theta)^{3/2}} \\ &- \frac{\{4-3\kappa^2+\kappa^2(\kappa^2-2)\sin^2\theta_0\}\sin 2\theta_0}{4r\kappa^2(1-\beta)(1-\kappa^2\sin^2\theta_0)^{3/2}}\Bigg\} \\ &+ \frac{4r\kappa^2(\kappa^2-1)\left(\cos 2\theta+\kappa^2\sin^4\theta\right)}{4\{r^4(\kappa^2-1)-1\}(1-\kappa^2\sin^2\theta)^2+\kappa^4\sin 2\theta+4\kappa^2\cos 2\theta(1-\kappa^2\sin^2\theta)} \\ &\Bigg\{-\frac{3r\tau}{\kappa^2(1-\beta)^{1/2}} + \frac{1+r^4+\kappa^2(1-r^4)}{r^2\kappa^4(1-\beta)(\kappa^2-1)}\Big\{E(\theta_0,\kappa)-E(\theta,\kappa)\Big\} + \left(\frac{r^4(\kappa^2-1)-1}{r^2\kappa^4(1-\beta)}\right) \\ &\left(F(\theta_0,\kappa^2)-F(\theta,\kappa^2)\right) - \frac{(\kappa^2(\kappa^2+1)\sin^2\theta_0-2)\sin 2\theta_0}{2r^2\kappa^2(1-\beta)(\kappa^2-1)(1-\kappa^2\sin^2\theta_0)^{3/2}} \\ &+ \frac{(\kappa^2(\kappa^2+1)\sin^2\theta-2)\sin 2\theta}{2r^2\kappa^2(1-\beta)(\kappa^2-1)(1-\kappa^2\sin^2\theta)^{3/2}} \\ &+ \frac{4\{r^4(\kappa^2-1)-1\}(1-\kappa^2\sin^2\theta_0)^2+\kappa^4\sin 2\theta_0+4\kappa^2\cos 2\theta_0(1-\kappa^2\sin^2\theta_0)}{4r^8\kappa^6(1-\beta)^2(\kappa^2-1)\sin 2\theta_0(1-\kappa^2\sin^2\theta_0)^{3/2}} \\ &\left(\left(\frac{p_0}{c}+\gamma_0\right)\left(1+\beta-r^4(1-\beta)\right)-2r^6(1-\beta)(1-\kappa^2)\right)\Bigg\} \\ &- \frac{\cos 2\theta_0+\kappa^2\sin^4\theta_0}{r^7\kappa^4(1-\beta)^2\sin 2\theta_0(1-\kappa^2\sin^2\theta_0)^{3/2}}\Bigg\{\left(\frac{p_0}{c}+\gamma_0\right)\left(1+\beta-r^4(1-\beta)\right) \\ &- 2r^6(1-\beta)(1-\kappa^2)\Bigg\}\Bigg]. \end{aligned} \tag{B.28}$$

Equation (B.28) can be rewritten as

$$D = 1 \mp \frac{kc\sqrt{1-\beta}}{\omega_{pe}} \Delta'^2 \sin 2kx_0 \Big(A1 + A2 - A3 \Big), \tag{B.29}$$

where

$$A1 = \frac{1}{4r\kappa^2(1-\beta)} \left[\frac{\Big((1-\kappa^2\sin^2\theta)(2-\kappa^2) + 2(1-\kappa^2) \Big) \sin 2\theta}{(1-\kappa^2\sin^2\theta)^{3/2}} \right. \tag{B.30a}$$
$$\left. - \frac{\Big((1-\kappa^2\sin^2\theta_0)(2-\kappa^2) + 2(1-\kappa^2) \Big) \sin 2\theta_0}{(1-\kappa^2\sin^2\theta_0)^{3/2}} \right],$$

$$A2 = \left(\frac{4(\kappa^2-1)(\cos 2\theta + \kappa^2\sin^4\theta)}{4(r^4(\kappa^2-1)-1)(1-\kappa^2\sin^2\theta)^2 + \kappa^4\sin^2 2\theta + 4\kappa^2\cos 2\theta(1-\kappa^2\sin^2\theta)} \right) \tag{B.30b}$$
$$\left[-\frac{3r^2\tau}{2\kappa^2(1-\beta)} + \frac{(r^4(\kappa^2-1)-1)}{(1-\beta)r^3(\kappa^2-1)} \left\{ \left(\frac{\kappa^2+1}{\kappa^2(\kappa^2-1)} \right) \Big(E(\theta_0,\kappa) - E(\theta,\kappa) \Big) + F(\theta_0,\kappa^2) \right. \right.$$
$$\left. - F(\theta,\kappa^2) \right\} + \frac{\Big(\kappa^2(\kappa^2+1)\sin^2\theta_0 - 2 \Big) \sin 2\theta_0}{2r(1-\beta)(1-\kappa^2\sin^2\theta_0)^{3/2}} - \frac{\Big(\kappa^2(\kappa^2+1)\sin^2\theta - 2 \Big) \sin 2\theta}{2r(1-\beta)(1-\kappa^2\sin^2\theta)^{3/2}}$$
$$+ \left\{ \left(\frac{p_0}{mc} + \gamma_0 \right) \Big(1 + \beta + (1-\beta)r^4 \Big) + 2r^6\kappa^2(\kappa^2-1)(1-\beta)^2 \right\}$$
$$\left. \left\{ \frac{4\Big(r^4(\kappa^2-1) - 1 \Big)(1-\kappa^2\sin^2\theta_0)^2 + \kappa^4\sin^2 2\theta_0 + 4\kappa^2\cos 2\theta_0(1-\kappa^2\sin^2\theta_0)}{4\, r^7\, \kappa^6\, (1-\beta)^3\, (\kappa^2-1) \sin 2\theta_0 (1-\kappa^2\sin^2\theta_0)^{3/2}} \right\} \right],$$

$$A3 = \frac{(\cos 2\theta_0 + \kappa^2\sin^4\theta_0)}{(1-\beta)^3 r^7\kappa^6 \sin 2\theta_0 (1-\kappa^2\sin^2\theta_0)^{3/2}} \left[2r^6\kappa^2(\kappa^2-1)(1-\beta)^2 + \Big\{ (1+\beta) \right. \tag{B.30c}$$
$$\left. + (1-\beta)r^4 \Big\} \left(\frac{p_0}{mc} + \gamma_0 \right) \right].$$

The relation between Eulerian and Lagrangian co-ordinate is given by,

$$
\begin{aligned}
kx =& kx_0 + k\int_0^\tau v_e(x_0,\tau^{'})d\tau^{'}, \\
kx =& kx_0 + k\int_0^\tau \frac{p_e}{\sqrt{1+\left(\frac{p_e}{mc}\right)^2}}d\tau^{'}, \\
kx =& kx_0 + k\int_0^\tau \left(-\frac{1}{\omega_{pe}^2}\frac{\partial^2 p_e}{\partial\tau^2}+v_0\right)d\tau^{'}, \\
kx =& kx_0 + kv_0\tau - \frac{k}{\omega_{pe}^2}\left[\frac{\partial p_e}{\partial\tau} - \frac{\partial p_e}{\partial\tau}\bigg|_{\tau=0}\right], \\
kx =& kx_0 + kv_0\tau \mp \frac{\sqrt{2}kc}{\omega_{pe}}\left[\left(a+\beta\frac{p_e}{mc}+\sqrt{1+\left(\frac{p_e}{mc}\right)^2}\right)^{1/2} - \left(a+\beta\frac{p_0}{mc}+\sqrt{1+\left(\frac{p_0}{mc}\right)^2}\right)^{1/2}\right], \\
kx =& kx_0 + kv_0\tau \mp \frac{kc\sqrt{1-\beta}}{\omega_{pe}}\left[\frac{r\kappa^2\sin 2\theta}{2(1-\kappa^2\sin^2\theta)^{1/2}} - \frac{r\kappa^2\sin 2\theta_0}{2(1-\kappa^2\sin^2\theta_0)^{1/2}}\right], \\
kx =& kx_0 + kv_0\tau \mp \frac{kc\,r\kappa^2\sqrt{1-\beta}}{\omega_{pe}}\left[\frac{\sin 2\theta}{2(1-\kappa^2\sin^2\theta)^{1/2}} - \frac{\sin 2\theta_0}{2(1-\kappa^2\sin^2\theta_0)^{1/2}}\right].
\end{aligned}
\tag{B.31}
$$

B.3 Solution Obtained Using Bogliubov-Mitropolaskii Method

In this appendix, we solve of equation (4.13) in the weakly relativistic limit using Bogoliubov-Mitrapolaskii [48] perturbation technique.

By Taylor expansion of denominator of second term of equation (4.13), yields

$$\frac{\partial^2 p_e}{\partial\tau^2} + \omega_{pe}^2 p_e\left(1-\frac{p_e^2}{2m^2c^2}\right) = m\omega_{pe}^2 v_0, \tag{B.32}$$

$$\frac{\partial^2 p_e}{\partial\tau^2} + \omega_{pe}^2 p_e = \frac{\omega_{pe}^2}{2m^2c^2}p_e^3 + m\omega_{pe}^2 v_0. \tag{B.33}$$

Solution for homogeneous part of the equation (B.33) can be written as

$$\frac{p_e(x_0,\tau)}{mc} = a\cos(\omega_{pe}\tau + \phi), \tag{B.34}$$

and the derivative w. r. t. time is given by

$$\frac{1}{mc}\frac{\partial p_e}{\partial \tau} = -a\omega_{pe}\sin(\omega_{pe}\tau + \phi). \tag{B.35}$$

We employ Bogoliubov-Mitropolaskii [48] perturbation technique to the solve the equation (B.33) by considering that a and ϕ are considered to be slow function of time, then the equations (B.34) and (B.35) can be rewritten in the normalized form as

$$p_e = a\cos(\omega_{pe}\tau + \phi) = a\cos\psi, \tag{B.36}$$

$$\frac{\partial p_e}{\partial \tau} = -a\sin(\omega_{pe}\tau + \phi) = -a\sin\psi, \tag{B.37}$$

where $\psi = \omega_{pe}\tau + \phi$. The normalization is followed as $p_e \to p_e/mc$, $\tau \to \omega_{pe}\tau$, $\beta \to v_0/c$.

Now the coefficient a and phase ϕ can be obtained [48] as follows

$$\frac{da}{d\tau} = -\frac{1}{2\pi}\int_0^{2\pi}\left(\frac{p_e^3}{2} + \beta\right)\sin\psi d\psi, \tag{B.38}$$

$$\begin{aligned}
\frac{da}{d\tau} &= -\frac{1}{2\pi}\int_0^{2\pi}\left(\frac{a^3}{2}\cos^3\psi + \beta\right)\sin\psi d\psi,\\
\frac{da}{d\tau} &= 0\\
a &= a_0.
\end{aligned} \tag{B.39}$$

$$\frac{d\phi}{d\tau} = -\frac{1}{2\pi}\int_0^{2\pi}\left(\frac{p_e^3}{2}+\beta\right)\cos\psi d\psi, \tag{B.40}$$

$$\begin{aligned}
\frac{d\phi}{d\tau} &= -\frac{1}{2\pi}\int_0^{2\pi}\left(\frac{a^3}{2}\cos^3\psi+\beta\right)\cos\psi d\psi,\\
\frac{d\phi}{d\tau} &= -\frac{3}{16}a_0^2,\\
\phi &= -\frac{3}{16}a_0^2\tau+\phi_0.
\end{aligned} \tag{B.41}$$

By eliminating a and ϕ using equations (B.39) and (B.41) from the equations (B.36) and (B.37) yields

$$\begin{aligned}
p_e &= a_0\cos\left(\tau-\frac{3}{16}a_0^2+\phi_0\right),\\
p_e &= a_0\cos\left(\tilde{\omega}_{pe}+\phi_0\right),
\end{aligned} \tag{B.42}$$

$$\frac{\partial p_e}{\partial \tau} = -a_0\sin\left(\tilde{\omega}_{pe}+\phi_0\right), \tag{B.43}$$

where $\tilde{\omega}_{pe} = 1-(3/16)a_0^2$.

Initial conditions are defined as

$$n_e(x_0,0) = n_0(1+\Delta\cos kx_0), \tag{B.44}$$

$$p_e(x_0,0) = p_0. \tag{B.45}$$

Using the initial conditions (B.44) and (B.45), a_0 and ϕ_0 and $\tilde{\omega}_{pe}$ are determined as

$$a_0 = \pm\sqrt{p_0^2+\Delta'^2\sin^2 kx_0}, \tag{B.46}$$

$$\phi_0 = \cos^{-1}\left(\frac{p_0}{a_0}\right), \tag{B.47}$$

$$\tilde{\omega}_{pe} = 1-\frac{3}{16}\left(p_0^2+\Delta'^2\sin^2 kx_0\right), \tag{B.48}$$

then the spatial derivatives of a_0 and ϕ_0 and $\tilde{\omega}_{pe}$ is given by

$$\frac{da_0}{dx_0} = \frac{\Delta^{'2}}{2a_0}\sin 2kx_0, \tag{B.49}$$

$$\frac{d\phi_0}{dx_0} = \frac{\Delta^{'}p_0}{a_0^2}\cos kx_0, \tag{B.50}$$

$$\frac{d\tilde{\omega}_{pe}}{dx_0} = -\frac{3}{16}\Delta^{'2}\sin 2kx_0. \tag{B.51}$$

Electron density can be obtained as follows

$$n_e(x_0,\tau) = \frac{n(x_0,0)}{D1}, \tag{B.52}$$

where

$$\begin{aligned}
D1 &= 1 + \frac{\partial}{\partial x_0}\int_0^{\tau} v_e(x_0,\tau^{'})d\tau^{'}, \\
D1 &= 1 - \frac{ck}{\omega_{pe}}\frac{\partial}{\partial x_0}\left(\frac{\partial p_e}{\partial \tau} - \left.\frac{\partial p_e}{\partial \tau}\right|_{\tau=0}\right), \\
D1 &= 1 - \frac{ck}{\omega_{pe}}\frac{\partial}{\partial x_0}\left(-a_0\sin(\tilde{\omega}_{pe}\tau+\phi_0) + a_0\sin\phi_0\right), \\
D1 &= 1 - \frac{ck}{\omega_{pe}}\left[-\frac{da_0}{dx_0}\sin(\tilde{\omega}_{pe}\tau+\phi_0) - a_0\sin(\tilde{\omega}_{pe}\tau+\phi_0)\left\{\tau\frac{d\tilde{\omega}_{pe}}{dx_0} + \frac{d\phi_0}{dx_0}\right\}\right. \\
&\quad \left. + \frac{da_0}{dx_0}\sin\phi_0 + a_0\cos\phi_0\frac{d\phi_0}{dx_0}\right],
\end{aligned} \tag{B.53}$$

eliminating da_0/dx_0, $d\phi_0/dx_0$ and $d\tilde{\omega}_{pe}/dx_0$ using equations (B.49), (B.50) and (B.51), then equation (B.52) becomes

$$\begin{aligned}
D1 = 1 - \Delta\cos kx_0\Bigg[&\frac{p_0^2}{a_0^2} + \frac{\Delta^{'2}}{a_0^2}\sin^2 kx_0 - \frac{\Delta^{'}}{a_0}\sin kx_0\sin(\tilde{\omega}_{pe}\tau+\phi_0) - \cos(\tilde{\omega}_{pe}\tau+\phi_0) \\
&\left\{\frac{p_0}{a_0} - \frac{3}{8}\Delta^{'}a_0\tau\sin kx_0\right\}\Bigg],
\end{aligned} \tag{B.54}$$

$$D1 = 1 - \Delta\cos kx_0\left[\frac{p_0^2}{a_0^2}(1-\cos\tilde{\omega}_{pe}\tau) + \frac{\Delta^{'2}}{a_0^2}\sin^2 kx_0\left(1 - \cos\tilde{\omega}_{pe}\tau - \frac{3}{8}a_0^2\tau\sin\tilde{\omega}_{pe}\tau\right)\right.$$

$$
+ \frac{3}{8}\Delta^{'} p_0 \tau \sin kx_0 \cos \tilde{\omega}_{pe}\tau \Bigg]. \tag{B.55}
$$

The relation between Eulerian x and Lagrangian x_0 position co-ordinates is given by

$$
\begin{aligned}
kx &= kx_0 + \frac{k}{\omega_{pe}} \int_0^{\tau} v_e(x_0, \tau^{'}) d\tau^{'}, \\
kx &= kx_0 + \frac{k}{\omega_{pe}} \int_0^{\tau} \frac{p_e}{\sqrt{1 + \left(\frac{p_e}{mc}\right)^2}} d\tau^{'}, \\
kx &= kx_0 + kv_0\tau - \frac{kc}{\omega_{pe}} \Bigg[- a_0 \sin(\tilde{\omega}_{pe}\tau + \phi_0) + a_0 \sin \phi_0 \Bigg], \\
kx &= kx_0 + kv_0\tau + \frac{\Delta p_0}{c} \sin \tilde{\omega}_{pe}\tau - \Delta \sin kx_0 (1 - \cos \tilde{\omega}_{pe}\tau).
\end{aligned} \tag{B.56}
$$

APPENDIX C

Solution of fourth order dispersion relation for Buneman instability

Linear dispersion relation can be written as

$$x^4 - 2x^3 - \alpha x^2 + 2\alpha x - \alpha = 0, \tag{C.1}$$

where $x = \omega/\omega_{pe}$ and $\alpha = m/M$. Equation is a fourth order polynomial. In this appendix we shall solve fourth order polynomial (C.1), using method given in Abramowitz & Stegun [124]. Coefficients of the quartic equation are written as $a_0 = -\alpha$, $a_1 = 2\alpha$, $a_2 = -\alpha$, $a_3 = -2$ and $a_4 = 1$. Quartic equation can be reduced in cubic equation as

$$z^3 + \alpha z^2 + 4\alpha = 0, \tag{C.2}$$

or

$$b_3 z^3 + b_2 z^2 + b_0 \alpha = 0, \tag{C.3}$$

where coefficients of cubic equation (C.2) are $b_0 = 4\alpha$, $b_1 = 0$, $b_2 = \alpha$ and $b_3 = 1$. For finding the roots of equation (C.2), lets consider

$$q = \frac{b_1}{3} - \frac{b_2^2}{9} = -\frac{\alpha^2}{9},$$

and

$$r = \frac{1}{6}(b_1 b_2 - 3b_0) - \frac{b_2^3}{3} = -2\alpha - \frac{\alpha^3}{27}.$$

Then roots of equation (C.2) can be written as

$$\begin{aligned} z_1 &= (s_1 + s_2) - \frac{b2}{3}, \\ z_2 &= -\frac{1}{2}(s_1 + s_2) - \frac{b_2}{3} + \frac{\iota\sqrt{3}}{2}(s_1 - s_2), \\ z_3 &= -\frac{1}{2}(s_1 + s_2) - \frac{b_2}{3} - \frac{\iota\sqrt{3}}{2}(s_1 - s_2), \end{aligned} \tag{C.4}$$

where s_1 and s_2 are given by

$$s_1 = [r + (q^3 + r^2)^{1/2}]^{1/3} = 0, \tag{C.5}$$

$$s_2 = [r - (q^3 + r^2)^{1/2}]^{1/3} = (-1)^{1/3}\, 2^{2/3}\, \alpha^{1/3}, \tag{C.6}$$

taking only real root of s_2

$$s_2 = -2^{2/3}\, \alpha^{1/3}. \tag{C.7}$$

Then roots of the cubic equation (C.2) can be written as

$$z_1 = -2^{2/3}\, \alpha^{1/3} - \frac{\alpha}{3}, \tag{C.8}$$

$$z_2 = \frac{\alpha^{1/3}}{2^{1/3}} - \frac{\iota\sqrt{3}}{2^{1/3}}\alpha^{1/3} - \frac{\alpha}{3}, \tag{C.9}$$

$$z_2 = \frac{\alpha^{1/3}}{2^{1/3}} - \frac{\iota\sqrt{3}}{2^{1/3}}\alpha^{1/3} - \frac{\alpha}{3}. \tag{C.10}$$

Now the four roots of quartic equation (C.1) can be determined by the solution of following two quadratic equations,

$$y^2 + \left[\frac{a_3}{4} \mp \left(\frac{a_3^2}{4} + z_1 - a_2\right)^{1/2}\right] y + \frac{z1}{2} \mp \left[\left(\frac{z_1}{2}\right)^2 - a_0\right]^{1/2} = 0. \tag{C.11}$$

First, taking positive sign gives the equation,

$$y^2 + \left[\frac{a_3}{4} + \left(\frac{a_3^2}{4} + z_1 - a_2\right)^{1/2}\right] y + \frac{z1}{2} + \left[\left(\frac{z_1}{2}\right)^2 - a_0\right]^{1/2} = 0, \tag{C.12}$$

elimination of a_3 and z_1 from the equation (C.12), yields

$$y^2 + \left[-1 + \left(1 - \frac{2\alpha}{3} - 2^{2/3}\,\alpha^{1/3}\right)^{1/2}\right] y - \frac{\alpha^{1/3}}{2^{1/3}} - \frac{\alpha}{6} + \left[\left(\frac{\alpha^{1/3}}{2^{1/3}} + \frac{\alpha}{6}\right)^2 + \alpha\right]^{1/2} = 0, \tag{C.13}$$

assuming $\alpha << \alpha^{1/3} \leq 1$, equation (C.13) takes the form

$$y^2 + \left[\frac{\alpha}{3} - \frac{\alpha^{1/3}}{2^{1/3}}\right] y - \frac{\alpha^{1/3}}{2^{1/3}} - \frac{\alpha}{6} + \left[\left(\frac{\alpha^{1/3}}{2^{1/3}} + \frac{\alpha}{6}\right)^2 + \alpha\right]^{1/2} = 0, \tag{C.14}$$

neglecting the terms $\mathcal{O}(\alpha^2)$ and above, we get

$$y^2 + \left[\frac{\alpha}{3} - \frac{\alpha^{1/3}}{2^{1/3}}\right] y + \frac{\alpha^{2/3}}{2^{2/3}} - \frac{\alpha}{6} = 0. \tag{C.15}$$

Then the two roots of above written quadratic equation are given by

$$\begin{aligned}
y_{1,2} &= \frac{1}{2}\left[\left(-\frac{\alpha}{3} + \frac{\alpha^{1/3}}{2^{1/3}}\right) \pm \left\{\left(-\frac{\alpha}{3} + \frac{\alpha^{1/3}}{2^{1/3}}\right)^2 - 4\left(+\frac{\alpha^{2/3}}{2^{2/3}} - \frac{\alpha}{6}\right)\right\}^{1/2}\right], \\
&= \frac{1}{2}\left[\left(-\frac{\alpha}{3} + \frac{\alpha^{1/3}}{2^{1/3}}\right) \pm \left(\frac{2\alpha}{3} - \frac{3\alpha^{2/3}}{2^{2/3}}\right)^{1/2}\right], \\
&= -\frac{\alpha}{6} + \frac{\alpha^{1/3}}{2^{4/3}} \pm \iota\frac{\sqrt{3}\alpha^{1/3}}{2^{4/3}} \mp \iota\frac{\alpha^{2/3}}{32^{2/3}\sqrt{3}}, \\
y_{1,2} &= (1 \pm \iota\sqrt{3})\,\frac{\alpha^{1/3}}{2^{4/3}},
\end{aligned} \tag{C.16}$$

Taking negative sign of equation (C.11), gives,

$$y^2 + \left[\frac{a_3}{4} - \left(\frac{a_3^2}{4} + z_1 - a_2\right)^{1/2}\right] y + \frac{z1}{2} - \left[\left(\frac{z_1}{2}\right)^2 - a_0\right]^{1/2} = 0, \tag{C.17}$$

now putting the values of a_3 and z_1, yields,

$$y^2 + \left[-1 - \left(1 - \frac{2\alpha}{3} - 2^{2/3}\,\alpha^{1/3}\right)^{1/2}\right] y - \frac{\alpha^{1/3}}{2^{1/3}} - \frac{\alpha}{6} - \left[\left(\frac{\alpha^{1/3}}{2^{1/3}} + \frac{\alpha}{6}\right)^2 + \alpha\right]^{1/2} = 0, \tag{C.18}$$

$$y^2 + \left[-2 + \frac{2\alpha}{3} + \frac{\alpha^{1/3}}{2^{1/3}}\right] y - 2^{2/3}\alpha^{1/3} - \frac{\alpha^{2/3}}{2^{5/3}} - \frac{\alpha}{6} = 0, \tag{C.19}$$

then the two roots of the above written quadratic equation are given by

$$\begin{aligned} y_{3,4} &= \frac{1}{2}\left[-2 + \frac{2\alpha}{3} + \frac{\alpha^{1/3}}{2^{1/3}} \pm \left\{\left(-2 + \frac{2\alpha}{3} + \frac{\alpha^{1/3}}{2^{1/3}}\right)^2 - 4\left(-2^{2/3}\alpha^{1/3} - \frac{\alpha^{2/3}}{2^{5/3}} - \frac{\alpha}{6}\right)\right\}^{1/2}\right], \\ y_{3,4} &= \frac{1}{2}\left[-2 + \frac{2\alpha}{3} + \frac{\alpha^{1/3}}{2^{1/3}} \pm \left(2 - \alpha + \frac{\alpha^{2/3}}{2^{8/3}} + \frac{\alpha^{1/3}}{2^{1/3}}\right)\right], \end{aligned} \tag{C.20}$$

which turns out to be real always.

Thus the roots of the quartic equation (C.1) can be written as

$$\begin{aligned} \omega &= (1 \pm \iota\sqrt{3})\left(\frac{m}{16M}\right)^{1/3} \omega_{pe}, \\ \omega &= \frac{\omega_{pe}}{2}\left[-2 + \frac{2}{3}\left(\frac{m}{M}\right) + \left(\frac{m}{2M}\right)^{1/3} \pm \left(2 - \frac{m}{M} + \left(\frac{m}{4M}\right)^{2/3} + \left(\frac{m}{2M}\right)^{1/3}\right)\right]. \end{aligned} \tag{C.21}$$

References

[1] *Introduction to Plasma Physics and Controlled Fusion*. Plenum, New York, 1984.

[2] *Plasma Instabilities and Nonlinear Effects*. Springer-Verlag Berlin Heidelberg, 1975.

[3] M A Malkov and L O'C Drury. In: *Reports on Progress in Physics* 64.4 (), p. 429.

[4] T. Amano and M. Hoshino. In: *The Astrophysical Journal* 661.1 (2007), p. 190.

[5] Takanobu Amano and Masahiro Hoshino. In: *Physics of Plasmas* 16.10, 102901 (2009).

[6] L. Yin et al. In: *Physics of Plasmas* 14.5, 056706 (2007).

[7] B. J. Albright et al. In: *Physics of Plasmas* 14.9, 094502 (2007).

[8] A. Bret and M. E. Dieckmann. In: *Physics of Plasmas* 15.1, 012104 (2008).

[9] A Bret. In: *Physica Scripta* 84.6 (2011), p. 065507.

[10] A. Bret. In: *The Astrophysical Journal* 699.2 (2009), p. 990.

[11] A. Bret and M. E. Dieckmann. In: *Physics of Plasmas* 17.3, 032109 (2010).

[12] A. Bret, L. Gremillet, and M. E. Dieckmann. In: *Physics of Plasmas* 17.12, 120501 (2010).

[13] D.R. Nicholson. *Introduction to plasma theory*. Wiley series in plasma physics. Wiley, 1983.

[14] Albritton J. In: *Nucl. Fusion* 15 (1975), p. 1199.

[15] Prabal Singh Verma, Sudip Sengupta, and Predhiman Kaw. In: *Physics of Plasmas* 19.3 (2012), p. 032110.

[16] Akhiezer A. I. In: *Dokl. Acad. Nauk. SSSR* 80 (1951), p. 193.

[17] Infeld E. In: *Phys. Rev. Lett.* 62 (1989), p. 1122.

[18] H. S. C. Wang. In: *The Physics of Fluids* 6.8 (1963), pp. 1115–1123.

[19] Michalis Psimopoulos and Sevim Tanriverdi. In: *Physics of Plasmas* 4.1 (1997), pp. 230–238.

[20] R.W.C. Davidson and P.P.J.M. Schram. In: *Nuclear Fusion* 8.3 (1968), p. 183.

[21] Abraham C L Chian. In: *Astrophys. Space Sci.* 97 (1985), p. 9.

[22] Mitchell C. Begelman, Roger D. Blandford, and Martin J. Rees. In: *Rev. Mod. Phys.* 56 (2 1984), pp. 255–351.

[23] Abraham C.-L. Chian. In: *Physics Letters A* 73.3 (1979), pp. 180 –182.

[24] Abraham C L Chian. In: *Plasma Physics* 21.6 (1979), p. 509.

[25] Abraham C. L. Chian. In: *Phys. Rev. A* 39 (5 1989), pp. 2561–2564.

[26] O. Buneman. In: *Phys. Rev.* 115 (3 1959), pp. 503–517.

[27] E. Atlee Jackson. In: *The Physics of Fluids* 3.5 (1960), pp. 786–792.

[28] N Singh. In: *Plasma Physics* 24.6 (1982), p. 639.

[29] Predhiman Kaw, Sudip Sengupta, and Prabal Singh Verma. In: *Physics of Plasmas* 19.10, 102109 (2012).

[30] Max Tabak et al. In: *Physics of Plasmas* 1.5 (1994).

[31] M. Tabak et al. In: *Physics of Plasmas* 12.5, 057305 (2005).

[32] M. Hoshino and N. Shimada. In: *The Astrophysical Journal* 572.2 (2002), p. 880.

[33] Nobue Shimada and Masahiro Hoshino. In: *Physics of Plasmas* 10.4 (2003).

[34] M. E. Dieckmann et al. In: *Physics of Plasmas* 7.12 (2000).

[35] M E Dieckmann et al. In: *Plasma Physics and Controlled Fusion* 54.8 (2012), p. 085015.

[36] R. A. Treumann, R. Nakamura, and W. Baumjohann. In: *Annales Geophysicae* 28.10 (2010), pp. 1935–1943.

[37] J. F. Drake et al. In: *Science* 299.5608 (2003), pp. 873–877.

[38] H. Che. In: *Physics of Plasmas* 24.8 (2017), p. 082115.

[39] A Hirose. In: *Plasma Physics* 20.5 (1978), p. 481.

[40] Charles J. Bartlett. In: *The Physics of Fluids* 11.4 (1968), pp. 822–831.

[41] O. Ishihara, A. Hirose, and A. B. Langdon. In: *Phys. Rev. Lett.* 44 (21 1980), pp. 1404–1407.

[42] O. Ishihara, A. Hirose, and A. B. Langdon. In: *Physics of Fluids* 24.3 (1981).

[43] Guo Jun. In: *Plasma Science and Technology* 15.4 (2013), p. 307.

[44] Roopendra Singh Rajawat and Sudip Sengupta. In: *Physics of Plasmas* 24.12 (2017), p. 122103.

[45] Y. Omura, H. Kojima, and H. Matsumoto. In: *Geophysical Research Letters* 21.25 (1994), pp. 2923–2926.

[46] Koichi Saeki and Hitoshi Genma. In: *Phys. Rev. Lett.* 80 (6 1998), pp. 1224–1227.

[47] R.C. Davidson. *Methods in nonlinear plasma theory.* Pure and Applied Physics Series. Academic Press, 1972.

[48] N.N. Bogoliiÿăuiÿąbov and MitropolÊźskiĭ. *Asymptotic Methods in the Theory of Non-linear Oscillations.*

[49] J J Honrubia and J Meyer ter Vehn. In: *Plasma Physics and Controlled Fusion* 51.1 (2009), p. 014008.

[50] A.P.L. Robinson et al. In: *Nuclear Fusion* 54.5 (), p. 054003.

[51] P. H. Yoon. In: *Physics of Plasmas* 17.11, 112316 (2010).

[52] P. H. Yoon and T. Umeda. In: *Physics of Plasmas* 17.11, 112317 (2010).

[53] F. Haas, B. Eliasson, and P. K. Shukla. In: *Phys. Rev. E* 86 (3 2012), p. 036406.

[54] M. Hashemzadeh, A.R. Niknam, and D. Komaizi. In: *Waves in Random and Complex Media* 23.4 (2013), pp. 383–395.

[55] Roopendra Singh Rajawat and Sudip Sengupta. In: *Physics of Plasmas* 23.10, 102110 (2016).

[56] Irving Langmuir. In: *Phys. Rev.* 26 (5 1925), pp. 585–613.

[57] D. Bohm and E. P. Gross. In: *Phys. Rev.* 75 (12 1949), pp. 1851–1864.

[58] D. Bohm and E. P. Gross. In: *Phys. Rev.* 75 (12 1949), pp. 1864–1876.

[59] J. R. Pierce. In: *Journal of Applied Physics* 19.3 (1948), pp. 231–236.

[60] O. Buneman. In: *Phys. Rev. Lett.* 1 (1 1958), pp. 8–9.

[61] Erich S. Weibel. In: *Phys. Rev. Lett.* 2 (3 1959), pp. 83–84.

[62] Burton D. Fried. In: *The Physics of Fluids* 2.3 (1959), pp. 337–337.

[63] A. Bret, L. Gremillet, and J. C. Bellido. In: *Physics of Plasmas* 14.3 (2007), p. 032103.

[64] G. Kalman, C. Montes, and D. Quemada. In: *The Physics of Fluids* 11.8 (1968), pp. 1797–1808.

[65] Godfrey B. B. In: *Phys. Fluids* 18 (1975), p. 346.

[66] A. Bret, M. E. Dieckmann, and C. Deutsch. In: *Physics of Plasmas* 13.8 (2006), p. 082109.

[67] A. Bret, M.-C. Firpo, and C. Deutsch. In: *Phys. Rev. E* 70 (4 2004), p. 046401.

[68] A. Bret and C. Deutsch. In: *Physics of Plasmas* 13.2, 022110 (2006).

[69] M. Lazar, R. Schlickeiser, and P. K. Shukla. In: *Physics of Plasmas* 13.10, 102107 (2006).

[70] Y. Omura et al. In: *Journal of Geophysical Research: Space Physics* 108.A5 (2003). 1197, n/a–n/a.

[71] Ira B. Bernstein, John M. Greene, and Martin D. Kruskal. In: *Phys. Rev.* 108 (3 1957), pp. 546–550.

[72] Prabal Singh Verma, Sudip Sengupta, and Predhiman Kaw. In: *Phys. Rev. Lett.* 108 (12 2012), p. 125005.

[73] Akhiezer A. I. In: *Sov. Phys. JETP* 3 (1956), p. 696.

[74] John M. Dawson. In: *Phys. Rev.* 113 (2 1959), pp. 383–387.

[75] Sudip Sengupta et al. In: *Phys. Rev. E* 79 (2 2009), p. 026404.

[76] Hari K. Sen. In: *Phys. Rev.* 97 (4 1955), pp. 849–855.

[77] R Kodama et al. In: *NATURE* 412 (2001), pp. 798–802.

[78] K. Shigemori Y. Toyama S. Fujioka H. Azechi H. Fujita H. Habara T. Hall Y. Izawa T. Jitsuno Y. Kitagawa K. M. Krushelnick K. L. Lancaster K. Mima K. Nagai M. Nakai H. Nishimura T. Norimatsu P. A. Norreys S. Sakabe K. A. Tanaka A. Youssef M. Zepf R. Kodama H. Shiraga and T. Yamanaka. In: *NATURE* 418 (2002), pp. 933–934.

[79] J D Jackson. In: *Journal of Nuclear Energy. Part C, Plasma Physics, Accelerators, Thermonuclear Research* 1.4 (1960), p. 171.

[80] T D Mantei, F Doveil, and D Gresillon. In: *Plasma Physics* 18.9 (1976), p. 705.

[81] R. C. Davidson et al. In: *Phys. Rev. Lett.* 24 (11 1970), pp. 579–582.

[82] Setsuo Ichimaru. In: *Journal of the Physical Society of Japan* 39.1 (1975), pp. 261–262.

[83] J.A. Ionson. In: *Physics Letters A* 60.1 (1977), pp. 27 –28.

[84] B. Shokri and A. R. Niknam. In: *Physics of Plasmas* 12.6, 062110 (2005).

[85] M M Hatami, B Shokri, and A R Niknam. In: *Physica Scripta* 82.6 (2010), p. 065503.

[86] Neeraj Jain, Takayuki Umeda, and Peter H Yoon. In: *Plasma Physics and Controlled Fusion* 53.2 (2011), p. 025010.

[87] A. R. Niknam, D. Komaizi, and M. Hashemzadeh. In: *Physics of Plasmas* 18.2, 022301 (2011).

[88] H. Che et al. In: *Physics of Plasmas* 20.6, 061205 (2013).

[89] Koichi Saeki and J. Juul Rasmussen. In: *Journal of the Physical Society of Japan* 60.3 (1991), pp. 735–738.

[90] M. Hashemzadeh and A. R. Niknam. In: *Physics of Plasmas* 21.9, 092309 (2014).

[91] M Hashemzadeh. In: *Plasma Physics and Controlled Fusion* 57.11 (2015), p. 115002.

[92] M. Hashemzadeh. In: *Physica A: Statistical Mechanics and its Applications* 459 (2016), pp. 68 –77.

[93] Kh.H. El-Shorbagy. In: *Physics Letters A* 372.9 (2008), pp. 1494 –1497.

[94] A. Hirose, O. Ishihara, and A. B. Langdon. In: *The Physics of Fluids* 25.4 (1982), pp. 610–616.

[95] J.P. Boris et al. *LCPFCT-A Flux-Corrected Transport Algorithm for Solving Generalized Continuity Equations*. Defense Technical Information Center, 1993.

[96] *C. K. Birdsall and A. B. Langdon, Plasma Physics via Computer Simulation*. Hilger, NewYork, 1991.

[97] R. W. Hockney and J. W. Eastwood. *Computer Simulation Using Particles*. Bristol, PA, USA: Taylor & Francis, Inc., 1988.

[98] Sudip Sengupta. *Private Communication*. IPR, INDIA, 2012.

[99] William H. Press et al. *Numerical Recipes 3rd Edition: The Art of Scientific Computing*. 3rd ed. New York, NY, USA: Cambridge University Press, 2007.

[100] J. F. Drake et al. In: *Phys. Rev. Lett.* 36 (4 1976), pp. 196–200.

[101] A. Modena et al. In: *Nature* 377 (1995), p. 606.

[102] V. Malka et al. In: *Science* 298.5598 (2002), pp. 1596–1600.

[103] A. Bret, L. Gremillet, and M. E. Dieckmann. In: *Physics of Plasmas* 17.12, 120501 (2010).

[104] H. de Kluiver, N.F. Perepelkin, and A. Hirose. In: *Physics Reports* 199.6 (1991), pp. 281 –381.

[105] Sircombe, N. J. et al. In: *A&A* 452.2 (2006), pp. 371–381.

[106] R. Bandara and J. Khachan. In: *Physics of Plasmas* 22.8, 082701 (2015).

[107] Martin Lampe et al. In: *Physics of Fluids* 17.2 (1974).

[108] J. Pavan, P. H. Yoon, and T. Umeda. In: *Physics of Plasmas* 18.4, 042307 (2011).

[109] H. Che. In: *Physics of Plasmas* 21.6, 062305 (2014).

[110] F. Haas, B. Eliasson, and P. K. Shukla. In: *Phys. Rev. E* 86 (3 2012), p. 036406.

[111] A. Bret, M. E. Dieckmann, and L. Gremillet. In: *Annales Geophysicae* 28.11 (2010), pp. 2127–2132.

[112] S. A. Bludman, K. M. Watson, and M. N. Rosenbluth. In: *Physics of Fluids* 3.5 (1960).

[113] D. T. Farley. In: *Journal of Geophysical Research* 68.2 (1963), pp. 401–413.

[114] O. Buneman. In: *Phys. Rev. Lett.* 10 (7 1963), pp. 285–287.

[115] PH Yoon et al. “Anomalous resistivity from Buneman instability: Theory and simulation”. In: *AGU Fall Meeting Abstracts*. Vol. 1. 2010, p. 08.

[116] S. Machida and C. K. Goertz. In: *Journal of Geophysical Research: Space Physics* 93.A9 (1988), pp. 9993–10000.

[117] K.-I. NISHIKAWA et al. In: *International Journal of Modern Physics D* 17.10 (2008), pp. 1761–1767.

[118] *Advances in Plasma Physics*. John Wiley and Sons, New York, 1971.

[119] L. E. Thode and R. N. Sudan. In: *Phys. Rev. Lett.* 30 (16 1973), pp. 732–735.

[120] M. Gedalin et al. In: *Physics of Plasmas* 17.3, 032108 (2010).

[121] V. Yu. Mart'yanov, V. V. Kocharovsky, and Vl. V. Kocharovsky. In: *Journal of Experimental and Theoretical Physics* 107.6 (2008), pp. 1049–1060.

[122] L F Ziebell et al. In: *Plasma Physics and Controlled Fusion* 50.8 (2008), p. 085011.

[123] Mark E. Dieckmann and Antoine Bret. In: *The Astrophysical Journal* 694.1 (2009), p. 154.

[124] M. Abramowitz and I.A. Stegun. *Handbook of Mathematical Functions: With Formulas, Graphs, and Mathematical Tables*. Applied mathematics series. Dover Publications, 1964.